Imperial College London
Department of Mechanical Engineering

Advanced methods for multi-row forced response and flutter computations

Sina Cornelia Stapelfeldt

January 29, 2014

Submitted in part fulfilment of the requirements for the degree of
Doctor of Philosophy in Mechanical Engineering of Imperial College London
and the Diploma of Imperial College London

Declaration

The work presented in this thesis is, to the best of the candidate's knowledge, original and the candidate's own work, except as acknowledged in the text. The material has not been submitted, either in whole or in part, for a degree or comparable award of Imperial College or any other university or institution.

Sina Stapelfeldt
January 2014

Abstract

This thesis presents the formulation and validation of a novel time-accurate method for the computation of forced response and flutter in multiple blade row turbomachinery.

Advanced gas turbine and aeroengine designs require unsteady computational methods to predict aeroelastic behaviour and prevent the occurrence of flutter or forced response which could ultimately lead to engine failure. Currently, time-accurate schemes can successfully represent unsteady flows across multiple blade rows if the domain encompasses the full circumference. However, the large domain size and range of time scales involved make this approach very expensive and unfeasible during the design cycle. More efficient methods take advantage of the inherent time-space periodicity in turbomachines to reduce the computational domain to a single bladed passage per row. These single-passage multi-row methods successfully model unsteadiness due to rotor-stator interaction or blade vibration by applying phase-lagged boundary conditions. However, they are limited to assemblies without passage-to-passage variations in the time-averaged flow field. In multi-stage turbomachinery, where the interaction of rows with unequal blade counts in the same frame of reference creates steady circumferential variations, single-passage methods cannot be applied as no phase-shifted temporal periodicity exists between adjacent passages. Similarly, it is not possible to represent non-axisymmetries such as inlet distortions or stagger profiles using a single passage approach. The time-domain Fourier method presented in this thesis models multi-row non-axisymmetric flows on a reduced number of passages. In order to capture stationary variations, the flow inside several discrete passages, which are located at different circumferential positions, is solved using a time-accurate scheme. Boundary conditions at the azimuthal and inter-row surfaces are approximated from a time-space Fourier series and couple the individual passages.

The method is validated for several applications including low engine order forcing in an aerodynamically mistuned assembly and rotor-rotor interaction. It is demonstrated that, within the limit of the Fourier approximation, the resulting solution is equivalent to the full circumference solution and requires only a fraction of the computational resources.

To my parents

Acknowledgements

Firstly, I would like to express my gratitude to my supervisor Dr. Luca di Mare for the opportunity to carry out this project and for his technical support throughout my studies. Much of my understanding of the subject, the project and the code is owed to him.

I also gratefully acknowledge Rolls-Royce plc for providing financial support toward this research. Additionally, particular thanks must go to Jeff Green, Paolo Adami and Arrigo Beretta for their valuable advice and guidance. Their input has substantially influenced the direction of my work and provided boosts of motivation for which I am very grateful.

Thanks are also due to Peter Higgs, who, in addition to taking care of all administrative matters during my time as a research student, took the time to read this thesis and improve its comprehensibility.

I would also like to thank my colleagues at the VUTC and in the Department of Aeronautics for assisting with technical issues and for creating a pleasant working environment. Among many others, who cannot all be named but know who they are, the ice-cream break enthusiasts in E256 deserve to be acknowledged for making the last four years merry ones.

Finally, I am extremely grateful to my sister for her cheerful emails and to my parents for their support, encouragement and everything else.

Contents

1. Introduction **26**
1.1. Background and Motivation . . . 26
1.2. Flow in axial compressors and turbines . . . 27
1.2.1. Three-dimensional flow features . . . 27
1.2.2. Potential Disturbances . . . 29
1.2.3. Wakes . . . 29
1.2.4. Shock waves . . . 31
1.3. The disturbance environment . . . 32
1.3.1. Rotor-stator interaction . . . 32
1.3.2. Rotor-rotor/stator-stator interaction . . . 34
1.3.3. Structural vibration patterns . . . 35
1.3.4. Other sources of circumferential non-uniformity . . . 36
1.3.5. Uncorrelated unsteadiness . . . 38
1.4. Aeroelasticity . . . 39
1.4.1. Definition . . . 39
1.4.2. Static aeroelasticity . . . 40
1.4.3. Dynamic aeroelasticity . . . 40
1.4.3.1. Forced response . . . 40
1.4.3.2. Flutter . . . 42
1.4.4. Aeroelastic stability and reduced frequency . . . 43
1.5. Summary . . . 44

2. Review of prediction methods for unsteady flows in turbomachinery **45**
2.1. Steady mixing plane approach . . . 47
2.2. Classical methods . . . 47
2.3. Time-linearised methods . . . 48
2.4. Non-linear frequency domain methods for axisymmetric flows . . . 50
2.4.1. SLIQ Approach . . . 51
2.4.2. Non-linear harmonic method . . . 51

2.4.3. Harmonic balance and time spectral techniques . . . 53
2.4.4. Time-linearised multi-row method . . . 54
2.5. Non-linear time-domain methods . . . 55
2.5.1. Multi-passage methods . . . 55
2.5.1.1. Whole annulus and periodic sector . . . 55
2.5.1.2. Modified blade counts . . . 55
2.5.1.3. Blade row interface treatment . . . 56
2.5.2. Single passage methods for axisymmetric flows . . . 56
2.5.2.1. Direct store method . . . 57
2.5.2.2. Time-inclination . . . 58
2.5.2.3. Shape correction method . . . 59
2.5.2.4. Gerolymos' partial substitution technique . . . 61
2.5.2.5. Single-passage multi-row shape correction . . . 63
2.5.2.6. Prescribed distortion . . . 64
2.6. Non-linear methods for non-axisymmetric flows . . . 65
2.6.1. Modified blade counts . . . 65
2.6.2. Interface disturbance truncation technique . . . 67
2.6.3. Frequency domain single passage . . . 68
2.6.4. Time-domain Fourier model . . . 69
2.7. Summary . . . 70

3. Objectives **72**

4. Methodology **75**
4.1. Time-domain Fourier approach . . . 75
4.1.1. Overview . . . 75
4.1.2. Definition: Temporal and circumferential averages . . . 76
4.1.3. Expression of chorochronic periodicity . . . 77
4.1.3.1. Unsteady fluctuations . . . 78
4.1.3.2. Stationary disturbance . . . 80
4.1.3.3. Circumferentially distorted travelling disturbance . . . 82
4.1.4. Grid creation and post-processing . . . 84
4.1.4.1. Sparse assembly grids . . . 84
4.1.4.2. Post-processing . . . 85
4.2. Multi-row coupling . . . 86
4.2.1. Blade row interference mechanisms . . . 87

4.2.2. Chorochronic representation of stator-rotor interaction with non-axisymmetry in the stator . . . 90
4.2.3. Phase correction at inter-row boundary . . . 91
4.2.4. Rotor-rotor/stator-stator interference . . . 92
4.3. Limitations of the time-domain Fourier model . . . 96
4.3.1. Theoretical limitations . . . 96
4.3.2. Practical limitations . . . 96
4.4. Information exchange across blade row boundaries . . . 97
4.5. Approximate modelling of multi-stage flows . . . 99

5. Validation **103**
5.1. Propagation of entropic perturbation through a duct . . . 103
5.1.1. Travelling wave in single-passage single-row domain . . . 104
5.1.2. Stationary wave in multi-passage single-row domain . . . 106
5.1.3. Modulated wave in multi-passage single-row domain . . . 111
5.1.4. Modulated wave in multi-passage multi-row domain . . . 112
5.1.5. Harmonic wave in multi-row domain with disturbance truncation . . . 116
5.2. Outlet guide vane in steady non-axisymmetric flow . . . 118
5.2.1. OGV with sinusoidal pressure variation . . . 119
5.2.2. OGV with N-wave pressure variation . . . 124
5.2.3. Restaggered OGV . . . 125
5.2.4. Convergence and error assessment . . . 129
5.2.4.1. Definitions . . . 129
5.2.4.2. OGV with sinusoidal pressure variation . . . 130
5.2.4.3. OGV with N-wave pressure variation . . . 130
5.2.4.4. Restaggered OGV . . . 133
5.2.4.5. Harmonic convergence summary . . . 134
5.3. Turbine stage with non-axisymmetry in the stator . . . 138
5.3.1. Configuration . . . 138
5.3.2. Frequency content . . . 138
5.3.3. Subsonic flow results . . . 141
5.3.3.1. Modal forces . . . 141
5.3.3.2. Spinning modes at blade row interface . . . 143
5.3.3.3. Rotor surface unsteady pressures . . . 147
5.3.4. Grid size comparison . . . 153

5.3.5. Transonic flow results . . . 160
5.3.5.1. Steady flow . . . 160
5.3.5.2. Unsteady flow . . . 161
5.3.6. Summary . . . 163
5.4. 1.5 stage compressor: rotor-rotor interaction . . . 168
5.4.1. Configuration . . . 168
5.4.2. Frequency content . . . 169
5.4.3. Results . . . 171
5.4.4. Grid size and convergence . . . 173

6. Applications **183**
6.1. Full span study of rotor-stator interaction in a turbine with throat area variation in the stator . . . 183
6.1.1. Configuration . . . 183
6.1.2. Grid convergence . . . 185
6.1.3. Steady flow through NGV with throat area variation . . . 192
6.1.4. Unsteady rotor-stator interaction . . . 199
6.1.5. Computational requirements and convergence . . . 204
6.1.6. Summary . . . 211
6.2. Part-span study of distortion transfer through a multi-stage turbine . . . 212
6.2.1. Background . . . 212
6.2.2. Test Case . . . 214
6.2.3. Computational domains and setup . . . 215
6.2.4. Results . . . 219
6.2.5. Summary . . . 221

7. Conclusions and Recommendations **225**
7.1. Accomplishment of objectives . . . 225
7.1.1. Formulation of reduced-passage method . . . 226
7.1.2. Validation . . . 226
7.1.3. Assessment of theoretical and practical limitations . . . 226
7.2. Recommendations for future work . . . 227

A. Appendix **239**
A.1. Flow solver . . . 239
A.1.1. Numerical discretisation . . . 241
A.1.2. Temporal discretisation . . . 243

A.2. Sliding plane search and interpolation procedure 244
A.3. A summary of relevant results from signal processing 247
A.3.1. Sampling theorem 248
A.3.2. Aliasing 248
A.3.3. Application to reduced-passage modelling 249
A.4. Non-reflecting boundary conditions: A review 250

List of Figures

1.1. Flow features in a compressor and turbine 28
1.2. Comparison of free stream and wake velocity triangles 29
1.3. Wake convection through 1.5 stage compressor 30
1.4. Shock patterns near the tip of a typical transonic compressor 31
1.5. Sign convention and periodic boundary notation 33
1.6. Phase shifted periodicity and interblade phase angle 34
1.7. Nodal diameter pattern 36
1.8. Travelling wave mode for structural vibrations 37
1.9. Classification of unsteady phenomena 38
1.10. Collar's triangle of forces 40
1.11. Schematic of a Campbell diagram 41
1.12. Flutter domains on the compressor map 42

2.1. Prediction methods for turbomachinery flows 46
2.2. Single passage domain with shadow point boundaries 56
2.3. Moving averages technique 61
2.4. Single passage grid with prescribed distortion 64
2.5. Computational domain for circumferential Fourier model 70

3.1. The gap in prediction methods for turbomachinery flows 74

4.1. Flow field decomposition 77
4.2. Sparse assembly domain for first order Fourier approximation of a 4ND stationary disturbance 81
4.3. Schematic of a 1ND sinusoidal stagger distribution in whole annulus and sparse assembly domain 86
4.4. Single-passage multi-row domain with sliding plane boundaries 87
4.5. Spinning modes in a turbine stage 88
4.6. Phase correction at blade row interface 93
4.7. Spinning modes in 1.5 stage compressor 95

4.8. Sliding plane boundary 98
4.9. Schematic of sparse assembly domain for distortion transfer with interface disturbance truncation 100
4.10. Filtering criteria for approximate multi-stage modelling 102

5.1. Single-passage single-row domain 104
5.2. Density histories for travelling wave in single-passage single-row domain . . 105
5.3. Multi-passage single-row domain 105
5.4. Density contours for stationary wave in multi-passage single-row domain . . 106
5.5. Circumferential variation for stationary wave in multi-passage single-row domain 107
5.6. Density histories for modulated wave in multi-passage single-row domain . . 108
5.7. Density contours for modulated wave in multi-passage single-row domain . 109
5.8. Convergence history for modulated wave in multi-passage single-row domain 110
5.9. Multi-passage multi-row domain 111
5.10. Density histories for modulated waves in multi-passage multi-row domain . 113
5.11. Density histories at the blade row interface for modulated waves in multi-passage multi-row domain 114
5.12. Amplitudes at blade row interface for modulated waves in multi-passage multi-row domain 115
5.13. Single-passage three-row domain 116
5.14. Density contours for travelling wave in multi-row domain with disturbance truncation at blade row interface 117
5.15. Density histories for travelling wave in multi-row domain with disturbance truncation at blade row interface 117
5.16. OGV mesh 119
5.17. OGV with sinusoidal pressure perturbation at outlet: Inlet pressure variation 120
5.18. OGV with sinusoidal pressure perturbation at outlet: Blade profiles 121
5.19. OGV with sinusoidal pressure perturbation at outlet: Differences in blade pressures between sparse assembly and whole annulus solution 121
5.20. OGV with N-wave pressure perturbation at outlet: Inlet pressure variation 122
5.21. OGV with N-wave pressure perturbation at outlet: Blade profiles 123
5.22. OGV with N-wave pressure perturbation at outlet: Difference in blade pressures between sparse assembly and whole annulus solution 123
5.23. Sinusoidal stagger distribution in the OGV 126
5.24. Restaggered OGV: Pressure variation at OGV outlet 127

5.25. Restaggered OGV: Blade profiles 128
5.26. Restaggered OGV: Blade pressure difference 128
5.27. Harmonic convergence based on unsteady pressures 131
5.28. OGV with sinusoidal pressure perturbation at outlet: Disturbance and error distribution 132
5.29. OGV with N-wave pressure perturbation at outlet: Error distribution . . . 132
5.30. Restaggered OGV: Error distribution 134
5.31. Restaggered OGV: Error distribution at leading and trailing edge 135
5.32. Restaggered OGV: Axial velocity in five passage solution 136
5.33. Throat area variation in the NGV 139
5.34. SPMR mesh for turbine stage 139
5.35. Sparse assembly domain for turbine stage with 5ND throat area variation in the NGV 140
5.36. Relative Mach number in steady state starting solution (subsonic case) . . . 143
5.37. Rotor modal force history in subsonic flow 144
5.38. Difference between whole annulus and sparse assembly modal force prediction in subsonic flow 145
5.39. Convergence of sparse assembly solution in subsonic flow 146
5.40. Spinning modes at stator outlet 146
5.41. Spinning modes at rotor inlet 147
5.42. Fourier spectrum at stator outlet in subsonic flow 148
5.43. Fourier spectrum at rotor inlet in subsonic flow (1/2) 149
5.44. Fourier spectrum at rotor inlet in subsonic flow (2/2) 150
5.45. Location of pressure probes on rotor surface 151
5.46. Pressure side pressure traces in subsonic flow 154
5.47. Suction side pressure traces in subsonic flow 155
5.48. Unsteady rotor surface pressure in subsonic flow: Amplitudes (1/2) 156
5.49. Unsteady rotor surface pressure in subsonic flow: Phases (1/2) 157
5.50. Unsteady rotor surface pressure in subsonic flow: Amplitudes (2/2) 158
5.51. Unsteady rotor surface pressure in subsonic flow: Phases (2/2) 159
5.52. Relative Mach number in steady state starting solution (transonic case) . . 161
5.53. Blade surface Mach number at nominal, minimum and maximum throat area 162
5.54. Comparison of blade surface Mach number on whole annulus and sparse assembly domain in transonic flow 164
5.55. Modal force in transonic flow 165
5.56. Unsteady rotor surface pressure in transonic flow: Amplitudes 166

5.57. Unsteady rotor surface pressure in transonic flow: Phases 167
5.58. 1.5 stage compressor test case 168
5.59. Computational domain for third order approximation of rotor-rotor interference 169
5.60. Unsteady surface pressures on first rotor 174
5.61. Unsteady surface pressures on second rotor 175
5.62. Unsteady surface pressures on embedded stator 176
5.63. Modal force history on first rotor 177
5.64. Modal force amplitudes and phases on first rotor 177
5.65. Modal force history on embedded stator 178
5.66. Modal force amplitudes and phases on embedded stator 178
5.67. Modal force history on second rotor 179
5.68. Modal force amplitudes and phases on second rotor 179
5.69. Time-averaged pressure variation on first rotor 180
5.70. Time-averaged pressure variation on second rotor 180
5.71. Modal force comparison between whole annulus and sparse assembly solution 182

6.1. Mesh movement 184
6.2. Pitch variation 185
6.3. 3D Mesh (Grid 1) 187
6.4. NGV boundary layer profiles at four chordwise positions 188
6.5. NGV pressure profiles 189
6.6. 2D Mesh (Grid 1) 190
6.7. Rotor static pressure from mixing plane starting solution 191
6.8. NGV wake profiles at 128% chord 193
6.9. NGV wake profiles at 128% chord: Amplitudes 194
6.10. NGV wake profiles at 128% chord: Phases 195
6.11. Total pressure contours at stator outlet 196
6.12. Comparison of wake locations at 20% and 90% span 197
6.13. Spanwise variation of exit flow angle 197
6.14. Blade surface pressure at datum throat area 200
6.15. Blade surface pressure at -4% throat area 201
6.16. Blade surface pressure at +4% throat area 202
6.17. Difference between sparse assembly and whole annulus blade surface pressures 203
6.18. Amplitudes of unsteady rotor surface pressure at 10% span 205
6.19. Phases of unsteady rotor surface pressure at 10% span 206

6.20. Amplitudes of unsteady rotor surface pressure at 50% span 207
6.21. Phases of unsteady rotor surface pressure at 50% span 208
6.22. Amplitudes of unsteady rotor surface pressure at 90% span 209
6.23. Phases of unsteady rotor surface pressure at 90% span 210
6.24. Formation of CO and NO_x with temperature 213
6.25. Multiple combustion chamber system with 6 out of 12 burners active 213
6.26. Temperature contours at combustor outlet 213
6.27. Circumferential variation of density and axial velocity at combustor outlet . 214
6.28. HP and IP turbine 216
6.29. Relative Mach number in steady state solution 217
6.30. Computational domains for 2-stage distortion transfer calculation 218
6.31. Schematic of Fourier coefficient convergence for different relaxation factors . 220
6.32. HP stator force history and Fourier spectrum 222
6.33. HP rotor force history and Fourier spectrum 223
6.34. IP stator force history and Fourier spectrum 223
6.35. IP rotor force history and Fourier spectrum 224

A.1. 2D vertex-centred grid cell 241
A.2. Boundary faces at blade row interface 245
A.3. Sliding plane search procedure 247
A.4. Aliasing of two signals 248
A.5. Possible aliases of frequency f sampled at rate f_S 249

List of Tables

2.1. Common time-linearised methods 49

5.1. OGV boundary conditions 118
5.2. OGV with N-wave pressure perturbation at outlet: Amplitudes of dominant harmonics 125
5.3. OGV with sinusoidal pressure perturbation at outlet: Normed amplitude of static pressure perturbation 130
5.4. OGV with N-wave pressure perturbation at outlet: Normed amplitude of static pressure perturbation 133
5.5. Restaggered OGV: Normed amplitude of static pressure perturbation 134
5.6. Spinning modes at stator-rotor interface 140
5.7. Frequency spectra in rotor and stator domain 140
5.8. Subsonic operating conditions 142
5.9. Modal force amplitudes of dominant frequencies in subsonic flow 145
5.10. Comparison of computational resources for thin-section turbine stage 158
5.11. Transonic operating conditions 160
5.12. Modal force amplitudes of dominant frequencies in transonic flow non-dimensionalised by steady state force 163
5.13. 1.5 stage compressor operating conditions 169
5.14. Spinning modes for three row compressor 170
5.15. Frequency spectra in compressor rows 170
5.16. Comparison of computational resources required for 1.5 stage compressor . 181

6.1. Stator geometry parameters 184
6.2. NGV grid dimensions 185
6.3. Total pressure amplitudes normalised by inlet stagnation pressure at 50% span (128% chord) 198
6.4. Difference in blade surface pressure between sparse assembly and whole annulus 199

6.5. Comparison of computational resources required for full span turbine stage 211
6.6. Cut-off frequencies for rotor passing disturbances at the blade row interfaces 216
6.7. Wave number and frequency spectra in sparse assembly model 218
6.8. Comparison of computational resources required for distortion transfer case 218

Nomenclature

Latin Symbols

a	Speed of sound
a_n, b_n	Real temporal Fourier coefficients for n^{th} harmonic
$A_{mn}, B_{mn}, C_{mn}, D_{mn}$	Real 2D Fourier coefficients for n^{th} temporal and m^{th} spatial harmonic
C_P	Pressure coefficient
c	Chord
E	Total energy per unit volume
F	Modal force
F_{ref}	Steady state modal force
f	Frequency
$\hat{f}$	Complex temporal Fourier coefficient
$f_{cut-off}$	Cut-off frequency
f_{red}	Reduced frequency
f_S	Sampling frequency
H	Total enthalpy per unit volume
k	Circumferential wave number
k_x	Axial wave number
M	Mach number
N	Number of grid nodes
N_A	Nodal diameter of aliased disturbance
N_B	Number of blades
N_D	Nodal diameter
N_H	Number of harmonics
N_L	Number of independent travelling disturbances
N_M	Number of spatial harmonics
N_N	Number of travelling disturbances
N_{MP}	Number of spatial harmonics
N_P	Number of passages
N_R	Rotor blade count

N_S	Stator blade count
N_T	Number of time steps per period
P_{01}	Total pressure at inlet
p	Pressure
Pr	Prandtl number
R	Gas constant
Re	Reynolds number
S	Blade-to-blade spacing [m]
t	Time
u_x, u_r, u_θ	Velocity components in cylindrical coordinates
u_x, u_y, u_z	Velocity components in Cartesion coordinates
$\mathbf{u}$	Vector of velocity components in cylindrical/Cartesion coordinates
U	Vector of flow variables
$\bar{U}$	Vector of passage-averaged flow variables
U_0	Vector of time-averaged flow variables
$\bar{U}_0$	Vector of time-averaged passage-averaged flow variables
U'	Vector of unsteady flow variables
$\tilde{U}$	Vector of circumferential perturbation
$\hat{U}$	Vector of complex Fourier coefficients
V_∞	Free stream velocity
v	Angular velocity
x, y, z	Cartesian coordinates
x, r, θ	Global cylindrical coordinates
x, r, ζ	Local (passage) cylindrical coordinates
$\mathbf{x}$	Vector of cylindrical/Cartesian coordinates

Greek Symbols

α_m, β_m	Real Fourier coefficients for m^{th} spatial harmonic
γ	Ratio of specific heats
ΔC_P	Amplitude of pressure perturbation non-dimensionalised by dynamic head
$\Delta\phi$	Phase shift
ΔT	Temporal phase lag between pitchwise boundaries
Δt	Time step
$\delta\Theta$	Pitch variation
$\delta\theta$	Variation in circumferential position
ϵ	Non-dimensionalised error

Θ	Pitch [rad]
θ	Circumferential coordinate
λ	Time inclination parameter
μ	Dynamic viscosity coefficient
ν	Kinematic viscosity coefficient
ρ	Density
σ	Inter-blade phase angle
Φ	Phase
ϕ	Phase
Ω	Rotational speed
ω	Angular frequency

Abbreviations

BPF	Blade passing frequency
EO	Engine order
FULL	Full circumference model
HEO	High engine order
HP	High pressure
IBPA	Inter-blade phase angle
IGV	Inlet guide vane
IP	Intermediate pressure
LE	Leading edge
LEO	Low engine order
ND	Nodal diameter
NGV	Nozzle guide vane
NRBC	Non-reflecting boundary condition
NSV	Non-synchronous vibration
OGV	Outlet guide vane
REF	Reference model
SFV	Separated flow vibration
SP/SPRS	Sparse assembly
SPMR	Single-passage multi-row
TE	Trailing edge
WA/WHOLE	Whole annulus model

Subscripts

h	Temporal harmonic index
i	Time step index
j	Passage index
l	Disturbance index
m	Spatial harmonic index
n	Travelling disturbance index

1. Introduction

1.1. Background and Motivation

Turbomachines generate work by transferring energy to or from a moving fluid by the dynamic action of one or more rotating blade rows. In aeroengines and gas turbines, work is imparted to the fluid in the compressor, energy is added by combustion of fuel and work is subsequently extracted from the fluid in the turbine. If the turbine extracts just enough work to power the compressor, the high pressure gas can be expanded in a propelling nozzle to create a fast moving jet and thrust the aircraft forwards. Alternatively, the additional power extracted in the turbine can be used to drive a generator or propeller.

Due to the relative rotation of blade rows, the flow in aeroengines and gas turbines is inherently unsteady. This can lead to the occurrence of aeroelastic phenomena which, under unfavourable circumstances, can lead to strong vibrations and ultimately engine failure. Understanding and predicting unsteady aerodynamics and consequent potential vibration issues is therefore crucial to engine design.

Computational Fluid Dynamics (CFD) has played an ever increasing role in the prediction of turbomachinery flows since the first appearance of computer-based numerical simulations of fluid flow in the 1960's. Initially, semi-analytical methods solved approximations to the flow governing equations on simplified geometries. As computing capacity increased, the geometries and models became more complex and began to take into account three-dimensional and viscous effects. Current state-of-the-art methods are able to solve the unsteady Navier-Stokes equations across multiple turbomachinery stages using appropriate models to approximate the effects of turbulence. On smaller domains and lower Reynolds numbers, Direct Numerical Simulation (DNS) is able to resolve the smallest turbulent scales and provide useful insights into the physics of turbulence. Even with today's computing capabilities, however, the time required to calculate flow through a whole turbine or compressor precludes routine use of unsteady CFD during the design cycle. Efficient numerical methods have been developed which make assumptions about time-space periodicity in unsteady turbomachinery flows and model only a fraction of the domain. Most of these methods require a blade-to-blade periodicity in the underly-

ing steady flow which is not strictly satisfied in turbomachines where distortions and the interaction of rows in the same frame of reference create stationary passage-to-passage (circumferential) perturbations.

The objective of this research is hence to develop a more general method which accurately models steady and unsteady circumferentially non-uniform flows on a reduced number of bladed passages. Similarly to existing reduced-domain models, the method proposed here exploits the chorochronic (space-time) periodicity inherent to turbomachines.

In order to explain the origin of this periodicity, the first chapter of this thesis describes the nature of steady and unsteady flows in axial compressors and turbines and introduces important parameters and nomenclature. It also provides an overview of common aeroelastic phenomena, the prediction of which is crucial to safety and performance and has motivated this work. A large part of the material in this chapter is based on the VKI Lecture Series on Aeroelasticity [32] and Blade Row Interference Effects [2].

1.2. Flow in axial compressors and turbines

1.2.1. Three-dimensional flow features

The flow around an axial compressor or turbine blade differs considerably from that around a cambered aerofoil. The presence of endwalls, neighbouring blades, tip gaps and centrifugal forces in rotating rows renders the flow highly three dimensional and gives rise to complex flow structures as illustrated in Figure 1.1.

When a boundary layer at hub or tip encounters a strong adverse pressure gradient in the blade vicinity, it separates. This 'corner stall' creates considerable blockage which in turn forces the mid-span flow to accelerate. The fluid in the hub and casing boundary layer is exposed to the same pressure gradient in the blade-to-blade direction as the faster moving mid-span fluid. This pressure gradient forces streamlines in the mid-span region to follow the curvature of the blade, but increases the curvature of streamlines in regions with lower velocity. A velocity component in the blade-to-blade direction from the pressure to the suction side therefore exists near the endwalls as shown in Figure 1.1. A similar phenomenon occurs in tip gap flows, as fluid particles from the high pressure side travels across the blade towards the suction side. Although tip gaps are relatively small (about 1% of the span) this tip leakage flow contributes greatly to losses and can significantly influence the onset of stall in transonic fans and compressors [89]. Another set of vortices is created when the boundary layer flow near the endwalls encounters a strong adverse pressure

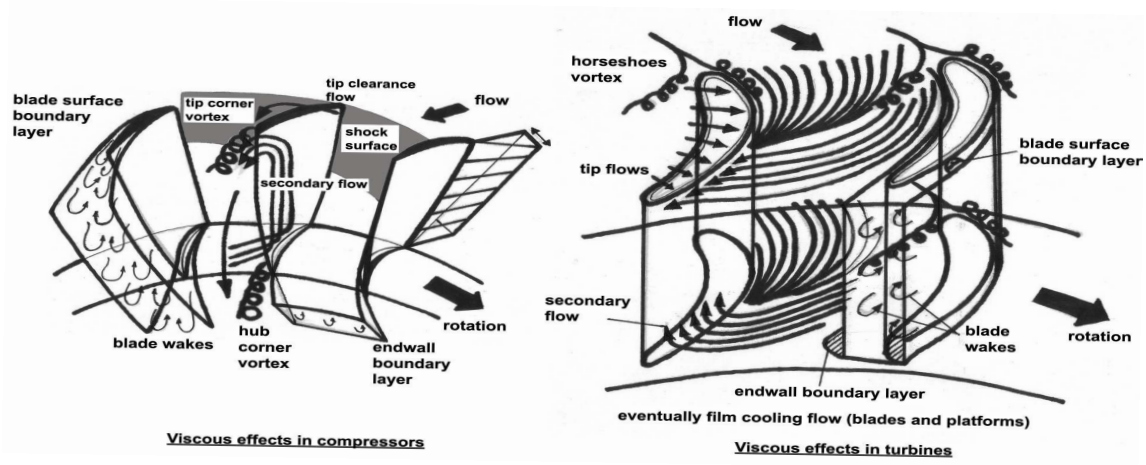


Figure 1.1.: Flow features in a compressor and turbine [32] (originally McNally, 1977 [76])

gradient at the leading edge stagnation point. This vortex rolls up and wraps around the leading edge to form a pair of vortices, a horseshoe vortex, which travel downstream on both side of the blade. The suction side vortex remains close to the surface as it is transported downstream and the pressure side vortex is swept across the passage. A passage vortex is formed from the endwall boundary layers and the pressure side leg of the horseshoe vortex.

The secondary flow effects described above contribute significantly to aerodynamic losses and create a strongly non-uniform flow field at the outlet of a bladed passage which contributes to unsteady fluctuations in downstream rows. Schlienger et al. [94] observed a stagnation pressure drop of 30% of dynamic head in the core of a passage vortex at the rotor exit of a shrouded axial turbine. The passage vortex covered up to 70% of the blade pitch at 20% span and changed in size as the downstream stator blade passed. This and similar research into secondary flows illustrates the considerable influence secondary flow structures have on unsteady blade row interaction. Any numerical method attempting to model multi-row flows thus ought to include secondary flow structures. However, as will be seen in later chapters, the presence of vortex shedding invalidates assumptions about time-space periodicity which form the basis for many advanced numerical methods and is thus often neglected.

Even in absence of three-dimensional flow structures, however, turbomachinery flows differ from external flows since the blade rows are not isolated and local flow fields are perturbed by potential fields, shocks or wakes from neighbouring blade rows.

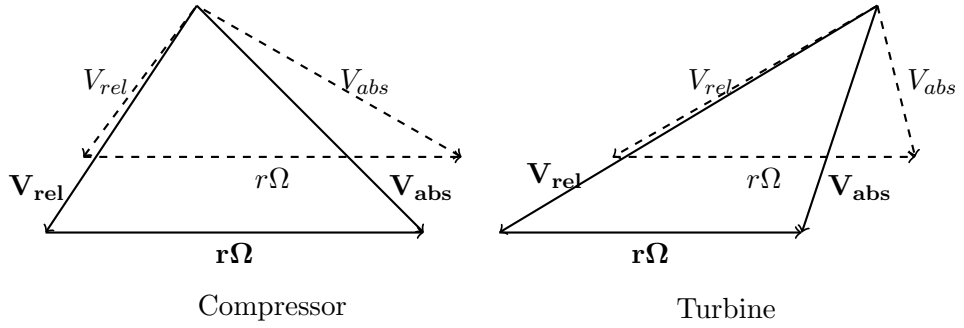


Figure 1.2.: Comparison of free stream (solid lines) and wake (dashed lines) velocity triangles in compressor and turbine rotor outlet

1.2.2. Potential Disturbances

The circulation around a blade creates a potential field and non-uniformities in static pressure in the inlet or outlet plane which result in fluctuations in adjacent rows. Pressure or acoustic waves propagate upstream and downstream with an attenuation governed by their wave length and Mach number. The waves amplitude decays approximately according to $\exp(-2\pi\sqrt{1-M^2}\frac{x}{S})$ where x is the axial distance, M is the local axial Mach number and S is the pitch [82].

This simplified model is based on the propagation of acoustic waves in purely axial flow. It indicates that in low subsonic flows potential disturbances decay in the axial direction and near sonic conditions they propagate almost unattenuated. Downstream potential interactions can therefore be expected to be much stronger in high Mach number flows or in configurations with small axial spacings. Furthermore, the decay rate varies between the upstream and downstream direction due to variations in local Mach number.

1.2.3. Wakes

Wakes produced by upstream blade rows contain entropy and vorticity components which differ from the free stream. The relatively slow moving wake fluid enters the downstream row at a different angle and velocity from the main stream. The resulting effect on downstream blades is different for compressors and turbines. Figure 1.2 compares mean velocity triangles at rotor outlet to the wake velocity vectors. In the relative frame of reference the wake velocity deficits of a compressor or turbine blade are similar but, due to the shape of the velocity triangles, the consequent change in incidence is more pronounced in the compressor while the change in velocity is more noticeable in the turbine. This change in

incidence and velocity produces fluctuating lift and drag forces in downstream rows as the wake passes [112] and contributes to the periodic unsteadiness found in turbomachines.

Inside the bladed passage, the negative jet (velocity deficit) is chopped into segments as the wake impinges on the downstream aerofoil. As they travel downstream, these segments become distorted by the pressure gradient and variations in velocity across the passage. When they enter rows in the same frame of reference as their origin but with different blade counts, the wake segments will appear at different circumferential positions relative to the blades as seen in Figure 1.3. This results in stationary circumferential 'aperiodicities' in downstream rows. The neglect of such a passage-to-passage variation in the time-averaged flow field is the main drawback of currently available fast prediction methods and its correct representation on a reduced domain forms the main contribution of the current research.

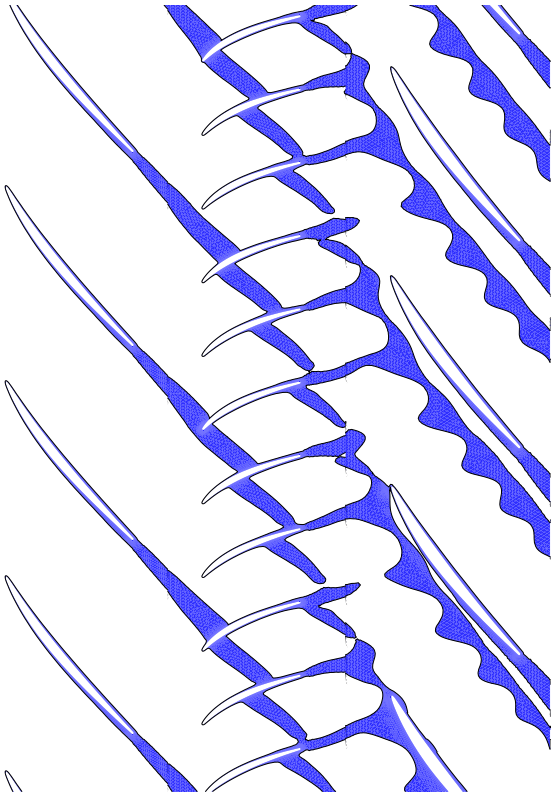


Figure 1.3.: Wake convection through 1.5 stage compressor

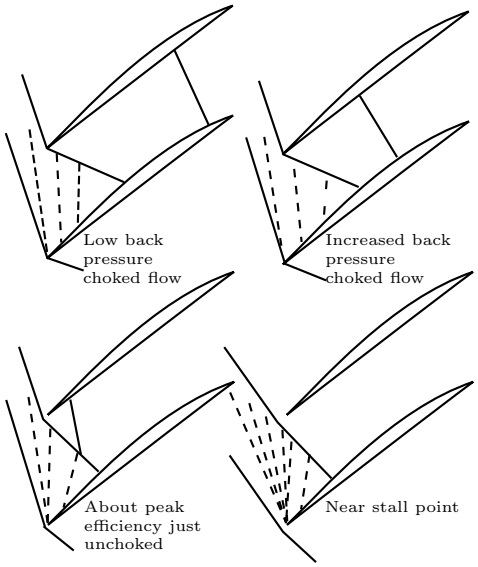


Figure 1.4.: Shock patterns near the tip of a typical transonic compressor [24]

1.2.4. Shock waves

Blade row interaction may be further complicated by the presence of shock waves. Shocks are characterised by abrupt changes in thermodynamic properties (a sharp rise in pressure, density and temperature and sudden drop in velocity) and form at different locations in a bladed passage as the flow is throttled. Figure 1.4 shows typical shock positions at four different operating conditions with supersonic inlet flow. At low back pressures, an attached oblique shock at the leading edge is accompanied by a passage shock towards the passage exit which moves upstream with increasing back pressure. As peak efficiency approaches, the passage shock is weakened and eventually disappears while the oblique leading edge shock strengthens and moves upstream to form a bow shock [111]. For even higher back pressures the bow shock detaches and extends upstream where it may impinge on the trailing edge of the upstream stator or inlet guide vane. Similarly, a trailing edge shock might impinge on the leading edge of a downstream blade row. When shocks hit the surface of neighbouring blades or upstream/downstream rows, they reflect which leads to the formation of complex shock structures inside cascades [8].

Shocks extending across blade row boundaries or moving on a vibrating blade pose a challenge to single-passage techniques which often rely on a Fourier decomposition of unsteady perturbations. This will be discussed in more detail in Chapter 2.

1.3. The disturbance environment

The flow features described in the previous sections create variations in the flow which may be steady in their own frame of reference but appear as travelling disturbances in neighbouring rows due to the relative motion of turbomachinery rows. As pressure, vorticity and entropy disturbances propagate between blade rows, they interact with the local flow field and can be partially reflected or transmitted further. Whether the fluctuation appears steady or unsteady depends on its origin and the local frame of reference. The complete flow field can therefore be regarded as a superposition of the time-averaged flow in an isolated passage and multiple stationary and travelling disturbances. These disturbances are characterised by their angular frequency and circumferential wave number which will be explained in this section.

1.3.1. Rotor-stator interaction

When a blade passes through the non-uniform flow field created by neighbouring rows it experiences a periodic forcing. The frequency of the unsteadiness is determined by the blade count and relative rotational speed of the two rows and is a multiple of the rotating frequency or engine order (EO):

$$EO = \frac{\Omega}{2\pi} \tag{1.1}$$

where EO is measured in Hz and Ω is the rotational speed in rad/s. If two rows (rotor and stator) with blade counts N_R and N_S are rotating at speed Ω_R and Ω_S (which may be zero) respectively, the fundamental frequencies of the unsteadiness are given by f_R and f_S in the rotor and stator frame of reference:

$$f_R = \frac{N_S(\Omega_S - \Omega_R)}{2\pi} \tag{1.2}$$

$$f_S = \frac{N_R(\Omega_R - \Omega_S)}{2\pi} \tag{1.3}$$

f_R and f_S are also known as the stator and rotor blade passing frequency (BPF) respectively.

When a row experiences such periodic fluctuations, neighbouring blades are subjected to the same flow conditions at different points in time. In other words, a phase shifted periodicity exists between blades or bladed passages. If the subscripts $left$ and $right$ denote the left and right periodic boundary of a bladed passage, where the right boundary follows the left boundary in the anti-clockwise direction when viewed in the positive x-

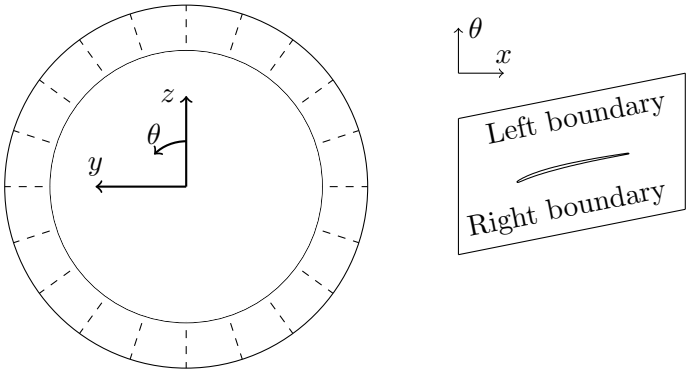


Figure 1.5.: Sign convention and periodic boundary notation

direction (see Figure 1.5), the periodicity can be expressed as:

$$U_{left}(\mathbf{x}, t) = U_{right}(\mathbf{x}, t \pm |\Delta T|) \tag{1.4}$$

In the rotor, the temporal phase shift $|\Delta T_R|$ is given by:

$$|\Delta T_R| = \frac{2\pi}{N_R|\Omega_S - \Omega_R|} = \frac{\sigma_R}{|2\pi f_R|} \tag{1.5}$$

where σ_R is the rotor inter-blade phase angle (IBPA):

$$\sigma_R = 2\pi \frac{N_S - kN_R}{N_R} \tag{1.6}$$

and k is the largest integer less than or equal to N_S/N_R. Similarly for the stator:

$$|\Delta T_S| = \frac{2\pi}{N_S|\Omega_R - \Omega_S|} = \frac{\sigma_S}{|2\pi f_S|} \tag{1.7}$$

where k is the largest integer less than or equal to N_R/N_S. The sign of the phase shift depends on the direction of the disturbance, i.e. the relative rotational speed of the two blade rows. If the disturbance is travelling in the direction of positive θ the left boundary lags the right boundary and vice versa.

Equations (1.1)-(1.7) govern the unsteadiness due to relative motion between neighbouring blade rows. In a multi-stage environment, this unsteady interaction is accompanied by the steady interaction of rows in the same frame of reference.

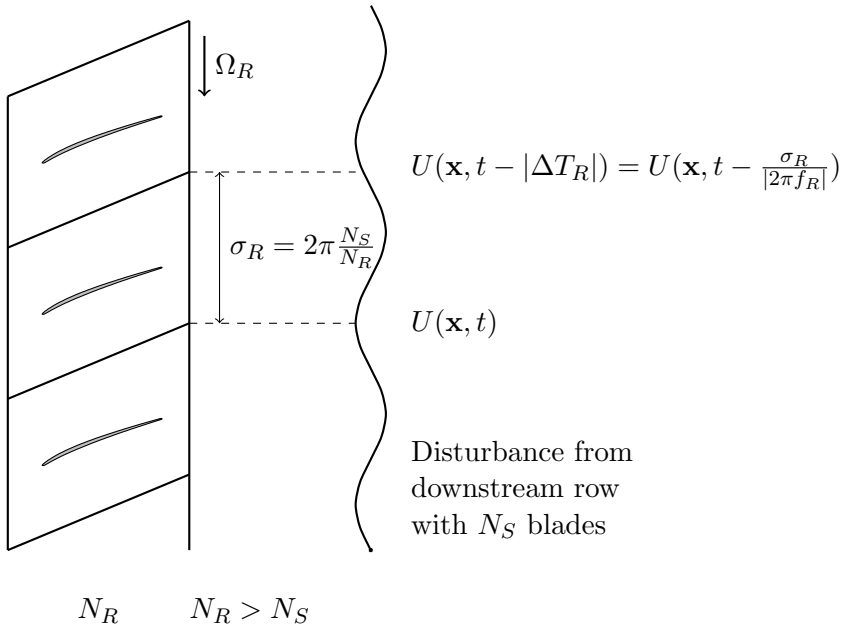


Figure 1.6.: Phase shifted periodicity and interblade phase angle

1.3.2. Rotor-rotor/stator-stator interaction

The circumferentially non-uniform flow field generated by one row is seen as a stationary disturbance in rows rotating at the same speed. A direct blade-to-blade periodicity exists if both rows have the same number of blades. If the blade counts are different, the row interaction creates a circumferential pattern. If the blade counts do not have a common divisor, the relative circumferential position between two rows only repeats after 360°. For a general case of two rows with N_{R1} and N_{R2} blades, a circumferential variation with nodal diameter $N_D = N_{R1} - kN_{R2}$ is created, where k is the closest integer to N_{R1}/N_{R2}.

As an example, consider a two-stage compressor with rotor blade counts N_{R1} and N_{R2}. If $N_{R1} = N_{R2}$ every passage in R2 sees the same spatial disturbance from R1. In other words, the zero frequency circumferential variation is periodic with a wave length equal to the pitch of R1 and the time-averaged flow in every passage is identical. If the two blade counts are different, the time-averaged flow fields in each rotor passage differ and a spatial phase shift exists between periodic boundaries.

$$U_{left}(x, r, \theta) = U_{right}(x, r, \theta + \phi) \tag{1.8}$$

This phase shift is equal to the inter-blade phase angle:

$$\phi_{R1} = \sigma_{R1} = 2\pi \frac{N_{R2} - kN_{R1}}{N_{R1}} \tag{1.9}$$

$$\phi_{R2} = \sigma_{R2} = 2\pi \frac{N_{R1} - kN_{R2}}{N_{R2}} \tag{1.10}$$

where as before k is equal to the largest integer less than or equal to N_{R2}/N_{R1} (Equation (1.9)) and N_{R2}/N_{R1} (Equation (1.10)).

Note that $N_{R2} - kN_{R1}$ is the circumferential wavenumber of the aliased disturbance when a disturbance with circumferential wavenumber N_{R1} impinges on N_{R2} blades (see Appendix A.3 for a description of aliasing). The interaction of two rows with N_{R1} and N_{R2} blades therefore creates a circumferential variation with wave number $N_{R2} - kN_{R1}$. While the magnitude of this disturbance in downstream rows may be small compared to blade passing disturbances, its wave length is comparatively large. The rate of decay in the axial direction is therefore slow and as a consequence stator-stator/rotor-rotor interaction can significantly influence the flow in downstream rows.

1.3.3. Structural vibration patterns

Circumferentially non-uniform unsteady flows can also be generated from the vibration of bladed disk assemblies. The vibration modes of an assembly differ from those of individual blades because the blades are mechanically and aerodynamically coupled. The extent to which the blades are mechanically coupled depends on the nature of the support structure; Shroudless blades on perfectly rigid disks experience no mechanical coupling and vibrate in single blade modes whereas assemblies with flexible disks or shrouds develop well defined assembly modes [101]. The assembly vibration modes are defined by nodal diameters which represents the number of radial lines at which the blades have zero displacement (Figure 1.7). If N_B is the number of blades in the assembly, the maximum number of nodal diameters is given by $(N_B - 1)/2$ for odd N_B and $N_B/2$ for even N_B. The zero and maximum nodal diameters (n_0 and n_{max}) are single standing waves. All other nodal diameters occur in pairs of modes with identical frequency and orthogonal mode shapes. The double modes can combine into forward or backward travelling waves where the nodal diameter pattern rotates along the disk. Convention defines a forward travelling wave as a wave travelling in the direction of rotation and a backwards travelling wave as a wave travelling in the opposite direction. Figure 1.8 illustrates displacements of a row of blade vibrating in travelling wave form.

In travelling wave mode, all blades vibrate with the same amplitude and frequency but

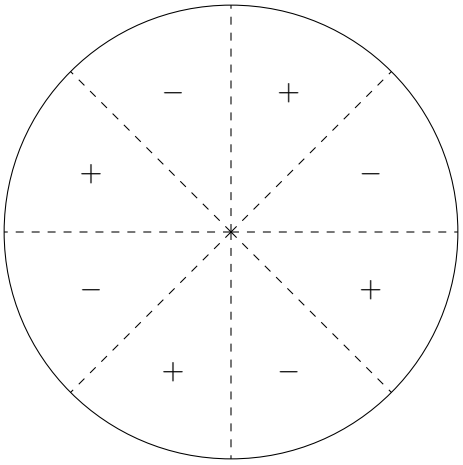


Figure 1.7.: Nodal diameter pattern (n=4)

at a different phase. This makes it possible to express the displacement u of the j^{th} blade in an assembly with N_B blades vibrating at frequency ω as as a sum of circumferential Fourier modes:

$$u_j(t) = \sum_{n=0}^{N_B-1} \hat{a}_n e^{i(\omega t-(j-1)2\pi n/N_B)} \tag{1.11}$$

where n is the nodal diameter. Any sinusoidal motion of the N_B blades can hence be characterised by N_B complex Fourier coefficients $\hat{a}_n = a_{n,re} + a_{n,im}$.

$$\phi_n = \frac{2\pi n}{N} \tag{1.12}$$

describes the phase lag between adjacent blades for a given mode n. It is analogous to the inter-blade phase angle for rotor-stator interaction and and was first introduced for flutter analysis by Lane [63]. The inter-blade phase angle is an important aeroelastic parameter as it is closely related to aerodynamic damping. For tuned assemblies with identical blades and stiff disks, all travelling wave modes are independent and can be calculated separately [18].

1.3.4. Other sources of circumferential non-uniformity

The blade-row interaction and vibration patterns described above are two major sources of unsteadiness in turbomachinery. However, periodically unsteady flows occur as a result of rotation through a non-uniform flow field and can thus be caused by any flow distortion.

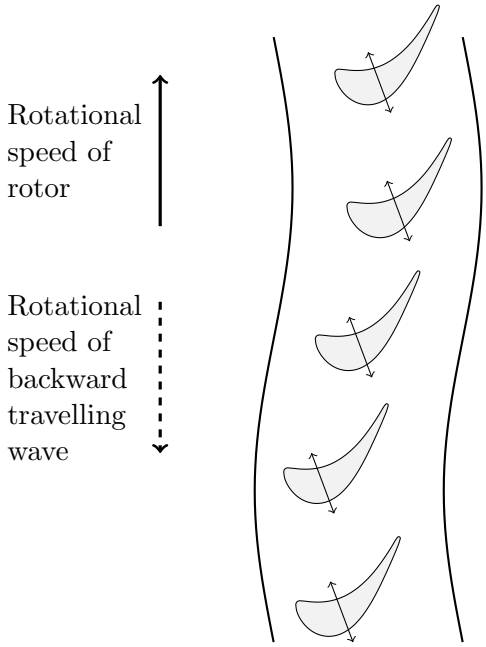


Figure 1.8.: Travelling wave mode for structural vibrations (after He, 2010 [53])

Inlet flow conditions are distorted when the aircraft is flying at an angle of attack or in cross wind conditions. Flow at an incidence creates regions of high or low momentum fluid in the intake. The presence of pylons or air frame boundary layers in integrated engines can also give rise to non-uniform intake flows. Inlet distortions tend to have a large wave length and can propagate a long distance with little decay.

Inside the engine, distortions may exist due to turning of the flow around upstream obstructions. The presence of struts, for example, can create large nodal diameter disturbances in turbines.

Furthermore, geometric variations between different blades in a blade row may exist. Imperfections during manufacture may alter local throat areas, tip gaps or exit flow angles and create non-uniform flow conditions. Larger variations can also occur during operation when guide vanes become displaced or fan blades are damaged by bird strike. Blade rows which contain non-identical blades are commonly referred to as 'mistuned assemblies' and are known to give rise to large wave length disturbances which propagate through the engine.

In turbines, large engine order distortions may also result from non-uniform flow conditions at the combustor exit. Modern cost and emission requirements have led to the development of a circumferentially staged combustion process with non-uniform tempera-

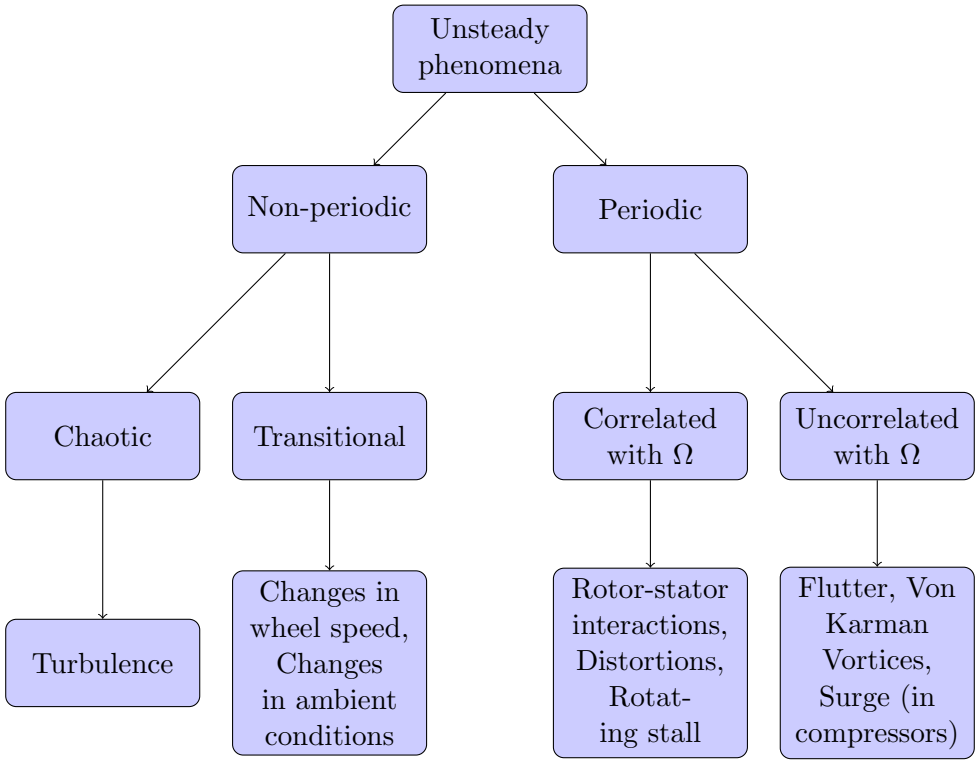


Figure 1.9.: Classification of unsteady phenomena (after Gourdain, 2005 [40])

ture distributions. The resulting hot streaks convect through the turbine and can impact performance, durability and structural integrity of turbine blades.

1.3.5. Uncorrelated unsteadiness

The above description has considered periodically unsteady flows resulting from rotation through a non-uniform flow field or self-excited vibration. However, unsteadiness in turbomachines is not necessarily correlated to the wheel speed of the engine or structural eigenfrequencies. Vortex shedding or global instabilities such as surge (characterised by large amplitude pressure oscillations) introduce distinctive frequencies which are not related to rotation. Furthermore, non-periodic unsteady flows arise from gusts, changes in operating conditions or turbulence. Figure 1.9 classifies different sources of unsteadiness according to their periodicity. The periodic unsteadiness correlated to the rotational frequency or natural vibration frequencies is generally known *a priori* which is exploited in some numerical prediction methods.

1.4. Aeroelasticity

Structural vibrations have been causing problems since the first appearance of turbomachines. These problems can manifest themselves as sudden failure or long-term fatigue and may be a consequence of flow-induced vibration (forced response) or self-excited vibration (flutter). When structural oscillations interact with aerodynamic forces which depend on the shape and orientation of the component itself, they induce changes on the load which consequently cause further structural distortion. This interaction of inertial, elastic and aerodynamic forces is called aeroelasticity. Aeroelasticity has become increasingly important for modern light-weight blades and is frequently considered the limiting factor in engine design.

This section provides an introduction to aeroelasticity and an overview of common aeroelastic phenomena in turbomachines.

1.4.1. Definition

Collar [17] defined aeroelasticity in terms of a triangle of forces with vertices representing inertial, elastic and aerodynamic forces.[1] The four major axes of the triangle in Figure 1.10 describe four disciplines: *Classical vibration* is concerned with the interaction of inertial and elastic forces, *Stability and control* are affected by the interaction of aerodynamic and inertial forces, *Static aeroelasticity* describes the interaction of aerodynamic and elastic forces and *Dynamic aeroelasticity* is the discipline which deals with the interaction of all three forces. In turbomachinery both static and dynamic aeroelasticity are a major cause of concern since blade rows are subjected to high centrifugal loads and unsteady aerodynamic forces. The dynamic response of a blade is determined by the balance of forces which, in absence of gravitational forces, is given by:

$$[M]\ddot{X} + [C]\dot{X} + [K]X = F \tag{1.13}$$

where $[M]$, $[C]$ and $[K]$ represent the mechanical mass, damping and stiffness matrices respectively, F is the aerodynamic forcing vector and X is the displacement vector.

[1] In high temperature environments where thermal stresses become significant this triangle becomes a tetrahedron and the field is known as aerothermoelasticity [73].

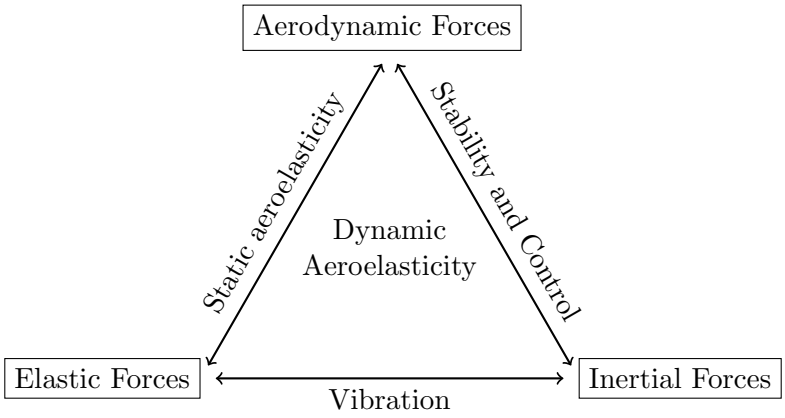


Figure 1.10.: Collar's triangle of forces

1.4.2. Static aeroelasticity

Static aeroelasticity describes the interaction of aerodynamic and elastic forces. It is, by definition, a vibration-free phenomenon and refers to the deformation of a structure under steady aerodynamic load. Aerodynamic load and elastic properties vary during the flight envelope: Gas properties and blade centrifugal loads change with the rotational speed of the engine and influence the stiffness of the blades, which deform elastically until they have reached an equilibrium state. Static aeroelasticity is concerned with the study of such deformation. The deformation between manufactured ('cold') and 'running' shapes can be significant and its prediction crucial to stability. Since aerodynamic requirements define the running shape, the design process must determine the manufacturing shape from an iterative procedure.

1.4.3. Dynamic aeroelasticity

Dynamic aeroelasticity is an unsteady problem caused by the interaction of aerodynamic, inertial and elastic forces. One differentiates between flow-induced vibration (forced response) or self-excited vibration (flutter). Both types are a potential source of blade failure in turbomachines and, in practice, it is often difficult to differentiate between them and define the exact reason for failure [32].

1.4.3.1. Forced response

The term forced response refers to rotor vibration which occurs when the frequency of an unsteady aerodynamic load coincides with the rotor assembly's natural frequency. The

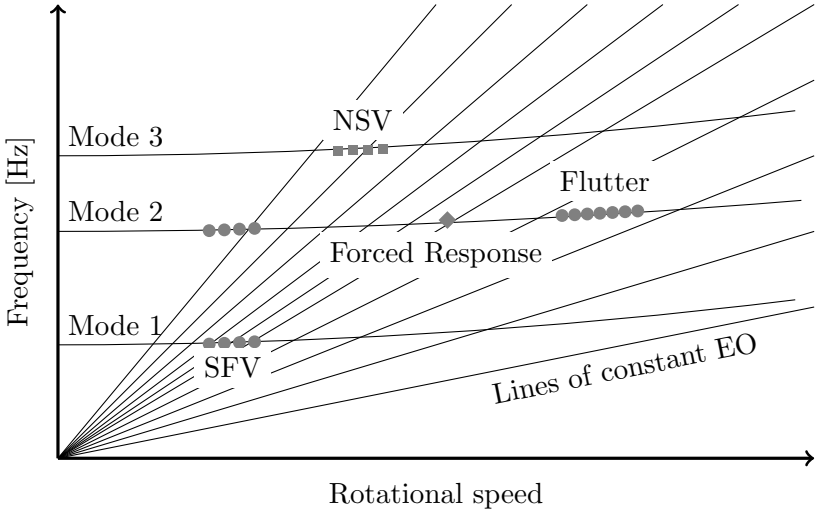


Figure 1.11.: Schematic of a Campbell diagram, SFV=Separated Flow Vibration, NSV=Non Synchronous Vibration (after Clark et al., 2012 [15])

unsteady aerodynamic load arises from the rotor's motion through a non-uniform flow field and its frequency is thus usually a multiple of the engine order (EO) as discussed in Section 1.3. One commonly differentiates between 'classical forced response' (high engine order), which is caused by the rotation of a rotor through the wake or potential field of an upstream or downstream stator, and low engine order (LEO) forced response caused by rotation through a large nodal diameter non-uniformity created, for example, by gusts, aerodynamically mistuned assemblies or staggered blades. Due to the relative rotation of blade rows forced response can occur in any part of a multi-stage engine.

In certain circumstances, aerodynamic instabilities such as trailing edge vortex shedding or rotating stall can generate periodic unsteadiness at non-integral multiples of the rotational frequency. This can lead to a phenomenon where the vortex shedding frequency becomes locked to the natural frequency of the structure and causes 'non-synchronous vibration' [15]. If the unsteadiness originates in the oscillating blade row, this type of vibration is in some sense self-excited. Nevertheless, in literature non-synchronous vibration is often classed as forced response.

An aeroelastic tool often used to predict the onset of forced response is the Campbell diagram shown in Figure 1.11 [10]. It relates rotational speed to eigenfrequencies-frequencies and is used to check for coincidence of excitation sources with natural frequencies.

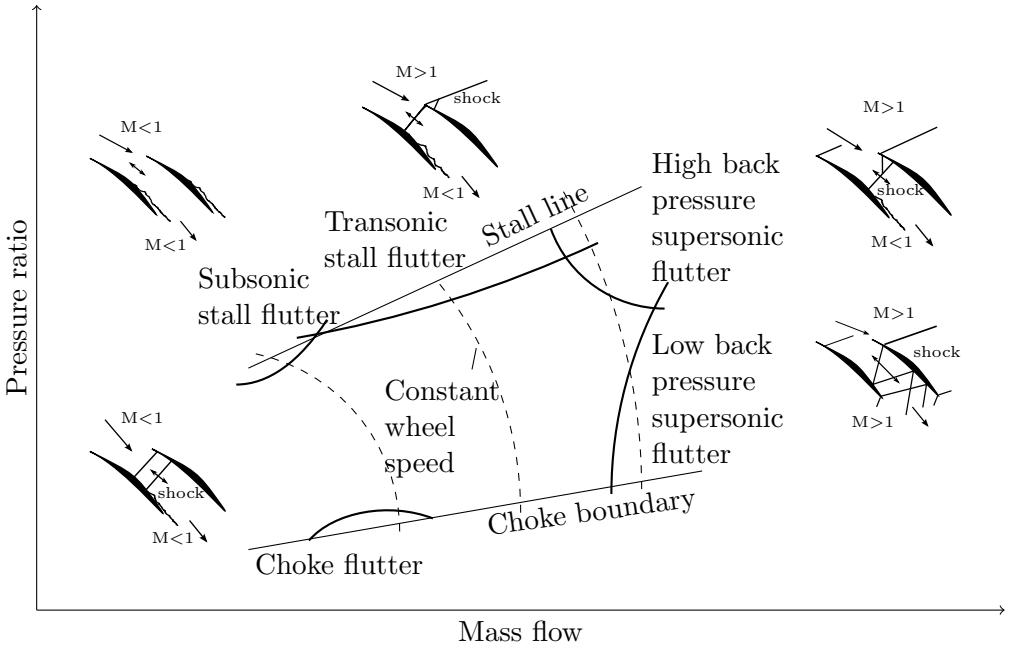


Figure 1.12.: Flutter domains on the compressor map (after Srinivasan, 1997 [101])

1.4.3.2. Flutter

Flutter is a *'sustained oscillation due to the interaction between aerodynamic forces, elastic response and inertia forces'* [1]. Unlike forced response it is a self-excited phenomenon which is not initiated by an unsteady aerodynamic load. Instead the vibration initially occurs at the natural (*in-vacuo*) modes and frequencies. In some situations, the aerodynamic forces resulting from the oscillations are large enough to alter the vibration and the structure exhibits flutter in a coupled mode which differs in shape and frequency from the individual *in-vacuo* modes. The extent to which a structure's natural modes are affected by aerodynamic forces depends on its mass ratio (the ratio of the mass of the blade to the fluid). Wings, for example, are light weight structures which typically flutter in a coupled bending-torsion mode whereas traditional turbomachinery blades predominantly flutter in a single mode shape close to their *in-vacuo* frequency [19]. However, coalescence (coupled bending-torsion) flutter has also been observed on modern low mass ratio, low solidity fans or turbines [15] [91].

Traditionally flutter is associated with fans and frontal compressor stages and one identifies different flutter regimes by their location on the compressor map shown in Figure 1.12.

Stall Flutter typically occurs at part-speed operation. As the mass flow decrease and

the pressure ratio increases, the blades operate at a higher angle of attack and become stalled. *Choke Flutter*, on the other hand, is situated near the choke line of the compressor map at reduced speed and incidence. When the maximum permissible mass flow rate for a given pressure ratio is reached, the flow becomes choked and a shock forms inside the passage. This shock oscillates with the blade motion and induces flow separation which can lead to excitation of certain vibration modes. Near design speed, a fan operating at supersonic tip Mach numbers can exhibit *supersonic stalled* flutter at high pressure ratios and *supersonic unstalled* flutter at low pressure ratios. The former is believed to be caused by movement of a strong passage shock and boundary layer separation while the latter is caused by the motion of a impinging shock originating from the neighbouring blade and is therefore associated with an inter-blade phase angle. [98] [32] [26]

Flutter may also occur when acoustic waves resulting from the blade vibration are reflected back onto the blade and excite a structural eigenfrequency. This kind of flutter is known as *Acoustic Flutter* and is almost exclusively found in front compressor stage when resonance in the intake duct affects flutter modes of the fan. Many researchers consider it the least understood of the flutter regimes and it remains an important area of research. [73]

It must be noted that the different flutter regimes are interwoven and the real mechanisms which cause flutter and boundaries between the different regimes may not easily be identifiable. [32][50]

1.4.4. Aeroelastic stability and reduced frequency

Flutter and forced response are aeroelastic instabilities which arise under certain structural and aerodynamic conditions. As seen above, flutter is characterised by a self-excited vibration and the resulting unsteadiness in the flow while forced response is driven by unsteady flow effects as described in Section 1.2. The unsteadiness may provide aerodynamic damping or feed energy into the vibration and thus clearly influences stability. In 1934 Theodorsen [105] derived a theory relating the unsteady lift and pitching moment of a thin aerofoil undergoing simple harmonic motion to a non-dimensional parameter known as reduced frequency:

$$f_{red} = \frac{2\pi f c}{V_\infty} \tag{1.14}$$

where f is the frequency of vibration, c is the chord length and V_∞ is the free stream velocity. In turbomachines free stream velocity is not defined and a new reference velocity must be chosen. Convention uses the upstream velocity for compressors, where the differ-

ence between inlet and outlet velocity is relatively small, and the downstream value for turbines, where a large difference between inlet and outlet velocity exists. The reduced frequency in this definition is the ratio of the time it takes a particle to travel a distance equal to the chord to the period of vibration. The reduced frequency is also commonly expressed with the semi-chord as the characteristic length:

> "*Consider an airfoil of chord length 2b oscillating at a frequency of* $\omega = \frac{2\pi}{T}$ *in a stream moving past it at a velocity* V*... . A sinusoidal wake will be formed, which is imbedded in the free stream and hence also moves relative to the airfoil at a velocity* V*, with wave length* $\lambda = VT = \frac{2\pi V}{\omega}$*. If we divide the airfoil chord by this wave length we obtain* $\frac{2b}{\lambda} = \frac{2b\omega}{2\pi V} = \frac{k}{\pi}$*. Thus, at low reduced frequency (*$k \approx 0.05$*) the wave length is very large relative to the chord while at high reduced frequency (*$k \approx 1$*) the wave length is not so large relative to the chord.*" [110]

The reduced frequency is therefore a measure of the unsteadiness of the flow. At low reduced frequencies the flow can be considered quasi steady. At higher reduced frequencies when the shed vortices move a relatively short distance downstream, their effect on the aerofoil lift becomes more pronounced. Theodorsen's theory can be used to find the reduced frequency at the onset of flutter for thin aerofoils in attached flow. [58]

In turbomachinery, the onset of flutter has been correlated to reduced frequencies in the range of 0.4 and 0.7 for modes with predominant first order torsion and for even lower reduced frequencies in the first bending mode. [101]

1.5. Summary

Aeroelastic phenomena can be self-excited or triggered by unsteady aerodynamic loads. The unsteadiness arises from a variety of sources and can be either periodic or aperiodic in nature. The fluid-structure interaction is characterised by several different parameters which determine the stability of the system. An unstable system experiences sustained vibration which causes high cycle fatigue and may ultimately result in engine failure. The ability to accurately model the unsteady flow and predict the onset of vibration is therefore crucial to safety and performance.

2. Review of prediction methods for unsteady flows in turbomachinery

Computational fluid dynamics (CFD) has become increasingly important in the design of gas turbines. Approximations to the governing flow equations are solved on a discretised domain using finite-difference, finite-element or finite-volume methods. This literature review focusses on methodologies for modelling unsteady turbomachinery flows. More specifically, it discusses different representations of periodically unsteady flows with frequencies which are known *a priori* (the right branch of Figure 1.9). These methodologies can generally be applied to any numerical scheme solving the flow governing equations. References [57],[65] and [64] provide introductions into numerical schemes commonly used in computational fluid dynamics. An example of a numerical scheme for solving the 3D Navier Stokes equations using a finite-volume discretisation is given in the Appendix A.1.

This chapter differentiates between 'classical' (analytical or semi-analytical) methods and time- or frequency-domain methods solving an approximate solution of the governing equations as mapped in Figure 2.1. Particular attention is paid to the suitability of these methods when applied to 'axisymmetric' turbomachinery flows with a passage-to-passage periodicity in the time-averaged flow field and 'non-axisymmetric' flows with stationary circumferential variations.

This review is not exhaustive but merely aims to introduce the concepts used throughout this thesis. For a detailed account of numerical methods the reader is referred to the references provided.

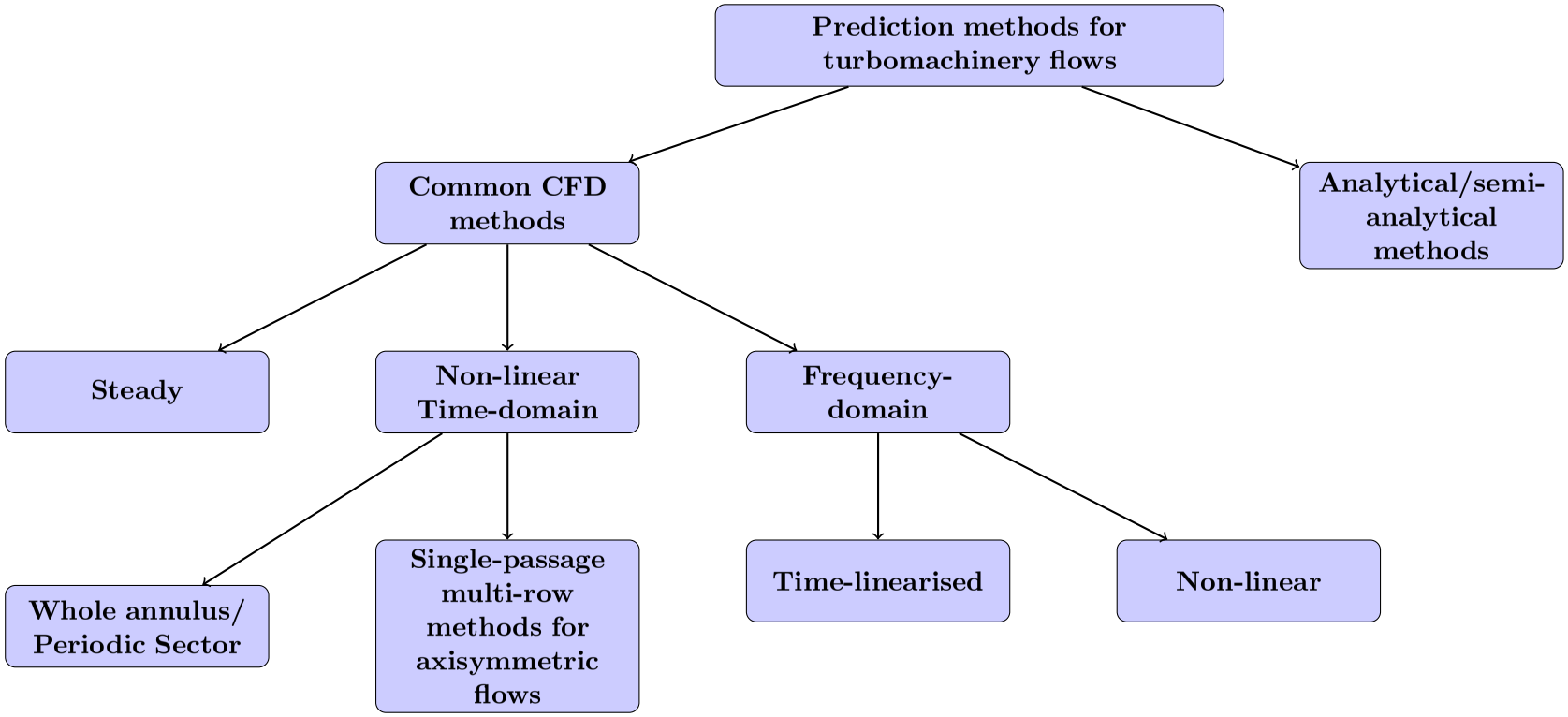


Figure 2.1.: Prediction methods for turbomachinery flows

2.1. Steady mixing plane approach

Before the discussion of unsteady numerical methods can begin, it should be noted that traditionally turbomachinery blades have been designed using single-passage steady flow methods [20]. The steady governing equations are solved on single passage domains with periodic boundaries in the blade-to-blade direction and circumferentially averaged flow conditions at the inter-row boundaries.

The first steady multi-stage computations which averaged unsteadiness at the blade row interface were performed by Denton in 1979 [22]. The circumferentially averaged flow at the outlet or inlet plane of one blade row served as boundary condition of the adjacent blade row. By simply averaging the flow circumferentially, the approach effectively assumes instantaneous mixing out of the non-uniform flow conditions at a 'mixing plane'. When compared to the gradual mixing process which occurs in a downstream blade row, this approach overestimates the mixing loss [33]. It has the additional disadvantage of imposing circumferentially uniform conditions close to the leading or trailing edge of a blade, leading to incorrect loading. More advanced mixing plane methods by Denton [23] or Adamczyk [4] improve estimates for mixing losses and blade loading by accounting for some circumferential non-uniformity at the mixing plane. When averaging unsteady flow, it is important to conserve those quantities which are relevant for the case considered. Cumpsty and Horlock [21] give a review of averaging techniques and their suitability to different applications.

Steady mixing plane calculations still remain an important design tool. However, aeroelastic phenomena such as forced response and flutter can only be predicted by unsteady methods such as the semi-analytical and CFD methods described in the next sections.

2.2. Classical methods

The first techniques developed for the analysis of unsteady aerodynamic or aeroacoustic problems were developed in the 1960's. They are analytical or semi-analytical solutions to significantly simplified versions of the governing flow equations and include linearised cascade, singularity, lifting line or frequency panel methods. The simplifying assumptions generally include small perturbations around a steady mean flow, simple geometries (thin aerofoils, no camber) in either subsonic or supersonic flow and inviscid, incompressible and irrotational flow - assumptions which are violated by most compressor and turbine blades. Nevertheless, the techniques developed provided useful insights into the physics of turbomachinery flow and were used for aerodynamic design [73].

Whitehead [107] developed one of the first analysis methods for flutter in turbomachinery by considering two-dimensional, incompressible flow through a cascade of vibrating flat plate aerofoils in uniform steady flow. The assumption of uniform mean flow significantly limits the applicability of this approach, as it neglects all steady loading on the aerofoils. A later extension of the linearised cascade method to include steady blade loading showed that it is an important factor in bending flutter [108]. The importance of steady loading was confirmed by Atassi and Akai [6] when they studied incompressible flows through a cascade of thick, cambered aerofoils. A few years later, the effects of compressibility were included in the models of Whitehead [109] and Smith [99]. Smith's model was partially successful as it accurately predicted cut-off behaviour and amplitude of acoustic waves for unloaded but not for steadily loaded cascades. The small perturbation model by Bendiksen [7] successfully included effects due to steady loading, camber and thickness and demonstrated the important role of shock motion in flutter prediction.

As computing capabilities evolved, models based on a discretisation of the flow governing equations were developed. The time-dependent Euler equations were solved very efficiently using the method of characteristics or simple time-marching procedures [77] with the ultimate goal being the solution of the three-dimensional unsteady Navier-Stokes equations. However, because of the large number of grid points and small time steps required for time-accurate analysis, these calculations remained prohibitively expensive when applied to large multi-row domains. Development therefore focussed on simplified and time-linearised models of the governing equations [73].

2.3. Time-linearised methods

Like classical methods, time-linearised frequency domain methods rely on the assumption that unsteady perturbations are periodic in time and small compared to an underlying steady-state flow. To linearise the equations, each variable is expressed as a mean value $\bar{U}$ and a small perturbation U' about that value [73]:

$$U(\mathbf{x}, t) = \bar{U}(\mathbf{x}) + U'(\mathbf{x}, t) \tag{2.1}$$

with

$$U'(\mathbf{x}, t) << \bar{U}(\mathbf{x}) \tag{2.2}$$

where $\mathbf{x} = (x, r, \theta)$ describes the coordinate of every node inside the discretised domain at which the solution is computed.

2D Linear potential	Ni & Sisto (1976)
	LTRAN2 - Ballhaus & Goorjian (1977,1978)
	LINFLO - Verdon & Caspar (1984)
	Surampudi & Adamczyk (1986)
	Usab & Verdon (1986,1991)
	FINSUP - Whitehead (1990)
3D Linear potential	XTRAN3S - Guruswamy & Goorjian (1984)
	CAP/TSD - Batina (1988)
	Henke et al. - 1991
2D Linear Euler	Hall & Crawley (1989)
	Hall & Clark (1991)
	Holmes & Chuang (1991)
3D Linear Euler	Hall & Lorence (1992)

Table 2.1.: Common time-linearised methods [73]

The steady part is obtained from a steady state calculation and the unsteady part is decomposed into its Fourier components, $\hat{U}_n$, which are solved separately from the steady flow.

$$U'(\mathbf{x},t) = \sum_{n=1}^{N_H} \hat{U}_n(\mathbf{x}) e^{i\omega_n t} \tag{2.3}$$

With the assumption of a harmonic perturbation, the time-derivative can be eliminated and the problem becomes linear and steady with variable coefficients depending only on the steady-state solution. Each Fourier harmonic can be solved separately using a pseudo-time marching method [79]. Since the steady solution is assumed to be periodic, an inter-blade phase angle can be determined for every harmonic component and the whole annulus solution can be computed on a single passage domain. This reduction in complexity and computational domain renders time-linearised methods very efficient. Acceleration techniques, such as preconditioning, local time-stepping and multi-grid, can also be used to reach the steady solutions. The main drawback of the time-linearised method is that all non-linearities, the interaction between steady and unsteady flow as well as the interaction between perturbations of different frequencies, is lost.

Historically, time-linearised methods have evolved and been applied to the potential, Euler and Navier-Stokes equations successively. Table 2.1 lists some well established linearised methods.

The linearised potential flow model provides a very efficient approach to the solution of

isentropic, irrotational flow with small perturbations. However, it has serious limitations in practical applications. In transonic flows, for example, the isentropic assumption violates the conservation of momentum across discontinuities. Furthermore, the potential model is not capable of representing three-dimensional flow with inlet swirl, as often found in turbomachinery applications. In order to reach beyond the limits of potential techniques, researchers began to develop linearised Euler methods.

The Euler equations describe inviscid, non-heat conducting flows and form a more suitable model for transonic flows and turbomachinery applications since they can account for vorticity and generation of entropy across discontinuities. Position and strength of shocks in transonic flows can be accurately predicted using shock fitting or shock capturing techniques. Shock fitting techniques, as applied to vibrating blades in transonic flow by Hall and Crawley [44], explicitly solve for shock motion and upstream and downstream states using the Rankine-Hugoniot relations. Shock capturing techniques as implemented, for example, by Lindquist and Giles [71], on the other hand, compute discontinuities as part of the solution. By using a conservative discretisation of the Euler equations and artificial dissipation they prevent the occurrence of numerical oscillations in shock vicinity. Modern shock capturing techniques adjust the amount of artificial dissipation based on local gradients and provide stable solutions even in the presence of strong shock waves.

The time-linearised Euler methods had proven to be a computationally efficient technique for modelling inviscid, unsteady subsonic and transonic flows and much later work was dedicated to their extension to three dimensional flows. However, a lot of the problems encountered in turbomachinery are a consequence of viscous effects which cannot be captured by the Euler equations. In order to include wakes, boundary layers or secondary flows, researchers developed time-linearised solvers for the Reynolds-Averaged Navier-Stokes equations with turbulence models to model the Reynolds stress terms. (see, for example, [16][11][59])

2.4. Non-linear frequency domain methods for axisymmetric flows

The time-linearised models of Section 2.3 only apply to small harmonic perturbations around a uniform mean-flow. Since the harmonic components are solved independently, potentially important non-linear interactions between different frequencies or between the unsteadiness and the mean flow are neglected. Furthermore, the time-linearised methods assume an isolated blade row in an infinite duct and ignore multi-stage effects. Harmonic

methods which incorporate some of these non-linear effects and multi-row coupling were developed in the 1990's. Four main approaches in the frequency domain are described in this section: Giles' SLIQ approach [38], the non-linear harmonic method by Ning and He [80], Hall's harmonic balance technique [43] and the time-linearised multi-row method by Hall and Silkowski [97].

2.4.1. SLIQ Approach

Having identified the lack of interaction between the steady solution and the first order unsteady perturbation as a drawback of time-linearised methods, Giles [38] developed the SLIQ (Steady LInear Quadratic) method based on previous work by Adamczyk [4]. The method incorporates the effect of unsteadiness on the mean flow by including quadratic terms with non-zero time-average. The flow variables are written as an asymptotic expansion:

$$\mathbf{U}(\mathbf{X},t) = \mathbf{U}^{(0)}(\mathbf{X}) + \epsilon\mathbf{U}^{(1)}(\mathbf{X},t) + \epsilon^2\mathbf{U}^{(2)}(\mathbf{X},t) + ... \tag{2.4}$$

where the parameter ϵ is a measure of the level of unsteadiness. Equation (2.4) contains the steady state $\mathbf{U}^{(0)}$ and first order unsteadiness $\mathbf{U}^{(1)}$, which are solved in conventional time linearised methods, and an additional second order term $\mathbf{U}^{(2)}$. Substituting this into the flow governing equations results in one equation for the steady state, a time-linearised equation for each harmonic with coefficients depending on the steady state and an additional equation for the second order unsteadiness. The time-average of the second order unsteadiness can then be combined with the steady state equation to give a time-linearised solution which includes the non-linear interaction between the unsteady perturbation and the mean flow.

However, there are several drawbacks with this method. The interaction between unsteady disturbances is still neglected. This may influence the accuracy of the time-averaged flow as the time-averaged solution depends on the unsteady perturbations. Furthermore, the time-averaged solution does not influence the harmonic solutions which makes the method equivalent to any time-linearised method as far as the unsteadiness is concerned.

2.4.2. Non-linear harmonic method

The non-linear harmonic method developed by Ning and He [80] is based on time-linearised frequency methods but uses a time-averaged instead of a steady state flow as basis for the unsteady perturbations. This way, the time-averaged flow also influences the harmonic

linearised solution and the main drawback of Giles' SLIQ approach is overcome. For the two-dimensional Euler equation, the method proceeds as follows:

The unsteady variables and fluxes are expressed as a superposition of a time-averaged part and an unsteady perturbation:

$$\mathbf{U} = \bar{\mathbf{U}} + \mathbf{U}' \quad \mathbf{F} = \bar{\mathbf{F}} + \mathbf{F}' \quad \mathbf{G} = \bar{\mathbf{G}} + \mathbf{G}' \tag{2.5}$$

where $\mathbf{U} = (\rho \quad \rho u_x \quad \rho u_y \quad \rho E)^T$ is the vector of flow variables and $\mathbf{F}$ and $\mathbf{G}$ are the axial and tangential flux vectors.

Assuming that the unsteady perturbations take the shape $\mathbf{U}' = \hat{\mathbf{U}} e^{i\omega t}$ and substituting the above expressions into the Euler equations gives the time-averaged equation:

$$\frac{\partial \bar{\mathbf{F}}}{\partial x} + \frac{\partial \bar{\mathbf{G}}}{\partial y} = 0 \tag{2.6}$$

and the first order unsteady perturbation equation:

$$i\omega \hat{\mathbf{U}} + \frac{\partial \hat{\mathbf{F}}}{\partial x} + \frac{\partial \hat{\mathbf{G}}}{\partial y} = 0 \tag{2.7}$$

where the time-averaged and unsteady fluxes are given by:

$$\bar{\mathbf{F}} = \begin{pmatrix} \overline{\rho u_x} \\ \bar{u}_x \overline{\rho u_x} + \bar{p} + \overline{(\rho u_x)' u_x'} \\ \bar{u}_y \overline{\rho u_x} + \overline{(\rho u_x)' u_y'} \\ \bar{H} \overline{\rho u_x} + \overline{(\rho u_x)' H'} \end{pmatrix} \overline{\mathbf{G}} = \begin{pmatrix} \overline{\rho u_y} \\ \bar{u}_x \overline{\rho u_y} + \overline{(\rho u_y)' u_x'} \\ \bar{u}_y \overline{\rho u_y} + \bar{p} + \overline{(\rho u_y)' u_y'} \\ \bar{H} \overline{\rho u_y} + \overline{(\rho u_y)' H'} \end{pmatrix} \tag{2.8}$$

$$\mathbf{F}' = \begin{pmatrix} (\rho u_x)' \\ u_x' \overline{\rho u_x} + p' + \bar{u}_x (\rho u_x)' \\ u_x' \overline{\rho u_y} + \bar{u}_x (\rho u_y)' \\ H' \overline{\rho u_x} + \bar{H} (\rho u_x)' \end{pmatrix} \mathbf{G}' = \begin{pmatrix} (\rho u_y)' \\ u_x' \overline{\rho u_y} + \bar{u}_x (\rho u_y)' \\ u_y' \overline{\rho u_y} + p' + \bar{u}_y (\rho u_y)' \\ H' \overline{\rho u_y} + \bar{H} (\rho u_y)' \end{pmatrix} \tag{2.9}$$

As seen in Equation (2.8), the time averaging of the non-linear flow equation results in additional terms, $\overline{(\rho u_x)' u_x'}$, $\overline{(\rho u_x)' u_y'}$, $\overline{(\rho u_x)' H'}$ and $\overline{(\rho u_y)' u_x'}$, $\overline{(\rho u_y)' u_y'}$ and $\overline{(\rho u_y)' H'}$ in the momentum and energy perturbation equations. These 'unsteady stress' terms account for the non-linear effects of the unsteadiness on the time-averaged flow [51] and are referred to as unsteady or deterministic stress terms because they look similar to the Reynolds stress terms. Since the two equations are steady, they can be marched to steady state in pseudo

time like conventional time-linearised methods. However, because the deterministic stress terms render the time-averaged and perturbation equation interdependent, the coupled system needs to be integrated simultaneously in time.

The non-linear harmonic methods offers advantages since it includes interactions between the first order perturbation and the mean flow - these are mainly visible in regions with shocks where conventional time-linearised methods fail to catch the smearing effects of non-linearities and predict sharp pressure peaks. However, non-linearities arising from the interaction between different disturbances are still neglected (although some coupling may result from the interaction with the time-averaged flow). [89]

The method was originally developed for a single-passage single-row domain but was later extended to model blade row interactions using a flux-averaged mixing plane approach [80] for the time-averaged variables. This method was shown to allow a better propagation of mixing losses than a conventional steady state solution [13]. The non-linear harmonic method was also successfully applied to stator-stator/rotor-rotor interferences [55] which is discussed in more detail in Section 2.6.3.

2.4.3. Harmonic balance and time spectral techniques

Further frequency methods include the 'harmonic balance technique' introduced by Hall [43] for cascade flows and the 'time-spectral method' for external flows by Gopinath and Jameson [39]. Both methods deduce the temporal behaviour of the solution from uniformly sampled 'snapshots' in time. For an analysis including N unsteady harmonics, steady state solutions at $2N + 1$ time levels are computed. The solutions are linked through phase-lagged boundary conditions and a spectral time-derivative operator in the interior domain. From the knowledge of the temporal behaviour in time, the temporal Fourier coefficients can be constructed. The technique has been applied to single row flutter [43] and flows with multiple frequencies and across multiple blade rows [29]. While non-linear frequency methods only contain the non-linear interaction between the time-averaged flow and the first temporal harmonics, the harmonic balance methods can also include higher order harmonics. This offers advantages but is comparatively expensive since each harmonic solution requires two steady state calculations (real and imaginary part) and all harmonic solutions must be computed at the same time. The computational time therefore scales with the number of harmonics to be included in the solution [43].

2.4.4. Time-linearised multi-row method

As mentioned above, time-linearised methods are attractive in terms of computational efficiency with the main drawback being the loss of all non-linearities including those resulting from blade row interference. The time-linearised multi-row methods developed by Silkowsi and Hall [97] and Hall and Ekici [45] offer a compromise between the efficiency of time-linearised methods and the capabilities of non-linear methods by including only those non-linearities which result from interaction between blade rows and not those created in the interior passage flow.

The approach was first implemented for two-dimensional potential flow by Silkowski and Hall [97]. The researchers used a coupled mode analysis to model interaction effects between neighbouring rows. The coupled mode approach is based on the theory of spinning modes, i.e. vorticity, entropy and pressure waves which travel between rows with predetermined circumferential wave numbers. The linearised potential model replaces the blades by reflection and transmission coefficients which describe how the spinning modes are reflected or become scattered by blades. The coefficients are obtained from isolated row models or analytical/semi-analytical methods.

The reflection and transmission coefficient approach becomes less advantageous if instead of the potential model the linearised Euler equations are considered because coefficients cannot be as easily computed. This has led to the development of the time-linearised multi-row model by Hall and Ekici [45]. Their method solves the linearised Euler equations on single passage domains and couples the solutions of the individual unsteady perturbations at the blade row interface such that disturbances can propagate unhindered. The methodology was validated on a 3D front compressor stage. Hall and Ekici compared solutions obtained with different levels of interaction or different spinning modes. They concluded that the fundamental spinning mode is the largest contributor to unsteady inter-row coupling. The method was later extended to the Navier-Stokes equations by Ekici et al. [30] and Saiz [89]. With a CPU time comparable to that of multiple state computations, the time-linearised multi-row approach is a very efficient technique to model blade row interactions.

2.5. Non-linear time-domain methods

2.5.1. Multi-passage methods

2.5.1.1. Whole annulus and periodic sector

With increasing computer capabilities it became possible to model unsteady phenomena in all their complexity by solving the 3D, unsteady, viscous flow in a whole annulus (360°) multi-row domain using time-accurate methods (see, for example, Sayma et al. [92]). Modelling the whole annulus is the most straightforward approach. Unlike more efficient techniques, time-accurate whole-domain computations make no assumptions about underlying periodicity or linearity and do not require adaptation of a numerical scheme. Unfortunately the approach is also the most cost-intensive. When the problem's geometry allows it, the computational domain can be truncated to a periodic sector. Periodic boundary conditions can then be applied to the pitchwise boundaries of the first and last passage in each row. However, such a periodic sector only exists if all blade rows have a common factor which becomes unlikely when multiple stages are considered. Furthermore, even if a periodic sector can be identified, it is not guaranteed that the circumferential wavelength of the unsteady disturbances in the domain also coincides with the periodic sector.

2.5.1.2. Modified blade counts

In order to achieve feasible computation times, it has been common practice in industry to modify blade counts to create a periodic sector. A compressor stage with 36 and 73 blades in the rotor and stator respectively, for example, could be modified to 36 and 72 blades to create a 1:2 rotor-to-stator ratio. This way, direct periodicity boundary conditions can be applied to $1/36^{th}$ of the computational domain. If the blades in the rotor are rescaled to maintain the stage characteristics, this can give satisfactory steady or time-averaged results. A variety of scaling techniques have been developed over the years (e.g. Rai [84] or, more recently, Mayorca et al. [75]). A disadvantage of the scaling approach is that it often fails to capture unsteady properties. If the excitation frequencies are modified, the prediction of multi-row interaction becomes difficult. Multi-row coupling depends greatly on the blade counts and cannot be recreated on modified geometries. The scaling approach for more than two rows will be reviewed in more detail in Section 2.6.1.

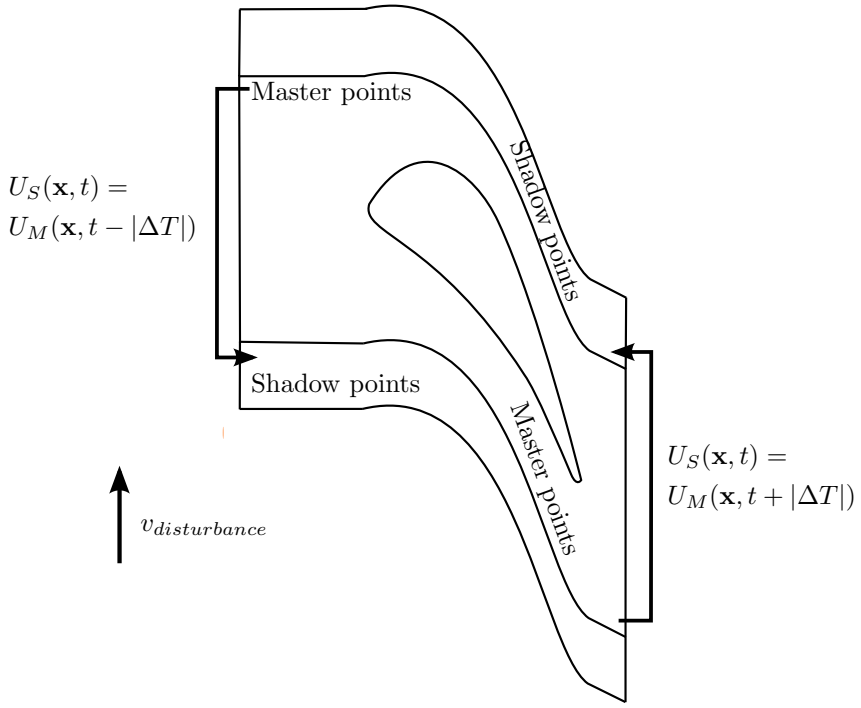


Figure 2.2.: Single passage domain with shadow point boundaries

2.5.1.3. Blade row interface treatment

Because of the relative rotation between stator and rotor rows, the simulation of the blade-row interface poses a major challenge in the computation of multi-row flows. Most implementations use grids which rotate with the blades resulting in a stationary mesh in the stator frame of reference and a moving grid in the rotor frame of reference. At every time step, the boundary conditions at the outlet surface of the stator must be determined from the flow field at the inlet of the rotor and vice versa. Sayma et al. [92] achieved this by linearly interpolating variables at the inlet or outlet surface of one row from the adjacent blade row and evaluating the boundary fluxes based on the interpolated variables. The fluxes are computed using a pseudo-3D conservative technique based on the formulation of Rai [85] which allows an undistorted propagation of discontinuities across the grid interface.

2.5.2. Single passage methods for axisymmetric flows

The whole annulus approach remains computationally expensive and is not practical in the design process. Over the past few decades time-domain single passage methods have

become available which offer considerable savings compared to whole annulus computations. The methods all rely on the time-space periodicity discussed in Section 1.3. With an appropriate representation of the phase-lagged periodic boundary conditions, it becomes possible to reduce the computational domain to one passage per row.

In order to implement the pitchwise boundary conditions, these single passage methods use additional 'dummy' or 'shadow' points which extend into the domain of the adjacent passage (see Figure 2.2). Each shadow point corresponds to a master point inside the single passage domain. By collecting information about the temporal variation on the master points, the flow variables at the shadow points, which form the pitch-wise boundary conditions, can be determined. The phase-lagged periodicity between master and shadow points is expressed as:

$$U_{Shadow}(\mathbf{x}, t) = U_{Master}(\mathbf{x}, t \pm |\Delta T|) \tag{2.10}$$

where the temporal phase shift $|\Delta T| = \sigma/|\omega|$ was defined in Equation 1.5 and 1.7.

2.5.2.1. Direct store method

The first of these single-passage methods was developed by Erdos in 1977 [31] and successfully modelled periodic flow through a fan stage by storing flow variables at the pitchwise boundaries over one disturbance cycle. The time histories of the master points inside the passage are used to update the corresponding shadow points according to phase-shifted periodicity. A disadvantage of the direct store method is that it requires large amounts of computer memory - particularly for large wavelength disturbances.

Erdos' store methods was also implemented on multiple rows by Mata et al. [74]. Their interface treatment relies on whole annulus copies of the inlet/outlet surfaces whereby the outlet or inlet conditions of adjacent rows are interpolated from the whole annulus image of the downstream or upstream row respectively. This interpolation procedure is identical to the sliding plane treatment in whole annulus calculations described in Section 2.5.1.3 [92]. The whole annulus images require storage for the 2D surface but no additional computational effort, since they only act as a link between adjacent rows.

However, updating the whole annulus images from the time histories can create difficulties. The sliding planes are initialised with the steady state solution and then updated progressively as time histories are collected. This leads to an initial mismatch between the inlet/exit surface and the boundary condition on the image of the adjacent blade row which creates spurious reflections. This single-passage multi-row (SPMR) method consequently exhibits a poor convergence rate. In order to overcome this issue, Mata et al. [74] applied

a non-reflecting treatment similar to that developed by Saxer and Giles [90]. The solution is stored and decomposed into Fourier modes. A one-dimensional characteristic treatment is then applied to the averaged value and the remaining part of the solution is updated from the sum of the harmonics. When adopted at the beginning of the computation this non-reflecting treatment removes reflections. It is limited to subsonic or supersonic flows without local flow reversal or large non-axial velocity components. However, since it acts merely as a convergence acceleration technique, the limitations were deemed acceptable.

An alternative to the non-reflecting treatment is the enforcement of spatial periodicity with wavelength less than one revolution by assuming an integer blade count ratio for the first few disturbance cycles. Once the time history for one beat period of the two modified blade passing frequencies is obtained, the whole annulus image can be updated instantaneously. After a few cycles, the image can be corrected. Mata et al. [74] report that this prevents numerical reflections and accelerates convergence.

2.5.2.2. Time-inclination

Giles [37] modelled stator-rotor interaction using a 'time inclination method'. By transforming the physical coordinates (x, y, t) to the computational coordinates (x', y', t'):

$$x' = x \quad y' = y \quad t' = t - \lambda y \tag{2.11}$$

where $\lambda = \Delta T/S$ is the ratio between the time lag between periodic boundaries and pitch. In the computational plane t' is constant at each time step. In multi-row calculations, the stator and rotor grids require different values of the transformation parameter λ since their pitches are different but the time step size is the same for both rows. If the equations are transformed and solved in the new coordinate system, the stator/rotor pitch ratio becomes unity and the phase lagged periodicity will automatically be satisfied.

This approach does not assume temporal periodicity and is thought to offer advantages in viscous flows, where physical instabilities such as vortex shedding induce frequencies which are not a multiple of the blade-passing frequency. However, due to stability requirements the method is restricted to certain blade count ratios. The time inclination parameter λ must lie in the domain of dependence of the physical solution. For most practical turbomachinery applications this corresponds to a pitch ratio in the range 0.6-1.5. Blade count ratios outside this range can be modelled by including multiple passages in the computational grid and thus altering the effective pitch ratio.

2.5.2.3. Shape correction method

The first Fourier decomposition based method in the time domain was developed by He [48] and applied to the solution of the Euler equations around oscillating blades. Like Erdos' method it uses only a single passage domain with additional dummy points at the periodic boundaries. The interior flow is still solved by a time-marching method but the temporal variation (shape) of the flow variables at the periodic boundaries is approximated from a Fourier series. This shape correction method works in a similar fashion to Erdos' direct store method but stores only Fourier coefficients of the flow variables. It assumes that the flow at the pitchwise boundaries can be decomposed into a time-averaged part $\bar{U}$ and an unsteady part U' which can be approximated by a N_H^{th} order time-wise Fourier series.

$$\begin{aligned} U(\mathbf{x},t) &= \bar{U}(\mathbf{x}) + U'(\mathbf{x},t) \\ U(\mathbf{x},t) &= a_0 + \sum_{n=1}^{N_H} a_n cos(n\omega t) + b_n sin(n\omega t) \end{aligned} \tag{2.12}$$

The Fourier coefficients depend on the axial, radial and tangential position, $\mathbf{x} = (x, r, \theta)$, of the boundary node. They are obtained by summation of the flow variables at the periodic boundaries over one disturbance cycle.

$$\begin{aligned} a_0 &= \frac{1}{N_T} \sum_{1}^{N_T} U(\mathbf{x},t) \\ a_n &= \frac{\omega \Delta t}{\pi} \sum_{1}^{N_T} U(\mathbf{x},t) cos(n\omega t) \\ b_n &= \frac{\omega \Delta t}{\pi} \sum_{1}^{N_T} U(\mathbf{x},t) sin(n\omega t) \end{aligned} \tag{2.13}$$

In order to update the solution on a pitchwise boundary the Fourier approximation from the opposite periodic boundary is applied with a phase shift. The Fourier approximations at the two boundaries then continuously correct each other until the solution becomes fully periodic. He [48] found that for most cases a few harmonics (<5) were sufficient to approximate the unsteady variation due to oscillation.

This method was later generalised for disturbances with multiple fundamental frequencies by assuming that the flow field can be expressed as a superposition of a time-average

and N_L distinctive disturbances [49]:

$$U(\mathbf{x},t) = \bar{U}(\mathbf{x}) + \sum_{l=1}^{N_L} U_l'(\mathbf{x},t) \tag{2.14}$$

If the unsteady perturbations U_l' are periodic in time and each have their own phase-shifted periodicity, they can be approximated by a Fourier series as in Equation 2.13. The discrete Fourier transform poses a problem as it requires integration over a period of the fundamental disturbance. In a case with multiple independent disturbances, this period would correspond to a beat wavelength of all the disturbances. This can lead to convergence issues if there is no small integer multiple of all disturbances concerned. By using the already existing Fourier coefficients to filter the signal, the disturbances can be separated. The discrete Fourier transform for one disturbance is then carried out over the period of this disturbance only. This approach was first used by He [49] and is known as 'partial substitution technique':

$$\begin{aligned} a_n &= \frac{\omega \Delta t}{\pi} \sum_{1}^{N_T} [U - R_l] cos(n\omega t) \\ b_n &= \frac{\omega \Delta t}{\pi} \sum_{1}^{N_T} [U - R_l] sin(n\omega t) \end{aligned} \tag{2.15}$$

R_l is the contribution of all disturbances except for the l^{th} disturbance, the Fourier coefficients of which can now be updated every period.

$$R_l = a_0 + \sum_{k \neq l}^{N_L} \sum_{n=1}^{N_H} a_{k,n} \cos(n\omega_k t) + b_{k,n} \sin(n\omega_k t) \tag{2.16}$$

Li and He [68] [66] used the shape correction technique for unsteady analysis of a vibrating fan with inlet distortion. They were able to improve stability by under-relaxing the Fourier coefficients and damping the flow flow variables at the periodic boundaries. The under-relaxation technique is employed during the first few cycles, when the solution is marched from the initial steady state to a periodic state:

$$\begin{aligned} a_{n(stored)} &= (1-\alpha) a_{n(stored)} + \alpha a_{n(new)} \\ b_{n(stored)} &= (1-\alpha) b_{n(stored)} + \alpha b_{n(new)} \end{aligned} \tag{2.17}$$

where $0 < \alpha \leq 1$ is the relaxation factor.

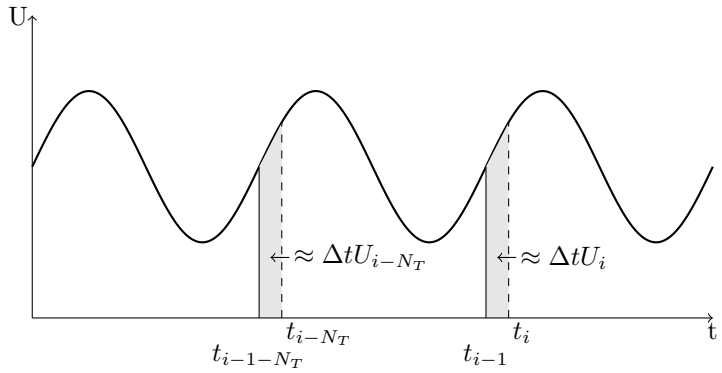


Figure 2.3.: Moving averages technique

Olausson et al. [81] also reported improvements if spurious frequencies are damped at the periodic boundaries and blade row interface. Their technique adds a numerical damping term to the flow variables at the sampling points for the Fourier transform:

$$\frac{\partial U}{\partial t} = ... - \epsilon[U(t) - \sum_{n=1}^{N_H} \hat{U}_n e^{i(\omega_n t)}] \tag{2.18}$$

The damping term consists of a damping factor, ϵ, and a correction to the flow variables based on the Fourier approximation. It thus effectively removes frequencies which are not part of the specified spectrum. As the solution marches to a periodic state, the damping term approaches zero.

2.5.2.4. Gerolymos' partial substitution technique

For large wavelength disturbances the shape correction method can still be impractical since the Fourier transform requires numerical integration over at least one period. Gerolymos [34] solved this problem by continuously updating the Fourier coefficients with a moving averages technique.

This process will be explained with reference to Figure 2.3. The Fourier coefficients at time t_i can be evaluated by summation of the flow variables over the last period, i.e. over

the time between the two dashed lines:

$$a_0|_i = \frac{1}{N_T} \sum_{j=i-N_T+1}^{i} U_j$$
$$a_n|_i = \frac{2}{N_T} \sum_{j=i-N_T+1}^{i} U_j cos(n\omega t_j)$$
$$b_n|_i = \frac{2}{N_T} \sum_{j=i-N_T+1}^{i} U_j sin(n\omega t_j) \tag{2.19}$$

Similarly, the previous coefficients at time t_{i-1} are obtained by numerical integration between the two solid lines:

$$a_0|_{i-1} = \frac{1}{N_T} \sum_{j=i-N_T}^{i-1} U_j$$
$$a_n|_{i-1} = \frac{2}{N_T} \sum_{j=i-N_T}^{i-1} U_j cos(n\omega t_j)$$
$$b_n|_{i-1} = \frac{2}{N_T} \sum_{j=i-N_T}^{i-1} U_j sin(n\omega t_j) \tag{2.20}$$

The difference between the two evaluations is a result of the difference between the two shaded areas:

$$a_0|_i - a_0|_{i-1} = \frac{1}{N_T}(U_i - U_{i-N_T})$$
$$a_n|_i - a_n|_{i-1} = \frac{2}{N_T}(U_i - U_{i-N_T})cos(n\omega t_i)$$
$$b_n|_i - b_n|_{i-1} = \frac{2}{N_T}(U_i - U_{i-N_T})sin(n\omega t_i) \tag{2.21}$$

Since U_{i-N_T} is the value of the flow variable one period earlier and equal to U_i for a periodic (converged) signal, it can be approximated using the Fourier coefficients of the previous time step $i-1$ evaluated at the current time step i:

$$U_{i-N_T} = U_i^* = a_0|_{i-1} + \sum_{n=1}^{N_H} a_n|_{i-1} cos(n\omega t_i) + b_n|_{i-1} sin(n\omega t_i) \tag{2.22}$$

Gerolymos' partial substitution technique then updates the Fourier coefficients for a single

disturbance at time step i by correcting those of the previous time step:

$$
\begin{aligned}
a_0|_i &= a_0|_{i-1} + \frac{1}{N_T}(U_i - U_i^*) \\
a_n|_i &= b_n|_{i-1} + \frac{2}{N_T}(U_i - U_i^*)cos(n\omega t_i) \\
b_n|_i &= b_n|_{i-1} + \frac{2}{N_T}(U_i - U_i^*)sin(n\omega t_i)
\end{aligned} \tag{2.23}
$$

At the first time step, the Fourier coefficients are initialised with the starting steady state solution, i.e. $a_0 = U_0$, $b_0 = 0$ and $a_{n\neq 0} = 0$ and $b_{n\neq 0} = 0$. This method filters the contribution from other disturbances - similar to He's partial substitution technique. When applied to flows with multiple perturbations, the choice of the relaxation parameter $1/N_T$ becomes difficult. For a fully converged solution, N_T can be different for each disturbance and equal to the number of time steps per period. Before the periodic state is reached, however, the filtering is not perfect and contributions from other frequencies may pollute the correction. A lower relaxation factor then acts in a similar fashion to Li and He's [66] under-relaxation and improves stability.

2.5.2.5. Single-passage multi-row shape correction

The shape correction method was applied to multiple blade rows by Dewhurst and He [25]. Blade row communication in this case takes place via whole annulus images. At a rotor-stator interface, for example, Fourier coefficients are obtained at every node on the rotor outlet and stator inlet surface and whole annulus copies of the outlet and inlet surface are updated. Boundary conditions for the adjacent row can then be interpolated from the whole annulus image. This resembles the blade row interface treatment used in conjunction with Erdos' direct store method [74]. The approach is straightforward to implement since the same interpolation procedure as for whole circumference multi-stage simulations can be used.

Gerolymos [34] developed a different interface treatment which further integrates the temporal Fourier coefficients along the pitch to obtain chorochronic Fourier modes. The Fourier modes correspond to the Tyler-Sofrin [106] aeroacoustic modes or spinning modes which are used to describe blade row interaction mechanisms (see Section 4.2.1). A disadvantage of this approach is that it requires an additional Fourier transform in the tangential direction. This is costly and difficult to implement - particularly if the grid-spacing in the tangential direction is non-uniform. This is often the case if the grid in the wake region is refined for wake-blade interaction calculations. Gerolymos [34] tackled this issue by ex-

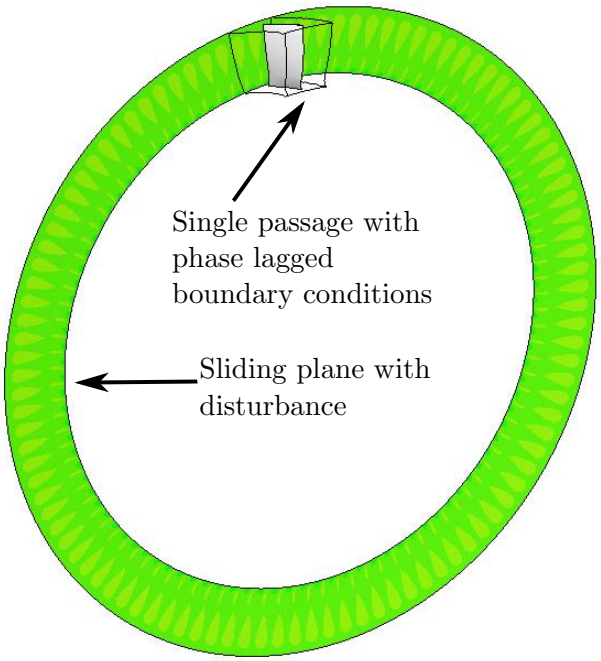


Figure 2.4.: Single passage grid with prescribed distortion

trapolating variables on a "chorochronic harmonic surface" with equidistant nodes. The extrapolated values are then used to compute the spinning modes in that row's frame of reference which in turn are used to determine the variables at boundary points of the adjacent row.

2.5.2.6. Prescribed distortion

A relatively simple approach for forced response prediction uses a prescribed distortion at the inlet or outlet of a single passage domain with phase lagged boundary conditions. The phase-lagged boundary conditions can be implemented using Erdos' direct store or the shape correction method described above and the distortion could be the steady exit/inlet flow field of an adjacent row. The distortion then acts as a rotating boundary condition to the single passage. The simplest way to implement this is to expand the distortion on the whole annulus plane, as seen in Figure 2.4, and rotate the single passage relative to it, while interpolating boundary conditions at every time step. The method usually underpredicts response levels because it cannot account for mutual interaction between rows or unsteady excitations in the adjacent blade row.[41]

2.6. Non-linear methods for non-axisymmetric flows

The methods described in the previous section were developed for unsteady axisymmetric flows as found in pure stator-rotor or rotor-stator interference problems. Limitations apply to the representation of non-axisymmetric configurations and interactions between more than two blade rows. As seen in Section 1.3.2, unequal blade counts of rows in the same frame of reference generate a steady circumferential non-uniformity which cannot be captured by single passage methods as no temporal phase-shifted periodicity exists.

However, the relative circumferential (clocking) position of blades in successive stator or rotor rows are known to affect the steady and unsteady loads and the flow conditions of downstream stages. The effect of clocking is particularly strong for equal number of blades and many studies have been performed to identify the optimum position of vanes or blades in successive rows in order to minimise losses. Observations from experimental investigations performed by Huber [60] and Halstead [47] showed that, for equal blade counts, the maximum efficiency occurs if the wake of the upstream blade impinges on the leading edge of the downstream blade. This has been confirmed in numerical studies by, for example, Dorney et al. [28],[27], Griffin et al. [42] and Arnone et al. [5].

Since equal blade counts are a rare occurrence and other factors such as the axial spacing and radial perturbations vary from case to case, there is a need for accurate and efficient numerical methods to predict multi-stage interactions. The development of efficient methodologies capable of predicting the unsteady interaction of neighbouring rows as well as the steady interaction of rows in the same frame of reference has seen significant progress in recent years.

2.6.1. Modified blade counts

The most straightforward solution to the problem of representing non-axisymmetric flows is the computation on a periodic sector to reduce the size of the computational domain. This is easily achievable if an integer blade count ratio exists but, since this is not typically the case, the blade counts may have to be modified to create a sector with direct periodicity.

A 1.5 stage compressor configuration with blade counts N_{S1}=54, N_{R2}=56, and N_{S2}=74, for example, could be modified by adding one vane to S1 and S2, such that the highest common factor between the two stators becomes five and only $1/5^{th}$ of the stator rows need to be included in the domain. Note, that a single passage is sufficient for the rotor as no stationary perturbation exists in the rotor frame of reference. Unsteady disturbances can be modelled using any one of the numerical approaches discussed in Sections 2.4 and 2.5.

As mentioned in Section 2.5.1, the approach of modified blade counts has also frequently been used to model the unsteady interaction between two rows in relative motion. It offers some advantages over the methods discussed in the previous section: the scaling approach makes no assumptions about temporal periodicity and does not require adaptations to the numerical treatment of the governing equations. It is therefore independent of the numerical scheme and can be used with any standard flow solver.[75]

Modifying the blade count while retaining the shape of the blades changes throat areas and thus the flow capacity, reaction, flow angles etc. In order to achieve a periodic sector without changing the stage characteristics, the geometry needs to be modified. A restaggering or rescaling of the aerofoils becomes necessary. Geometrical modifications are chosen to minimise effects on performance. This is typically achieved by maintaining the solidity (pitch-to-chord) ratio or pitch-to-throat ratio.

A variety of scaling techniques have been developed and their effects on the prediction of steady and unsteady aerodynamic loads have been investigated (see, for example, Mayorca et al. [75]). The majority of research focuses on the prediction of the unsteady interaction of neighbouring rows, but the effects of scaling in multi-stage computations have also been studied [113] [67]. There is obviously a limit to the amount of scaling which can be tolerated. When investigating turbine forced response, Clark et al. [14] found that even small amounts of scaling had relatively large effects on unsteady pressure prediction. Schmitz et al. [95], on the other hand, demonstrated that the scaling approach can provide an accurate prediction of aerodynamic forcing of a turbine rotor by the adjacent stator.

An alternative approach, which is effectively a modification of blade counts without rescaling of the blades, was investigated by Van Zante et al. [113]. The researchers compared performance estimates for 2.5 compressor stages obtained with three different models: 1) Single-passage model with phase lagged boundary conditions, 2) Hybrid single-passage/multi-passage grids with phase lagged boundary conditions and 3) a periodic sector. The hybrid single-passage/multi-passage model was chosen to have sufficient spatial coverage to directly capture stator-stator/rotor-rotor interaction. However, the phase-lagged boundary conditions nevertheless enforced a spatial periodicity which was inconsistent with the actual blade counts. The single-passage model was lacking all interaction of rows in the same frame of reference and overestimated adiabatic efficiency. The hybrid model showed some evidence of stator-stator/rotor-rotor interaction but did not capture the true coupling between rows in the same frame of reference. The resulting discrepancies can lead to significant differences in performance estimates when accumulated over multiple stages.

Similarly, Li and He [67] observed serious inaccuracies when comparing predictions

from a numerical study of NGV-rotor-stator interaction with modified stator blade count to experimental data. The inaccuracies were attributed to large changes in blade row interference lengths due to the modified stator blade passing frequency.

2.6.2. Interface disturbance truncation technique

The interface disturbance truncation technique by Li and He [70] offers an efficient way to approximate multi-stage interactions if the main point of interest is the simultaneous unsteady forcing of a blade by one upstream and one downstream row rather than stator-stator or rotor-rotor coupling. The method is not strictly speaking a method for non-axisymmetric flows, as it does not model any stationary circumferential perturbations, but it provides a way of removing these perturbations from multi-stage flows. The technique was developed as a tool to find the optimum combination of upstream and downstream axial spacing of a 1.5 stage compressor. Previous work by Silkowski and Hall [97] and Li and He [69] had shown that multi-stage effects and inter-row gaps had considerable impact on aerodynamic damping of the middle row. The objective was hence to optimise inter-row gaps for a IGV-rotor-stator configuration, taking into account the simultaneous forcing on the rotor from IGV and stator. If the IGV-stator interaction is negligible, a phase-shifted (temporal) periodicity can be defined in all rows. The IGV and stator experience an unsteadiness at multiples of the rotor blade passing frequency only, while the rotor sees two fundamental unsteady disturbances: the IGV and stator blade passing. This situation can then be modelled on single-passage/multi-row grids using He's shape correction method.

The interface disturbance technique enforces the necessary phase-lagged periodicity by removing IGV disturbances at the rotor-stator interface and stator disturbances at the IGV-rotor interface. This is achieved by including only certain disturbances when reconstructing the whole annulus sliding planes. The exclusion of disturbances results in a mismatch of flow variables between the two sides of the interface. At the IGV-rotor boundary, for example, a disturbance with the frequency of the stator blade passing exists in the rotor domain but no equivalent disturbance exists in the IGV frame of reference. This jump may lead to artificial reflections in both domains, which Li and He [69] prevented by a local 1D characteristic non-reflective treatment.

More recently Gerolymos [35] also filtered disturbances at the blade-row interfaces for the approximate analysis of multi-stage interactions. In fact, his procedure for transferring information across the interface naturally filters disturbances which cannot be represented on both sides of the interface [34]. Gerolymos uses a two-dimensional (time-space) decom-

position of Fourier modes at the blade row interface. Once the time-space harmonics for a given radial and axial location are obtained, the signal can be reconstructed at arbitrary circumferential positions in the adjacent blade row. However, not all modes are used in the reconstruction. Instead, only those modes which exist on both sides of the interface, i.e. blade row interaction modes (Tyler-Sofrin spinning modes [106]), are selected. This approach thus automatically filters out all disturbances which are not compatible with the interaction of immediately adjacent blade rows. However, it makes no allowances for a potential mismatch of variables across the interface and resulting reflections.

2.6.3. Frequency domain single passage

The non-linear harmonic approach has been extended to multiple stages by He and Chen [55]. The researchers used the method to investigate stator-stator and rotor-rotor clocking effects. The treatment of the circumferential variation in the time-averaged flow is based on the following idea:

The rotor-rotor interaction in a three row configuration with rotor 1 (R1), stator (S1) and rotor 2 (R2) at arbitrary clocking positions can be obtained if the circumferential variation at R2 inlet due to the presence of R1 is known. In order to obtain the amplitude of variation at S1 outlet, the amplitude of the unsteady disturbance in the stator frame is pitch-wise phase averaged. Once the amplitude of the disturbance from R1 is known at the inlet of R2, its influence on the time-averaged flow in the passages of R2 needs to be evaluated.

First, the passage-averaged time-averaged flow $\bar{U}_{PA}$ in R2 is defined as:

$$\bar{U}_{pa} = \frac{1}{N_{R2}} \sum_{n=1}^{N_{R2}} \bar{U}_n \tag{2.24}$$

where $\bar{U}_n$ is the time-averaged flow in passage n. The circumferential variation to $\bar{U}_{pa}$ due to the presence of R1 must now be found. He and Chen took advantage of the fact that the spatial averaging would be equivalent to a temporal averaging if R1 was rotating very slowly (in a quasi-steady manner) with respect to R2. This allows the quasi-steady harmonic perturbation $\tilde{U}_{pa}$ to be solved for in the same fashion as any unsteady perturbation by setting the frequency to zero. The time-averaged flow in passage n can then be found from:

$$\bar{U}_n = \bar{U} + \tilde{U}_{pa} e^{i(n-1)\sigma} + \tilde{U}_{-pa} e^{-i(n-1)\sigma} \tag{2.25}$$

and the corresponding stationary circumferential perturbation is given by:

$$\hat{U}_n = \bar{U}_n - \bar{U}_{PA} \tag{2.26}$$

where $\sigma = (N_{R1}/N_{R2})2\pi$ is the inter-blade phase angle.

Clocking effects can easily be evaluated using this approach as the time-averaged flow field can be determined for every relative position [55].

2.6.4. Time-domain Fourier model

Recently, time-domain Fourier methods have been developed by He [52] which adequately model non-axisymmetric steady and unsteady flows. The approach uses several circumferential mesh points or discrete passages which are placed evenly across the circumference as illustrated in Figure 2.5. Any circumferential variation in the steady or unsteady flow field is then approximated by:

$$U(x,r,\theta,t) = \bar{U}(x,r,t) + \sum_{m=1}^{N_M} [A_m(x,r,t)sin(m\theta) + B_m(x,r,t)cos(m\theta)] \tag{2.27}$$

where N_M is the number of spatial harmonics, $\bar{U}$ is the circumferential average and A_m and B_m are the spatial Fourier coefficients obtained by summation of the flow variables at circumferential positions i:

$$\begin{aligned}
\bar{U}(x,r,t) &= \frac{1}{2N_M+1} \sum_{i=1}^{2N_M+1} U_i \\
A_m(x,r,t) &= \frac{1}{2N_M+1} \sum_{i=1}^{2N_M+1} U_i sin(m\theta) \\
B_m(x,r,t) &= \frac{1}{2N_M+1} \sum_{i=1}^{2N_M+1} U_i cos(m\theta)
\end{aligned} \tag{2.28}$$

The sampling points i are uniformly spaced points along the circumference. The Fourier coefficients are time-dependent and need to be evaluated at every time step of the time marching scheme to approximate the instantaneous distribution. In 2006 He validated the circumferential Fourier model on an intake duct subjected to cross wind and steady OGV-pylon interaction [52]. The inlet distortion was modelled as a sinusoidal circumferential perturbation in circumferential and radial flow angle with a 10% amplitude. This distribution was successfully approximated on 11 circumferential mesh cells instead of the

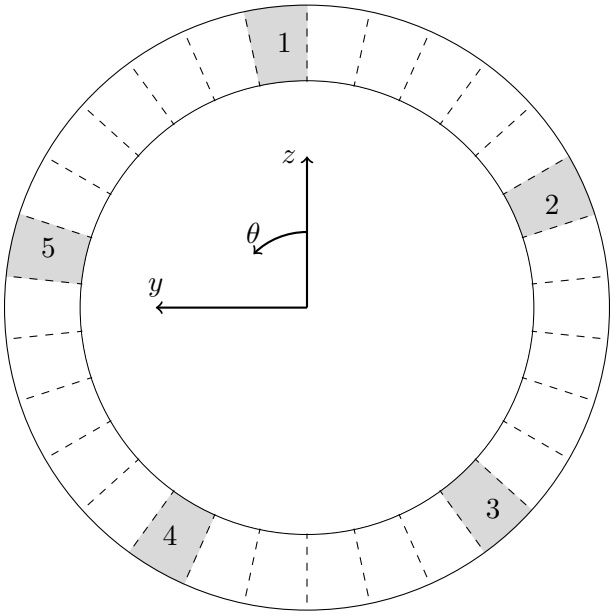


Figure 2.5.: Computational domain for circumferential Fourier model

300 circumferential cells of the whole 360° domain. Similarly, a comparison between static pressure distribution for the OGV-Pylon interaction showed that the OGV domain can be truncated from 30 OGVs to 5 discrete passages without significant loss of accuracy.

The method has also been applied to non-axisymmetric unsteady flows in rotor-stator disk cavities by the same author [54]. It shows very good agreement between reduced passage and whole annulus solutions and results in significant computational savings. He estimates a speed-up of approximately half the mesh size reduction due to the overhead associated with the spatial Fourier transform.

It is important to note that the existence of a chorochronic (space-time) periodicity is the only condition necessary for time-accurate Fourier methods such as the single-passage multi-row shape correction and spatial Fourier method. Unlike time-linearised methods, the time-domain Fourier methods fully capture non-linearities inside the domain and coupling between the time-averaged and unsteady modes.

2.7. Summary

The numerical methods discussed in this chapter represent, to the author's knowledge, the state-of-the-art in the prediction of unsteady multi-row turbomachinery flows. Researchers have demonstrated that it is possible to accurately model the viscous, three-dimensional

flows across multiple stages using time-accurate methods, albeit at high computational cost. Frequency domain and single passage methods were shown to provide very good approximations at lower cost. However, they are typically limited to periodically unsteady perturbations around a uniform time-averaged flow and ignore potentially important variations in the underlying steady flow field. Methods such as He and Chen's frequency-domain single-passage method [55] and He's time-domain Fourier model [52] which allow the representation of steady circumferential variations were only developed in recent years and have not yet reached their full potential.

3. Objectives

It was seen in the last two chapters that large nodal diameter circumferential perturbations exist in aeroengines and gas turbines which are known to affect aerothermal performance and aeroelastic stability but can currently only be predicted by full-circumference multi-row simulations. These computations are time-consuming and unfeasible during the design cycle where a large number of solutions is sought in a short time frame. The objective of this work is hence to develop a time-domain method which models both steady and unsteady circumferentially non-uniform flows on a reduced number of passages thereby offering an efficient alternative to more expensive whole annulus computations.

The reduced-passage model is based on He's shape correction method [49] and time-domain spatial Fourier model [52]. A time-accurate scheme solves the flow inside several discrete passages which act as sampling points for a spatial Fourier transform. Boundary conditions are obtained from a time-space Fourier approximation and couple the individual passages. Unlike SPMR methods, the current approach does not assume a blade-to-blade periodicity in the time-averaged flow which makes it possible to represent non-axisymmetric flows or flows past non-axisymmetric configurations. The method can thus be considered as an extension of single-passage multi-row methods to flows with stationary circumferential non-uniformities as illustrated in Figure 3.1.

The time-domain Fourier model is valid for all flows which can be decomposed into a finite number of a temporal and spatial Fourier components. With regard to the representation of unsteady perturbations, it offers advantages over time-linearised methods since it makes no assumptions about linearity of the flow. The non-linear interaction between the time-averaged flow and unsteadiness as well as the interaction between different unsteady perturbations is fully captured as long as sufficient frequencies are included in the Fourier model. The representation of stationary circumferential perturbations on a finite number of passages, on the other hand, requires the spatial perturbation to be small compared to the mean flow. Non-linear effects such as separation or shock formation on individual blades of an aerodynamically mistuned assembly cannot be modelled. The reduced-passage model preserves blade counts and geometry and can be applied to any blade count ratio. As passages can be placed at arbitrary circumferential locations,

the size of the reduced passage model is independent of blade count ratios and merely determined by the number of harmonics to be retained in the Fourier approximation.

The research aims to demonstrate that the reduced passage method can provide solutions which are equivalent to the full domain solutions but require only a fraction of the computational effort. The objectives of this thesis are thus:

1. Formulation of a reduced-passage time-domain methods for steady and unsteady non-axisymmetric flows across multiple blade rows
2. Validation of this method for:
   (a) Steady flows with a stationary circumferential perturbation
   (b) Steady flows past non-axisymmetric configurations
   (c) Unsteady rotor-stator interaction with non-axisymmetry in the stator/rotor
   (d) Rotor-rotor (stator-stator) interaction
3. Assessments of the theoretical and practical limitations of the proposed method

The methodology is developed in the next chapter and the validation and discussion are combined in the following chapter where the reduced-domain model is applied to representative test cases. In order to reduce computational time, the initial validation is performed on thin sections at mid-span. The last chapter contains a full-span application with comparison against experimental measurements and a study of distortion transfer in an industrial turbine.

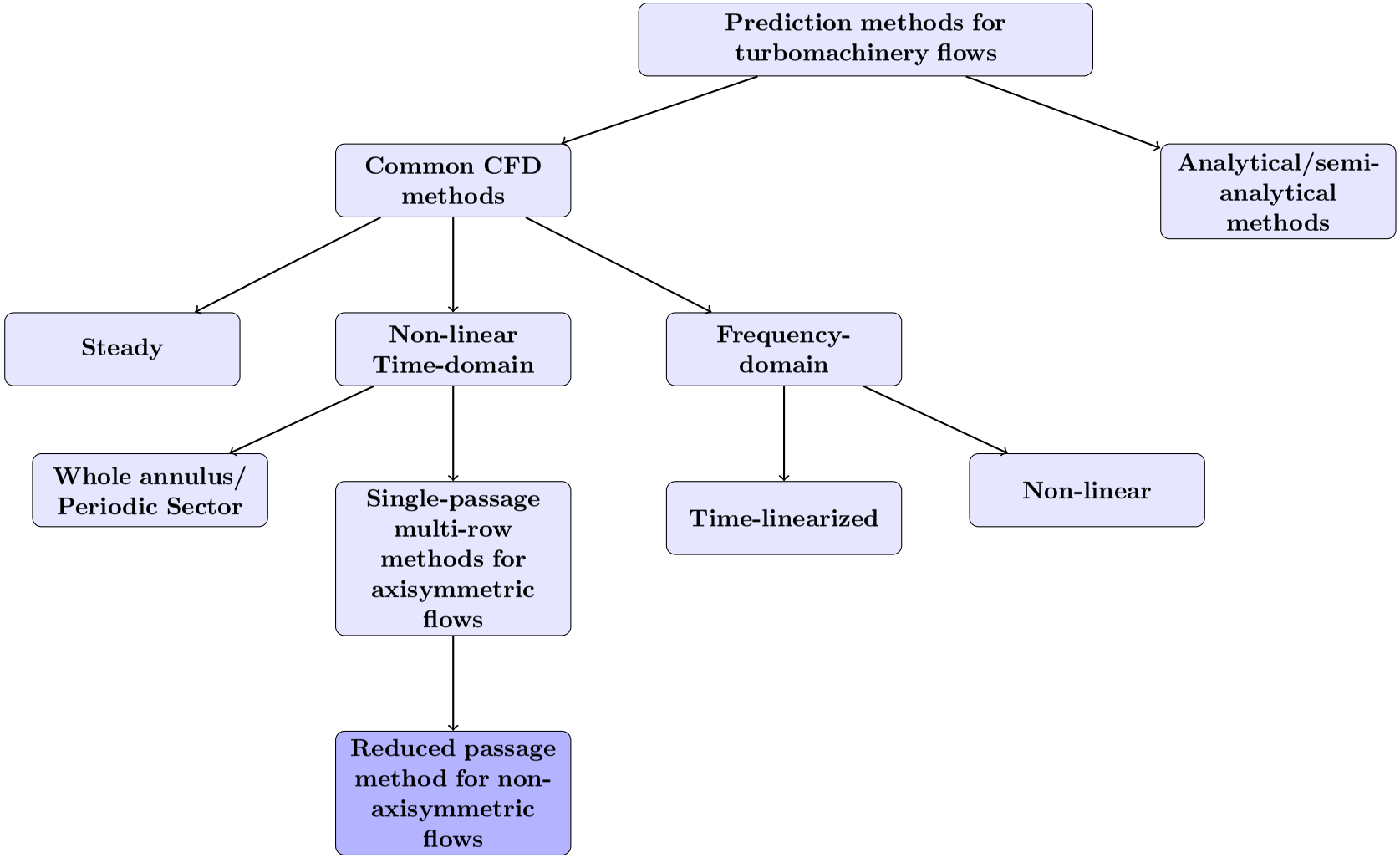


Figure 3.1.: The gap in prediction methods for turbomachinery flows

4. Methodology

4.1. Time-domain Fourier approach

4.1.1. Overview

A typical multi-row turbomachinery flow field as described in Chapter 1 is to be modelled on a reduced number of passages. In order to represent both travelling and stationary circumferential perturbations, the current methodology uses several discrete passages coupled through pitchwise and inter-row boundaries.

The passages are uniformly spaced across one circumferential wave length of the fundamental stationary disturbance and thus act as sampling points for a circumferential Fourier transform. This approximation of stationary disturbances from discrete solutions in space was first proposed by He [52] and has been briefly discussed in Section 2.6.4. It is analogous to Hall's harmonic balance method [43] which uses solutions at discrete time levels to deduce information about the temporal variation of flow variables. For the representation of unsteady perturbations, the current methodology relies on temporal Fourier transforms and phase-lagged boundary conditions. The treatment of periodically unsteady perturbations is thus similar to that of traditional single-passage multi-row methods which were discussed in Section 2.5.2.

This chapter first defines temporal and circumferential averages in bladed passages and then describes the treatment of steady and unsteady perturbations. It starts from the representation of unsteady perturbations on a single-passage and then extends the approach to flows with stationary circumferential perturbations and finally to multiple blade rows.

The methodology developed in this section is implemented on a finite-volume time-accurate Reynolds-Averaged Navier-Stokes solver. The code (AU3D) was developed at Imperial College and is briefly described in Appendix A.1. Sayma et al. [92] provide a more detailed description.

4.1.2. Definition: Temporal and circumferential averages

Before the methodology is developed, it is necessary to define the terms "time average" and "circumferential average" as used in the context of this thesis.

Consider a row with N_B blades exposed to a travelling disturbance with frequency $\frac{1}{T}$ and a stationary circumferential variation with wave length $\frac{2\pi}{k}$. In absence of a stationary disturbance, the time-averaged flow is the same in every passage. However, in presence of a stationary disturbance the time-averaged flow field varies from passage to passage and it becomes necessary to define a circumferential average (or passage-average). The flow variables must still depend on the circumferential coordinate inside the passage but the passage-averaged flow field is identical in every passage. We therefore define the vector $\mathbf{x} = (x, r, \zeta)$ which describes the local coordinate system inside the passage and the vector $\mathbf{x_g} = (x, r, \theta)$ which describes the global coordinate system. The local circumferential coordinate ζ is referenced to the blade. The transformation from local to global coordinate system is described by:

$$x_{local} = x_{global} = x \tag{4.1}$$

$$r_{local} = r_{global} = r \tag{4.2}$$

$$\theta_j = \zeta + 2\pi \frac{j-1}{N_B} \tag{4.3}$$

$U_j(x, r, \zeta, t) = U(x, r, \theta_j, t)$ describes the flow field in the j^{th} passage. This allows the definition of a passage-dependent time-average:

$$U_0(x, r, \theta_j) = \frac{1}{T} \int_0^T U(x, r, \theta_j, t) dt \tag{4.4}$$

and a passage-averaged or circumferentially averaged flow field:

$$\bar{U}(x, r, \zeta, t) = \bar{U}(\mathbf{x}, t) = \frac{1}{N_P} \sum_{j=1}^{N_P} U(x, r, \theta_j, t) \tag{4.5}$$

where N_P is the minimum number of passages required to complete an integer number of wave lengths of the stationary disturbance. If the blade count is not an integer multiple of the circumferential wave number, the beat wave length is the full circumference and $N_P = N_B$:

$$N_B \bmod k \neq 0 \quad \Rightarrow \quad N_P = N_B \tag{4.6}$$

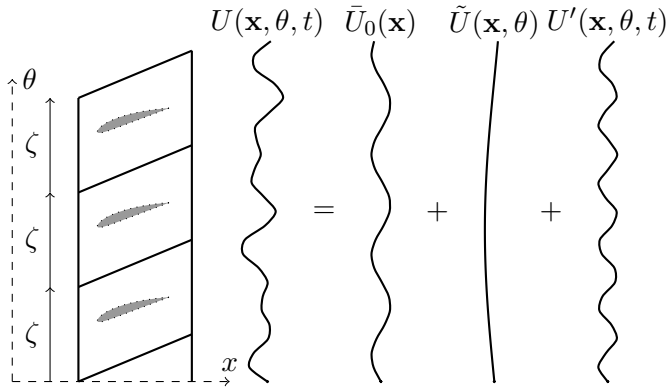


Figure 4.1.: Flow field decomposition into time-space average, circumferential variation and unsteady perturbation

This leads to the definition of the time-space averaged flow field:

$$\bar{U}_0(\mathbf{x}) = \frac{1}{N_P}\frac{1}{T}\sum_{j=1}^{N_P}\int^{T} U(x,r,\theta_j,t)dt \tag{4.7}$$

Or, in the discrete case with N_T equally discretised time steps per period of the travelling disturbance, i.e. $\Delta t = \frac{T}{N_T}$ and $t_i = i\Delta t$:

$$\bar{U}_0(\mathbf{x}) = \frac{1}{N_P}\frac{1}{N_T}\sum_{j=1}^{N_P}\sum_{i=1}^{N_T} U(x,r,\theta_j,t_i) \tag{4.8}$$

For multiple disturbances, the variables must be averaged over the beat wave length which corresponds to the least common multiple of all wave lengths.

4.1.3. Expression of chorochronic periodicity

The time-domain Fourier method then assumes that the flow variables inside the single passage domain can be expressed as a superposition of a space-time average, stationary circumferential (passage-to-passage) variations and unsteady disturbances as illustrated in Figure 4.1.

$$U(x,r,\theta,t) = \bar{U}_0(\mathbf{x}) + \tilde{U}(\mathbf{x},\theta) + U'(\mathbf{x},\theta,t) \tag{4.9}$$

Note that the space-time average, $\bar{U}(x,r,\zeta)$, is different for every point inside

the passage and that the stationary variation, $\tilde{U}(\mathbf{x}, \theta)$, and unsteady fluctuation, $U'(\mathbf{x}, \theta, t)$, vary in amplitude and phase inside the single passage domain due to interaction with the steady flow field. If these conditions are satisfied, a well defined time-space (chorochronic) periodicity exists between adjacent passages and it becomes possible to express unsteady and steady variations by means of temporal and spatial Fourier components respectively.

4.1.3.1. Unsteady fluctuations

The unsteady fluctuations typically take the shape of travelling waves with constant angular velocity v and angular frequency ω. For blade row interaction problems, the frequency and wave length are determined by the rotational speed and blade count of adjacent blade rows. For self-excited vibration, the frequency and circumferential wave number of the unsteady perturbation are the vibration frequency and nodal diameter pattern. If more than one of these perturbations are present, the unsteady fluctuation can be described as a superposition of N_L independent disturbances:

$$U'(\mathbf{x}, \theta, t) = \sum_{l=1}^{N_L} U'_l(\mathbf{x}, \theta, t) \tag{4.10}$$

where $U'_l(\mathbf{x}, \theta, t)$ is the unsteady part of the l^{th} perturbation. The number of independent disturbances depends on the nature of the flow. For flows without strong interactions the independent disturbances are the fundamental perturbations at the source of the problem (e.g. travelling distortions, oscillating blades or blade passing disturbances). For flows with significant interactions between the fundamental perturbations, the induced frequencies should also be included in the independent disturbances.

If the time-averaged flow in every passage is the same, i.e. $\tilde{U}(\mathbf{x}, \theta) = 0$ in Equation (4.9), and the unsteadiness consists of one or more disturbances of the nature described above, a time-space periodicity applies which is characterised by the angular frequency ω and circumferential wavenumber $\frac{\omega}{v}$, where v is the rotational speed of the disturbance. It then becomes possible to decompose each disturbance into its

temporal Fourier components:

$$U_l'(\mathbf{x},\theta,t) = \sum_{h=1}^{N_H} a_h^l(\mathbf{x})\cos(h\frac{\omega_l}{v_l}\theta - h\omega_l t) + b_h^l(\mathbf{x})\sin(h\frac{\omega_l}{v_l}\theta - h\omega_l t) \tag{4.11}$$

where N_H is the number of harmonics. For conciseness, the following will assume the same number of harmonics N_H per independent disturbance and combine the indices of independent disturbances l and their harmonics h into a disturbance index n such that:

$$\begin{aligned} N_N &= N_H N_L \\ \omega_n &= \omega_{(l-1)N_H+h} = h\omega_l \\ v_n &= v_{(l-1)N_H+h} = hv_l \end{aligned} \tag{4.12}$$

The unsteady perturbation is hence expressed as a superposition of N_N travelling disturbances.

$$U'(\mathbf{x},\theta,t) = \sum_{n=1}^{N_N} a_n(\mathbf{x})\cos(\frac{\omega_n}{v_n}\theta - \omega_n t) + b_n(\mathbf{x})\sin(\frac{\omega_n}{v_n}\theta - \omega_n t) \tag{4.13}$$

The time-average is obtained by setting $n = 0$ with $\omega_0 = 0$:

$$\bar{U}(\mathbf{x},\theta) = a_0(\mathbf{x},\theta) \tag{4.14}$$

The temporal Fourier coefficients $a_n(\mathbf{x})$ and $b_n(\mathbf{x})$ are obtained from a partial substitution technique developed by Gerolymos [34] which continuously updates the Fourier coefficients. The coefficients at time step i are obtained from a correction

to those of the previous time step:

$$
\begin{aligned}
a_0(\mathbf{x})|_i &= a_0(\mathbf{x})|_{i-1} + \frac{1}{N_T}[U(\mathbf{x},\theta,t_i) - U^*(\mathbf{x},\theta,t_i)] \\
a_n(\mathbf{x})|_i &= a_n(\mathbf{x})|_{i-1} + \frac{1}{N_T}[U(\mathbf{x},\theta,t_i) - U^*(\mathbf{x},\theta,t_i)]\cos(\frac{\omega_n}{v_n}\theta - \omega_n t_i) \\
b_n(\mathbf{x})|_i &= b_n(\mathbf{x})|_{i-1} + \frac{1}{N_T}[U(\mathbf{x},\theta,t_i) - U^*(\mathbf{x},\theta,t_i)]\sin(\frac{\omega_n}{v_n}\theta - \omega_n t_i)
\end{aligned} \tag{4.15}
$$

where $U^*(\mathbf{x},\theta,t_i)$ are the flow variables at time step i as evaluated from the coefficients of time step $i-1$.

$$
\begin{aligned}
U^*(\mathbf{x},\theta,t_i) = \sum_{n=0}^{N_N} & a_n(\mathbf{x})|_{i-1}\cos(\frac{\omega_n}{v_n}\theta - \omega_n t_i) \\
& + b_n(\mathbf{x})|_{i-1}\sin(\frac{\omega_n}{v_n}\theta - \omega_n t_i)
\end{aligned} \tag{4.16}
$$

With the Fourier coefficients from Equation (4.15), the flow variables at time step i on the opposite boundary are updated according to:

$$
\begin{aligned}
U(\mathbf{x},\theta+\Theta,t_i) = \bar{U}(\mathbf{x}) + \sum_{n=1}^{N_N} & a_n(\mathbf{x})\cos(\frac{\omega_n}{v_n}(\theta \pm \Theta) - \omega_n t_i) \\
& + b_n(\mathbf{x})\sin(\frac{\omega_n}{v_n}(\theta \pm \Theta) - \omega_n t_i)
\end{aligned} \tag{4.17}
$$

where $\Theta = \frac{2\pi}{N_B}$ is the pitch. The use of absolute phase angles in the Fourier transform and reconstruction ensures that the conditions on the opposite boundary are updated with the correct phase lag.

4.1.3.2. Stationary disturbance

So far it was assumed that the time-averaged flow does not vary from passage to passage. However, if a stationary disturbance with circumferential wave number k is superimposed onto a steady flow, it also becomes necessary to represent the stationary circumferential variation $\tilde{U}(\mathbf{x},\theta)$. Similarly to the temporal variation, it

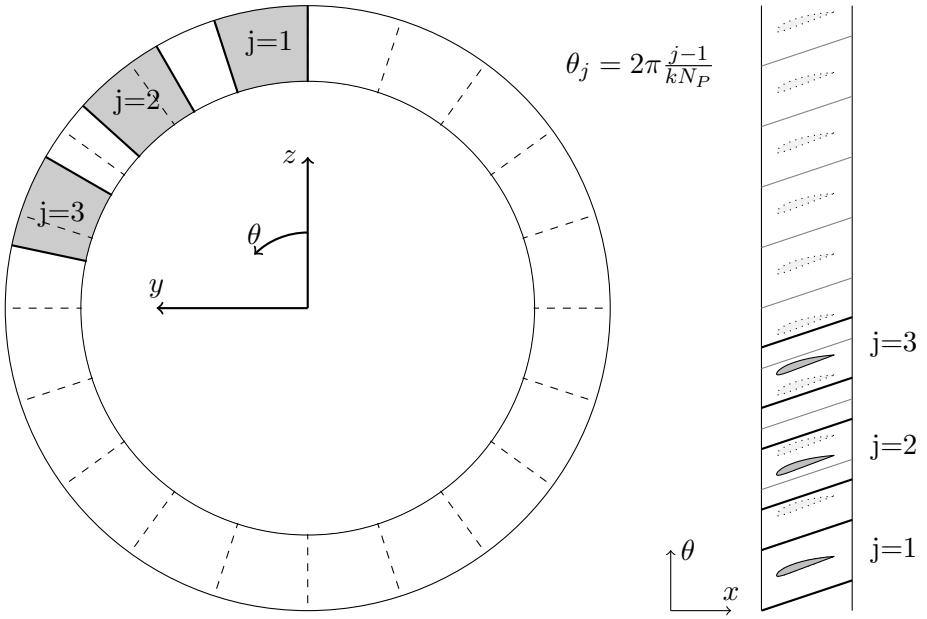


Figure 4.2.: Sparse assembly domain for first order Fourier approximation of a 4ND stationary disturbance

can be approximated by a circumferential Fourier series:

$$\tilde{U}(\mathbf{x},\theta) = \sum_{m=1}^{N_M} \alpha_m(\mathbf{x})\cos(mk\theta) + \beta_m(\mathbf{x})\sin(mk\theta) \tag{4.18}$$

where N_M is the number of spatial harmonics. For the evaluation of the spatial Fourier coefficients $\alpha_m(\mathbf{x})$ and $\beta_m(\mathbf{x})$, N_P passages are distributed over $\frac{1}{k}^{th}$ of the circumference. The passages form a *sparse assembly* and act as sampling points for the circumferential Fourier transform:

$$\begin{aligned}\alpha_m(\mathbf{x}) &= \sum_{j=1}^{N_P} U(\mathbf{x},\theta_j)\cos(mk\theta_j) \\ \beta_m(\mathbf{x}) &= \sum_{j=1}^{N_P} U(\mathbf{x},\theta_j)\sin(mk\theta_j)\end{aligned} \tag{4.19}$$

A sparse assembly domain with $2N_M + 1$ passages distributed over $1/k^{th}$ of the circumference allows a spatial Fourier approximation of order N_M. Figure 4.2 shows a schematic of a sparse assembly domain for a 4ND stationary disturbance in a row

with 20 blades. The discrete passages with shadow point boundaries are placed such that their origin ($\zeta = 0$) is located at:

$$\theta_j = \frac{j-1}{kN_P} 2\pi \tag{4.20}$$

where $N_P = 3$ is the number of passages and $k = 4$ is the circumferential wave number of the stationary perturbation. This domain allows a first order representation of a 4ND stationary disturbance.

For cases with multiple stationary disturbances, the passages would have to be distributed over the beat wave length. This may increase the size of the computational domain significantly. As with travelling disturbances, the interaction of a single stationary disturbance with the time-space averaged flow field manifests itself in different amplitudes and phases inside the single passage domain.

4.1.3.3. Circumferentially distorted travelling disturbance

Finally, we consider a flow where a stationary disturbance with circumferential wave number k interacts with an unsteady flow field. It can no longer be assumed that the temporal Fourier coefficients are uniform from passage to passage as the travelling wave can become modulated in the circumferential direction ($a_n(\theta) \neq a_n(\theta + \Theta)$ and $b_n(\theta) \neq b_n(\theta + \Theta)$). The n^{th} travelling disturbance then takes the shape:

$$\begin{aligned} U'_n(\mathbf{x}, \theta, t) = a_n(\mathbf{x}, \theta) \cos(\frac{\omega_n}{v_n}\theta - \omega_n t) \\ + b_n(\mathbf{x}, \theta) \sin(\frac{\omega_n}{v_n}\theta - \omega_n t) \end{aligned} \tag{4.21}$$

Similarly to the stationary disturbance, we can approximate the circumferential variation of a_n and b_n from a spatial Fourier transform:

$$\begin{aligned} a_n(\mathbf{x}, \theta) = \sum_{m=1}^{N_M} A_{mn}(\mathbf{x}) \cos(mk\theta) \\ + B_{mn}(\mathbf{x}) \sin(mk\theta_j) \\ b_n(\mathbf{x}, \theta) = \sum_{m=1}^{N_M} C_{mn}(\mathbf{x}) \cos(mk\theta) \\ + D_{mn}(\mathbf{x}) \sin(mk\theta) \end{aligned} \tag{4.22}$$

where, as before, the spatial Fourier coefficients are obtained by summation over N_P passages whereby the origin of the j^{th} passage is located at $\theta_j = \frac{j-1}{kN_P}2\pi$:

$$\begin{aligned}
A_{mn}(\mathbf{x}) =& \frac{1}{N_P}\sum_{j=1}^{N_P} a_n(\mathbf{x},\theta_j)\cos(mk\theta_j) \\
B_{mn}(\mathbf{x}) =& \frac{1}{N_P}\sum_{j=1}^{N_P} a_n(\mathbf{x},\theta_j)\sin(mk\theta_j) \\
C_{mn}(\mathbf{x}) =& \frac{1}{N_P}\sum_{j=1}^{N_P} b_n(\mathbf{x},\theta_j)\cos(mk\theta_j) \\
D_{mn}(\mathbf{x}) =& \frac{1}{N_P}\sum_{j=1}^{N_P} b_n(\mathbf{x},\theta_j)\sin(mk\theta_j)
\end{aligned} \tag{4.23}$$

Combining Equation (4.23) and the evaluation of the temporal Fourier coefficients $a_n(\mathbf{x},\theta)$ and $b_n(\mathbf{x},\theta)$ in Equation (4.15) gives:

$$\begin{aligned}
A_{mn}(\mathbf{x})|_i &= A_{mn}(\mathbf{x})|_{i-1} \\
&\quad + \frac{1}{N_P N_T}\sum_{j=1}^{N_P}[U(\mathbf{x},\theta_j,t_i) - U^*(\mathbf{x},\theta_j,t_i)]\cos(\frac{\omega_n}{v_n}\theta_j - \omega_n t)\cos(mk\theta_j) \\
B_{mn}(\mathbf{x})|_i &= B_{mn}(\mathbf{x})|_{i-1} \\
&\quad + \frac{1}{N_P N_T}\sum_{j=1}^{N_P}[U(\mathbf{x},\theta_j,t_i) - U^*(\mathbf{x},\theta_j,t_i)]\cos(\frac{\omega_n}{v_n}\theta_j - \omega_n t)\sin(mk\theta_j) \\
C_{mn}(\mathbf{x})|_i &= C_{mn}(\mathbf{x})|_{i-1} \\
&\quad + \frac{1}{N_P N_T}\sum_{j=1}^{N_P}[U(\mathbf{x},\theta_j,t_i) - U^*(\mathbf{x},\theta_j,t_i)]\sin(\frac{\omega_n}{v_n}\theta_j - \omega_n t)\cos(mk\theta_j) \\
D_{mn}(\mathbf{x})|_i &= D_{mn}(\mathbf{x})|_{i-1} \\
&\quad + \frac{1}{N_P N_T}\sum_{j=1}^{N_P}[U(\mathbf{x},\theta_j,t_i) - U^*(\mathbf{x},\theta_j,t_i)]\sin(\frac{\omega_n}{v_n}\theta_j - \omega_n t)\sin(mk\theta_j)
\end{aligned} \tag{4.24}$$

Substituting back into Equation (4.9), it becomes possible to approximate the full

variation in time and space.

$$
\begin{aligned}
U(\mathbf{x},\theta,t) = \sum_{n=0}^{N_N}\sum_{m=0}^{N_M} & A_{nm}(\mathbf{x})\cos(mk\theta)\cos(\frac{\omega_n}{v_n}\theta-\omega_n t)+ \\
& B_{nm}(\mathbf{x})\sin(mk\theta)\cos(\frac{\omega_n}{v_n}\theta-\omega_n t)+ \\
& C_{nm}(\mathbf{x})\cos(mk\theta)\sin(\frac{\omega_n}{v_n}\theta-\omega_n t)+ \\
& D_{nm}(\mathbf{x})\sin(mk\theta)\sin(\frac{\omega_n}{v_n}\theta-\omega_n t)
\end{aligned} \tag{4.25}
$$

Note that the approximation for steady circumferential disturbance and the undistorted travelling wave is recovered by setting $n = 0$ and $m = 0$ respectively.

4.1.4. Grid creation and post-processing

4.1.4.1. Sparse assembly grids

The sparse assembly or reduced passage domain shown in Figure 4.2 consists of multiple single passage grids with shadow point boundaries. The reduced passage computation is best started from a steady-state starting solution obtained from a single passage mixing plane calculation. The grid and corresponding solution is then created as follows:

1. Extend the single passage domain into neighbouring passages by duplicating points in vicinity of the periodic boundaries on the opposite boundary. The correspondence between master and shadow points is stored. Scalar flow variables at the shadow points and master points are retained and velocities simply rotated by the pitch.

2. Create the reduced passage model by duplicating and rotating the grid with shadow points.

$$
\begin{pmatrix} x \\ y \\ z \end{pmatrix}_j = \begin{pmatrix} 1 & 0 & 0 \\ 0 & \cos\theta_j & \sin\theta_j \\ 0 & -\sin\theta_j & \cos\theta_j \end{pmatrix} \begin{pmatrix} x \\ y \\ z \end{pmatrix}_1 \tag{4.26}
$$

where θ_j is the circumferential position of passage j given by:

$$\theta_j = \frac{j-1}{kN_P} 2\pi \tag{4.27}$$

where k is the circumferential wave number of the fundamental stationary disturbance. The correspondence between master/shadow points in the first passage and their duplicates in additional passages is stored. Every master point has got a matching point in the first passage and every shadow point is linked to the same master as the shadow point in the first passage. Information is collected on the master points for the spatial and temporal Fourier transform.

Four Fourier coefficients (Equation (4.24)) per time-space harmonic must be stored for each master point. Since $2N_M + 1 = N_P$ constants are needed for a Fourier approximation of order N_M, the total number of Fourier coefficients required is given by:

$$N = (2N_N + 1)N_P N_{MP} \tag{4.28}$$

where N_{MP} is the number of master points in a single passage and $N_N + 1$ is the number of travelling disturbances plus the time-average.

3. If the blades in the whole assembly are not identical, a pattern can be created by changing the stagger, pitch or lean of the blades in the sparse assembly row. An example of such a case is shown in Figure 4.3 where the stagger of individual blade varies sinusoidally. When the geometry is modified in such a manner, it is important that the master and shadow points as well as points on the inlet/outlet boundary must not be moved since they are sampling points for the circumferential Fourier transform which requires uniform spacing.

4.1.4.2. Post-processing

Once converged, a steady sparse assembly solution can be decomposed into spatial Fourier components and reconstructed on the full circumference. Unsteady solutions can be post-processed in a similar manner but a time history of the flow variables at all nodes (including the interior domain) has to be stored over one disturbance cycle.

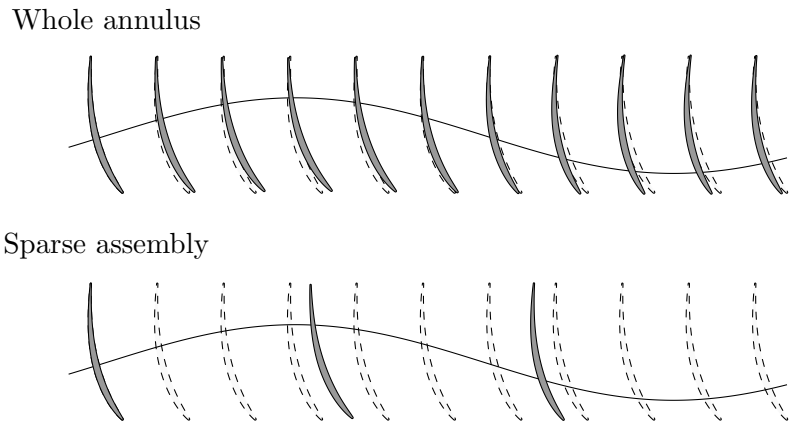


Figure 4.3.: Schematic of a 1ND sinusoidal stagger distribution in whole annulus and sparse assembly domain with three blades (solid line=restaggered blade, dashed line=nominal blade)

4.2. Multi-row coupling

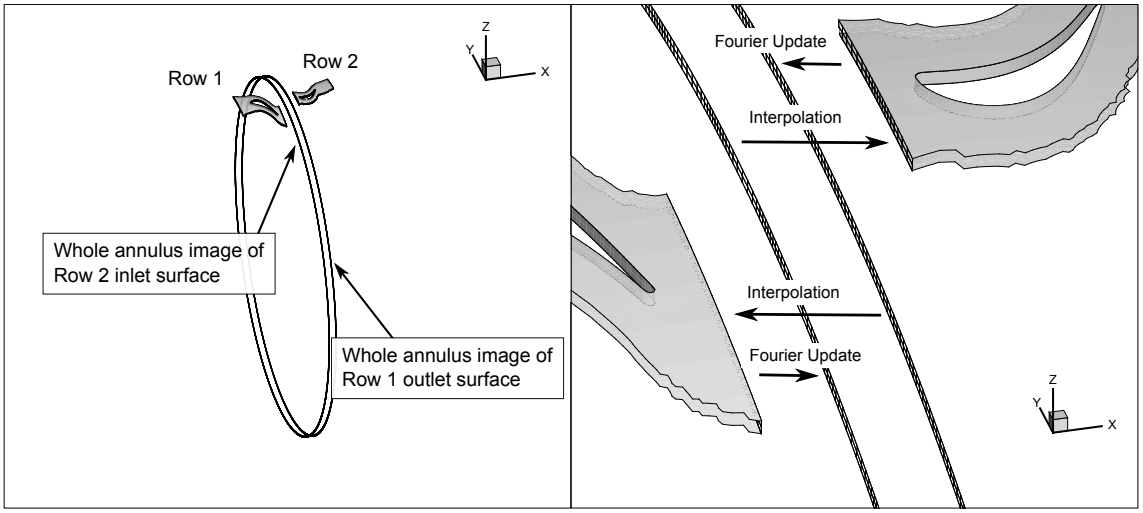
The circumferential and temporal variation of variables at inter-row boundaries can be approximated in the same manner as the pitchwise boundary conditions using the chorochronic Fourier model discussed in the previous section. Flow variables at the inlet/outlet surfaces are decomposed into Fourier coefficients and a whole annulus image of the surfaces is reconstructed. The boundary conditions of the adjacent row are then interpolated from the whole annulus sliding plane. A schematic of a single-passage multi-row set-up with sliding plane boundaries is shown in Figure 4.4. The sliding plane interpolation is identical to that used in full circumference solutions and is briefly described in Section 4.4.

In order to apply the chorochronic Fourier model to multi-row coupling, two questions must be answered:

1. How do we determine the frequencies and circumferential wave numbers required for an accurate representation of multi-row interaction?

2. How do we ensure a representation of disturbances in the sparse assembly domain which is consistent with the whole annulus?

In order to determine the frequencies and wave numbers to be included in the Fourier transform for multi-row cases, we refer to the theory of spinning modes or Tyler-Sofrin [106] modes which describes the scattering and frequency shifting of



(a) SPMR domain (b) Information exchange at interface

Figure 4.4.: Single-passage multi-row domain with sliding plane boundaries

entropic, vortical or acoustic waves as they travel between blade rows. The spinning mode theory is summarised in the first part of this section before the treatment of these modes in the reduced passage model is discussed.

4.2.1. Blade row interference mechanisms

The concept of spinning modes was first developed by Tyler and Sofrin to describe multi-row coupling and has since been used widely in frequency domain analysis [45]. It applies to flows with small amplitude perturbations that are decomposed in the frequency domain and hence provides an appropriate framework for the analysis of blade row coupling in the combined time-domain/frequency-domain method.

It is assumed that perturbations at the blade row boundary can be modelled in terms of a mean flow $U_0(x, r)$ and N_N perturbations with circumferential wave number k and angular frequency ω :

$$U(x, r, \theta, t) = U_0(x, r) + \sum_{n=1}^{N_N} \hat{U}_n(x, r) e^{i(k_n \theta - \omega_n t)} \tag{4.29}$$

where $\hat{U}_n$ is the complex Fourier amplitude of mode n. The spinning mode theory

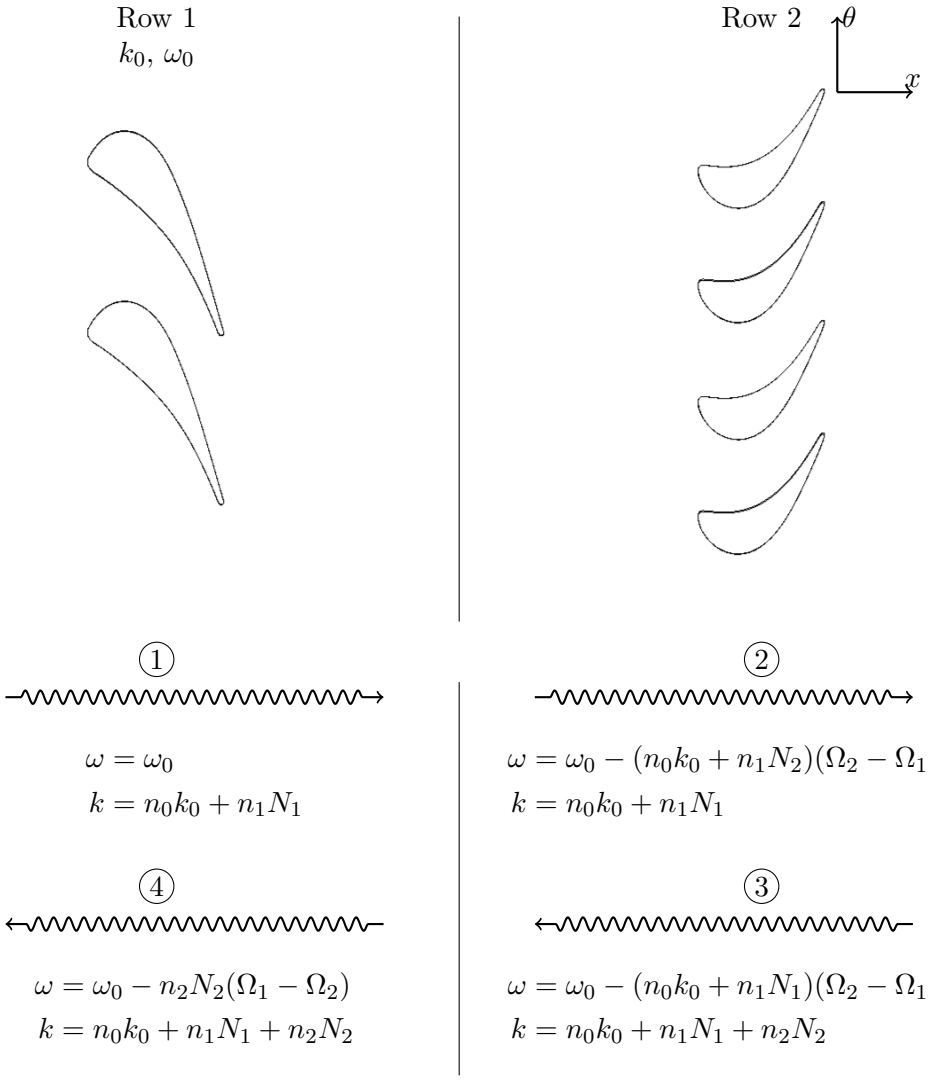


Figure 4.5.: Spinning modes in a turbine stage: N= number of blades, $n \in \mathbb{Z}$ (after Hall and Ekici, 2005 [45])

then describes how these modes becomes frequency shifted and scattered as they travel between blade rows and thus provides the circumferential wave numbers and frequencies at the interface. The scattering and frequency shifting will be explained by means of an example.

Consider a two row case with blade counts N_1 and N_2 respectively with the blades in the first row vibrating at angular frequency ω_0 and circumferential wave number k_0. The vibration produces entropic, acoustic and vortical waves which propagate between blade rows and interact with the local flow field. Figure 4.5 depicts the waves as they travel into the adjacent blade row and become scattered and reflected. The creation of spinning modes proceeds as follows:

1. If Row 1 has got a fundamental disturbance with frequency ω_0 and circumferential wave number k_0, the flow in Row 1 can be expressed as a superposition of waves of frequency $\omega = \omega_0$ and an infinite number of circumferential wave numbers $k = n_0 k_0 + n_1 N_1$.

2. Some of these waves travel into the neighbouring blade row where they appear with a different frequency due to the relative rotation of the two rows. The frequency is shifted by $(n_0 k_0 + n_1 N_1)(\Omega_2 - \Omega_1)$.

3. As the waves impinge on the blades in Row 2, they maintain their frequency but become circumferentially distorted by the flow field in Row 2 with circumferential wave number $k = n_2 N_2$. Some of these distorted waves reflect back towards Row 1.

4. As the waves travel back into the first row, the circumferential wave number does not change but they once again appear with a different frequency due to the Doppler shift. Shifted by $(n_0 k_0 + n_1 N_1 + n_2 N_2)(\Omega_1 - \Omega_2)$ the new frequency becomes $\omega = \omega_0 - (n_2 N_2)(\Omega_1 - \Omega_2)$.

At the blade row interface we can therefore expect to find waves with circumferential wave numbers $k = n_0 k_0 + n_1 N_1 + n_2 N_2$ appearing with frequencies $\omega_1 = n_0 \omega_0 - (n_2 N_2)(\Omega_1 - \Omega_2)$ and $\omega_2 = n_0 \omega_0 - (n_0 k_0 + n_1 N_1)(\Omega_2 - \Omega_1)$ in Row 1 and Row 2 respectively. In theory, the number of circumferential modes n_1, n_2 is infinite but research has shown that only a few modes significantly contribute to the blade row interaction mechanism [45].

Once the disturbances at the row interface have been identified, we need to ensure that they are correctly represented in the Fourier approximation and can propagate

without unphysical distortion between the sparse assembly domains. We shall consider two fundamental examples; forced response in a stator-rotor configuration with stationary circumferential perturbation in the stator and the stationary interaction between rotors in a rotor-stator-rotor configuration.

4.2.2. Chorochronic representation of stator-rotor interaction with non-axisymmetry in the stator

Let us consider a stator-rotor case ($\Omega_1 = 0, \Omega_2 \neq 0$) with a stationary circumferential perturbation in the stator ($\omega_0 = 0$, $k_0 \neq 0$) which travels into the rotor, becomes distorted and is reflected back into the stator. The number of blades in the stator and rotor are denoted by N_1 and N_2 respectively.

In the stator domain, the rotor blade passing appears as a superposition of $n_2 N_2$ nodal diameter disturbances travelling at rotational speed $v = \Omega_2$. The rotor blade passing is undistorted when it enters the stator domain and satisfies the relationship $v = \Omega_2 = \omega/k$. It therefore needs to be included as a travelling disturbance in the Fourier approximation. When the rotor passing disturbance impinges on the stator it becomes distorted. This distortion manifests itself as different amplitudes and phases inside the single passage domain and does not require special treatment.

In the stator domain, the stationary circumferential variation with wave number k_0 can be approximated with a N_M^{th} order spatial Fourier series if $2N_M + 1$ passages are distributed over $1/k^{th}$ of the circumference. The interaction of the stationary perturbation and the stator flow field creates disturbances with circumferential wave number $k = n_0 k_0 + n_1 N_1$ travelling at rotational speed $-\Omega_2$ in the rotor frame of reference. These disturbances are undistorted and travel at phase velocity $v = -\Omega_2 = \omega/k$. We therefore need to include the stator blade passing, the passing of the fundamental stationary disturbances and their linear combinations as independent travelling disturbances in the Fourier approximation in the rotor frame of reference.

In the rotor frame of reference these disturbance may also become distorted through interaction with the local flow field. As before, this distortion manifests itself as different amplitudes and phases inside the single passage domain and does not require special treatment.

Finally, let us consider the reflection of these distorted disturbances. If the wave $k = n_0 k_0 + n_1 N_1 + n_2 N_2$ with frequency $\omega = -(n_0 k_0 + n_1 N_1)\Omega_2$ in the rotor frame of reference enters the stator domain, it appears as the rotor passing frequency

$\omega = n_2 N_2 \Omega_2$ distorted by the stationary perturbation with circumferential wave number $k = n_0 k_0 + n_1 N_1$. The reflected distorted disturbance can therefore also be represented in the stator frame of reference since both, the rotor passing frequency and its modulating disturbance can be represented. The same principle applies to rotor passing disturbances which become distorted in the stator before travelling back into the rotor.

When stationary disturbances are modelled on a reduced passage domain, it is important that they appear with the correct phase in every passage. In certain sparse assembly configurations this may require a phase correction at the blade row interface.

4.2.3. Phase correction at inter-row boundary

Stationary disturbances which are transferred between blade rows do not necessarily appear with the correct phase if the passage locations do not coincide with locations in the physical assembly. To illustrate, let us consider the example of a reflected disturbance in a rotor-stator configuration with 10 stators and an arbitrary number of rotors (Figure 4.6). The stator row contains a 1ND stationary disturbance. Interaction with the local stator flow field creates, amongst others, a 11ND disturbance at the blade row interface. This 11ND disturbance is travelling in the rotor frame of reference where it is represented through a temporal Fourier transform. If this disturbance reflects back into the stator domain, it must appear in phase with the 1ND disturbance which originally created it. In other words, the 11ND disturbance must be aliased to a 1ND disturbance. This is automatically achieved on the whole annulus or if an integer ratio between the number of blades in the whole assembly and the number of passages in the sparse assembly exists: If the passages are in physical locations and the flow variables are simply interpolated from the whole annulus image according to the passage's current rotational position, the disturbance automatically aliases to 1ND. However, if the passages are not in their physical locations and the disturbance is interpolated from the whole annulus plane the relative phase between passages will create a different aliasing pattern.

To illustrate, let us assume that the stator row is modelled by three passages distributed over the whole circumference (see Figure 4.6). In a whole annulus, this disturbance would get aliased to 1ND ($N_A = k - nN_B$, where n is the closest integer to k/N_B). The aliasing is illustrated by the grey crosses and curve in Figure 4.6. On

the sparse assembly, however, a new disturbance would be created. The corresponding phase in each passage is marked by black crosses in Figure 4.6. We therefore apply a passage-dependent phase shift $\Delta\Phi_j$ when reconstructing a disturbance with circumferential wave number k which is stationary in the stator for interpolation to the j^{th} passage in the stator. This phase shift effectively offsets the interpolation position by

$$\Delta\theta_j = (\frac{N_A}{k} - 1)\theta_j \tag{4.30}$$

where θ_j is the angular position of the j^{th} passage. The corrected phase is then given by:

$$\begin{aligned} \Phi'_j &= k\theta'_j \\ &= k(\theta_j + (\frac{N_A}{k} - 1)\theta_j) \\ &= N_A\theta_j \end{aligned} \tag{4.31}$$

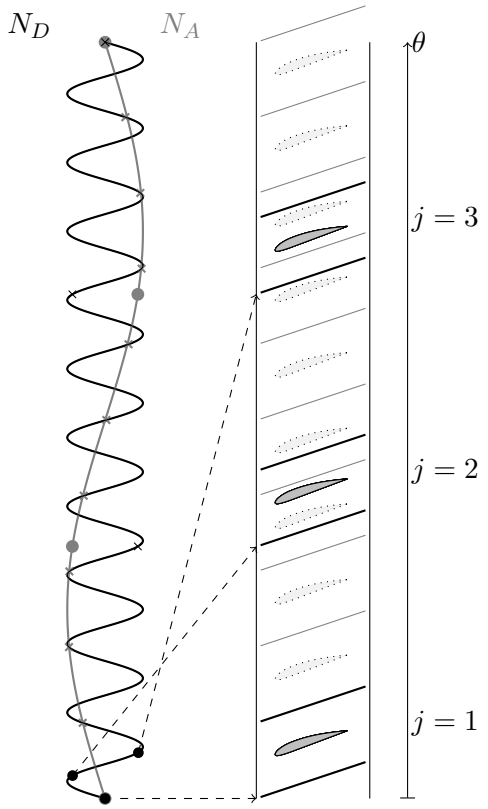
which is the correct aliasing phase.

A reflected disturbance with wave length equal to the stator pitch would therefore appear with the same phase in every stator passage. A possible distortion of the reflected disturbances by the rotor flow field will also be captured, since the local Fourier coefficients on the rotor inlet surface vary in amplitude and phase.

Disturbances which are travelling in the stator frame of reference do not require special treatment. The inter-passage phase lag in the stator frame of reference is automatically satisfied since the passage location is taken into account when the spatial and temporal Fourier coefficients are computed.

4.2.4. Rotor-rotor/stator-stator interference

The spinning modes for three or more blade rows follow the same pattern as in Section 4.2.2 and are depicted in Figure 4.7 for a rotor-stator-rotor configuration with N_{R1}, N_{S1} and N_{R2} blades respectively. Note that with $k_0 = 0$, the only stationary perturbation in Rotor 1 is due to interference with Rotor 2 and vice versa. The circumferential wave numbers of stationary perturbations are therefore equal to the blade counts of upstream/downstream rows in the same frame of reference. Since blade count ratios are likely to be close to unity, the disturbances become



N_D = Disturbance nodal diameter
N_B = Number of blades
N_P = Number of passages
N_A = Aliased disturbance

$$\Delta\theta_j = (1 - N_A/N_D)\theta_j$$
$$\theta_j = 2\pi\frac{j-1}{N_P}$$

Figure 4.6.: Phase correction of a 11ND disturbance at inlet of a row with 10 passages (black=11ND disturbance, grey=aliased 1ND disturbance)

aliased and both Rotor 1 and Rotor 2 appear to contain a stationary disturbance with circumferential wave number $N_{R1} - N_{R2}$. This can be represented on the sparse assembly by distributing passages over $1/(N_{R1} - N_{R2})^{th}$ of the circumference.

In order to fully capture multi-stage coupling, the dominant spinning modes need to be approximated by the circumferential and temporal Fourier transform. For a rotor-stator-rotor configuration with $k_0 = 0$ and $\omega_0 = 0$, the unsteady perturbations in the rotor domain are all multiples of the stator blade passing frequency $-n_2 N_{S1}\Omega$. The stator domain, on the other hand, sees linear combinations of the two rotor blade passings, i.e. waves with circumferential wave numbers $n_1 N_{R1} + n_3 N_{R2}$ travelling at rotational speed Ω.

As before, modes which satisfy $v = \Omega/k$ need to be specified as distinctive travelling disturbances in the Fourier approximation (Equation 4.25). The scattering of these modes through the local flow field is then accounted for in the circumferential Fourier transform or through the interaction with the local flow field. For example, consider mode $(n_1, n_2, n_3) = (1, 1, -1)$ in Rotor 1. This corresponds to a travelling wave with circumferential wave number $n_2 N_{S1}$ and rotational velocity $-\Omega$ being modulated by a stationary disturbance with circumferential wave number $N_{R1} - N_{R2}$. It can therefore be fully represented by the circumferential variation of the temporal Fourier coefficients described previously if the stationary disturbance due to the rotor-rotor interaction, i.e. wave number $N_{R1} - N_{R2}$, can be represented. When a disturbance which is stationary in the rotor frame of reference is reconstructed on the stator sliding plane for interpolation to the rotor, a phase correction needs to be applied as described above for the two row case.

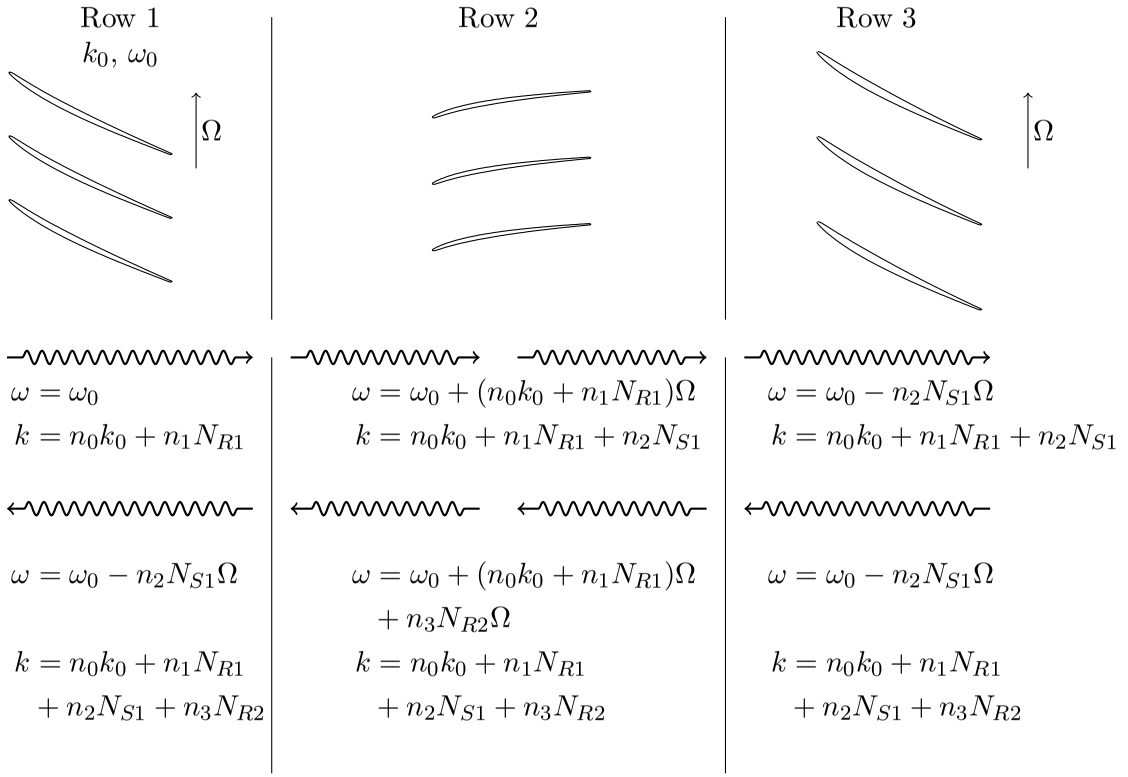


Figure 4.7.: Spinning modes in 1.5 stage compressor

4.3. Limitations of the time-domain Fourier model

4.3.1. Theoretical limitations

The use of a Fourier decomposition limits the above methodology to turbomachinery flow fields characterised by the following properties:

1. **Spatial periodicity:** Any stationary circumferential variation in the flow field must be periodic, representable by a finite number of harmonics and small compared to the mean flow. Circumferential non-uniformities such as random mistuning patterns cannot be represented on a reduced number of passages.

2. **Temporal periodicity:** Any unsteadiness must take the form of a travelling wave since the representation of unsteady disturbances is based on phase-lagged boundary conditions. Only spinning modes can be captured by the temporal Fourier model and all non-rotating modes are lost.

3. **Predetermined frequency and wave number spectrum:** The frequencies and wave numbers of the disturbances must be known *a priori*. This is usually the case for flutter or forced response problems, where initial estimates can be made based on rotational speed and circumferentially wave number content, but prevents the modelling of indeterminate unsteady features such as rotating stall.

In multi-stage simulations across multiple spools a further limitation may arise when different wheel speeds need to be modelled. The combination of two shaft speeds creates unsteadiness with a period equal to the least common multiple of the individual periods. In practice, this may cause periods in the range of 10-100 revolutions which cannot realistically be modelled using temporal Fourier approximations. However, the reduced passage model may still be used on multi-spool assemblies if a linear superposition of rotor spinning modes is assumed in the stator frame of reference and rotor-rotor coupling modes are neglected.

4.3.2. Practical limitations

Although theoretically applicable to any number of blade rows and disturbances, certain flow characteristics can cause practical difficulties for the reduced passage model. To assess the suitability of the time-domain Fourier model, the following should be considered:

1. **Frequency spectrum:** A wide frequency spectrum can cause convergence problems. The use of a common relaxation factor for all frequencies leads to an over-relaxation of high frequency perturbations and under-relaxation of low frequency perturbations which delays convergence.

2. **Wave number spectrum:** To resolve a large number of independent stationary circumferential perturbations, a comparatively large number of passages is required. The domain size will vary with blade count ratios and wave numbers but computational benefits are likely to diminish with the number of stationary disturbances.

3. **Number of blade rows:** A multi-row calculation is not only likely to contain wide frequency and wave number spectra, but also impedes convergence as the solution must reach a periodic state in one row before disturbances can be correctly transferred to adjacent rows.

4. **Supersonic flows and oscillating shocks:** To resolve sharp gradients across moving shocks a large number of harmonics is required. This renders the reduced passage model unsuitable to supersonic compressors where shocks cross blade row boundaries and transonic/supersonic flutter problems.

5. **High working line and separated flows:** The unsteadiness associated with flow separation at high pressure ratios cannot be represented on the reduced passage model because it is non-rotating. Vortices are shed at the Strouhal frequency but a phase-lag between adjacent blades cannot be defined.

Most of the points listed above are limiting factors because they tend to result in slow convergence. It may be possible to accelerate convergence by adjusting time steps and relaxation factors during the course of the computation as will be briefly discussed in Section 7.2.

4.4. Information exchange across blade row boundaries

As described in Section 4.2, the method presented here uses whole annulus sliding planes for transferring information between adjacent sparse assembly rows. Each sliding plane is a full circumference copy of an inlet or outlet surface and contains a Fourier reconstruction of its master surface. The boundary values for a given row

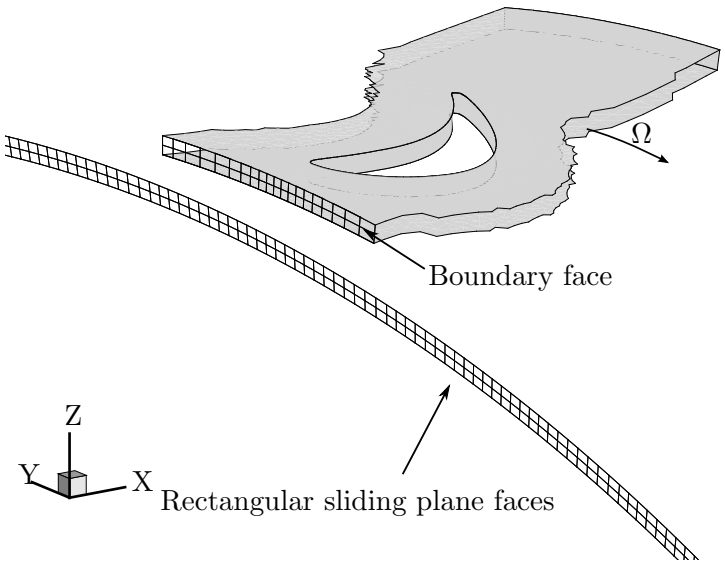


Figure 4.8.: Sliding plane boundary

are then obtained by interpolating flow variables from the sliding plane belonging to the adjacent blade row as indicated in Figure 4.4 and Figure 4.8. The flow variables are stored on the grid nodes of the sliding plane. For the interpolation to a boundary node of the neighbouring node, the rectangular sliding plane faces are divided into triangles. A search algorithm finds the triangle which contains the boundary node at its current circumferential position. Its value is then updated by area interpolation. The search and interpolation procedure and computation of boundary fluxes are identical to that of the whole annulus computation and described in A.2.

An important difference between the sparse assembly and SPMR implementation of Mata et al. [74] is the timing of the reconstruction process. For SPMR methods, the whole annulus field is fully reconstructed at the end of the time-step and the variables are interpolated from the sliding plane without further adjustments. Sparse assembly passages, however, may require a passage-dependent phase correction as described in 4.2.3. As a consequence, the reconstruction process must take into account the location of the destination passage, i.e. the passage for which boundary conditions are being interpolated. The reconstruction is hence best performed for each destination boundary node independently. An advantage of this approach is

that only sliding plane nodes which are required for interpolation at the current time step are updated and a wasteful reconstruction of the full circumference flow field is avoided.

4.5. Approximate modelling of multi-stage flows

Section 4.2 has examined the representation of non-axisymmetric flows across two and three blade rows. While it is theoretically possible to extend the modelling approach to three or more rows in the same fashion, the set-up is likely to become complicated and the reduction in domain size less beneficial.

An accurate representation of dominant multi-stage coupling modes would require the passages to be distributed over the beat wave length of all interaction modes. If the differences between blade counts of successive stator or rotor rows are not integer multiples of each other, the beat wave length becomes the full circumference and a Fourier representation would require a considerable number of passages. Consider the case of rotor-rotor interaction in a three stage compressor with $N_{R1} = 61$, $N_{R2} = 59$ and $N_{R3} = 54$ blades in the three rotor rows respectively. The first order interaction would create stationary circumferential variations of 2ND, 5ND and 7ND, which can be represented on a minimum of 15 passages per rotor row. As more and more stages are added, the resulting reduction in computational effort may no longer warrant the complexity of set-up.

However, the sparse assembly approach can still be beneficial for multi-stage modelling if a true representation of multi-stage coupling is not necessary. The transfer of an inlet or combustor distortion through a compressor or turbine, for example, may be of interest from an aeroelastic point of view. In this case, only the correct propagation of the distortion is important and the interaction of successive rows need not be modelled in detail.

In order to neglect multi-row coupling modes, certain disturbances need to be suppressed at the inter-row boundaries. This approach was successfully employed in the past for the approximate modelling of multi-stage flows and was referred to as 'interface disturbance truncation' technique by Li and He [70] (see Section 2.6.2). The technique filters the disturbances at the blade row interface and allows only those to pass, which can be represented in the adjacent row. In the simplest form, this allows modelling of multi-stage flows by disregarding the interaction of rows in the same frame of reference and considering only the interaction between adjacent

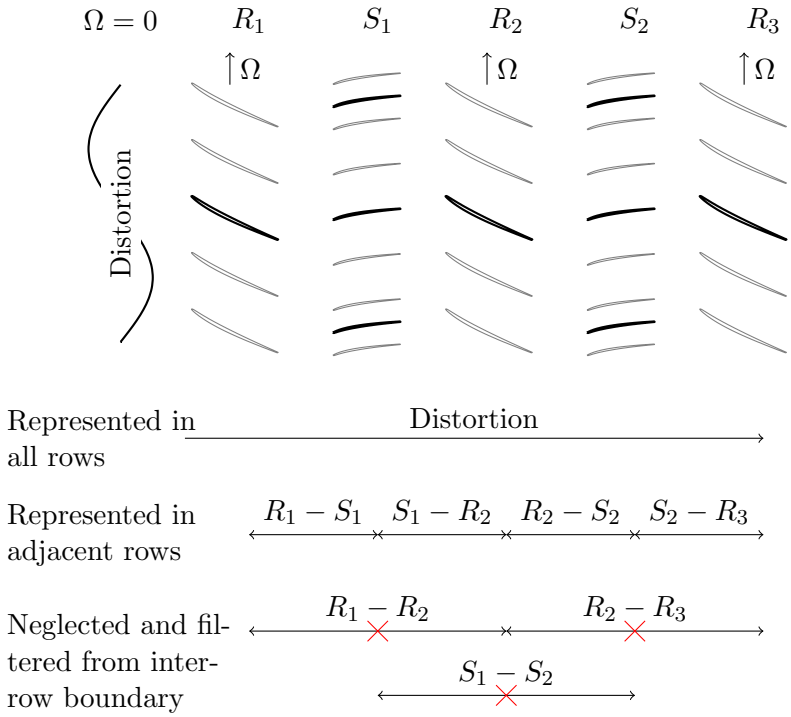


Figure 4.9.: Schematic of sparse assembly domain for approximate modelling of distortion transfer across 2.5 stages whereby the distortion transfer and unsteady rotor-stator interaction are captured but rotor-rotor and stator-stator interactions are neglected

stators and rotors. When used in conjunction with the sparse assembly method, the transfer of disturbances across multiple stages can also be modelled.

At each interface, a filter is used when reconstructing the flow variables on the sliding plane. This way only disturbances which are travelling in the adjacent row's frame of reference or disturbances which are stationary in the adjacent row's frame of reference and can be captured by the spatial Fourier transform are allowed to pass through to the adjacent blade row. To illustrate, let us consider a 2.5 stage compressor subjected to a large engine order stationary circumferential distortion as seen in Figure 4.9, where the sparse assembly and full circumference blades are represented by black and grey lines respectively. The distortion is travelling in the rotor's frame of reference and can be represented on a single passage with phase lagged boundary conditions. In the stator the distortion is stationary and can be approximated to first order on three passages. The computational domain therefore contains a single passage in rotating rows and multiple passages distributed over the

wave length of the distortion in stationary rows. This allows representation of the interaction between immediately adjacent rows and the distortion in all blade rows. All other blade row interaction modes, i.e. rotor-rotor or stator-stator interaction modes need to be filtered from the inter-row boundaries.

The decision which disturbance to filter at each interface and which ones to reconstruct on the adjacent row can be made at the beginning of the computation based on the frequency and nodal diameter of the disturbance and the blade count and number and location of passages in the adjacent blade rows. If the disturbance is stationary in the adjacent blade row and its circumferential wave number is a multiple of the blade count, e.g. for reflected disturbances, it can be represented. Similarly if a stationary disturbance with nodal diameter k can be approximated by a N_M^{th} order spatial Fourier transform and more than $2N_M + 1$ passages are distributed over $1/k^{th}$ of the circumference it can be represented. The filtering criteria are outlined in Figure 4.10.

The truncation of disturbances at the row interface leads to a mismatch of flow variables across the inter-row boundary. This mismatch can cause spurious reflections which can be avoided if a non-reflecting treatment is added to the blade row interfaces. Two fundamental kinds of non-reflecting treatments exists; non-reflecting boundary conditions (NRBC) based on a characteristic decomposition of the flow field and buffer layers.

NRBC are based on a linearisation about an underlying steady flow field. The unsteadiness is decomposed into Fourier modes of different frequencies and wave numbers which are further decomposed into pressure, vorticity and entropy waves according to characteristic theory. The non-reflecting treatment then forms the boundary conditions by using the contribution from the incoming waves from outside the domain and from the outgoing waves from inside the domain.

Buffer layers or sponge layers artificially damp out any reflections by gradually coarsening the grid or adding artificial dissipation towards the boundary. A review of available non-reflecting treatments is given in Appendix A.4.

A non-reflecting treatment is required to properly filter disturbances from an interface. However, the approximate distortion transfer model suggested here already assumes that the disturbances which are to be filtered, i.e. rotor-rotor/stator-stator interaction modes, are weak and insignificant compared to the modes of interest. In other words, it assumes that the filtered modes are cut-off and decay by the time they reach the filtering interface. A standard interface treatment is hence deemed

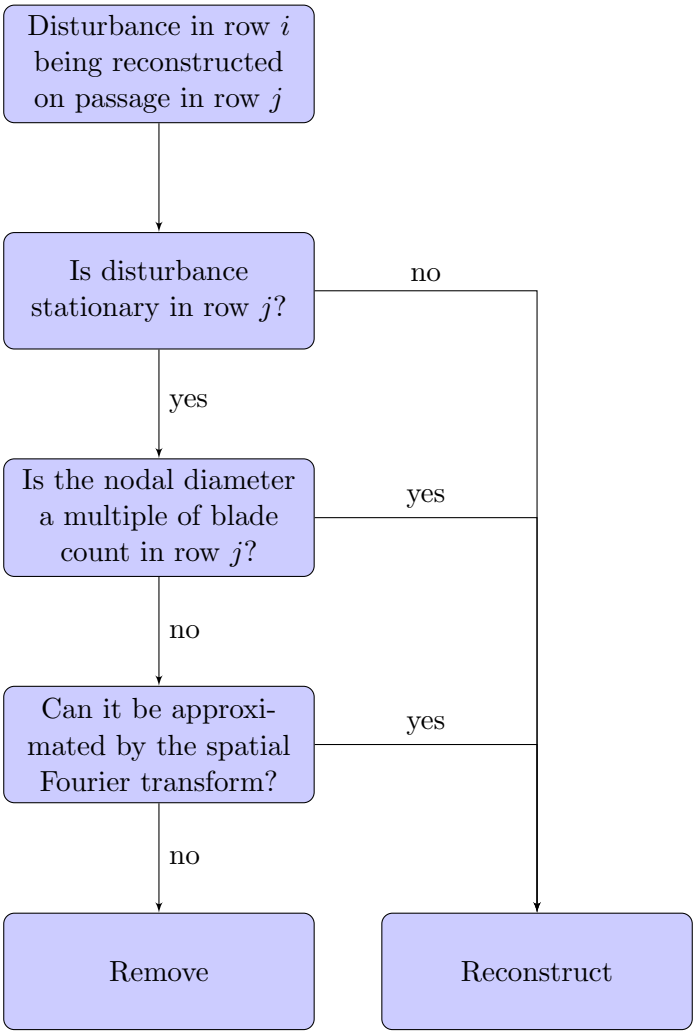


Figure 4.10.: Filtering criteria for approximate multi-stage modelling

acceptable for the approximate modelling of multi-stage flows. [1]

[1] This approach is further justified by the results of Gerolymos [35] and Castillon [12]. In two separate studies, they used a filtered chorochronic interface without non-reflecting treatment for multi-stage analyses and found satisfactory continuity across the interface and agreement with the reference solution.

5. Validation

5.1. Propagation of entropic perturbation through a duct

For the initial validation of the sparse assembly method, a first set of test cases studies the propagation of an entropy perturbation through a thin, annular duct with uniform mean flow ($u_x = 193\text{m/s}$). The geometry simplifies the problem considerably compared to a bladed passage but nevertheless provides an opportunity to validate the Fourier approximation at pitch-wise and blade row boundaries. An entropy wave was chosen for this validation, since it is simply convected downstream with the mean flow and does not reflect from inlet or outlet boundaries.

A harmonic variation in linearised entropy $\tilde{w} = \partial\rho - \partial p/a^2$ is prescribed at the inlet boundary:

$$\begin{aligned} w(\theta) &= \bar{w} + \tilde{w}(\theta) \\ &= \bar{w} + \sum_{n=1}^{N} \hat{w}_n e^{i(\omega_n t + k_n \theta)} \end{aligned}$$

where $\bar{w}$ is the circumferentially averaged entropy at inlet and ω_n and k_n are the angular frequency and circumferential wave number of the n^{th} disturbance. The angular frequency and circumferential wave numbers were chosen such as to cover a range of disturbances and the results from three representative cases are shown in this section.

The sparse assembly solution is compared to the full (360°) circumference solution by means of density traces collected along a meridional line ($x = 0.15104\text{m}$, $r = 0.24966\text{m}$) and, for multi-row domains, on selected points at the blade row interface. The full domain rather than the analytical solution was chosen for validation since numerical dissipation may cause the wave to decay.

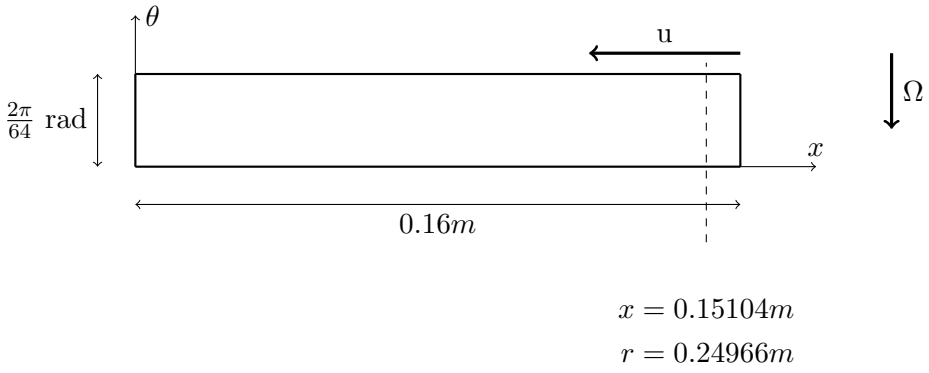


Figure 5.1.: Single-passage single-row domain

5.1.1. Travelling wave in single-passage single-row domain

The first case considers a single-row single-passage domain where the duct is modelled by a single $\frac{2\pi}{64}$ sector with shadow point boundaries. Dimensions are shown in Figure 5.1. The duct is rotating with an angular velocity $\Omega = -728.53$ rad/s.

A linear superposition of a stationary and travelling disturbance is considered. In the absolute frame of reference, the perturbation at the inlet surface takes the form:

$$\begin{aligned}\tilde{w} &= 0.020\bar{w}\sin(5\theta) \\ &\quad + 0.016\bar{w}\sin(64\theta + 64\Omega t)\end{aligned}$$

The rotating frame of reference hence sees a 5ND disturbance travelling at rotational speed $-\Omega$ and a stationary disturbance with wave length equal to the pitch of the duct. The travelling disturbance is discretised by 150 time steps per cycle ($\Delta t = 1.1499e-5s$), which results in a 1.35e-5s phase lag between a master and its shadow point. The wave is travelling into the direction of positive θ with respect to the duct; the left boundary's master points lag their shadow points and the right master points lead their shadow points. The average value of the density and the amplitude of its variation are the same at the master and shadow points. Figure 5.2 shows the recorded densities at two sets of master and shadow points at each boundary. The whole annulus and single passage solutions are identical with the phase lags between master and shadow points as described above.

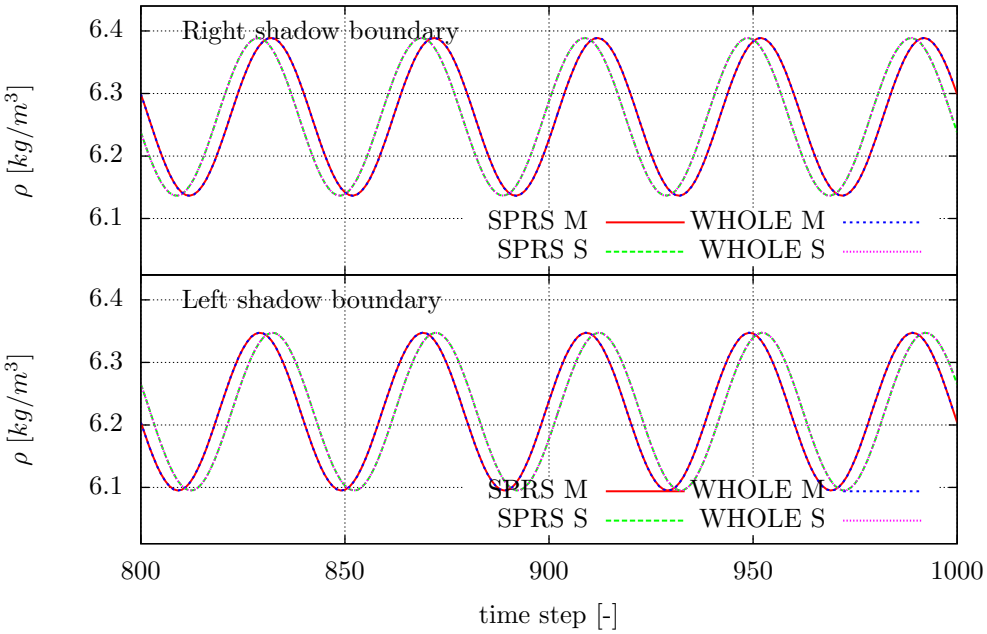
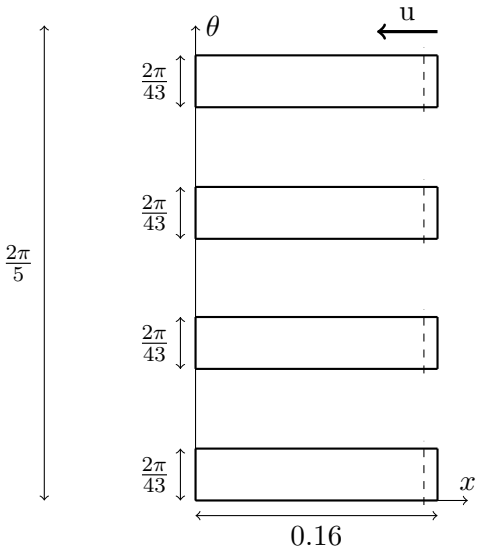


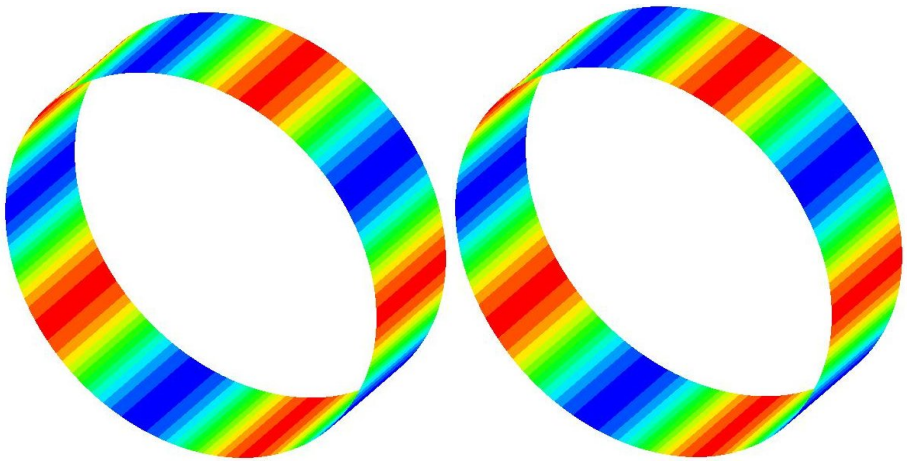
Figure 5.2.: Density histories for travelling wave in single-passage single-row domain (M=Master point, S=Shadow point)



$x = 0.15104$

$r = 0.24966$

Figure 5.3.: Multi-passage single-row domain



(a) Reconstruction (b) Whole annulus

Figure 5.4.: Density contours for stationary wave in multi-passage single-row domain

5.1.2. Stationary wave in multi-passage single-row domain

As in the previous section, this case studies the propagation of entropy waves through a thin, annular duct with uniform mean-flow. In order to represent stationary disturbances with a wave length not equal to the pitch, the computational domain is extended. It includes four $2\pi/43$ sectors with shadow point boundaries which are distributed over $1/5^{th}$ of the circumference. A sketch of the set-up is shown in Figure 5.3. The passages are stationary and a 5ND stationary entropy disturbance is imposed at the inlet:

$$\tilde{w} = 0.02\bar{w}\sin(5\theta)$$

Figure 5.4 shows density contours for the whole annulus and the reconstruction from the reduced passage solution. The variation in the circumferential direction is clearly visible. Figure 5.5 compares the circumferential variation of the 360° domain with the reconstructed sparse assembly solution. The difference between the two solutions shows the same sinusoidal variation as the entropy perturbation with high frequency 'wiggles'. The oscillations are purely numerical with a wave length matching the circumferential grid resolution. Considering the precision of the flow solver the difference between the two predictions, which is less than $5 \times 10^{-}5$ kg/m^3, is negligible.

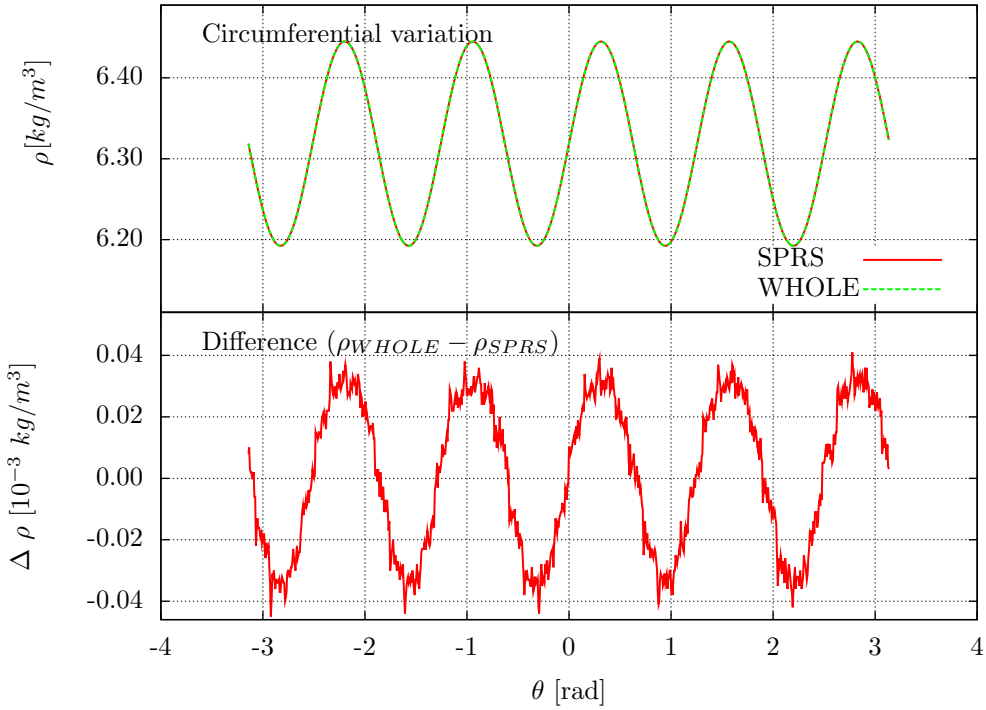


Figure 5.5.: Circumferential variation for stationary wave in multi-passage single-row domain

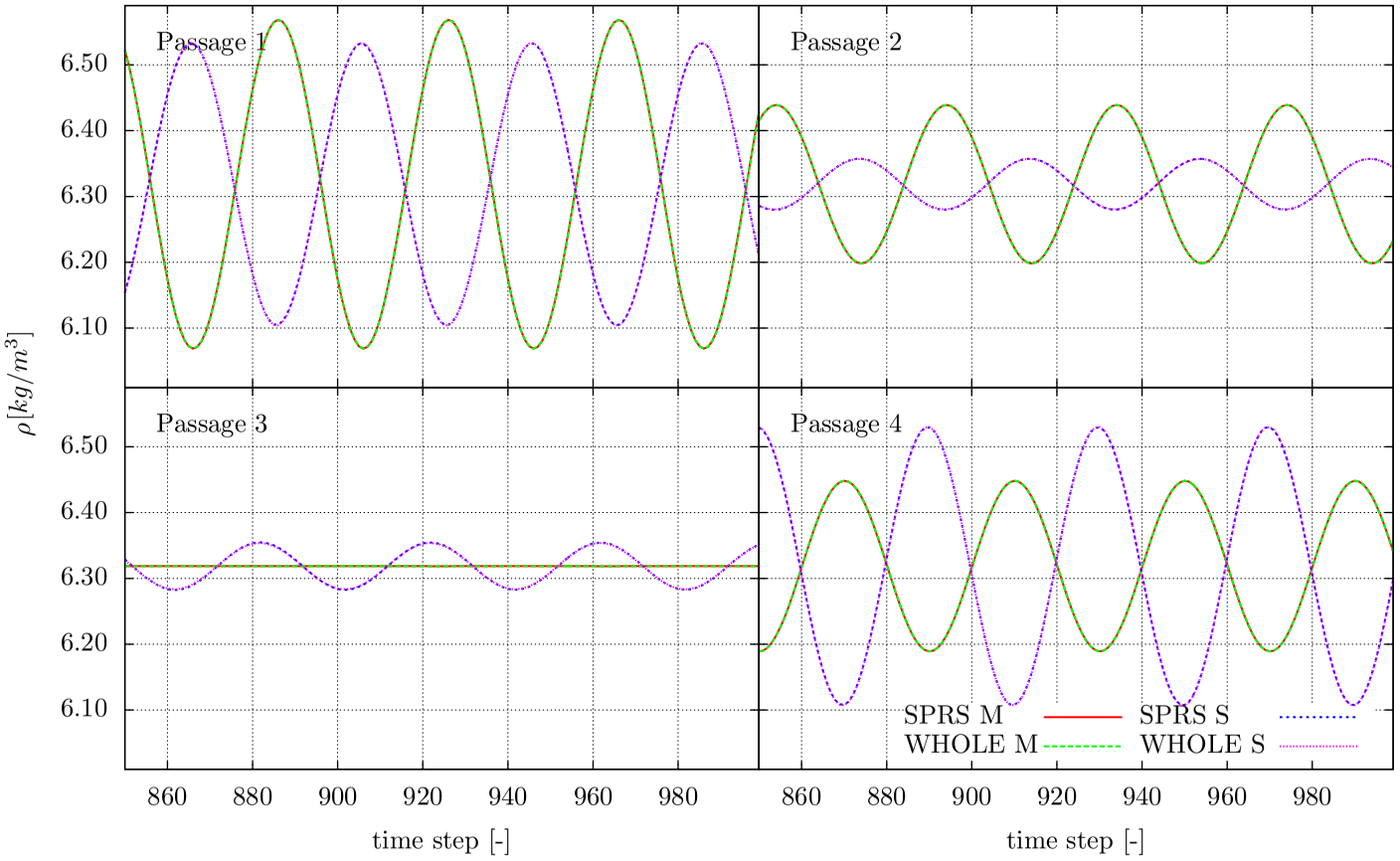


Figure 5.6.: Density histories for modulated wave in multi-passage single-row domain (Left shadow boundary, M=Master point, S=Shadow point)

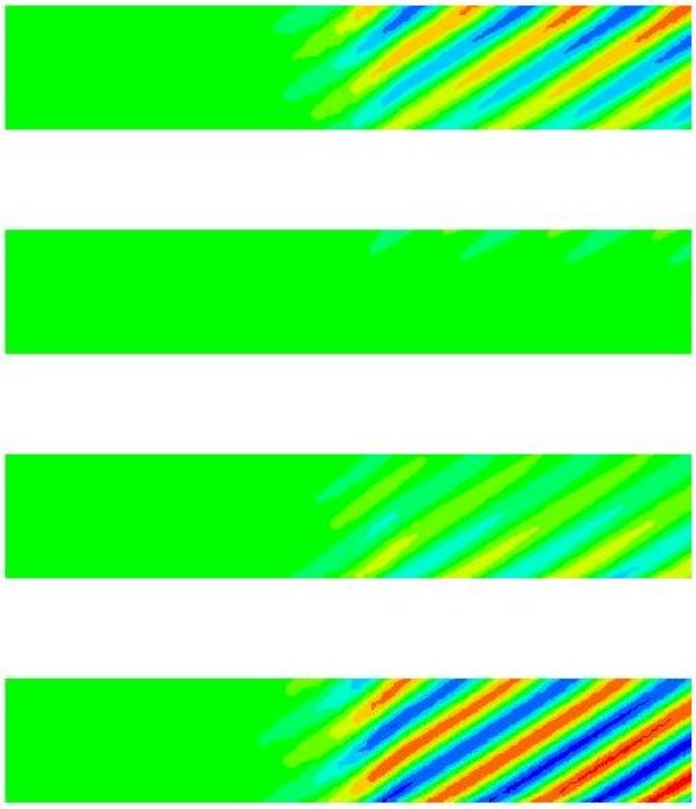


Figure 5.7.: Density contours for modulated wave in multi-passage single-row domain

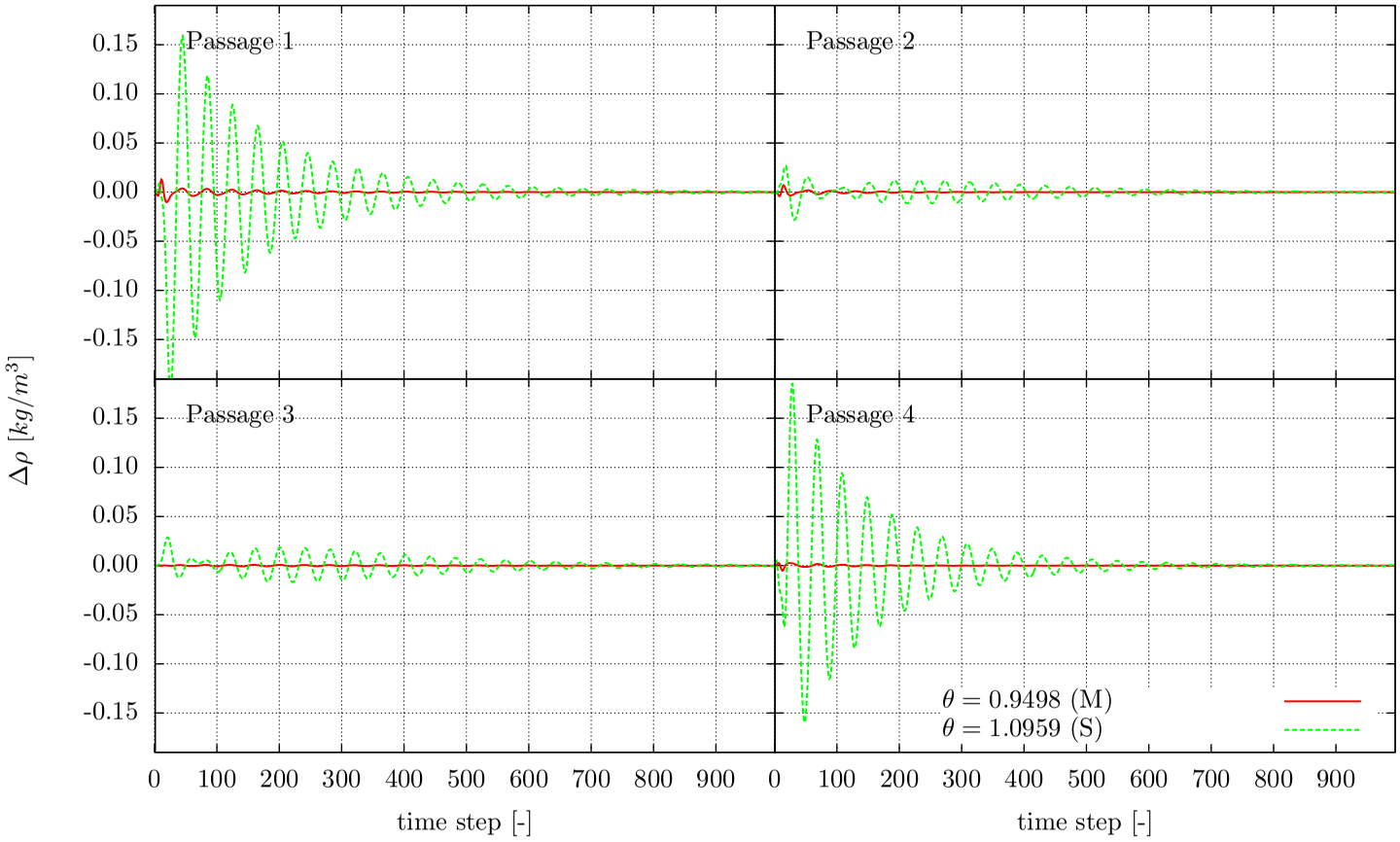


Figure 5.8.: Convergence history for modulated wave in multi-passage single-row domain (Left shadow boundary, M=Master point, S=Shadow point)

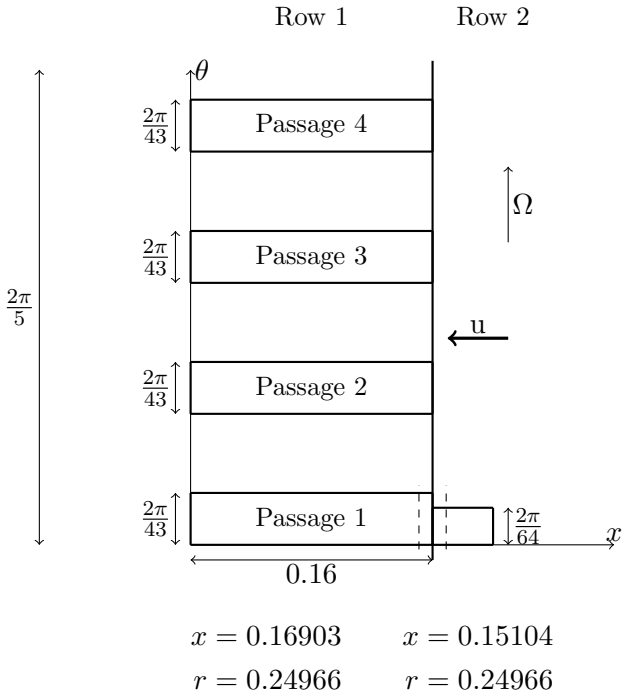


Figure 5.9.: Multi-passage multi-row domain

5.1.3. Modulated wave in multi-passage single-row domain

The second case tests the treatment of undistorted and distorted travelling waves in the multi-passage domain of Figure 5.3. The following perturbation (in the absolute frame of reference) is prescribed at the inlet surface:

$$\tilde{w} = [0.02 + 0.02\cos(5\theta)]\bar{w}\sin(64\theta - 64\Omega t)$$

In the duct's frame of reference, the perturbation consists of a 64ND sinusoidal travelling wave which is distorted by a 5ND stationary variation. The 64EO disturbance is resolved by 40 time steps per cycle. Figure 5.6 shows the converged density history at a master and its shadow point. The two solutions are in good agreement. The variation in amplitude in the circumferential direction is clearly visible from the density traces in Figure 5.6 and contours in Figure 5.7.

Since the reference solution is periodic, it is possible to assess the convergence of the sparse assembly solution by comparing it against the reference solution. Figure 5.8 plots the difference between the two solutions at selected points over the first 900 time steps. The convergence behaviour differs from passage to passage with the

slowest convergence in Passage 3 where the amplitude is smallest.

5.1.4. Modulated wave in multi-passage multi-row domain

This section tests the propagation of entropy waves through two thin annular ducts in relative rotation. The sparse assembly set-up contains two rows with $\frac{2\pi}{43}$ and $\frac{2\pi}{64}$ sectors respectively. Row 2 is rotating at angular velocity $\Omega = -728.53$ rad/s. The method is validated on a set-up for cases with a 5ND stationary disturbance in Row 1; i.e. four passages in Row 1 and one passage in Row 2 (Figure 5.9). Since the sparse assembly passage locations do not coincide with the whole assembly locations, no exact match between grid points exists for all passages. The solution will hence be assessed by comparing density traces at one axial position in the first passage of each row and at the inter-row boundaries.

The validation procedure involved tests with several travelling and stationary waves. For conciseness, only the final case is shown. It combines the features of the previous cases and tests:

1. The correct representation of a stationary disturbance with a wave length equal to the pitch of the multi-passage duct (43ND) which is treated as a time-space average in Row 1 and should appear with the same phase in each passage

2. The distortion of a stationary disturbance (43ND) by another stationary disturbance. The sidebands created by this modulation appear as two travelling waves in the rotating frame of reference.

3. The distortion of a travelling wave (64ND) by a stationary circumferential disturbance with a wave length equal to the pitch of the stationary blade row.

4. The distortion of a travelling wave (64ND) by a stationary large nodal diameter disturbance (5ND).

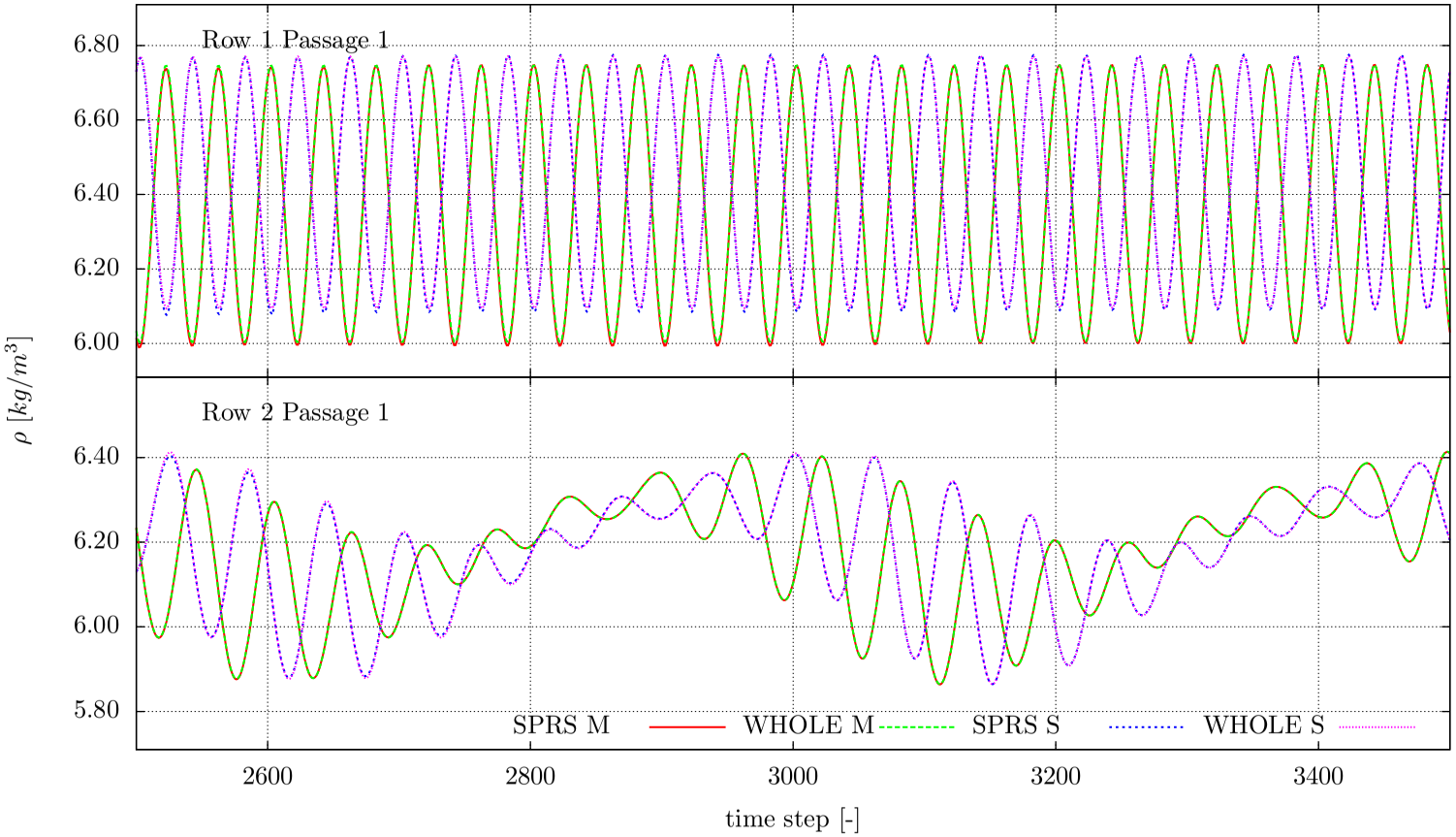


Figure 5.10.: Density histories for modulated waves in multi-passage multi-row domain

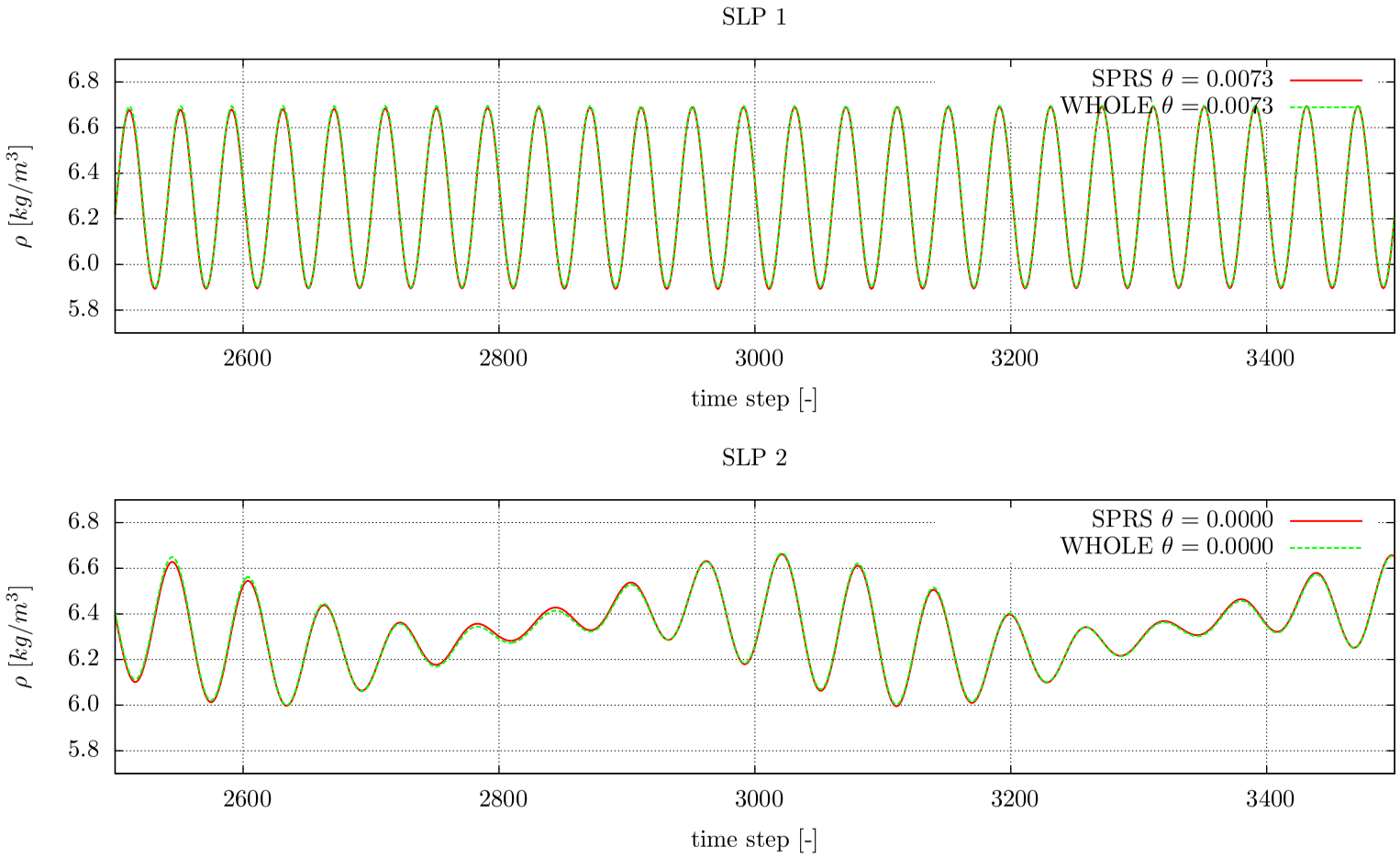


Figure 5.11.: Density histories at the blade row interface for modulated waves in multi-passage multi-row domain

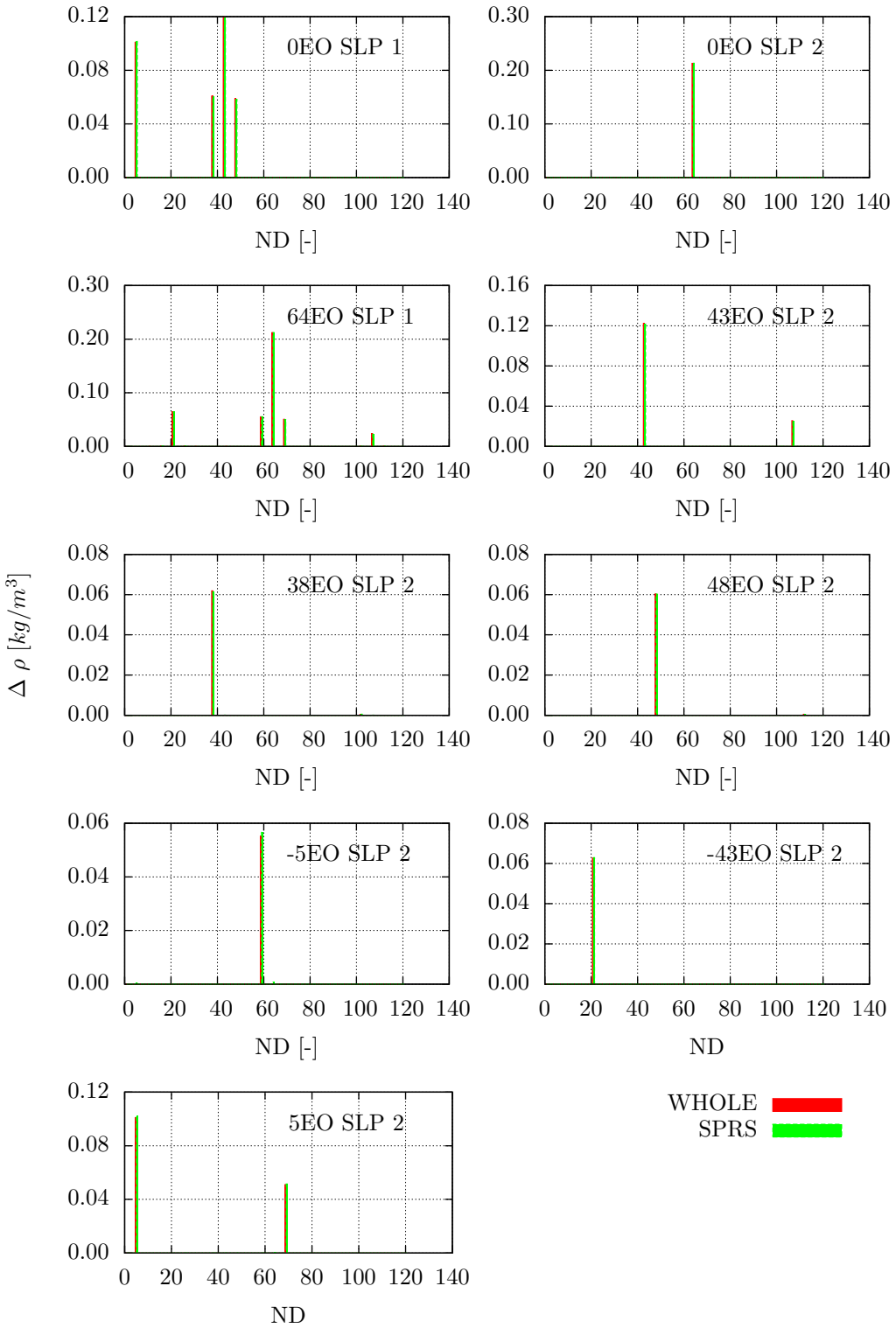


Figure 5.12.: Amplitudes at blade row interface for modulated waves in multi-passage multi-row domain

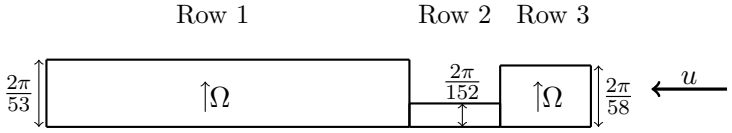


Figure 5.13.: Single-passage three-row domain

The inlet perturbation takes the shape:

$$\begin{aligned}\tilde{w} &= 0.020\bar{w}\sin(64\theta + 64\Omega t)\\ &+ 0.020\bar{w}\sin(43\theta)\\ &+ 0.016\bar{w}\sin(5\theta)\\ &+ 0.020\bar{w}\cos(5\theta)\sin(43\theta)\\ &+ 0.020\bar{w}\cos(5\theta)\sin(64\theta + 64\Omega t)\\ &+ 0.020\bar{w}\cos(43\theta)\sin(64\theta + 64\Omega t)\end{aligned}$$

Figure 5.10 and Figure 5.11 compare density histories in the first passage of each row and points on the inter-row sliding planes respectively. Generally, the two solutions are in good agreement but initially the modulation is not captured to the full extent at the inlet of the first duct (Figure 5.11). A 2D (time and space) Fourier analysis of the sliding plane densities indicated that all modes were present at the blade row interface. The amplitudes of dominant frequencies are compared in Figure 5.12, which shows no noticeable difference between the two solutions.

5.1.5. Harmonic wave in multi-row domain with disturbance truncation

The final test case is designed to validate the implementation of the disturbance filter at a blade row interface. For this purpose, we consider the three row domain sketched in Figure 5.13. The first and third rows are rotating at angular velocity $\Omega = 844.71$ rad/s. An entropy perturbation with circumferential wave length equal to the circumferential size of Duct 3 is imposed at the inlet. The calculation is performed with a 24.5ms time step. The perturbation is stationary in the first and third frames of reference but appears as a travelling wave in Row 2. The 58ND wave cannot be represented on the $2\pi/53$ sector of Row 1 and must thus be filtered at the interface.

The density contours in Figure 5.14 clearly show the successful filtering of the

58ND disturbance at the boundary between Row 1 and Row 2. Figure 5.15 shows the fluctuation in density at a master and its shadow point in Row 2 and Row 3. The phase lag in Row 2 is 200 time steps or 0.49 ms as expected. As the signal in Row 2 converges to a periodic state, Row 3 observes small fluctuations but once the solution is converged the disturbance is successfully removed as it travels from the rotating domain of Row 2 into the stationary domain of Row 1.

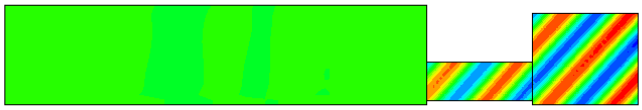


Figure 5.14.: Density contours for travelling wave in multi-row domain with disturbance truncation at blade row interface

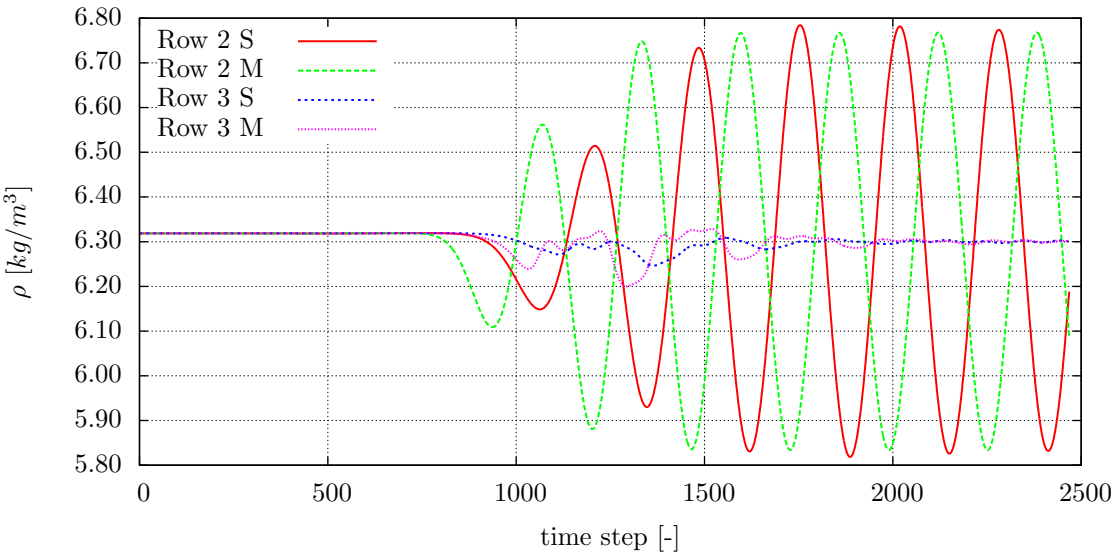


Figure 5.15.: Density histories for travelling wave in multi-row domain with disturbance truncation at blade row interface (M=Master point, S=Shadow point)

5.2. Outlet guide vane in steady non-axisymmetric flow

After the preliminary validation of the Fourier model on the simple geometries of the previous section, this section models a row of outlet guide vanes (OGVs) in steady non-axisymmetric flow. In a real engine configuration, OGVs are exposed to a non-uniform potential field generated by a downstream pylon with a wave length equal to the full circumference. The first two cases cases in this section consider the OGV row in isolation and artificially impose a pressure perturbation at the outlet. In the third case, non-axisymmetry is created by a stagger pattern and the boundary conditions are uniform.

To reduce computational times, only a thin (7%) section at mid-span is considered here. All calculations were performed on the same grid which was created by an in-house mesh generator [93] and is unstructured in the axial and tangential direction and structured in the radial direction. A 2D section of the grid is shown in Figure 5.16. For the initial validation, mesh convergence was not assessed to reduce computational efforts. This has no impact on the validity of the results, as the same passage grids are used for the sparse assembly and whole annulus calculations.

The row consisting of 44 OGVs was run at subsonic operating conditions with an isentropic outlet Mach number 0.45. Table 5.1 shows a summary of the boundary conditions. A converged single-passage steady state solution was used as the starting

	Inlet	Outlet
P_0 [kPa]	126.25	125.78
P [kPa]	102.52	109.19
T [K]	308.72	314.63
U_x [m/s]	166.53	160.71
U_θ [m/s]	99.99	5.57
U_r [m/s]	5.57	-4.91
M_{is} [-]	0.55	0.45

Table 5.1.: OGV boundary conditions

solution for the non-axisymmetric computations. The whole annulus solution (WA) is compared to sparse assembly solutions (SP) with different passage counts. The sparse assembly solution is reconstructed on the full domain in a post-processing step and the accuracy is assessed by comparing the inlet pressure variation and blade surface pressures.

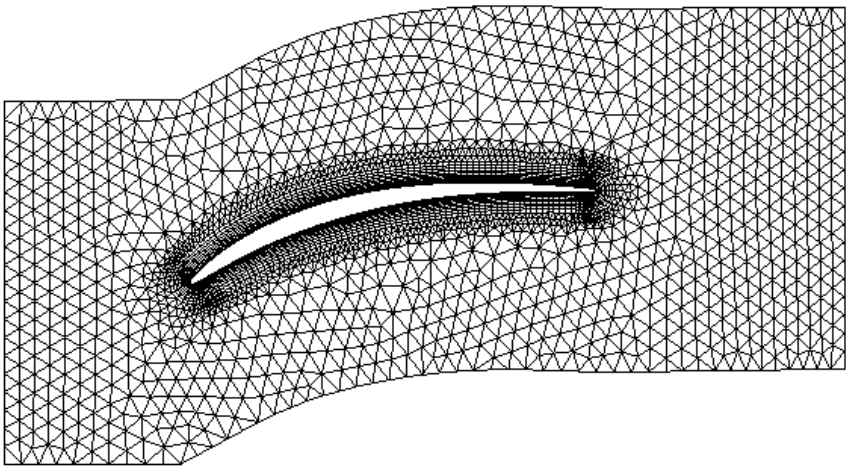


Figure 5.16.: OGV mesh

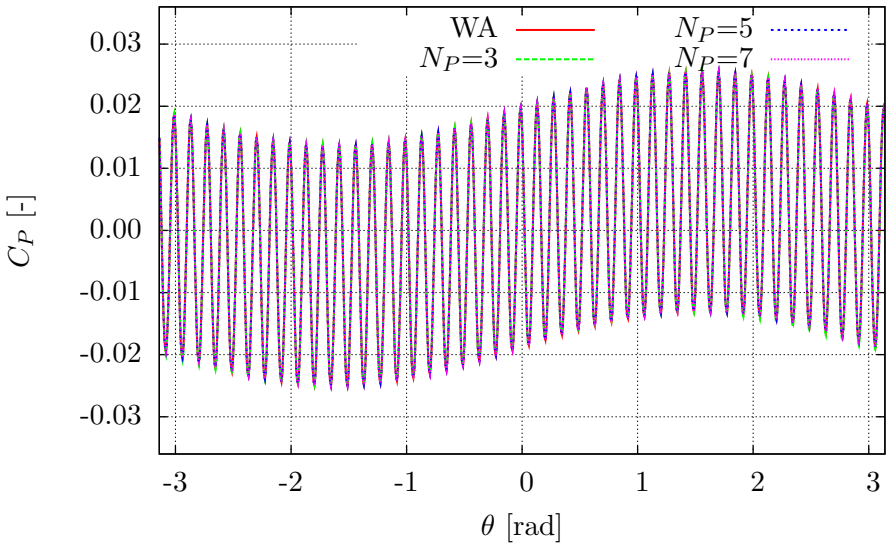
5.2.1. OGV with sinusoidal pressure variation

For the first test case, the OGV is exposed to a stationary sinusoidal pressure perturbation with wave length equal to the full circumference. The amplitude of the pressure variation is 0.1% of the static pressure at outlet.

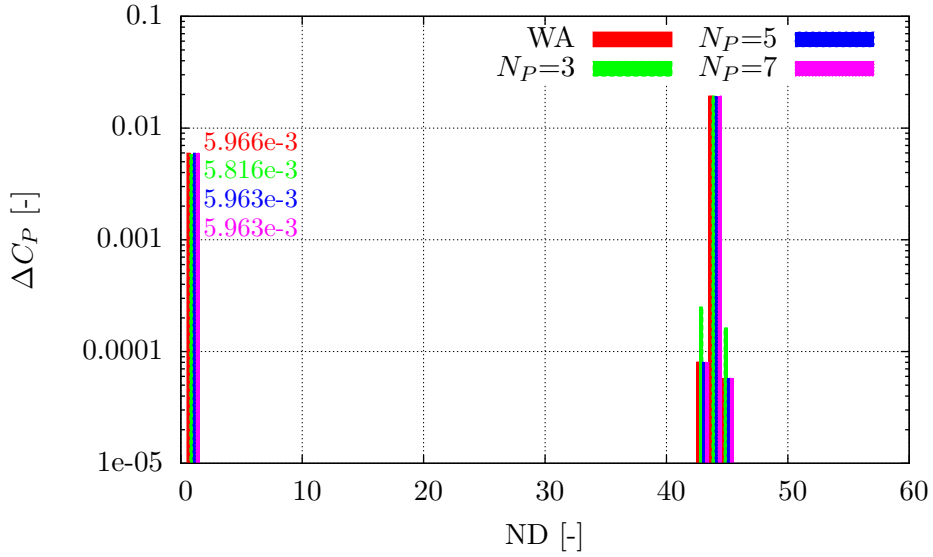
Figure 5.17 show the circumferential pressure variation and Fourier components at the OGV inlet. From the pressure variation it is apparent that, for this simple harmonic disturbance, three passages in the Fourier model are sufficient to capture the effects of the downstream pressure perturbation. However, the Fourier analysis shows a small improvement as the number of passages is increased. The difference between the sparse assembly and whole annulus solutions decreases from 2.5% for three passages to 0.05% for five passages.

The Fourier transform furthermore shows that higher harmonics, although relatively weak, are present in the solution. The second spatial harmonic of the blade count nodal diameter is two orders of magnitude smaller than the fundamental. The amplitude of the 44ND (blade effects) is insensitive (differences less than 0.02%) to the number of passages used for the Fourier approximation.

The solution exhibits disturbances with 43ND and 45ND which are linear combinations of the wave lengths associated with the outlet pressure perturbation and blade pressure field. The representation of these side-bands in the sparse assembly



(a) Circumferential variation



(b) Circumferential wave number spectrum

Figure 5.17.: OGV with sinusoidal pressure perturbation at outlet: Inlet pressure variation

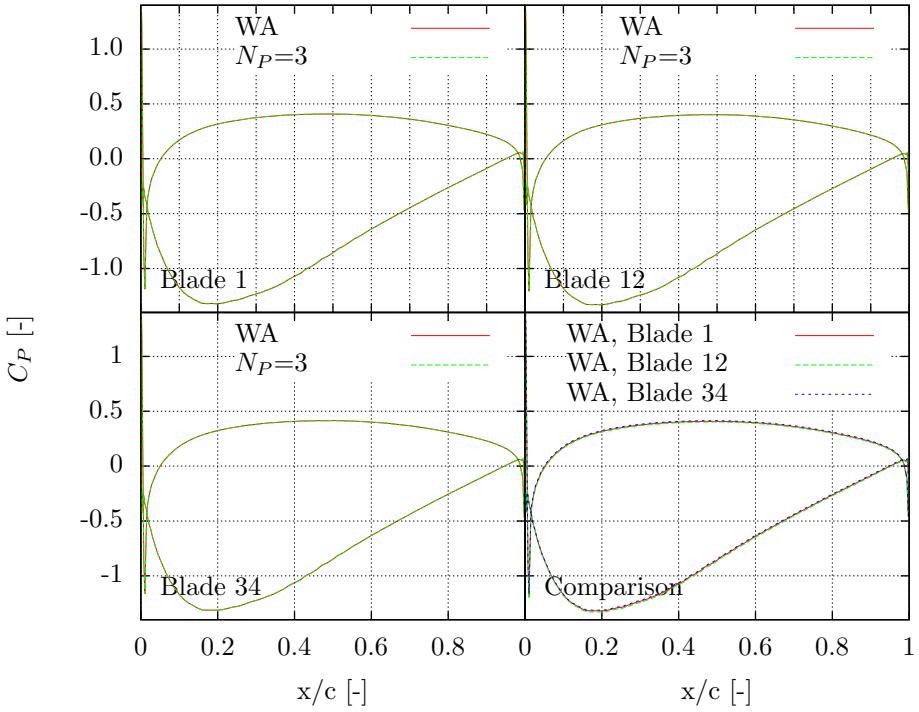
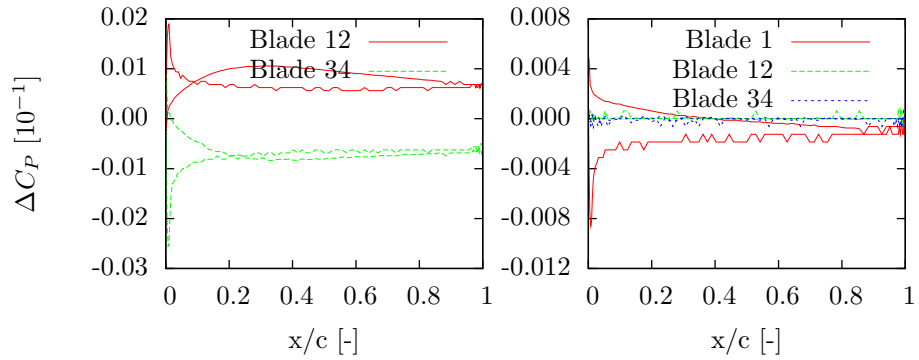
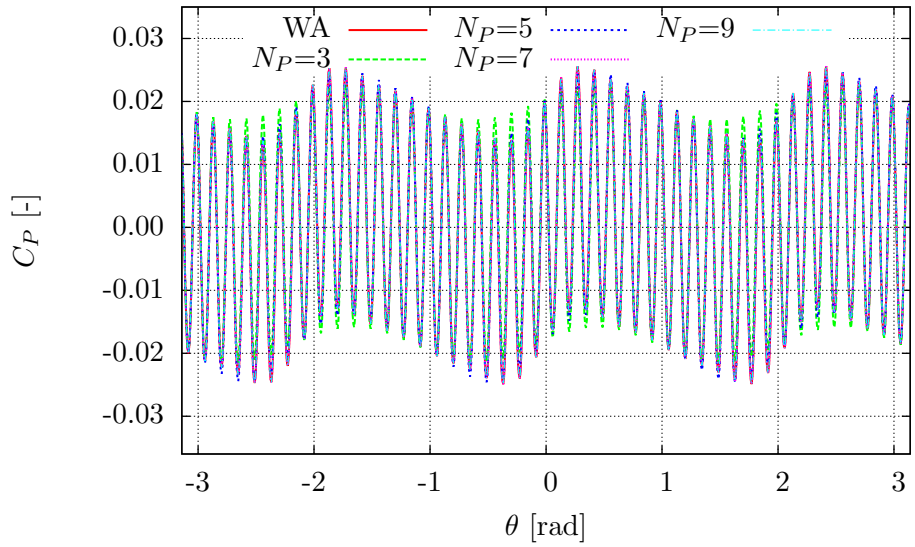


Figure 5.18.: OGV with sinusoidal pressure perturbation at outlet: Blade profiles

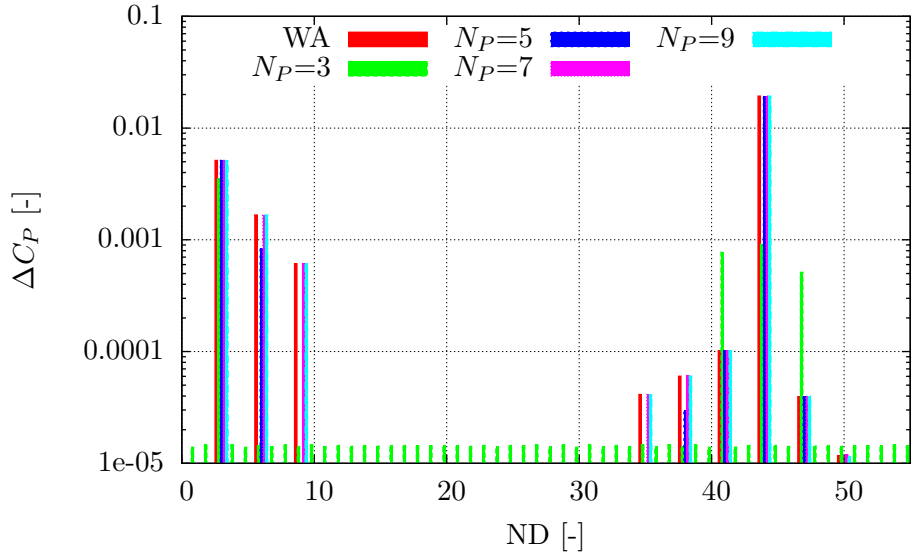


(a) Deviation from nominal blade (b) Deviation from whole annulus

Figure 5.19.: OGV with sinusoidal pressure perturbation at outlet: Differences in blade pressures between sparse assembly and whole annulus solution



(a) Circumferential variation



(b) Circumferential wave number spectrum

Figure 5.20.: OGV with N-wave pressure perturbation at outlet: Inlet pressure variation

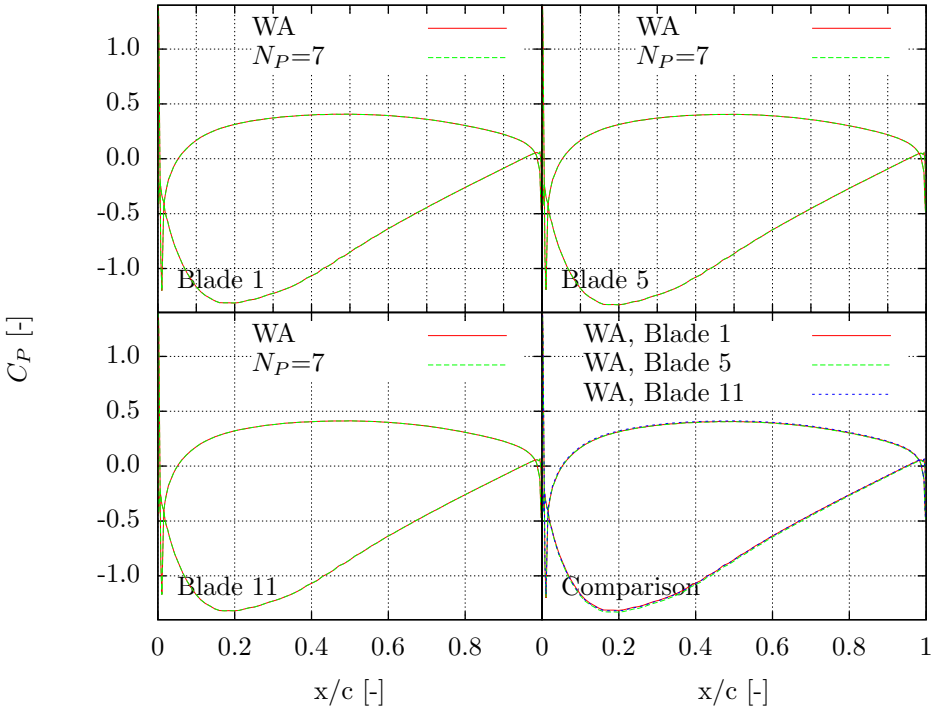
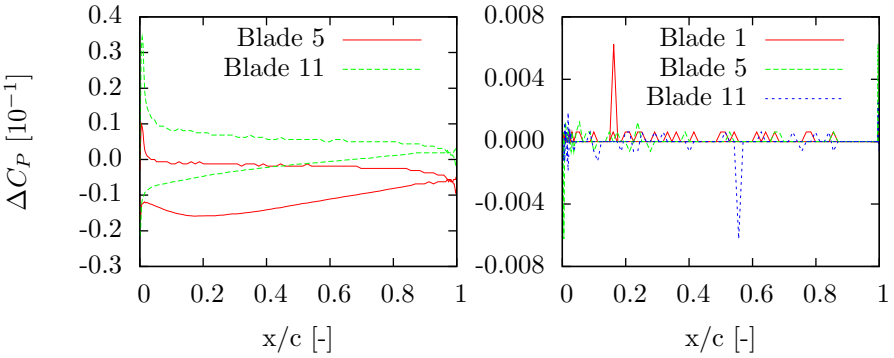


Figure 5.21.: OGV with N-wave pressure perturbation at outlet: Blade profiles



(a) Deviation from nominal blade (b) Deviation from whole annulus

Figure 5.22.: OGV with N-wave pressure perturbation at outlet: Difference in blade pressures between sparse assembly and whole annulus solution

improves as more passages are added. A Fourier approximation with only three passages underestimates the amplitude of the side-bands by about 30% of the whole annulus amplitude. For this particular case, the side bands are two orders of magnitude smaller than the two fundamental wave numbers. This difference can be considered insignificant for an aeroelastic analysis, where one is interested in the excitation of certain frequencies in upstream or downstream blade rows, but it may have an effect on performance. As Figure 5.17 shows, the difference between the two solutions decreases significantly as the number of passages increases. This highlights the importance of harmonic convergence which will be further discussed in Section 5.2.4.

Generally, the differences between the whole annulus and sparse assembly solution discussed in this section are very small which demonstrates that the reduced passage model can accurately represent sinusoidal perturbations.

The reduced passage models also deliver a very good approximation of the blade surface pressures. Figure 5.18 shows that there are no notable differences between the two solutions. The amplitude of the pressure disturbance is comparatively small and hence the difference in peak suction between the blades with maximum and minimum outlet pressure is only about 0.2% (see Figure 5.19). Difference between the whole annulus and sparse assembly surface pressures are small as seen in Figure 5.19. The maximum difference exists on Blade 1 where the two solutions differ by approximately 10% of the blade-to-blade variation at peak suction. This was not further investigated, since the absolute errors are less than 0.1% of the surface pressure.

5.2.2. OGV with N-wave pressure variation

For the next test case, the sinusoidal outlet pressure variation is replaced with the N-wave:

$$\Delta p(\theta) = \sum_{n=1}^{3} \frac{\bar{p}}{n} sin(3n\theta) \tag{5.1}$$

where $\bar{p}$ is the static pressure at the outlet. In order to represent this 3ND wave on a sparse assembly, at least 7 passages distributed over one third of the circumference are required. To assess convergence, the sparse assembly with 3, 5, 7 and 9 passages is compared to the full circumference solution. Calculations on 3 and 5 passages are

	Reference	$N_P = 3$	$N_P = 5$	$N_P = 7$	$N_P = 9$
3ND	5.16E-03	3.53E-03	5.16E-03	5.16E-03	5.16E-03
6ND	1.67E-03	-	8.34E-04	1.67E-03	1.67E-03
9ND	6.12E-04	-	-	6.16E-04	6.11E-04
41ND	1.02E-04	7.80E-04	1.02E-04	1.02E-04	1.02E-04
44ND	1.94E-02	9.13E-04	1.94E-02	1.94E-02	1.94E-02
47ND	3.96E-05	5.13E-04	4.01E-05	3.97E-05	4.01E-05

Table 5.2.: OGV with N-wave pressure perturbation at outlet: Amplitudes of dominant harmonics [ΔC_P]

performed to gain insight into behaviour of the reduced passage model when the solution is undersampled.

Figure 5.20 contains the circumferential variation at OGV inlet and its Fourier spectrum. From the Fourier spectrum it is evident that an undersampling of the harmonics leads to errors in harmonics which are correctly sampled as energy from the undersampled harmonics is wrongly attributed to the lower harmonics. In the case of the three passage solution, both the amplitude of the 3ND and the 44ND perturbation are underestimated, whilst their first linear combinations, 41ND and 47ND, are overestimated. A similar phenomenon can be observed for the five passage solution, where as the 6ND and 37ND disturbance are underestimated despite being sampled at the Nyquist rate.

The amplitudes of dominant harmonics are listed in Table 5.2 for all solutions. Once the number of passages is increased past the Nyquist rate of the highest harmonic, the solutions differ only slightly. Both 7 and 9 passages predict amplitudes within 1% of the whole annulus reference solution.

In terms of blade pressure profiles (Figure 5.21), the maximum difference between the two solutions (Figure 5.22) is approximately 2.5% of the maximum blade-to-blade variation.

5.2.3. Restaggered OGV

This test case aims to validate the method for aerodynamically mistuned assemblies. The vanes from the previous two cases are restaggered according to a 1ND sinusoidal pattern with maximum variation of 1° as illustrated in Figure 5.23. Solutions for sparse assemblies with three, five and seven passages were computed and the results evaluated by comparing the outlet and blade surface pressure profiles (Figure 5.24

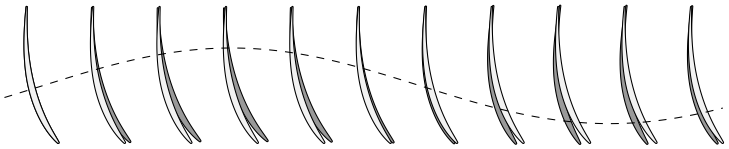
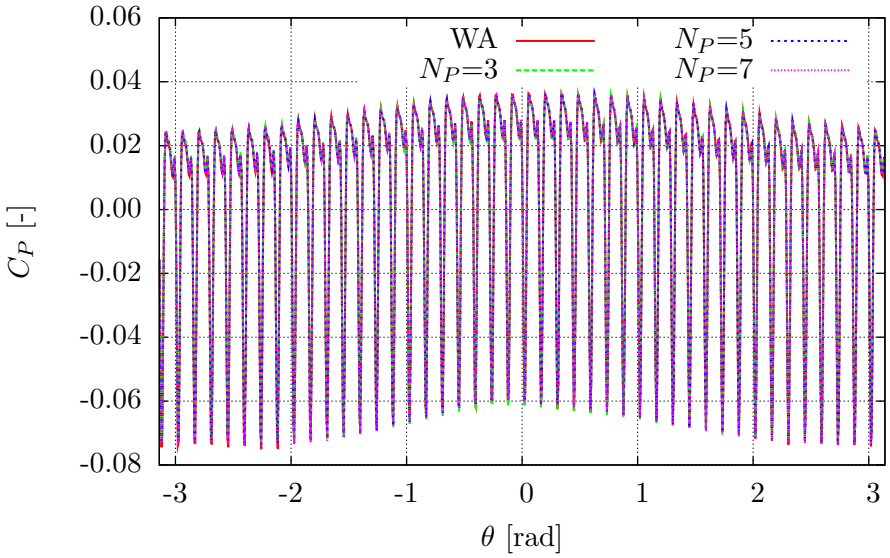


Figure 5.23.: Sinusoidal stagger distribution in the OGV (every fourth blade, not to scale)

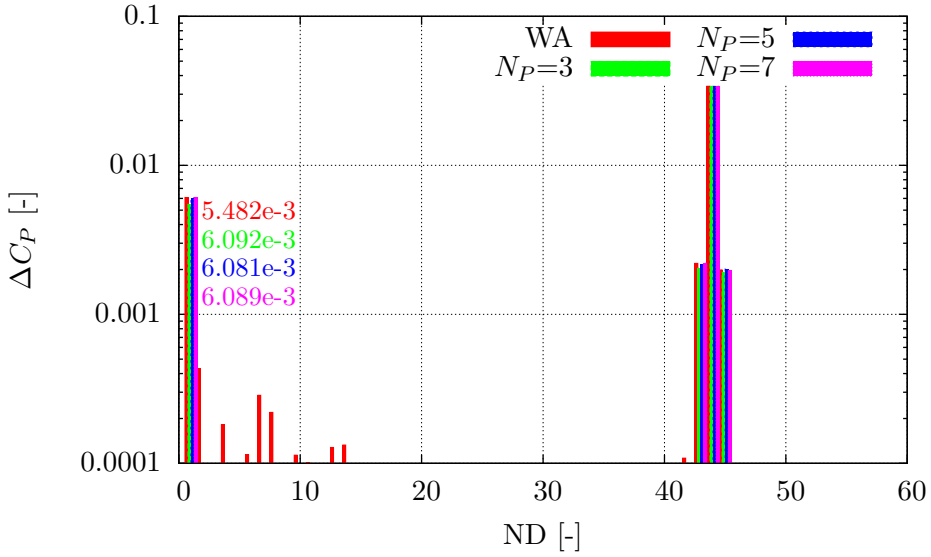
to 5.26).

Due to non-linear effects such as trailing edge separation on the closed passages, which is visible in Figure 5.32, increasing the number of passages in the sparse assembly has a larger influence on the Fourier approximation than in the case of a purely sinusoidal outlet pressure variation. A Fourier transform of the outlet pressure field (Figure 5.24) shows that the whole annulus contains higher harmonics which cannot be identified by the sparse assembly solutions. Since their amplitude is small compared to the effects of the stagger or blades, they do not have a large effect on the resulting flow field and the sparse assembly solution provides a very good approximation of the outlet pressure field and blade pressure coefficients.

A comparison of the nominal blade with the least and most staggered blades (Blade 12 and Blade 34 respectively) in Figure 5.25 shows how the point of peak suction moves slightly towards the leading edge for Blade 34 and towards the trailing edge for Blade 12. It is clear from Figure 5.25 and 5.26 that the sparse assembly method provides a good estimate for the lift distribution on staggered blades.



(a) Circumferential variation



(b) Circumferential wave number spectrum

Figure 5.24.: Restaggered OGV: Pressure variation at OGV outlet

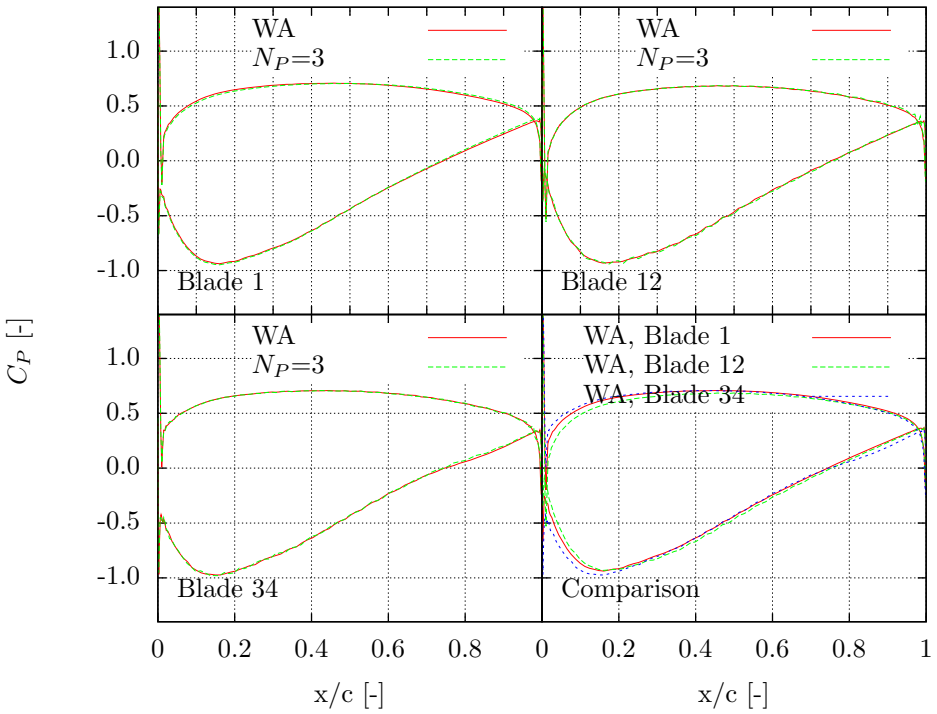
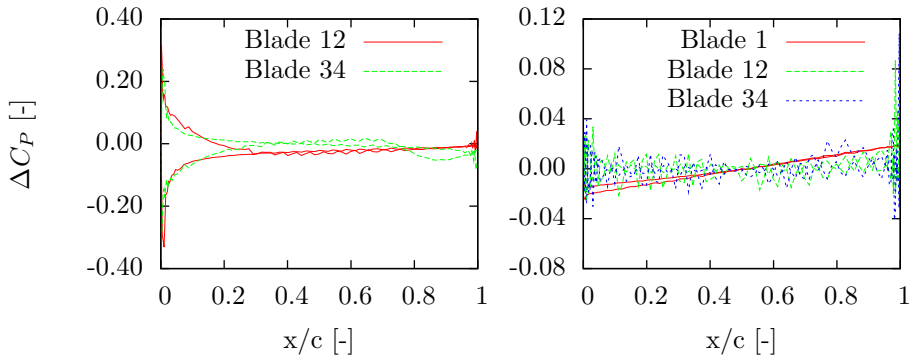


Figure 5.25.: Restaggered OGV: Blade profiles



(a) Deviation from nominal blade (b) Deviation from whole annulus

Figure 5.26.: Restaggered OGV: Blade pressure difference

5.2.4. Convergence and error assessment

5.2.4.1. Definitions

In order to gain a better understanding of the strong and weak points of the method, the difference between the sparse assembly and whole annulus solutions is assessed more quantitatively in this section. For every harmonic, the error ϵ_h is defined as the L^2 norm of the complex difference of the Fourier coefficients over the whole domain and then non-dimensionalised by the L^2 norm of the whole annulus amplitude. The value at every node i is weighed by the volume of the element Ω_i.

$$\begin{aligned}\epsilon_h &= \frac{(\int_\Omega (\hat{f}_{h_{SP}} - \hat{f}_{h_{WA}})^2 d\Omega)^{1/2}}{(\int_\Omega \hat{f}^2_{h_{WA}} d\Omega)^{1/2}} \\ &\simeq \frac{[\sum_{i=1}^{N} [(\hat{f}_{h_{SP}} - \hat{f}_{h_{WA}})^2_i \Omega_i]]^{1/2}}{[\sum_{i=1}^{N} [(\hat{f}_{h_{WA}})^2_i \Omega_i]]^{1/2}}\end{aligned} \tag{5.2}$$

The error estimate can only be valid for harmonics which exist in the solution. Likewise, we can define the L^2 norm of the amplitudes and compare the nodal diameter content of the whole domain.

$$\|\Delta C_{P_h}\| = \left(\frac{1}{\Omega} \sum_{i=1}^{N} [\Delta C^2_{P_h} \Omega]_i \right)^{1/2} \tag{5.3}$$

Furthermore, we can define a local error ϵ_{h_i} for each harmonic and analyse the error distribution to identify the source of discrepancies.

$$\epsilon_{h_i} = \frac{(\hat{f}_{h_{SP}} - \hat{f}_{h_{WA}})^2_i}{(\hat{f}_{h_{WA}})^2_i} \tag{5.4}$$

The Fourier coefficients and errors in this section are evaluated using the static pressure perturbation, as this is the quantity of interest for aeroelastic analysis, but can equally be expressed in terms of other flow variables. When applied to the test cases of Section 5.2, this analysis allows us to identify weak points in the domain and assess the convergence behaviour as the number of passages is increased.

	$\|\|\Delta C_P\|\|$ $[10^{-2}]$
WA	0.683
$N_P = 3$	0.675
$N_P = 5$	0.683
$N_P = 7$	0.683

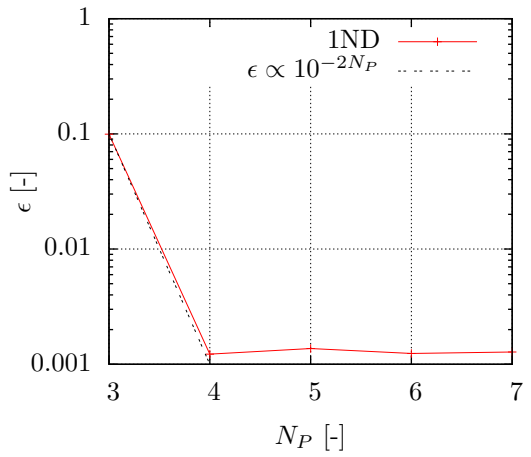
Table 5.3.: OGV with sinusoidal pressure perturbation at outlet: Normed amplitude of static pressure perturbation

5.2.4.2. OGV with sinusoidal pressure variation

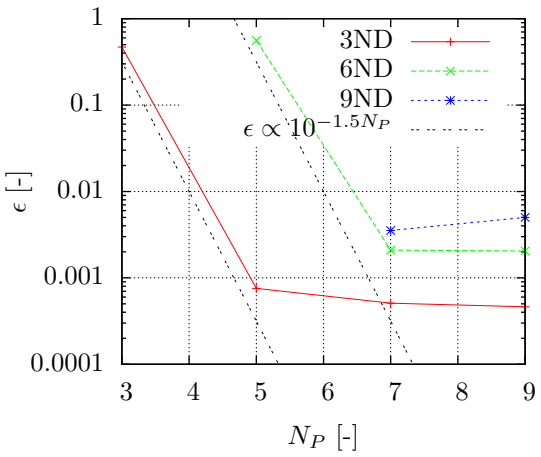
The error analysis for the test case described in Section 5.2.1 is limited to the first harmonic as the solution only contains the fundamental harmonic. Comparing the higher order Fourier coefficients is meaningless. Overall, the Fourier approximation of the first harmonic is noticeably more accurate if more than three passages are used. The amplitude of the 1ND disturbance is approximately 0.7% of the free stream dynamic head in the whole annulus solution (see Table 5.3). The sparse assembly underestimates this amplitude if three passages are used but the approximation improves with five and seven passages. Similarly, the error decreases from 10% for the three passage solution to approximately 0.1% for four and more passages (Figure 5.27a). This improvement from three to four passages shows that better accuracy can be achieved by simply adding one passage without increasing the order of the Fourier approximation. The use of odd passage numbers for maximum efficiency may hence have to be reconsidered. The local error can exceed the error defined in Equation (5.2) significantly. Figure 5.28c and 5.28d show how discrepancies between the whole annulus and sparse assembly solutions accumulate around the leading edge and trailing edge stagnation points. Errors in this region can reach 140%. However, this relative value is misleading since the magnitude of the Fourier coefficients is very small in this region (Figure 5.28a and 5.28b).

5.2.4.3. OGV with N-wave pressure variation

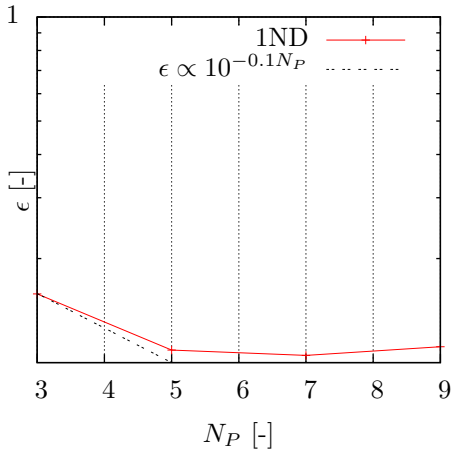
Since the N-wave pressure perturbation contains three harmonics, a minimum of seven passages is required to correctly represent the disturbance. If fewer passages are used, the higher harmonics become aliased and their energy is wrongly attributed to a lower harmonic resulting in a high error for these harmonics (see Figure 5.27b). Once a sufficient number of passages is used, however, the error tends to be lower



(a) Sinusoidal pressure perturbation at outlet

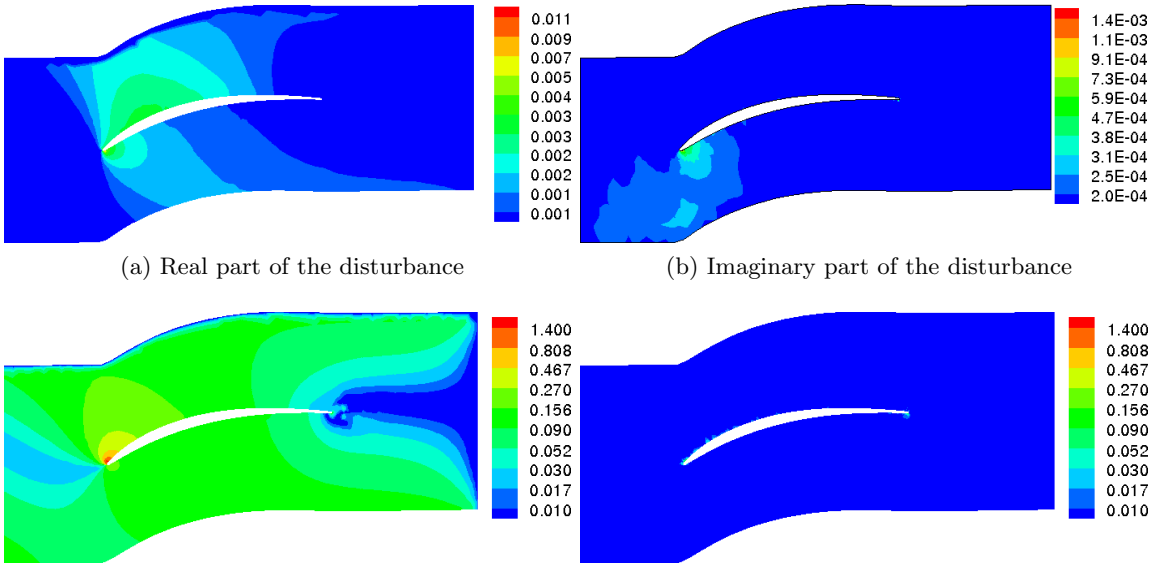


(b) N-wave pressure perturbation at outlet



(c) Restaggered OGV

Figure 5.27.: Harmonic convergence based on unsteady pressures



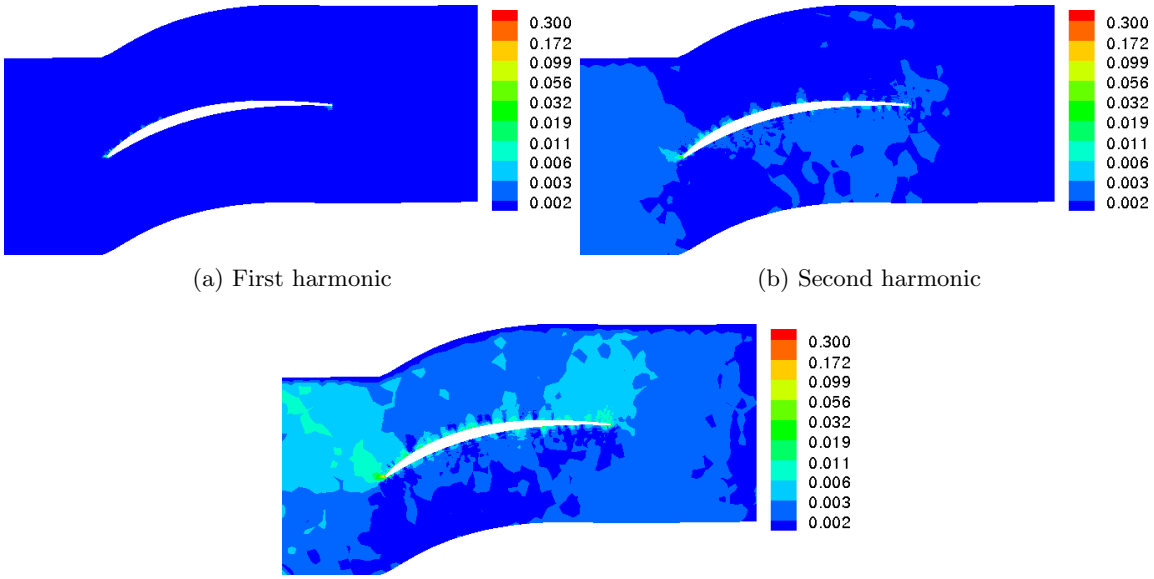
(a) Real part of the disturbance

(b) Imaginary part of the disturbance

(c) Error $N_P = 3$

(d) Error $N_P = 5$

Figure 5.28.: OGV with sinusoidal pressure perturbation at outlet: Disturbance and error distribution



(a) First harmonic

(b) Second harmonic

(c) Third harmonic

Figure 5.29.: OGV with N-wave pressure perturbation at outlet: Error distribution

	$\|\|\Delta C_P\|\|$ $[10^{-2}]$		
	1ND	2ND	3ND
WA	0.622	0.240	0.118
$N_P = 7$	0.622	0.240	0.115
$N_P = 9$	0.622	0.240	0.117

Table 5.4.: OGV with N-wave pressure perturbation at outlet: Normed amplitude of static pressure perturbation

than for the equivalent sinusoidal perturbation. Although representing the third harmonic on seven passages is equivalent to sampling the fundamental harmonic on three passages in terms of Fourier truncation, the error associated with the third harmonic in this case is less than the 10% of the sinusoidal wave's fundamental harmonic. This is likely to be due to the smaller wave length of the disturbance and its quicker rate of decay. Figure 5.29 compares the error distribution for three harmonics over the domain at 60% span. The distribution is similar to the previous case, where high errors are concentrated around the blade surface and in particular at the trailing and leading edge. The contour plots show higher percentage errors for the higher harmonics.

5.2.4.4. Restaggered OGV

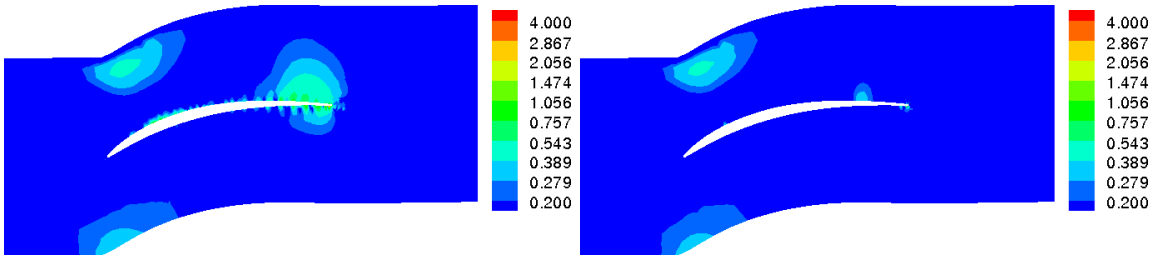
Comparing Figure 5.27c to Figure 5.27a and 5.27b, it is evident that restaggered blades exhibit a slower harmonic convergence than boundary perturbations. For the sinusoidal pressure perturbation the normalised error decreases two orders of magnitude as the number of passages increases from 3 to 4 whereas the error in the restaggered case only decreases by approximately 25% (Figure 5.27c).

For the restaggered guide vanes the error based on complex Fourier coefficients, ϵ_h, does not fall below 20%, whilst the error in amplitude only differs by approximately 3% (Table 5.5). It can therefore be assumed that the error is largely due to a difference in phase between the two solutions. Since relative phase angles between different harmonics and points in the domain, rather than absolute phase angles, define the unsteadiness, this error may be unrepresentative of the solution quality. In the following unsteady test cases the quality of the solution will hence be assessed by comparing the variation of phase along the blade surface.

The variation in stagger results in a different error distribution over the domain.

	$\|\|\Delta C_P\|\|$ $[10^{-2}]$
WA	1.87
$N_P = 3$	1.77
$N_P = 5$	1.82
$N_P = 7$	1.82

Table 5.5.: Restaggered OGV: Normed amplitude of static pressure perturbation



(a) Three passages

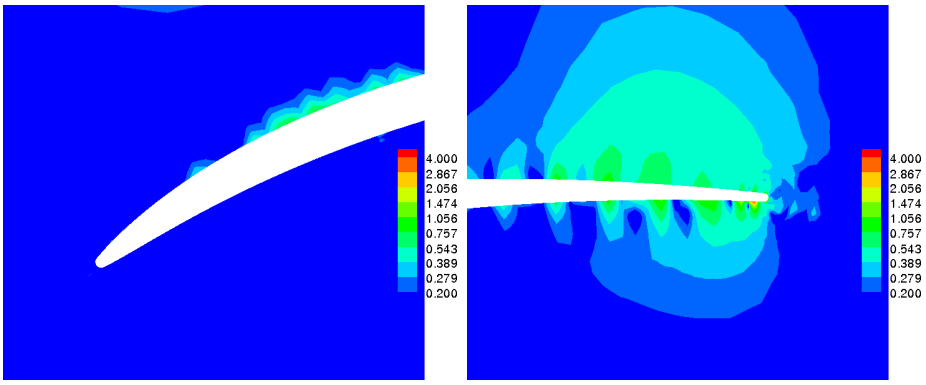
(b) Five passages

Figure 5.30.: Restaggered OGV: Error distribution

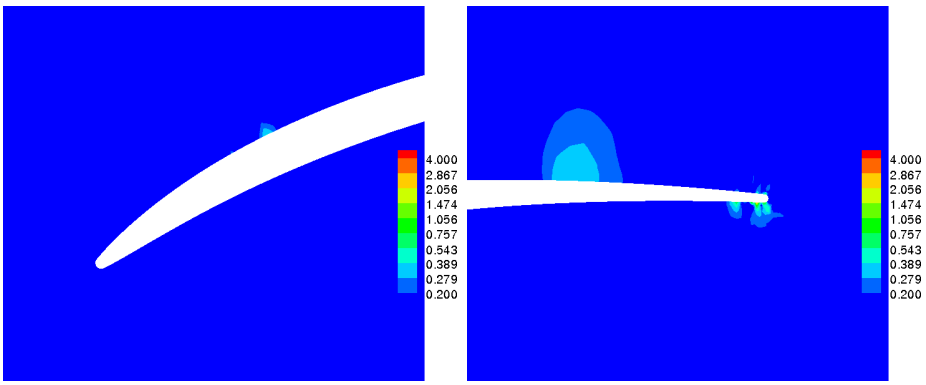
Large errors appear predominantly on the blade suction side and in the trailing edge region and reduce significantly as the number of passages increases (see Figure 5.30 and Figure 5.31). A comparison with the axial velocity contours in Figure 5.32 indicates that these errors are located in the peak suction and trailing edge separation regions. This observation confirms the statements made in Section 4.3 regarding limitations of the reduced passage model. If the flow over restaggered vanes becomes separated, the assumption of small circumferential variations from the mean flow is violated and a Fourier representation is unsuitable.

5.2.4.5. Harmonic convergence summary

It is difficult to establish a criterion on harmonic convergence, as the convergence is always problem-dependent. Similarly to grid- or time-step dependent problems, it needs to be established that a sparse assembly solutions is harmonic-independent before it can be used to analyse a particular problem. High harmonic dependence exists for regions with higher flow spatial gradients (e.g. regions near the blade surface). The inlet/outlet and periodic surfaces tend to contain fewer harmonics and are less sensitive to the order of the Fourier approximation. Since the time-

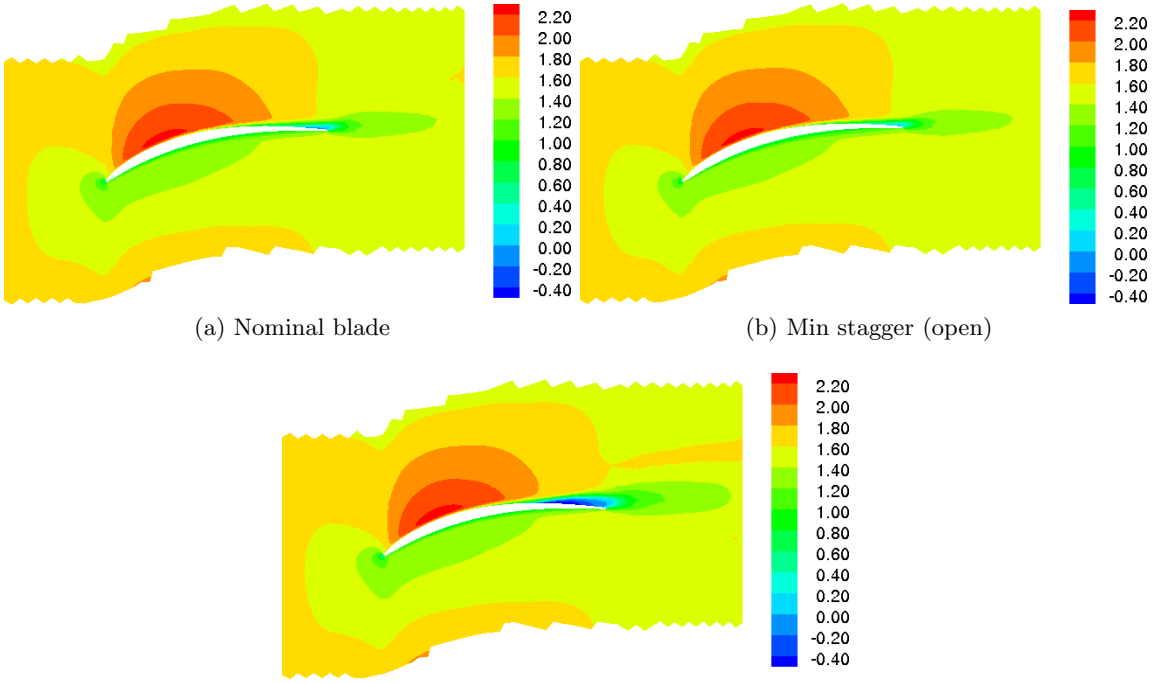


(a) Leading edge $N_P = 3$ (b) Trailing edge $N_P = 3$



(c) Leading edge $N_P = 5$ (d) Trailing edge $N_P = 5$

Figure 5.31.: Restaggered OGV: Error distribution at leading and trailing edge



(a) Nominal blade

(b) Min stagger (open)

(c) Max stagger (closed)

Figure 5.32.: Restaggered OGV: Axial velocity in five passage solution [10^2 m/s]

domain Fourier approach only approximates the boundary conditions, its harmonic convergence is expected to be quicker than that of frequency domain methods where flow variables are approximated over the whole domain [53].

The cases investigated in this section exhibited an exponential convergence rate. The error was found to decrease proportionally to 10^{-cN_P} as the number of passages was increased above the minimum $N_P = 2N_H + 1$, where N_H is the number of harmonics in the disturbance. The constant c varied between 2 for the sinusoidal pressure perturbation and 0.1 for the restaggered guide vanes. Once converged, the error in the approximation of the pressure perturbation was approximately 0.1% while the error in approximating the effects of the sinusoidal stagger pattern remained higher at approximately 10%. The comparatively slow convergence rate of the sparse assembly method when applied to restaggered guide vanes is a consequence of the trailing edge flow separation seen in Figure 5.32. Flow separation significantly alters the flow field around the closed blades and invalidates the assumption of a sinusoidal passage-to-passage variation resulting in high local errors.

Since viscous phenomena such as flow separation and the associated non-linearity of the flow prove difficult for the sparse assembly method, the method could perhaps equally be implemented in an Euler solver without great loss of applicability.

5.3. Turbine stage with non-axisymmetry in the stator

The unsteady sparse assembly method is validated on a high pressure turbine stage with throat area variation in the nozzle guide vane (NGV). The turbine was designed as part of the Brite/EuRam project "Aeroelastic Design of Turbine Blades II" (AdTurBII) which investigated low engine order excitations in turbines. Experimental investigations at DLR and KTH studied the effects of variations in stator throat area and cooling flow rate at two different operating conditions [86][61]. Only one configuration is chosen for the initial validation of the sparse assembly method and only a thin section at mid-span is considered. A more detailed full span study and comparison with experimental data follows in Section 6.1. [1]

5.3.1. Configuration

The stage contains 43 NGVs and 64 rotor blades. A moderate 5ND throat area variation exists in the NGVs resulting in low-engine-order excitation of the rotor blades. We compare the sparse assembly solution with the whole annulus solution in terms of modal forces and unsteady pressures on the rotor surface and at the sliding plane interface.

The reduced passage model contains six NGV passages distributed over $1/5^{th}$ of the circumference allowing a second order Fourier approximation of the throat area variation. The blades in the sparse assembly are shifted according to the same pattern as the whole annulus blades. The resulting throat area variation is shown in Figure 5.33. The rotor contains only travelling disturbances and can therefore be modelled by a single passage. The SPMR grid and sparse assembly domain are shown in Figure 5.34 and Figure 5.35 respectively. As for all validation cases, the reduced passage and full circumference passage grids are topologically identical. For the unsteady calculation, 150 time steps per rotor passing were used.

5.3.2. Frequency content

In order to correctly represent the periodic unsteadiness due to stator-rotor interaction all dominant frequencies have to be included in the temporal Fourier transform. This includes the blade passing frequencies, the LEO unsteadiness due to the

[1] Some of the material in this section was presented at the 12^{th} International Symposium on Unsteady Aerodynamics, Aeroacoustics and Aeroelasticity of Turbomachines [102].

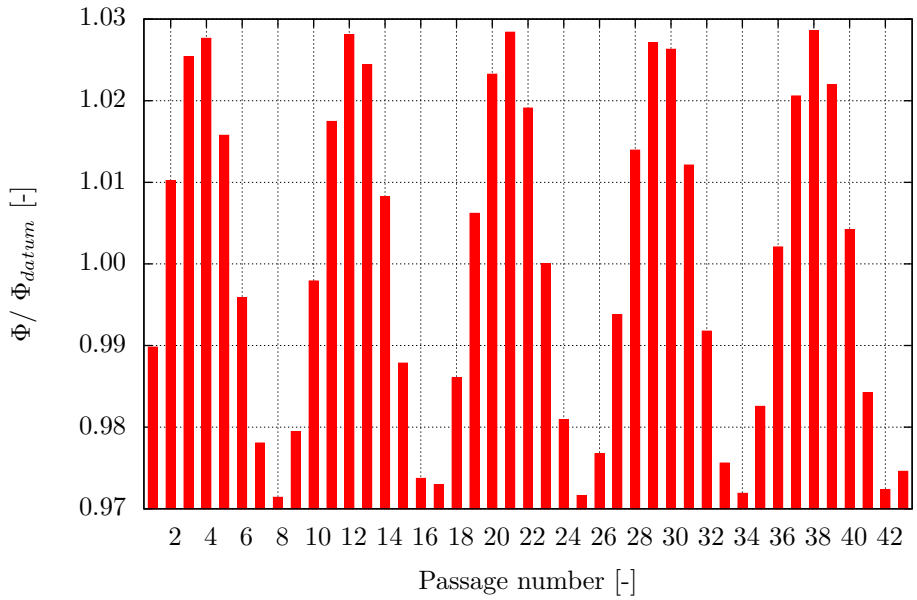


Figure 5.33.: Throat area variation in the NGV

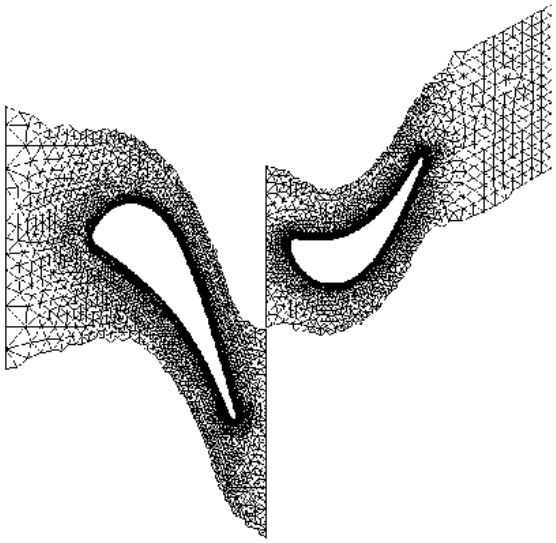


Figure 5.34.: SPMR mesh for turbine stage

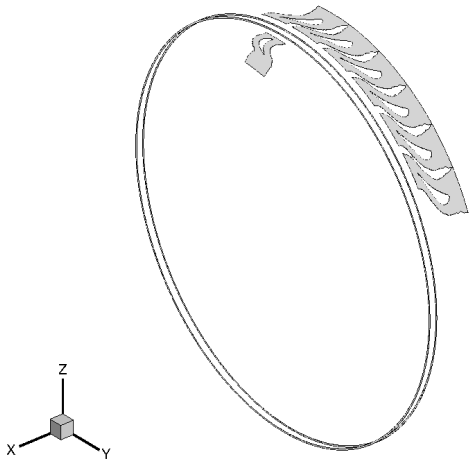


Figure 5.35.: Sparse assembly domain for turbine stage with 5ND throat area variation in the NGV

Mode	n_0	n_S	n_R	N_D	ω_S	ω_R
1	0	0	0	0	0	0
2	0	0	1	64	$64\Omega_R$	0
3	0	1	0	43	0	$-43\Omega_R$
4	0	1	1	107	$64\Omega_R$	$-43\Omega_R$
5	0	-1	1	21	$64\Omega_R$	$43\Omega_R$
6	1	0	0	5	0	$-5\Omega_R$
7	1	0	1	69	$64\Omega_R$	$-5\Omega_R$
8	1	1	0	48	0	$-48\Omega_R$
9	1	1	1	112	$64\Omega_R$	$-48\Omega_R$
10	1	-1	1	26	$64\Omega_R$	$38\Omega_R$
11	-1	0	1	59	$64\Omega_R$	$5\Omega_R$
12	-1	1	0	38	0	$-38\Omega_R$
13	-1	1	1	102	$64\Omega_R$	$-38\Omega_R$
14	-1	-1	1	16	$64\Omega_R$	$48\Omega_R$

Table 5.6.: Spinning modes at stator-rotor interface (*grey = travelling waves in rotor frame of reference, blue = travelling waves in stator frame of reference*)

	Stator	Rotor
Blade passing	64Ω	43Ω
LEO	-	5Ω
Modulations	-	$m43\Omega \pm n5\Omega$ for $m = 1, 2, 3$ and $n = 1, 2$

Table 5.7.: Frequency spectra in rotor and stator domain

throat area variation and linear combinations of the two frequencies. The frequencies and circumferential wave numbers are identified using the theory of spinning modes described in Section 4.2.1.

Referring to Figure 4.5, we can set $k_0 = 5$ and $\omega_0 = 0$ to account for the NGV throat area variation. The resulting first 14 spinning modes are summarised in Table 5.6. As discussed previously only modes which satisfy $\omega = \Omega k$ need to be specified as independent frequencies. Note furthermore that $(n_0 = 0, n_S = 0, n_R = 1)$ and $(n_0 = 0, n_S = 0, n_R = -1)$, and $(n_0 = -1, n_S = 1, n_R = 0)$ and $(n_0 = 1, n_S = -1, n_R = 1)$ etc. are complex conjugates. The corresponding waves are travelling in the same direction and differ only in phase. Only positive nodal diameters are explicitly included in the Fourier transform and Table 5.6.

It is assumed that the first ten stator blade passing harmonics, the first two throat area harmonics and linear combinations of the frequencies associated with the throat area variation and the first three blade passings suffice to capture rotor-stator interaction. The stator frame of reference only contains multiples of the rotor blade passing frequency. For a summary of the independent frequencies, please refer to Table 5.7.

5.3.3. Subsonic flow results

The turbine is run at a pressure ratio of 1.05 in subsonic conditions with isentropic exit Mach number 0.85. The operating conditions are shown in Table 5.8 with the subscript 1 denoting upstream and the subscript 2 denoting downstream conditions. The downstream isentropic Mach number $M_{2,is}$ is calculated by applying the gasdynamic relation:

$$M_{2,is} = \sqrt{\frac{2}{\gamma - 1}\left[\left(\frac{P_2}{P_{01}}\right)^{(\gamma-1)/\gamma} - 1\right]} \tag{5.5}$$

Steady state Mach number contours are shown in Figure 5.36.

5.3.3.1. Modal forces

Results from the sparse assembly and full circumference models are compared for a test mode shape of the form $(0, -z, y)$. Figure 5.37 compares the modal force after two revolutions. Both the time traces and its Fourier transform show a good

P_{01}	132 kPa
T_{01}	311 K
P_{01}/P_{02}	1.52
RPM	6957
$M_{is,2}$	0.81

Table 5.8.: Subsonic operating conditions

agreement between the two solutions. The 5ND and blade passing frequencies contain an error in amplitude of approximately 1%. The error in sidebands is more significant (see Table 5.9) but remains below 10%. It is to be noted that the sidebands have smaller magnitudes and the absolute value of the error approaches the precision of the flow solver. The largest discrepancy is visible in the phase of the 10ND perturbation.

The evolution of difference between sparse assembly and whole annulus is shown in Figure 5.38, where the absolute difference in modal forces is calculated as $\Delta F = F_{full} - F_{sparse}$. This difference is used to calculate the L^2 norm of the error over one revolution non-dimensionalised by the steady state modal force, F_{ref}:

$$\epsilon_{rev} = \frac{\left[\frac{1}{N_{rev}} \sum_{i=1}^{N_{rev}} \Delta F_i^2\right]^{1/2}}{F_{ref}} \tag{5.6}$$

where N_{rev} is the number of time steps per revolution.

Since the full annulus solution converges to a periodic state much quicker (after half a revolution), the difference between the two solutions can provide useful insights into convergence of the reduced passage model. After one revolution the difference between the two solutions becomes less than 1% of the average modal force (Figure 5.38 and Figure 5.39).

An analysis of the convergence rate of the different harmonics could provide further insight but is difficult to perform in practice since the necessary Fourier transform relies on the periodicity of the signal and the harmonics cannot be separately rigorously in a converging signal.

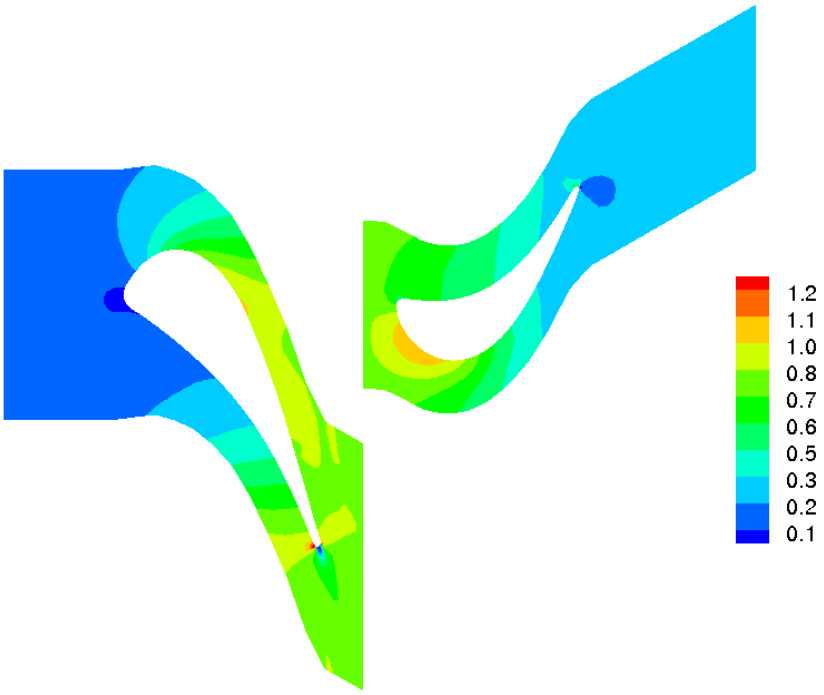


Figure 5.36.: Relative Mach number in steady state starting solution (subsonic case)

5.3.3.2. Spinning modes at blade row interface

A circumferential and temporal Fourier transform of unsteady pressures at the sliding plane provides the spinning modes found at the blade row interface. The identified modes are depicted in Figure 5.40 and 5.41.

As expected, the rotor inlet contains a number of disturbances along the line $ND = EO$. This corresponds to disturbances in travelling wave form with $\omega = vk$ formed by the interaction of stator blade passing and throat area variation. The other spinning modes lie along parallel lines shifted by 64ND and correspond to scattered NGV passing disturbances.

The stator outlet contains only frequencies which are multiples of the rotor blade passing. The interaction with the stator flow field creates additional circumferential wave numbers shifted by linear combinations of 43ND and 5ND.

Figures 5.42 to 5.44 display the amplitudes and wave number content of the dom-

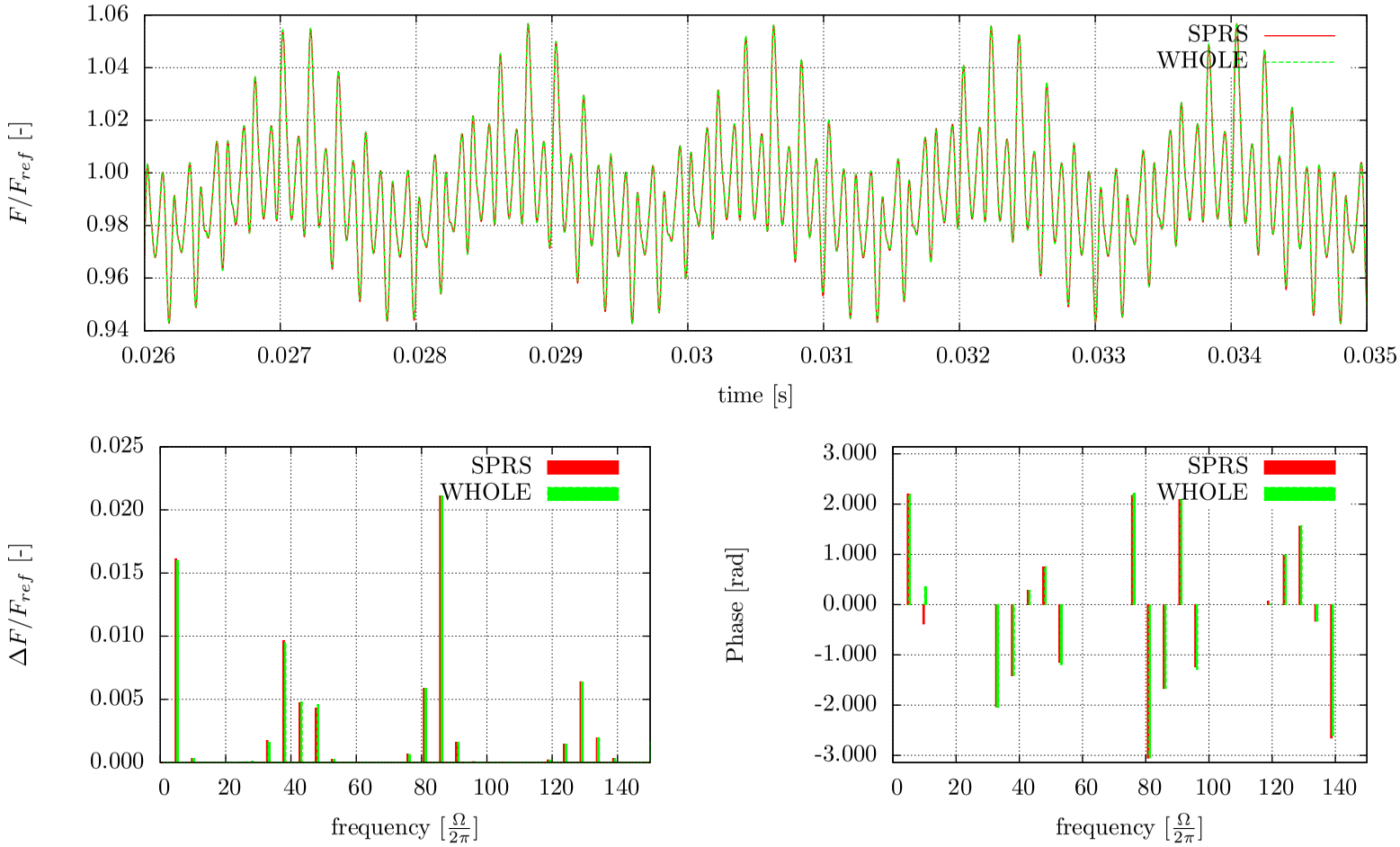


Figure 5.37.: Rotor modal force history in subsonic flow

EO	SPRS	FULL	%
5	1.61	1.59	1.1
10	0.03	0.03	1.0
43	0.47	0.48	0.9
86	2.11	2.11	0.2
38	0.97	0.95	1.8
48	0.43	0.46	6.2
33	0.17	0.16	9.8
53	0.02	0.02	0.0

Table 5.9.: Modal force amplitudes of dominant frequencies in subsonic flow non-dimensionalised by steady state force, F_{ref} [%]

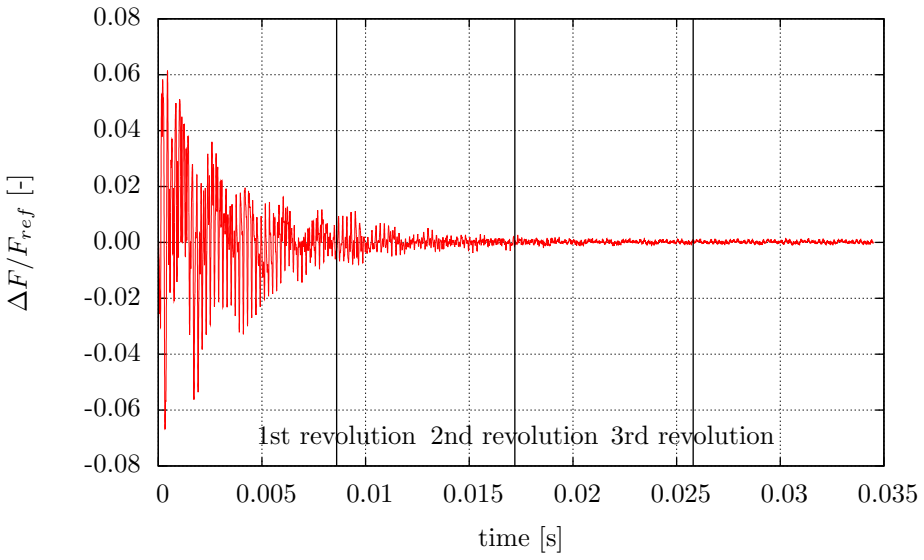


Figure 5.38.: Difference between whole annulus and sparse assembly modal force prediction in subsonic flow

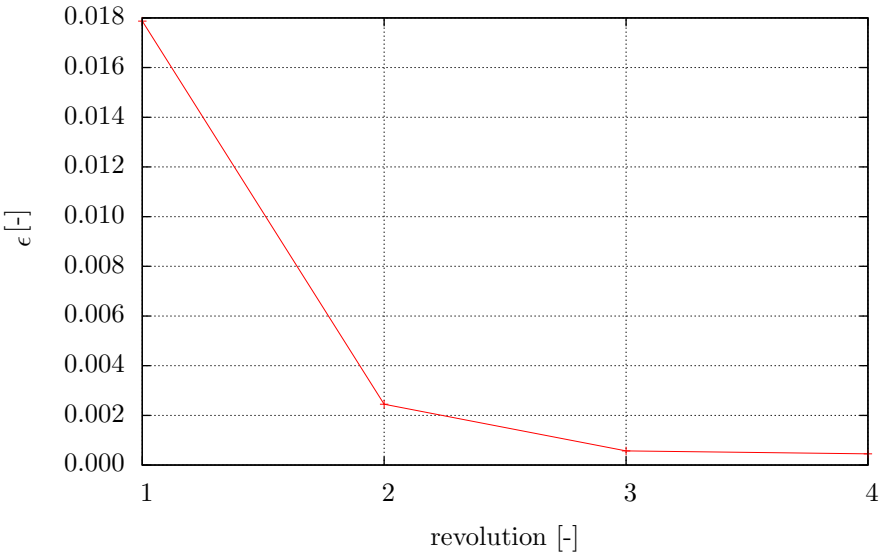


Figure 5.39.: Convergence of sparse assembly solution in subsonic flow

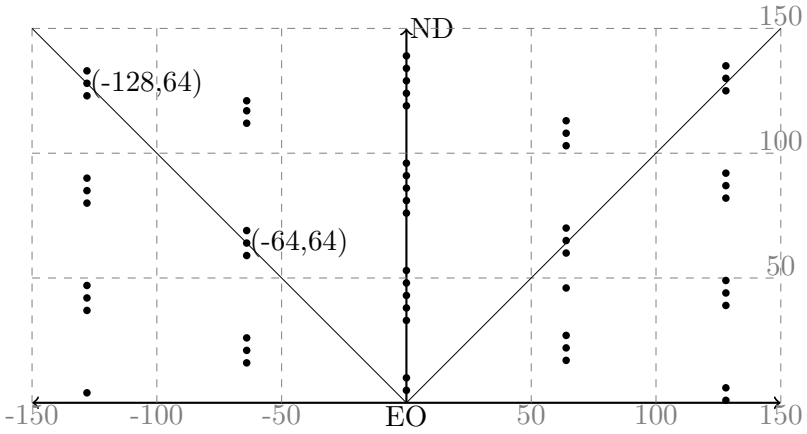


Figure 5.40.: Spinning modes at stator outlet

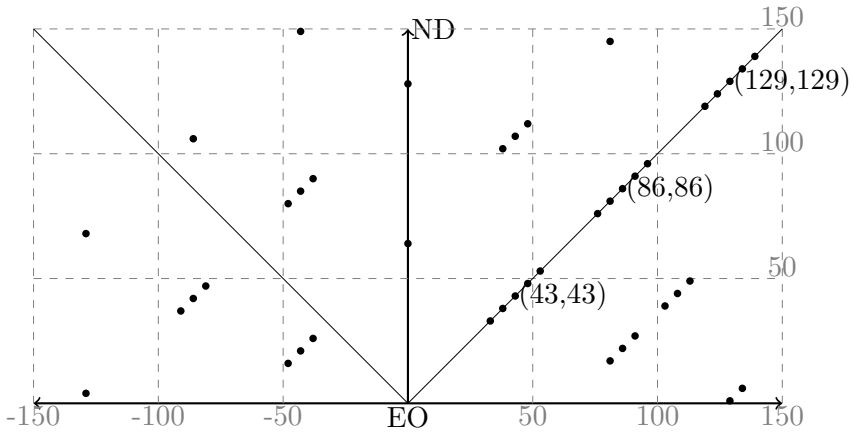


Figure 5.41.: Spinning modes at rotor inlet

inant frequencies. The time-averaged flow at stator outlet contains only linear combination of 43ND and 5ND (Figure 5.42). All major circumferential wave numbers are captured on the sparse assembly domain. The whole annulus domain also shows evidence of 15ND which was neglected in the reduced passage model. The rotor blade passing frequencies ($\omega = -64\Omega$ and $\omega = -128\Omega$) show a similar circumferential wave number content. The travelling waves with wave numbers $k = 64$ and $k = 128$ are modulated by 5ND, 43ND and higher harmonics, which creates sets of circumferential wave numbers centred around $64 - n43$ and $128 - n43$, all of which are present in the sparse assembly. Note that $\omega = -128\Omega$ contains 4ND, the remaining wave numbers of this group are represented by their conjugates in $\omega = 128\Omega$ at $ND = 1$ and $ND = 6$.

The combinations of blade passing and throat area variation appear as travelling disturbances with a well-defined phase lag in the rotor frame of reference. In absence of a stationary perturbation in the rotor, these disturbance are only modulated by the time-averaged flow. The circumferential wave number content of the distinct frequencies is therefore significantly cleaner as seen in Figure 5.43 and 5.44.

5.3.3.3. Rotor surface unsteady pressures

The blade surface pressures are compared by means of local pressure traces and amplitude and phase of unsteady pressure perturbations. The pressure probes are located at 10%, 30%, 70% and 90% axial chord as illustrated in Figure 5.45. Figure 5.46 and 5.47 show pressure traces on the pressure and suction side respectively

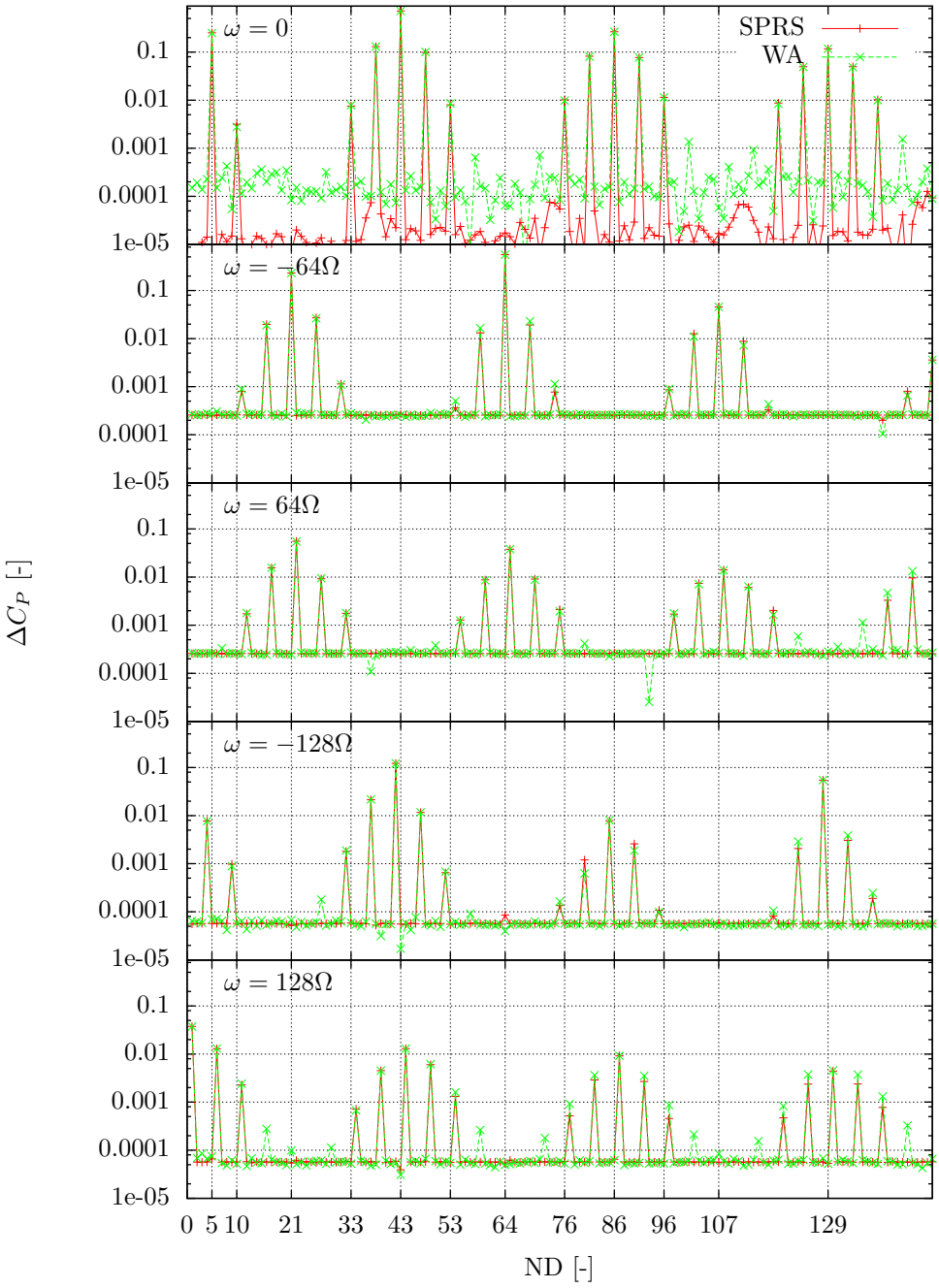


Figure 5.42.: Fourier spectrum at stator outlet in subsonic flow

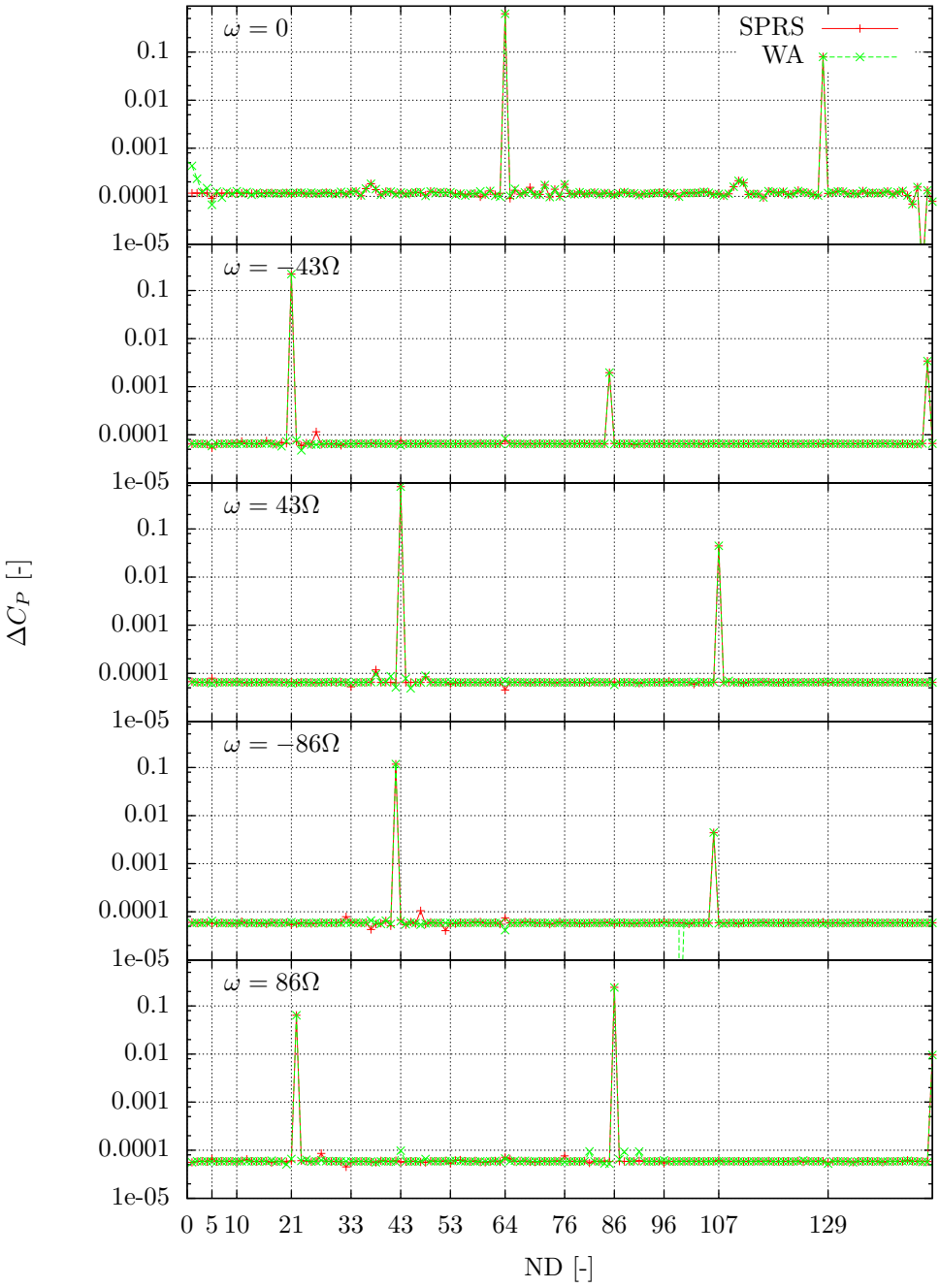


Figure 5.43.: Fourier spectrum at rotor inlet in subsonic flow (1/2)

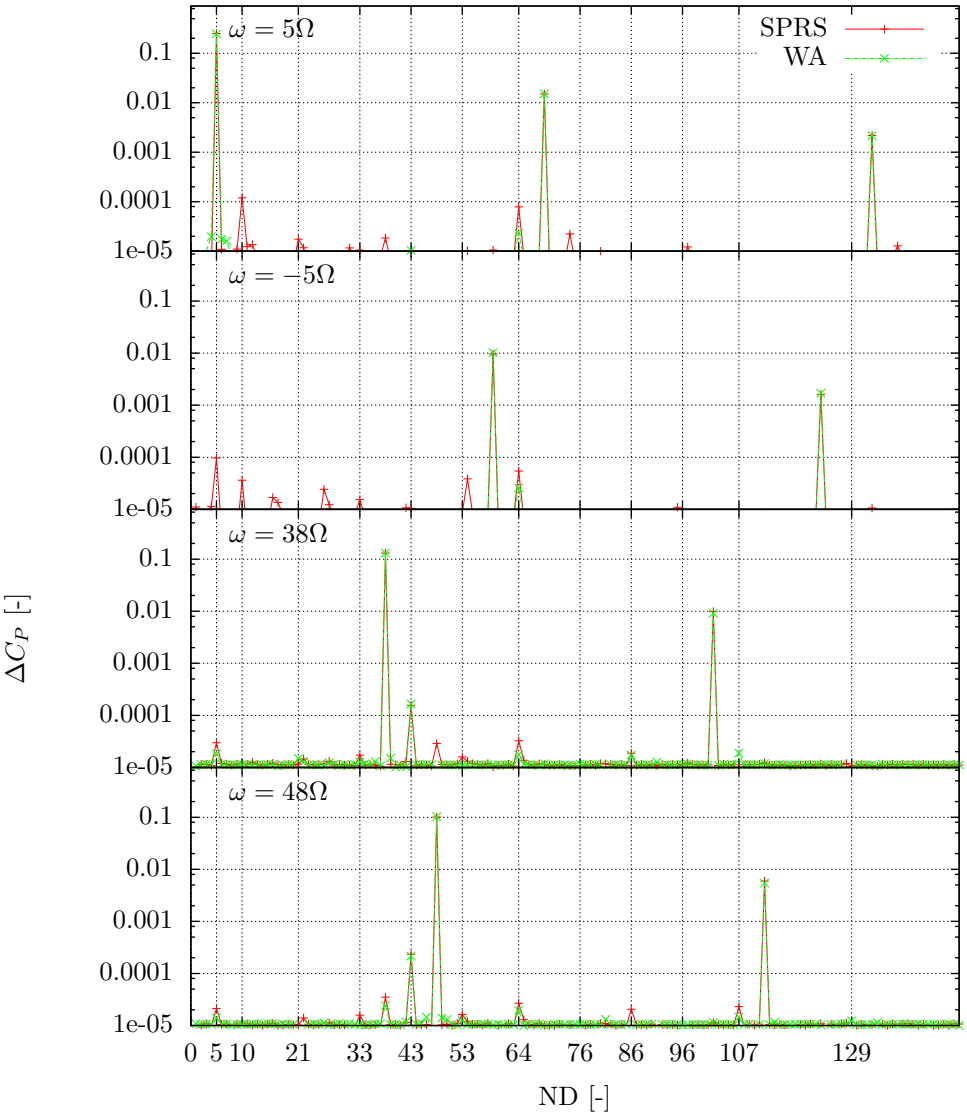


Figure 5.44.: Fourier spectrum at rotor inlet in subsonic flow (2/2)

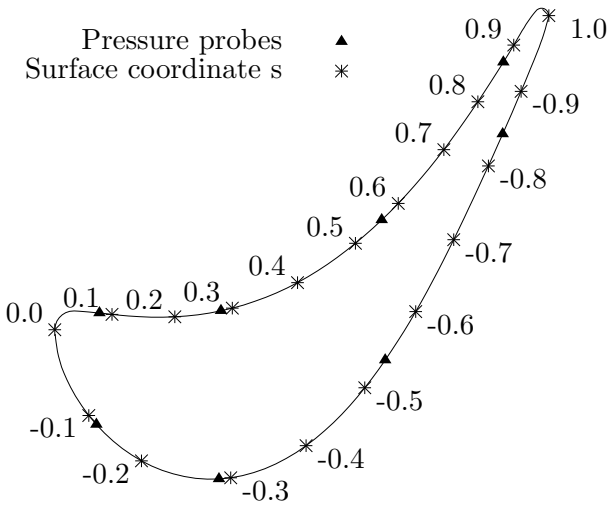


Figure 5.45.: Location of pressure probes on rotor surface

over a fraction of a revolution. The sparse assembly predicts the same local surface pressure as the whole annulus model. The highest variation in pressure due to the stator blade passing can be found in the mid-chord region. On the pressure side at 30% axial chord the peak-to-peak variation reaches approximately 4% of the inlet stagnation pressure (top right of Figure 5.46). The effect of stator blade passing then decreases again towards the trailing edge where it reaches approximately 1.6% on the pressure side (bottom right of Figure 5.46). On the suction side in Figure 5.46, the mid-chord fluctuations are of a similar magnitude but at 90% axial chord the peak-to-peak variation is only approximately 0.2%. The decrease in the total variation increases the relative significance of the higher harmonics.

A temporal Fourier analysis of the rotor surface pressure (see Figure 5.48 to 5.51) gives insight into the behaviour of disturbances along the rotor surface.

As briefly mentioned in Section 1.2.2 the attenuation of a pressure perturbations in space depends on the local flow conditions. From two-dimensional inviscid theory it can be seen that a pressure wave's axial wave length is a function of its frequency, circumferential wave length and local axial and circumferential Mach number. When a pressure wave propagates along a blade surface its wave length and velocity change. A pressure perturbation of a given frequency and circumferential wave length can hence be cut-on (propagating without decay) over part of the blade and cut-off

(decaying in the direction of propagation) over another part of the blade. The plots of phase, Φ, against surface coordinate, s, in Figure 5.49 and 5.51 provide insights into the local wave behaviour. Since the slope, $d\Phi/ds$, is a measure of the local wave length and the propagation velocity, v_s, is related to the angular frequency, ω, and wave length, k_s, through $v_s = \omega/k_s$, the slope is inversely proportional to the local wave velocity. A zero slope indicates that the wave is cut-off and propagating purely in a direction normal to the blade (similar to spiral waves in a circular duct), whereas a steep slope is representative of very small wave lengths as expected in sonic regions.

Figure 5.48 to 5.51 compare the local amplitudes, which are non-dimensionalised by free stream dynamic pressure, and propagation speeds on the full circumference and reduced passage domain.

All disturbance reach their maximum amplitude on the suction side in the leading edge region. The peak amplitude of the blade passing disturbances is the most significant and approximately equal to the free stream dynamic head. The second harmonic and throat area variation reach approximately half this amplitude, while linear combinations of the throat area and blade passing appear much smaller.

Although a very good match in terms of amplitude and phase exists for some linear combinations, differences exist in disturbances of comparable magnitude but different frequency. Comparing, for example, 81ND and 38ND, one observes noticeable differences in both amplitude and phase of the 38ND disturbance whilst a very good agreement exists for the 81ND disturbance. The phase plots indicate that the 81ND disturbance propagates faster (smaller slope) and is not reflected as often as the 38ND on the pressure side. However, differences in amplitude also exists for the 48ND disturbance despite an approximately constant wave speed on the pressure side. In general, differences between the two solution are most pronounced in the weaker perturbations (i.e. 33ND and 53ND). With a peak amplitude of 1% of the blade passing disturbances, however, this can be considered negligible.

Despite its large wave length, the amplitude of the 5ND disturbance varies considerably from pressure to suction side. There is a sharp drop in amplitude from the suction side to the pressure side on the leading edge. The amplitude then drops as the disturbance travels along the suction side. This is accompanied by a reflection at about midway between leading edge and trailing edge and a consequent increase in speed. On the pressure side, the wave is initially cut-off but becomes cut-on in the vicinity of the trailing edge before it is reflected. The higher frequency disturbances

are more susceptible to changes in the flow field and change speed and direction repeatedly on both sides.

5.3.4. Grid size comparison

The above results demonstrate that the sparse assembly method provides a very good approximation to the full circumference solution despite using only a fraction of the computational domain. Table 5.10 lists the grid sizes and computational times for the two solutions. Both simulations were run on the Imperial College High Performance Computing cluster with Nehalem CPUs running at 2.93GHz, 8 cores per node with 24GBytes of fast memory. In order to give an estimate of the speed-up achieved with the sparse assembly method, the wall-clock time to convergence for the two calculations is compared. To take into account the number of processors used, we define

$$\text{Total Elapsed Time} = (\text{Elapsed Real Time to Convergence}) \times (\text{Number of CPUs}) \tag{5.7}$$

By using a spatial Fourier approximation and phase-lagged boundary conditions, the total grid size can be reduced from approximately 1M points to 88K points. This results in an approximately four-fold reduction in terms of total elapsed time compared to the full circumference solution. It must be noted that the reduced size of the sparse assembly solution offers additional benefits as it can be obtained and post-processed on a standard workstation.

Further savings could potentially be made by reducing the order of the spatial or temporal Fourier approximation. The current test case used five passages for a second order approximation of the 5ND throat area variation. The circumferential wave number spectrum at stator outlet (top plot of Figure 5.42), however, indicates that the second harmonic is two orders of magnitude smaller than the fundamental harmonic. It may thus be possible to achieve a similar level of accuracy using only three passages.

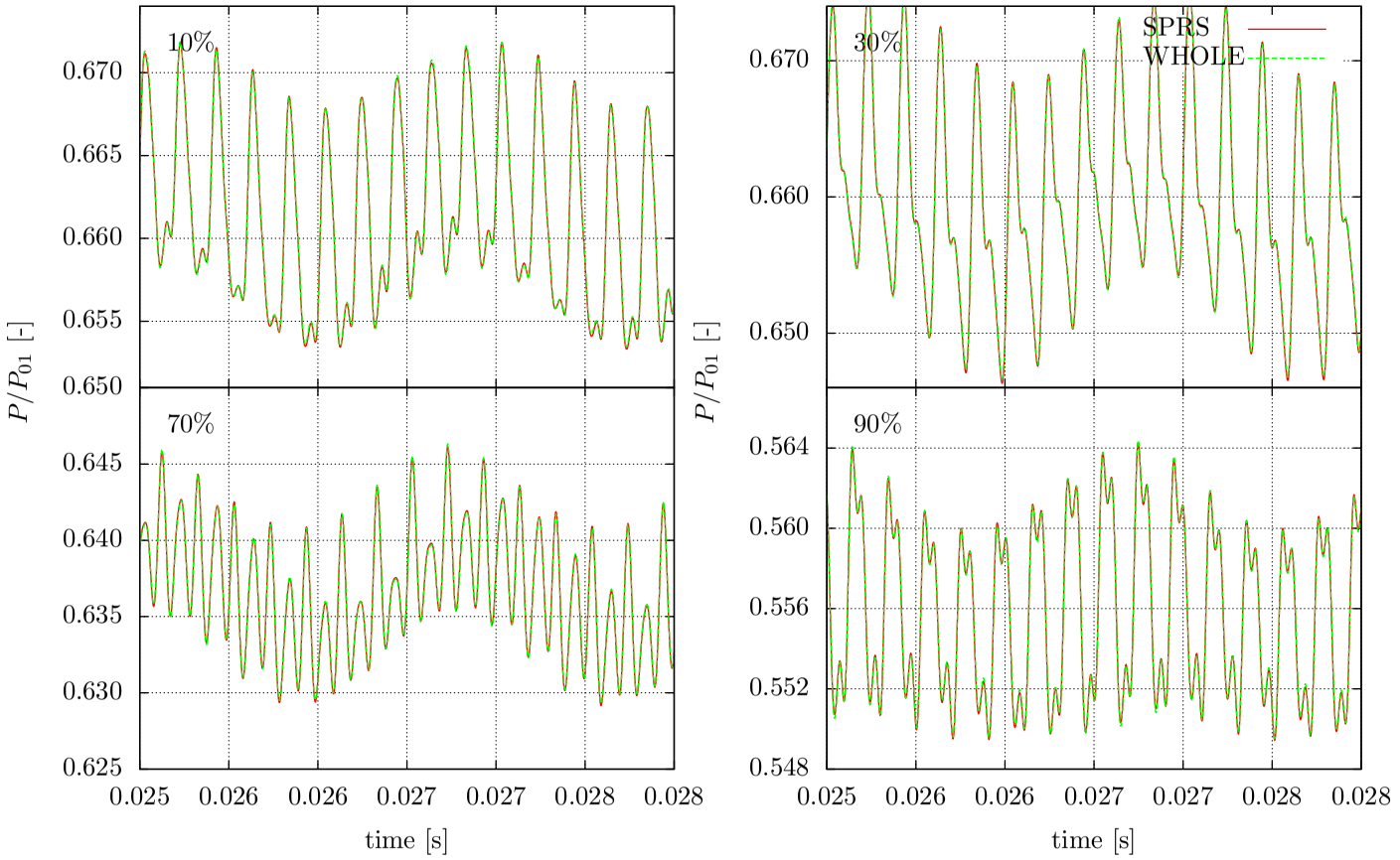


Figure 5.46.: Pressure side pressure traces in subsonic flow

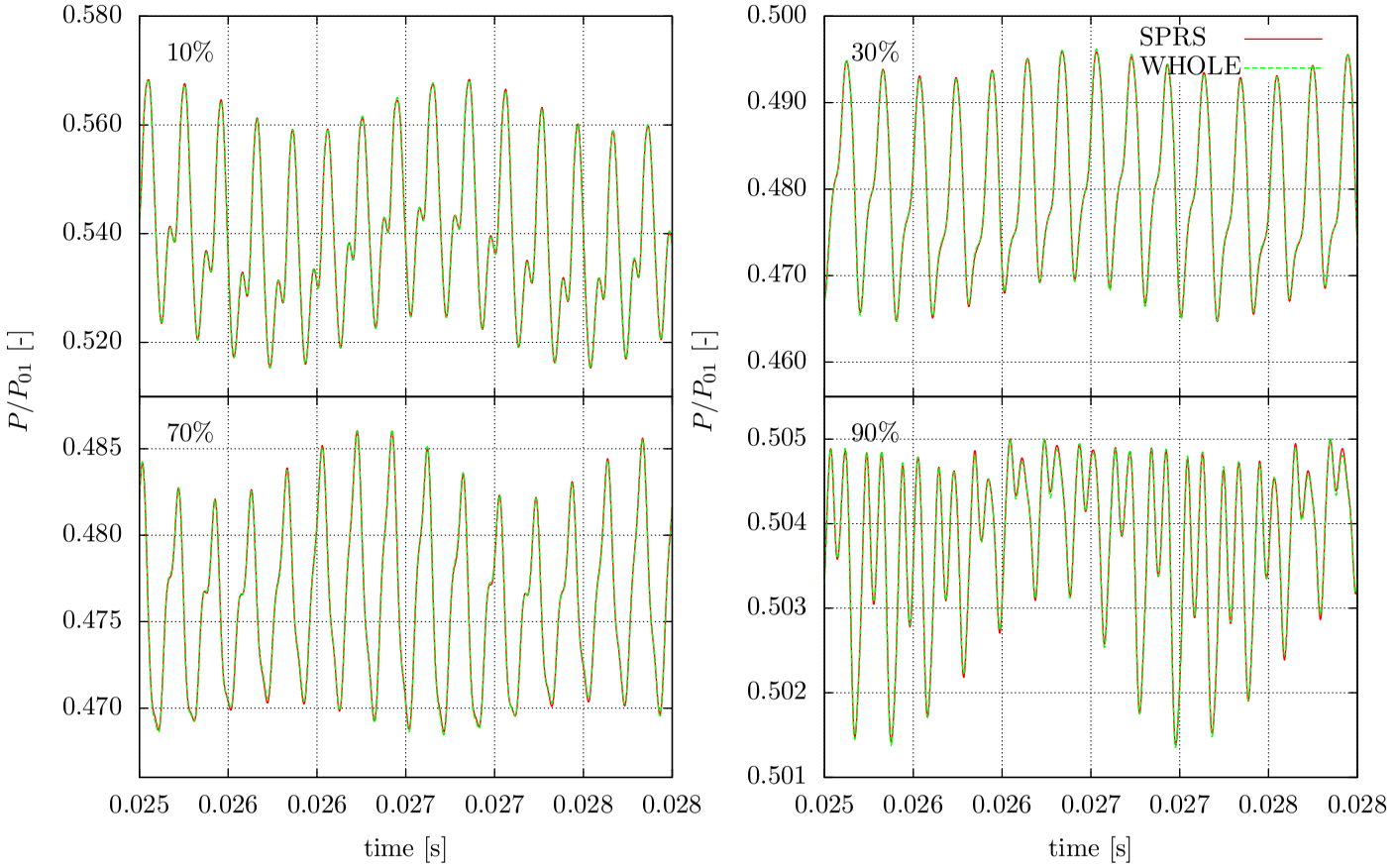


Figure 5.47.: Suction side pressure traces in subsonic flow

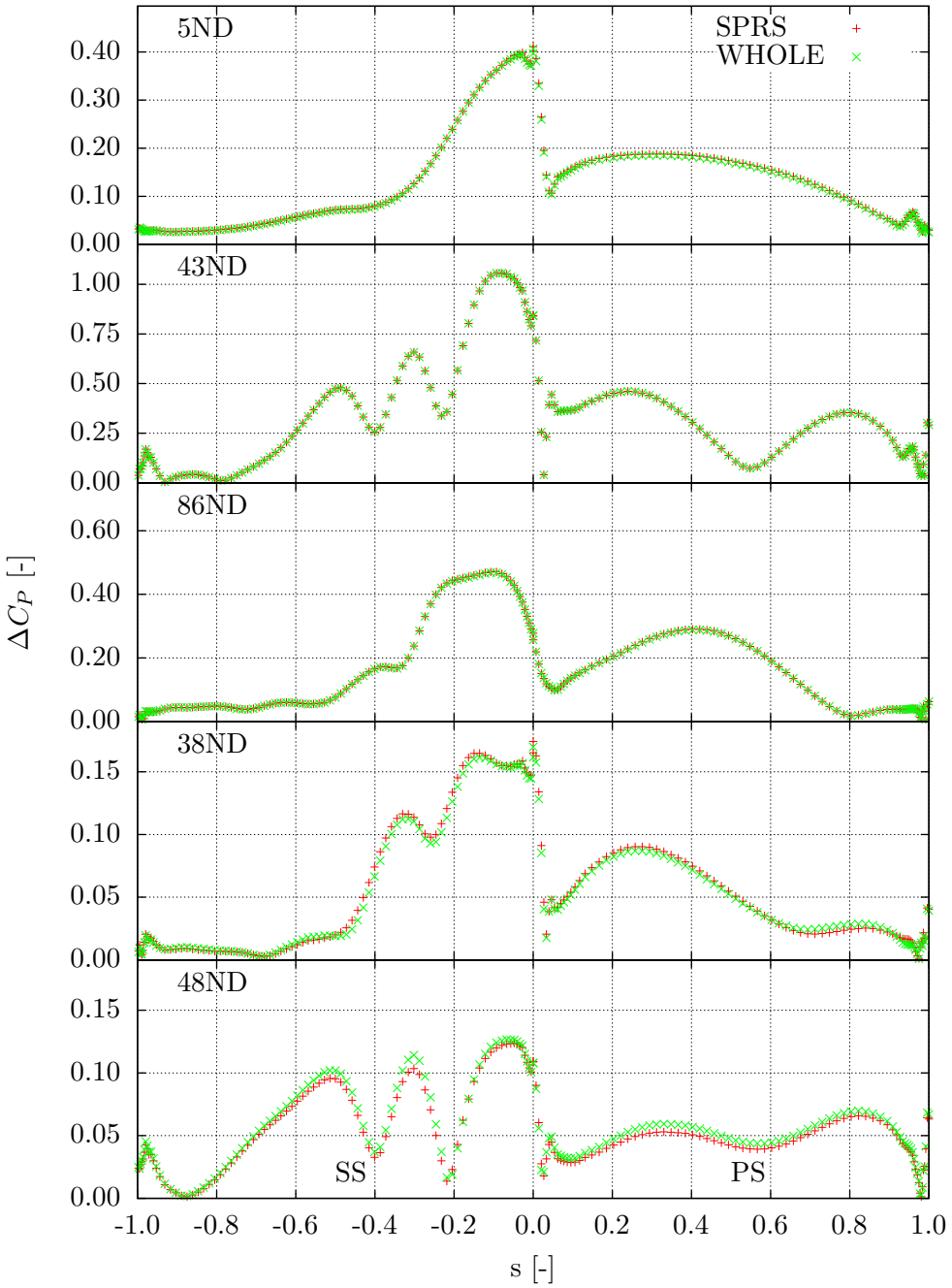


Figure 5.48.: Unsteady rotor surface pressure in subsonic flow: Amplitudes (1/2)

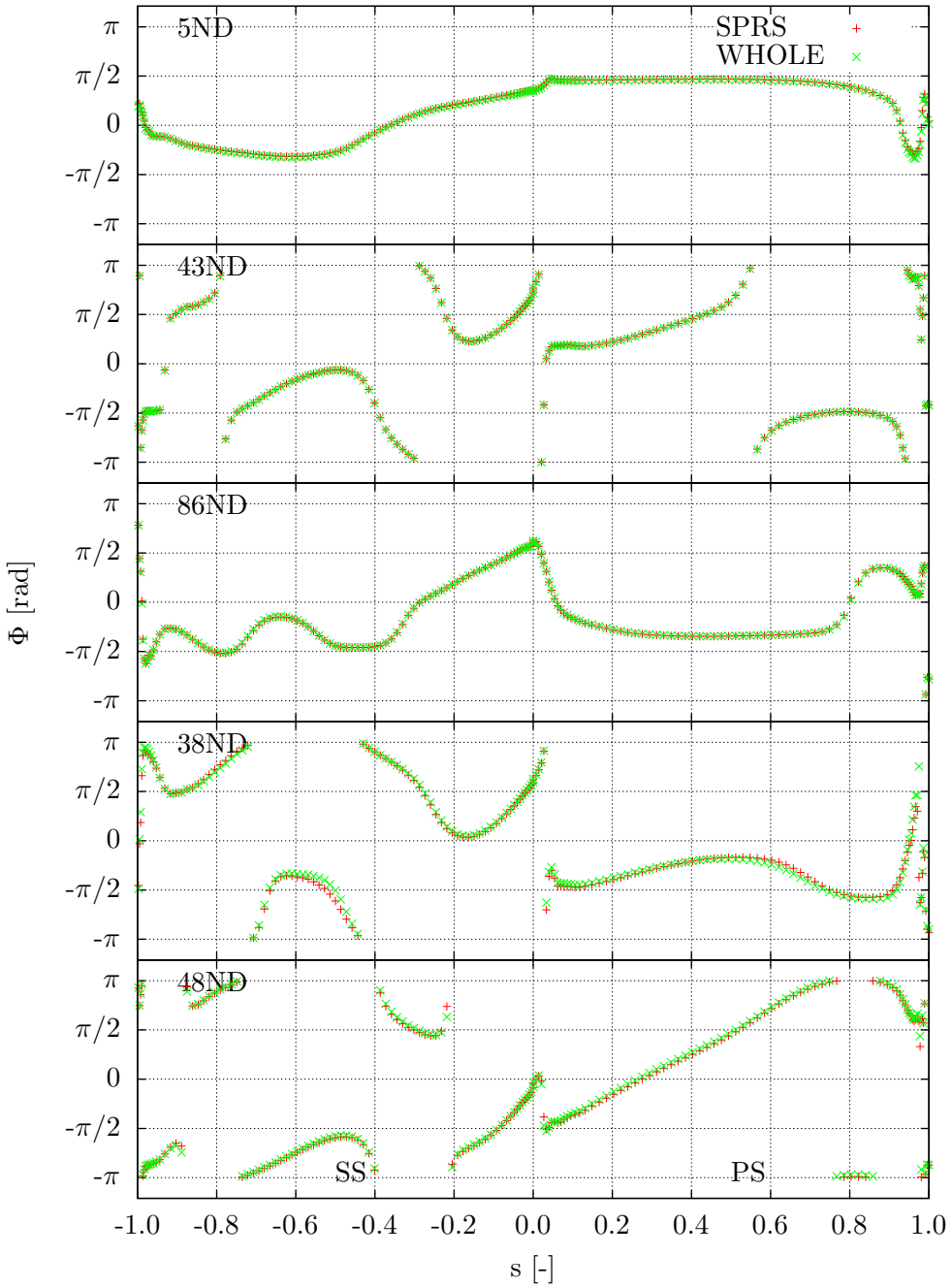


Figure 5.49.: Unsteady rotor surface pressure in subsonic flow: Phases (1/2)

	SPRS	FULL
Grid points	88K	1M
Number of CPUs	8	32
Total elapsed time [h]	112	416

Table 5.10.: Comparison of computational resources for thin-section turbine stage

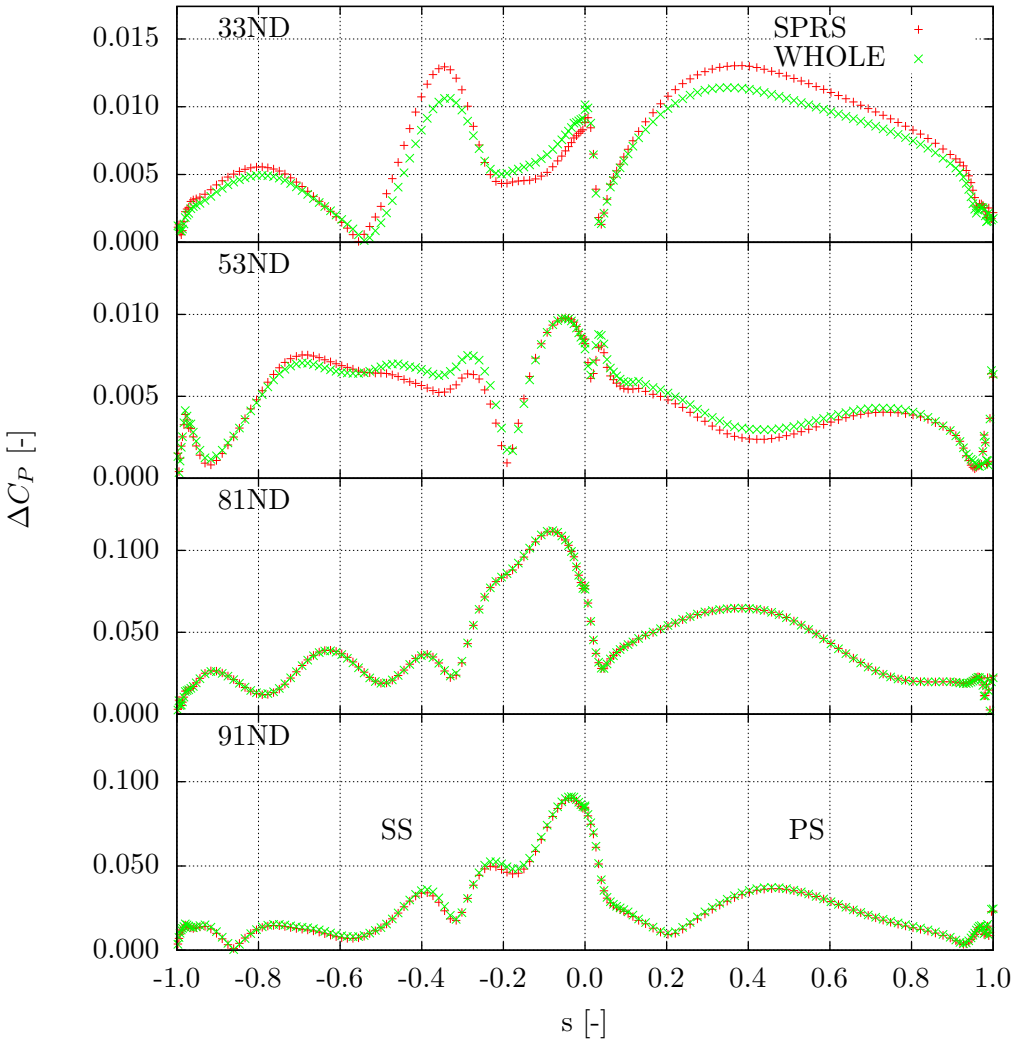


Figure 5.50.: Unsteady rotor surface pressure in subsonic flow: Amplitudes (2/2)

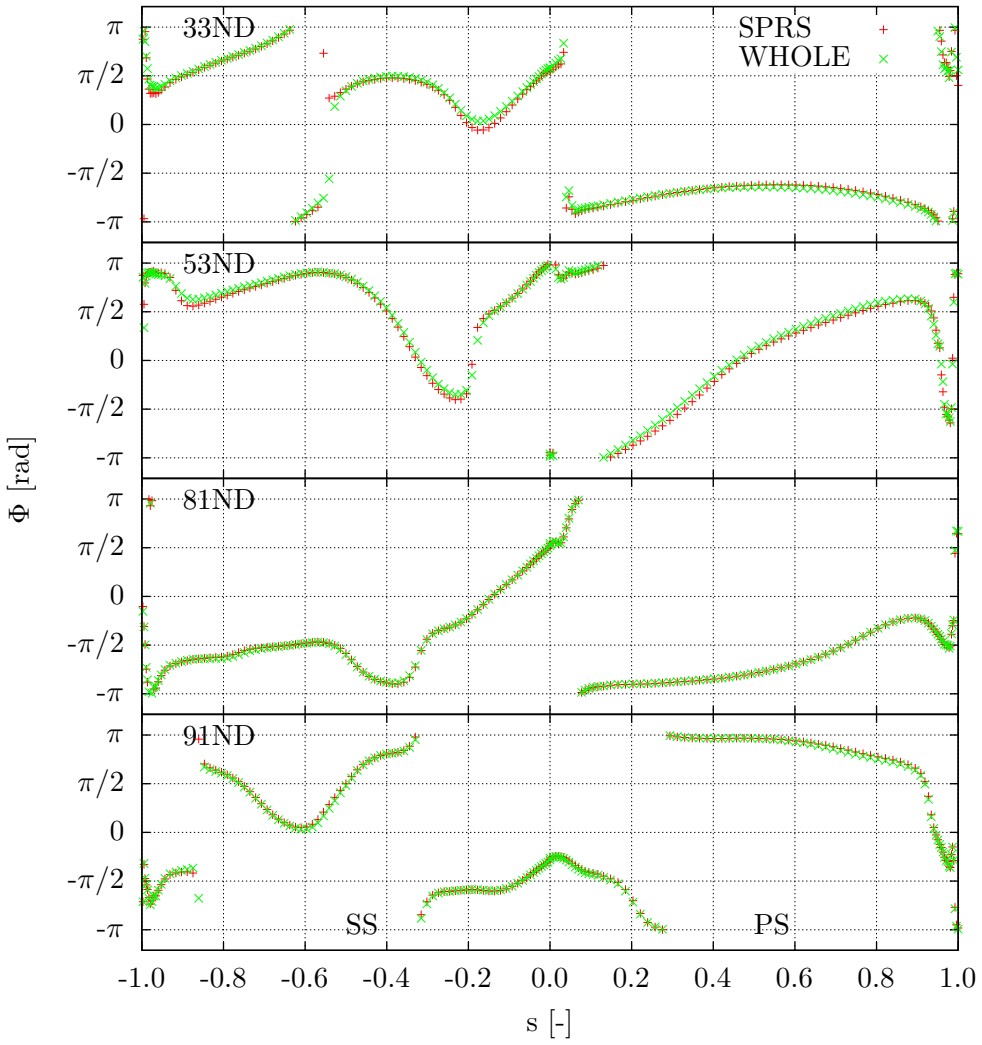


Figure 5.51.: Unsteady rotor surface pressure in subsonic flow: Phases (2/2)

P_{01}	132 kPa
T_{01}	311 K
P_{01}/P_{02}	3.00
RPM	6957
$M_{is,2}$	1.01

Table 5.11.: Transonic operating conditions

5.3.5. Transonic flow results

In order to validate the method for transonic flows, the same turbine stage is run at lower back pressure. The isentropic Mach number at stator exit flow is thus increased to 1.01. The operating conditions are listed in Table 5.11. The conditions are such that the flow is subsonic over most of the NGV with a small passage shock reaching from the suction side towards the trailing edge of the adjacent blade (see Figure 5.52). In the rotor, the flow is supersonic on the leading edge suction side and subsonic over the remaining blade. Since the passage shock is stationary in the stator frame of reference and does not cross the inter-row boundary, the accuracy of the sparse assembly solution should not be affected by its presence. In order to represent shock movement across a pitchwise or inter-row boundary the temporal Fourier approximation would require more harmonics to resolve the gradients across the shock.

5.3.5.1. Steady flow

Initially, the sparse assembly method is tested on the steady NGV-only configuration. The steady flow field can be reconstructed on the full circumference and a direct comparison of blade pressure profiles is thus possible.

Figure 5.53 compares the surface Mach numbers of the whole annulus solution at nominal, maximum and minimum throat area. Due to higher velocities after the throat, the rear loading has significantly increased compared to the subsonic case. The shock moves slightly upstream as the throat area increases. The sparse assembly method provides a very good approximation to the blade profiles as seen in Figure 5.54. There are no significant differences between the two solutions and the rise in pressure across the shock is well captured.

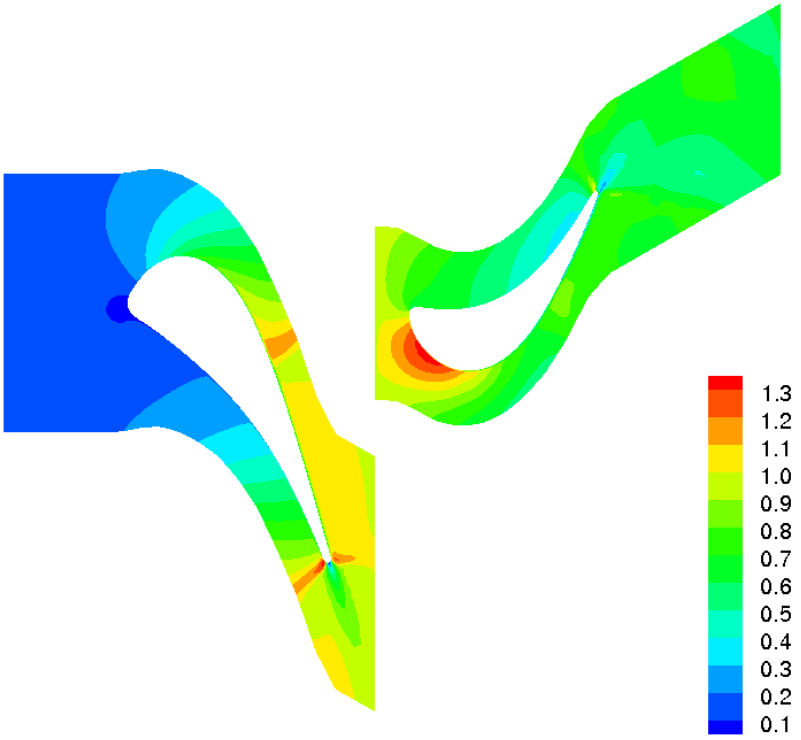


Figure 5.52.: Relative Mach number in steady state starting solution (transonic case)

5.3.5.2. Unsteady flow

Since the shocks do not cross the inter-row boundary, the unsteady analysis for the transonic case was performed using the same number of harmonics as in the subsonic case. A comparison of modal forces (Figure 5.55) shows a good agreement between the whole annulus and sparse assembly predictions. The difference in amplitude of the 5ND is less than 0.2% and the blade passing disturbance is predicted similarly well with differences less than 2%. Table 5.12 lists the amplitudes of the dominant perturbations. The relative magnitude of the blade passing harmonics has shifted from the subsonic case. In transonic flow the first blade passing frequency contributes the most to the rotor modal forces. Figure 5.55 indicates that there is a small phase lag between the two solutions which is particularly noticeable for the blade passing disturbances and measures 3° for the first blade passing harmonic.

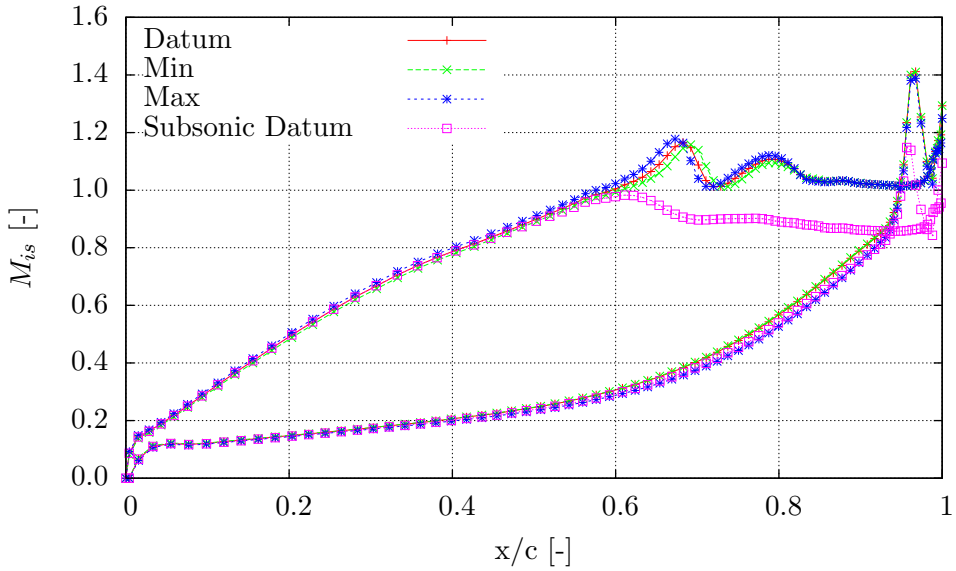


Figure 5.53.: Blade surface Mach number at nominal, minimum and maximum throat area

Since this corresponds to only a fraction of a time step, its origin is not further investigated.

A Fourier analysis of the unsteady rotor pressures (Figure 5.56 and 5.57) shows larger amplitudes for the blade passing frequencies than in the subsonic case. The leading edge amplitudes of the first and second harmonics have more than doubled. The unsteady forcing is largest in the leading edge region and all disturbances see a sudden drop in magnitude in the supersonic region on the suction side where the wave reflects. This feature is less pronounced for the 5ND wave which, similarly to the subsonic case, is cut-off up to mid-chord (as indicated by the near-zero slope on the phase plot in Figure 5.57) and then accelerates towards the trailing edge. In general, the amplitudes are more uniform on the pressure side where wave speeds are lower. For most of the blade surface, the reduced passage model predicts the same amplitude and local wave speeds as the whole annulus model (see Figure 5.57) and the main difference between the two solutions is a small and constant off-set in phase. The origin of the offset in phase in unknown. However, since it appears consistently across all frequencies and along the whole blade surface, it is likely to be caused by a small time lag between the two solutions. The time lag need not necessarily exist in the solver but may arise from post-processing and the repeated restarting of the full circumference solution. The Fourier analysis is based on blade

	$\Delta F/F_{ref}$ $[10^{-2}]$	
	Sparse assembly	Whole annulus
5ND	1.626	1.632
10ND	0.044	0.032
33ND	0.146	0.152
38ND	1.672	1.658
43ND	3.705	3.643
48ND	0.404	0.406
53ND	0.038	0.026
81ND	0.640	0.646
86ND	1.611	1.594
91ND	0.167	0.161

Table 5.12.: Modal force amplitudes of dominant frequencies in transonic flow non-dimensionalised by steady state force

surface pressures which were recorded every five time steps. An interruption of the calculation at time steps not divisible by 5 would hence lead to a small shift in the recorded pressure signal. Because simpler test cases did not exhibit this behaviour and it is not the absolute value but the slope of the phase angles which is of interest, this discrepancy was not investigated further.

There is a small difference in slope of the 43ND phase at the suction side trailing edge ($s \approx -0.7$), where the acceleration is overpredicted by the reduced passage model, but otherwise the sparse assembly predicts the same wave speeds as the whole annulus calculation.

5.3.6. Summary

The above analysis of the unsteady rotor-stator interaction in a turbine stage with throat area variation in the NGV illustrates that the time-domain Fourier method is capable of capturing a moderate sinusoidal throat area variation and multi-row coupling modes at the blade row interface. A comparison of the reduced-passage and whole annulus solutions showed a very good agreement in terms of unsteady forces on the rotor surface thereby validating the sparse assembly method for the prediction of high and low engine order excitations. There were no notable differences between subsonic and transonic flow conditions in terms of the performance of the reduced passage model.

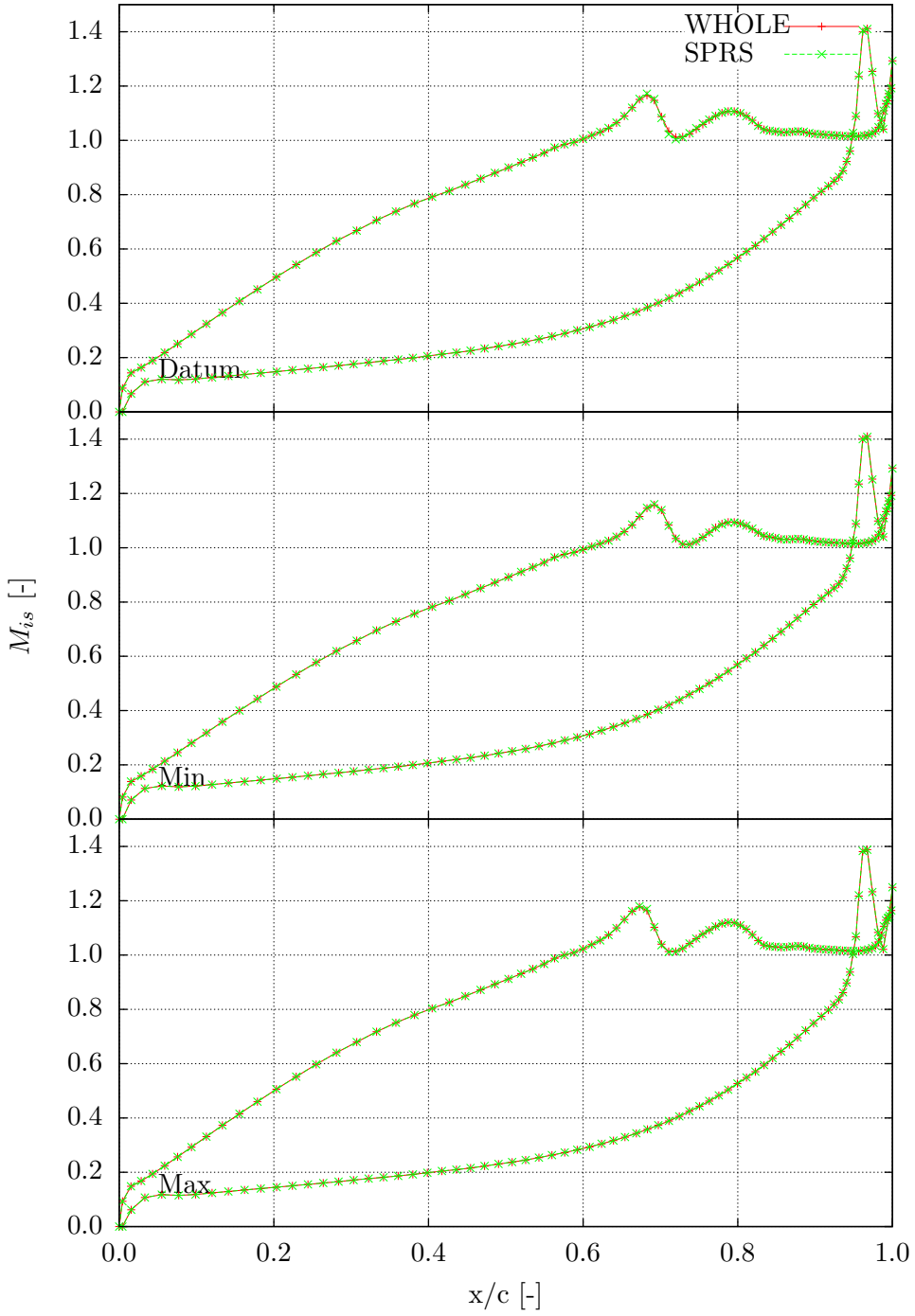


Figure 5.54.: Comparison of blade surface Mach number on whole annulus and sparse assembly domain in transonic flow

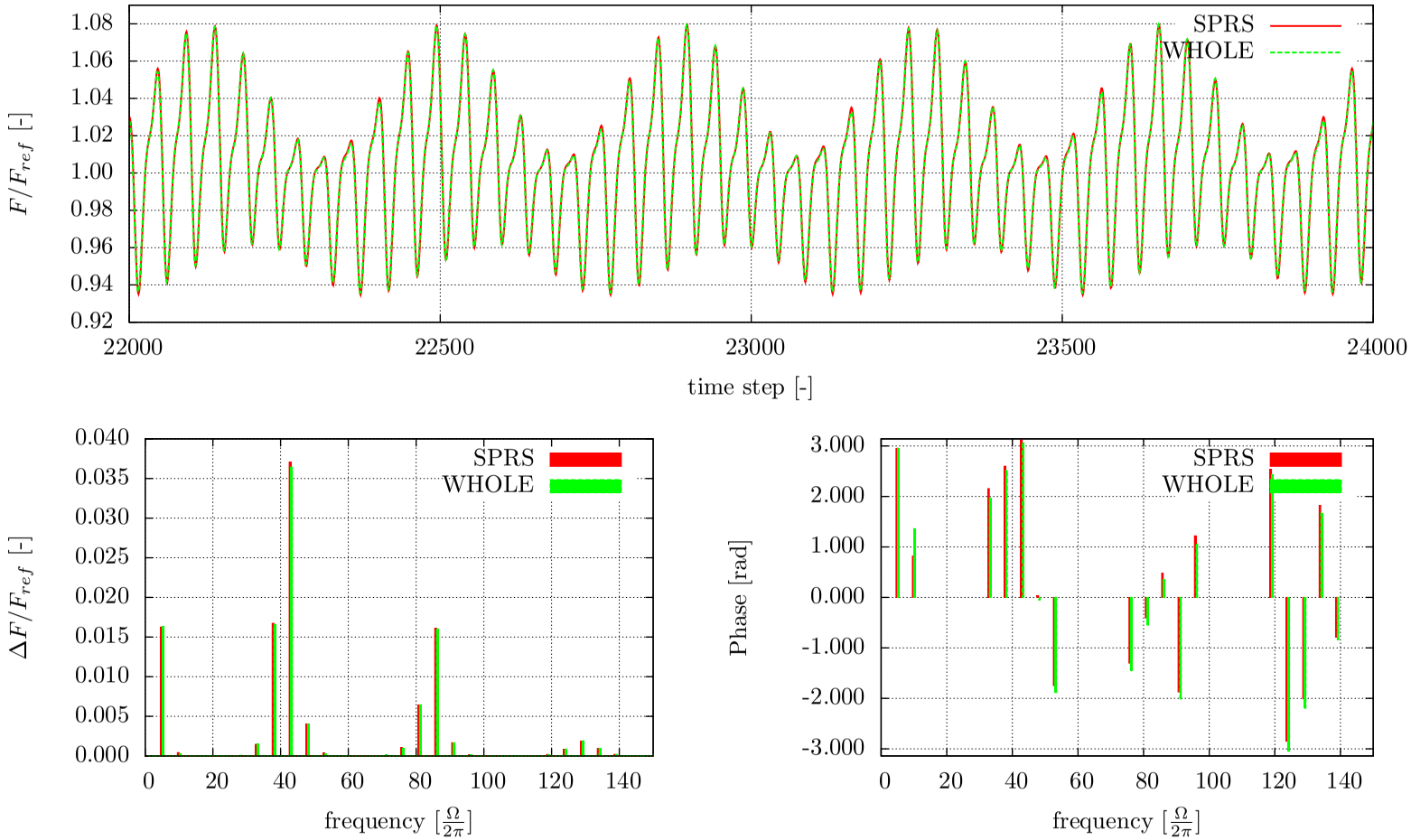


Figure 5.55.: Modal force in transonic flow

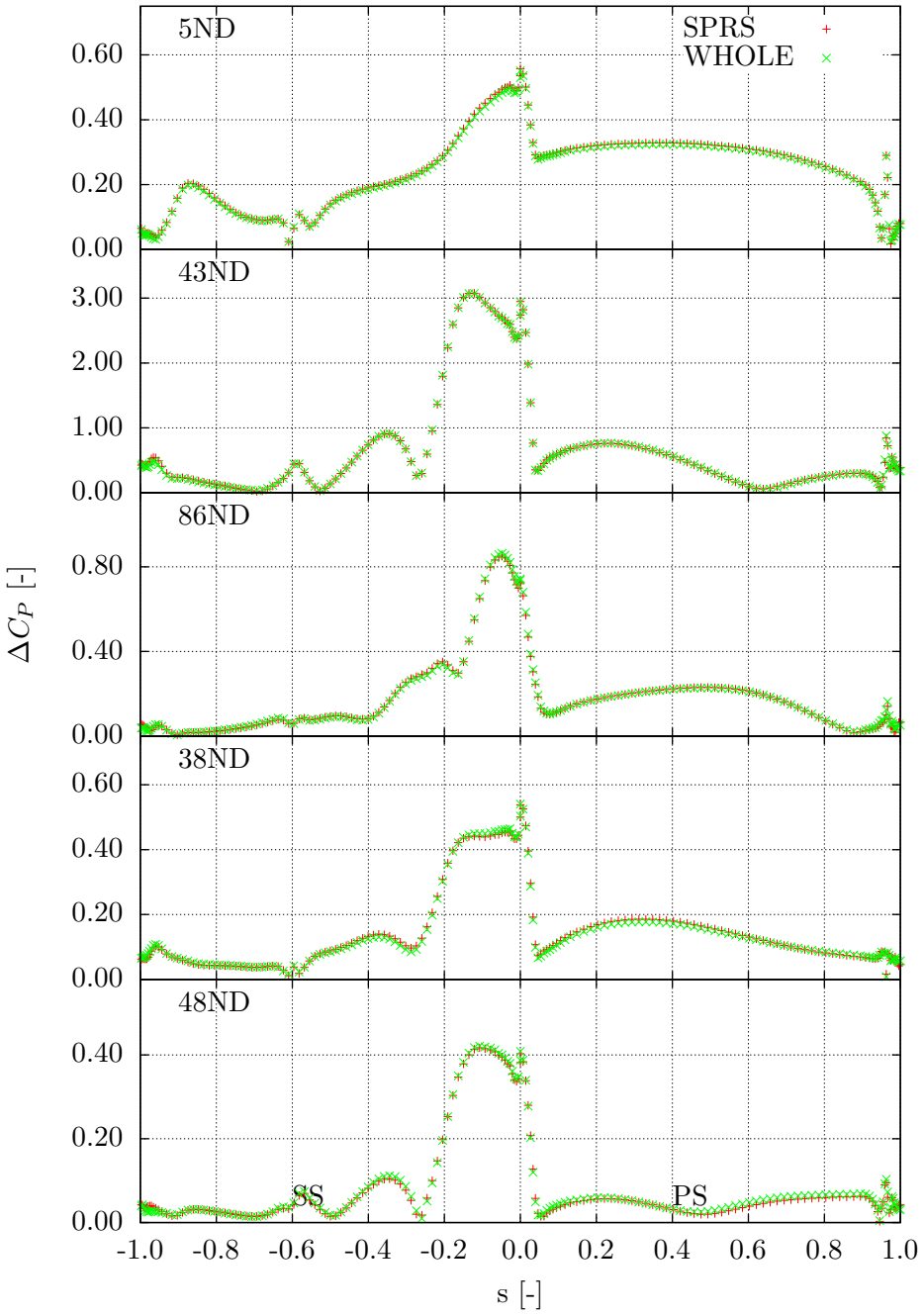


Figure 5.56.: Unsteady rotor surface pressure in transonic flow: Amplitudes

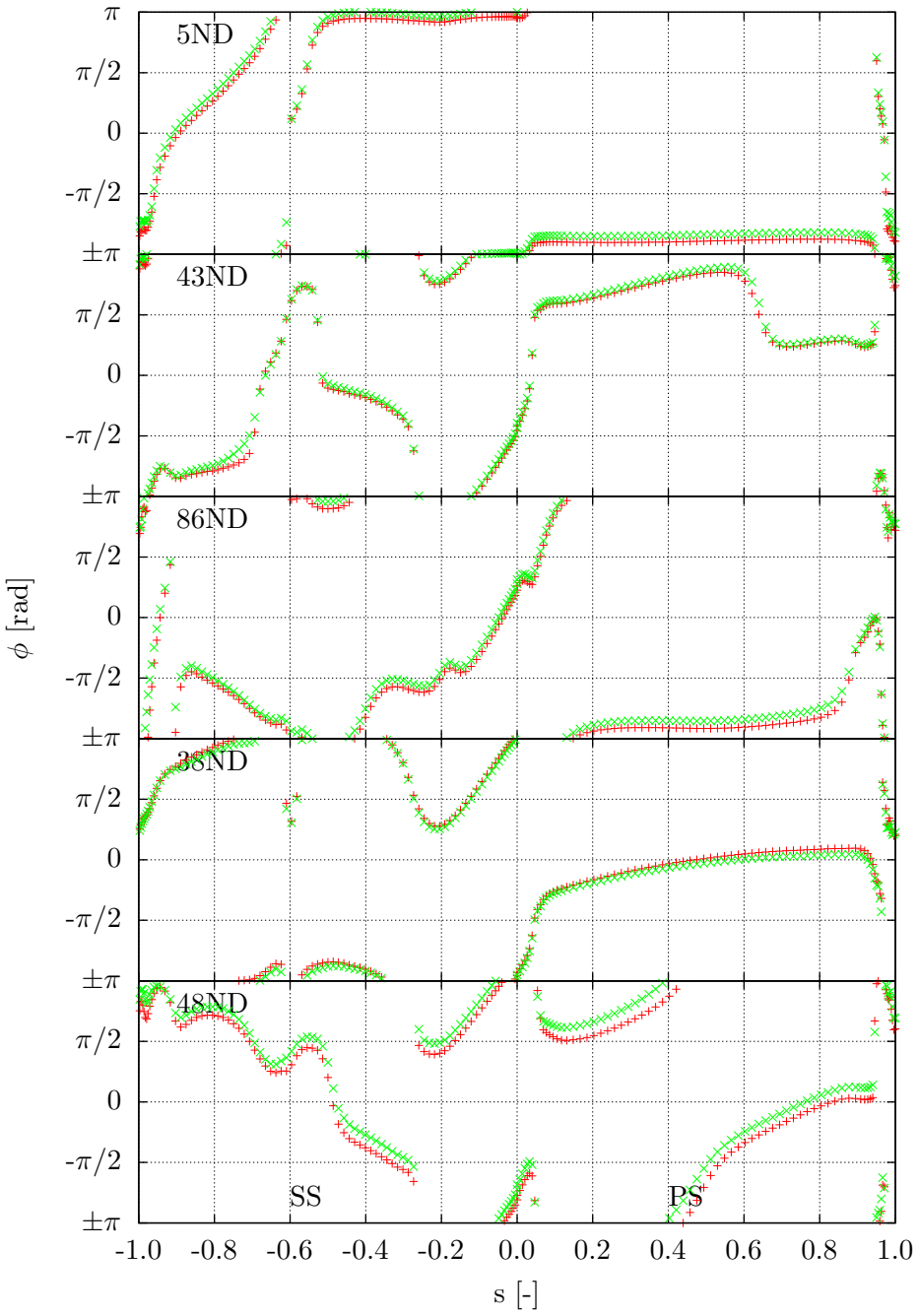


Figure 5.57.: Unsteady rotor surface pressure in transonic flow: Phases

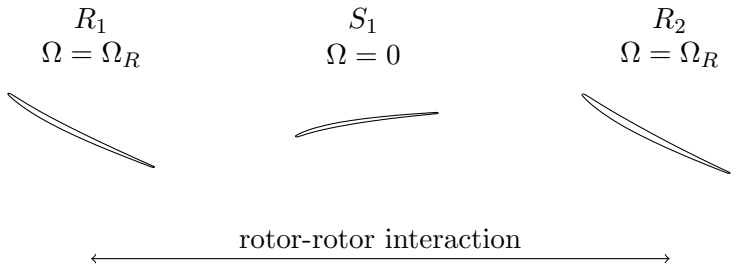


Figure 5.58.: 1.5 stage compressor test case

5.4. 1.5 stage compressor: rotor-rotor interaction

After the sparse assembly method was validated for steady and unsteady non-axisymmetric flows across two blade rows, this section investigates its ability to capture the interference of rows in the same frame of reference. [2]

5.4.1. Configuration

The test case models the mid-span section of a 1.5 stage compressor with blade counts N_{R1}, N_{S1} and N_{R2} as sketched in Figure 5.58. The circumferential wave number of the non-uniformity resulting from rotor-rotor interference is hence $N_{aliased} = N_{R1} - N_{R2}$. The interaction is modelled on seven passages per row which are distributed over the fundamental wave length of the aliased disturbance. The embedded stator contains no stationary circumferential perturbation and a single passage is sufficient. Figure 5.59 shows the computational domain for the reduced passage model where the blade rows and sliding planes have been shifted for illustrational purposes. Seven passages in the rotor domain allow a third order Fourier approximation of the rotor-rotor interaction. The number of passages was increased to seven after initial tests with five passages did not converge. In order to capture the rotor-rotor interference, the mesh was refined in the wake region of the first rotor and the grid in the downstream stator and rotor was adapted to match the refined wake region in the first rotor.

The compressor is run at subsonic operating conditions with isentropic exit Mach number 0.45. Table 5.13 lists the operating conditions. The three-row calculation is started from a converged mixing plane solution.

[2] Some of the material in this section was presented at the 10^{th} European Conference on Turbomachinery [103].



Figure 5.59.: Computational domain for third order approximation of rotor-rotor interference

Flow coefficient	0.51
Load coefficient	0.52
Exit Mach number	0.45

Table 5.13.: 1.5 stage compressor operating conditions

5.4.2. Frequency content

As in the previous test case, the theory of spinning modes described in Section 4.2.1 is used to identify the independent frequencies required to capture all blade row interference effects. The first 15 coupling modes for a three-row compressor with blade counts N_{R1}, N_{S1} and N_{R2} are listed in Table 5.14. The highlighted modes satisfy $\omega = \Omega k$ and appear as travelling waves in the stator or rotor reference frame. They need to be explicitly specified in the temporal Fourier approximation. The unsteadiness is approximated from three harmonics per rotor/stator blade passing and the first 15 rotor-rotor interaction modes ($n_{R1} = -2, -1, 0, 1, 2$ and $n_{R3} = -2, -1, 0, 1, 2$) (see Table 5.15). Note that modes $(n_{R1}, 0, n_{R3})$ and $(-n_{R1}, 0, -n_{R3})$ are complex conjugates and appear as the same disturbance in the stator.

Mode	N_{R1}	N_{S1}	N_{R2}	k	ω_S	ω_R
1	0	0	0	0	0	0
2	0	0	1	N_{R2}	$N_{R2}\Omega_R$	0
3	0	1	0	N_{S1}	0	$-N_{S1}\Omega_R$
4	0	1	1	$N_{S1}+N_{R2}$	$N_{R2}\Omega_R$	$-N_{S1}\Omega_R$
5	0	-1	1	$N_{R2}-N_{S1}$	$N_{R2}\Omega_R$	$N_{S1}\Omega_R$
6	1	0	0	N_{R1}	$N_{R1}\Omega_R$	0
7	1	0	1	$N_{R1}+N_{R2}$	$(N_{R1}+N_{R2})\Omega_R$	0
8	1	1	0	$N_{R1}+N_{S1}$	$N_{R1}\Omega_R$	$-N_{S1}\Omega_R$
9	1	1	1	$N_{R1}+N_{S1}+N_{R2}$	$(N_{R1}+N_{R2})\Omega_R$	$-N_{S1}\Omega_R$
10	1	-1	1	$N_{R1}-N_{S1}+N_{R2}$	$N_{R2}\Omega_R$	$N_{S1}\Omega_R$
11	-1	0	0	$-N_{R1}$	$-N_{R1}\Omega_R$	0
12	-1	0	1	$-N_{R1}+N_{R2}$	$(-N_{R1}+N_{R2})\Omega_R$	0
13	-1	1	0	$-N_{R1}+N_{S1}$	$-N_{R1}\Omega_R$	$-N_{S1}\Omega_R$
14	-1	1	1	$-N_{R1}+N_{S1}+N_{R2}$	$(-N_{R1}+N_{R2})\Omega_R$	$-N_{S1}\Omega_R$
15	-1	-1	1	$-N_{R1}-N_{S1}+N_{R2}$	$(-N_{R1}+N_{R2})\Omega_R$	$N_{S1}\Omega_R$

Table 5.14.: First 15 spinning modes for three row-compressor (*grey = travelling waves in stator frame of reference, blue = travelling waves in rotor frame of reference*)

	Stator	**Rotor**
Blade passing	$N_{R1}\Omega$, $N_{R2}\Omega$	$N_{S1}\Omega$
Rotor-rotor interference	$(n_{R1}N_{R1} \pm n_{R2}N_{R2})\Omega$ for $n_{R1}=0,1,2$ and $n_{R2}=0,1,2$	0

Table 5.15.: Frequency spectra in compressor rows

5.4.3. Results

We aim to validate the reduced passage model by comparing the unsteady and time-averaged rotor blade pressures to those predicted on the whole 360° domain. For this purpose, unsteady pressure histories on all sparse assembly blades are collected and post-processed. Post-processing transforms the histories in space and time and allows a reconstruction of instantaneous and time-averaged pressure profiles at arbitrary circumferential positions. Figures 5.60 to 5.62 compare time-averaged and unsteady pressures for the fundamental blade passing frequencies at the first blade ($\theta = 0$) of each row.

It can be seen that the effect of the stator blade passing is stronger in the downstream direction than in the upstream direction. In the first rotor, the wave from the stator blade passing impinges on the pressure side trailing edge where it becomes reflected as indicated by the amplitude peak and change in slope on the phase plots in Figure 5.60. A pressure wave of the same frequency then travels along the pressure side with decreasing amplitude towards the leading edge. The wave completes approximately 1.5 cycles along the pressure surface. On the suction side, the wave travels along the suction side at approximately constant speed towards the point of peak suction where it becomes cut-off. The amplitude of the stator disturbance is small along most of the suction side surface. In the second rotor (Figure 5.61), the disturbance impinges on the leading edge and the unsteady effects are similar on both sides. The phase completes approximately 1.5 cycles on both surfaces with variations in amplitude as the wave reflects. The amplitude in the leading edge region of the second rotor is approximately three times larger than that in the trailing edge region of the first rotor.

Figure 5.62 shows the amplitude and phase of the unsteady pressure on the stator due to the fundamental rotor passing disturbances. The effect of the upstream rotor is stronger than that of the downstream rotor. Both amplitudes peak in the leading edge region. The wave from the downstream rotor impinges the stator near the trailing edge and then travels at approximately constant speed along the stator surface. Due to the comparatively large wave length the unsteadiness has a similar amplitude on the suction and pressure side. The disturbance from the upstream rotor impinges on the leading edge and is repeatedly reflected as it travels downstream on the pressure side. On the suction side, reflections occur only at the leading and trailing edge and the wave velocity does not vary much over the

rest of the blade. The amplitude of the rotor-rotor interaction (wave number $k = N_{R1} - N_{R2}$) on the stator surface is significantly smaller than that of the individual blade passing disturbances. Due to its large wave length the wave only completes approximately $1/8^{th}$ of a cycle on both suction and pressure side.

The sparse assembly method captures all main features described above although small differences between the sparse assembly and whole annulus solution are visible in amplitude and phase - particularly in the stator surface pressure (Figure 5.62). While the phases of the second rotor disturbance match perfectly, the phase of the first rotor blade passing and rotor-rotor interaction is offset by a constant amount. However, the slope of the phase plots match very well between the two solutions. This demonstrates that the sparse assembly method correctly models the propagational velocity of the disturbances.

The amplitudes of the rotor passing disturbances are predicted very well in the stator domain but the sparse assembly slightly underpredicts the amplitude of the R1-R2 passing disturbance. This disturbance is an order of magnitude smaller than the fundamental ones. The observation that large amplitude perturbations are better approximated than weaker perturbations was already made in the turbine test case in Section 5.3.3.3. Two (related) possible explanations exist for this behaviour; differences of the order of 0.01% total inlet pressure exist in all frequencies but are only noticeable in perturbation of a similar magnitude or the Fourier approximation is polluted as weaker perturbations are more susceptible to influences from other disturbances.

For the compressor test case, slow convergence of the rotor-rotor interference frequency may also be responsible for the discrepancies in amplitude. Convergence was assessed by comparing pressure forces on the blades over consecutive cycles. Since force is an integrated quantity, it is possible that the solution appears converged despite certain frequencies not having reached a periodic state.

The unsteady pressures were integrated and the corresponding forces on the blade for a dummy mode shape (0,-z,y) were calculated. Figure 5.63 to 5.67 compare the forces after approximately two revolutions. The sparse assembly method approximates the unsteady forcing in the stator domain due to the upstream and downstream rotor well. A Fourier analysis (Figure 5.66) shows that the two blade passing frequencies and their linear combination are captured. The signal on the rotor blades contains only the stator blade passing frequency. The amplitude of the forcing on the upstream rotor (Figures 5.63 and 5.64) is very well approximated but

the average loading is offset by approximately 0.04%. The Fourier spectrum of the sparse assembly solution contains noise in the lower frequencies. This is an indication of a not fully converged solution and might be the reason for the discrepancies in average of the two solutions. The downstream interaction is predicted accurately and the forces in the second rotor blade match well in average loading and unsteady amplitude.

Figure 5.69 and Figure 5.70 compare the blade-to-blade variation of blade surface pressures at 5%, 50% and 95% chord as predicted by the whole annulus and the sparse assembly model. The effect of the downstream rotor on the upstream rotor is most noticeable in the pressure side leading edge region where the maximum blade-to-blade variation reaches approximately 0.2% of the passage-averaged value. In the downstream direction, rotor-rotor interaction is stronger and more localised with a maximum variation of approximately 0.8% in the pressure side leading edge region. Despite the relatively small blade-to-blade variations the reduced passage model reproduces the interaction pattern. In the downstream direction both amplitude and shape of the blade-to-blade variation are in good agreement. Differences between the two solutions are less than 2% of the maximum blade-to-blade variation in R2. The sparse assembly method also captures interaction in the upstream direction but differences between the two solutions are more noticeable and locally reach up to 10% of the blade-to-blade variation.

5.4.4. Grid size and convergence

The sparse assembly domain is approximately 10 times smaller than the full circumference. Table 5.16 compares the computational effort required for the two models. Both simulations were run on the Imperial College High Performance Computing cluster with Nehalem CPUs running at 2.93GHz, 8 cores per node with 24GBytes of fast memory. As before, total elapsed time is defined as the number of elapsed wall clock hours to convergence multiplied by the number of CPUs. The reduction in total elapsed time does not scale directly with grid size due to the additional calculation of Fourier components and increased time to convergence. The reduced passage model takes just over two revolutions to reach a periodic state, while the full circumference model produces a converged solution after the first revolution. Nevertheless, the sparse assembly method reduced the total elapsed time by a factor of 4.

Figure 5.71 compare the evolution of modal forces on the nominal blade in each

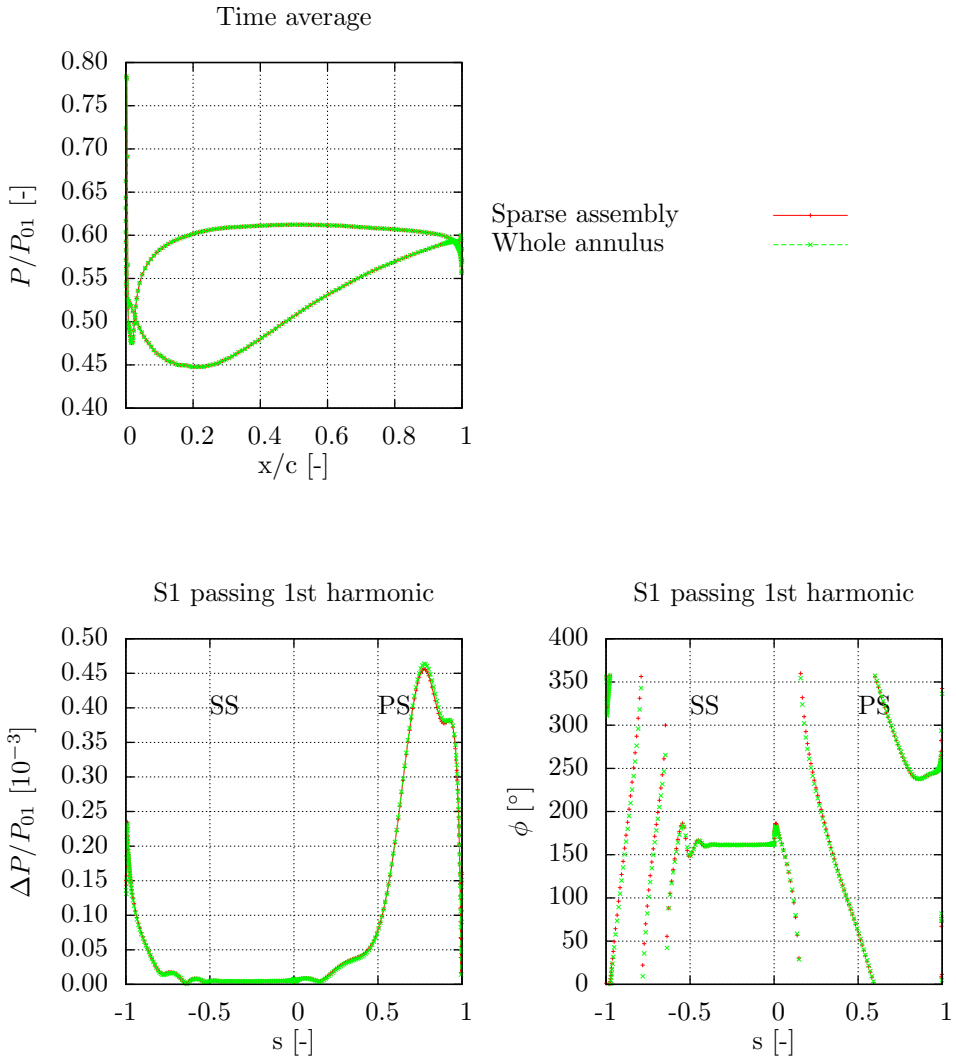


Figure 5.60.: Unsteady surface pressures on first rotor

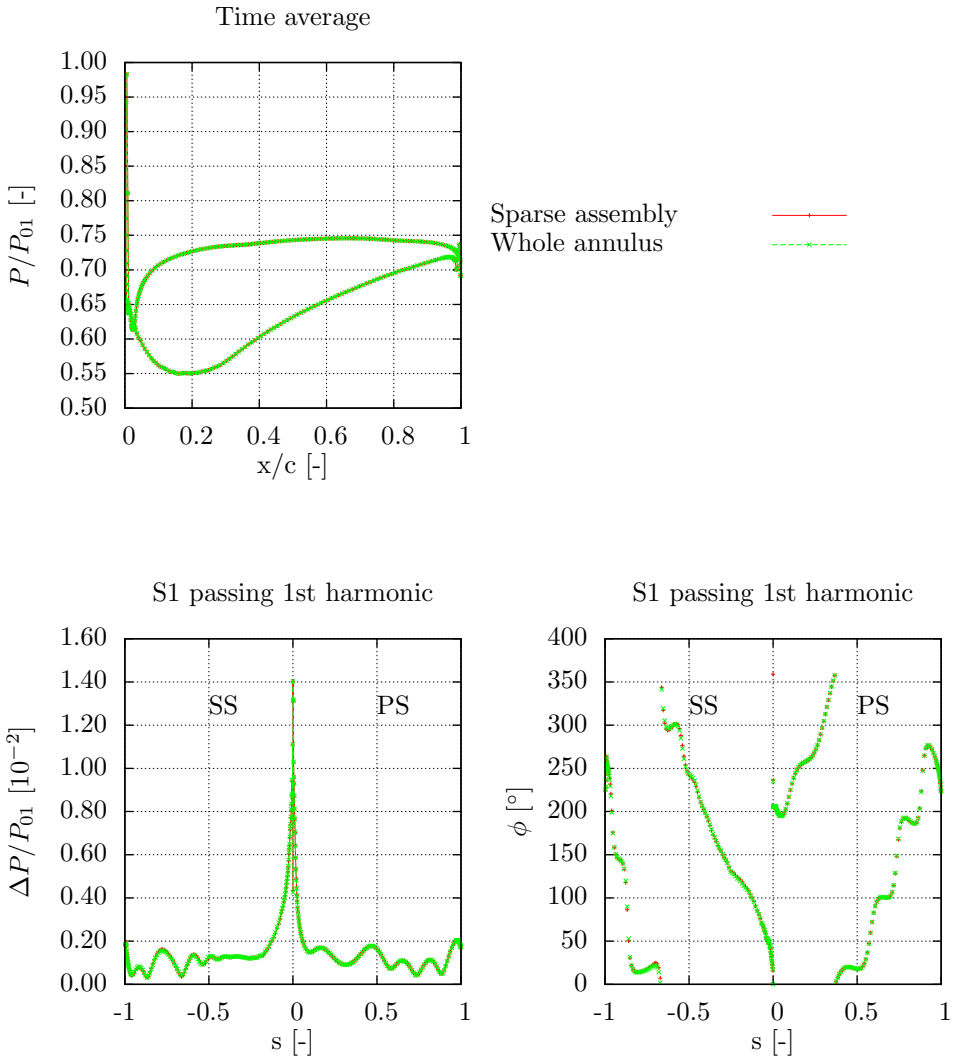


Figure 5.61.: Unsteady surface pressures on second rotor

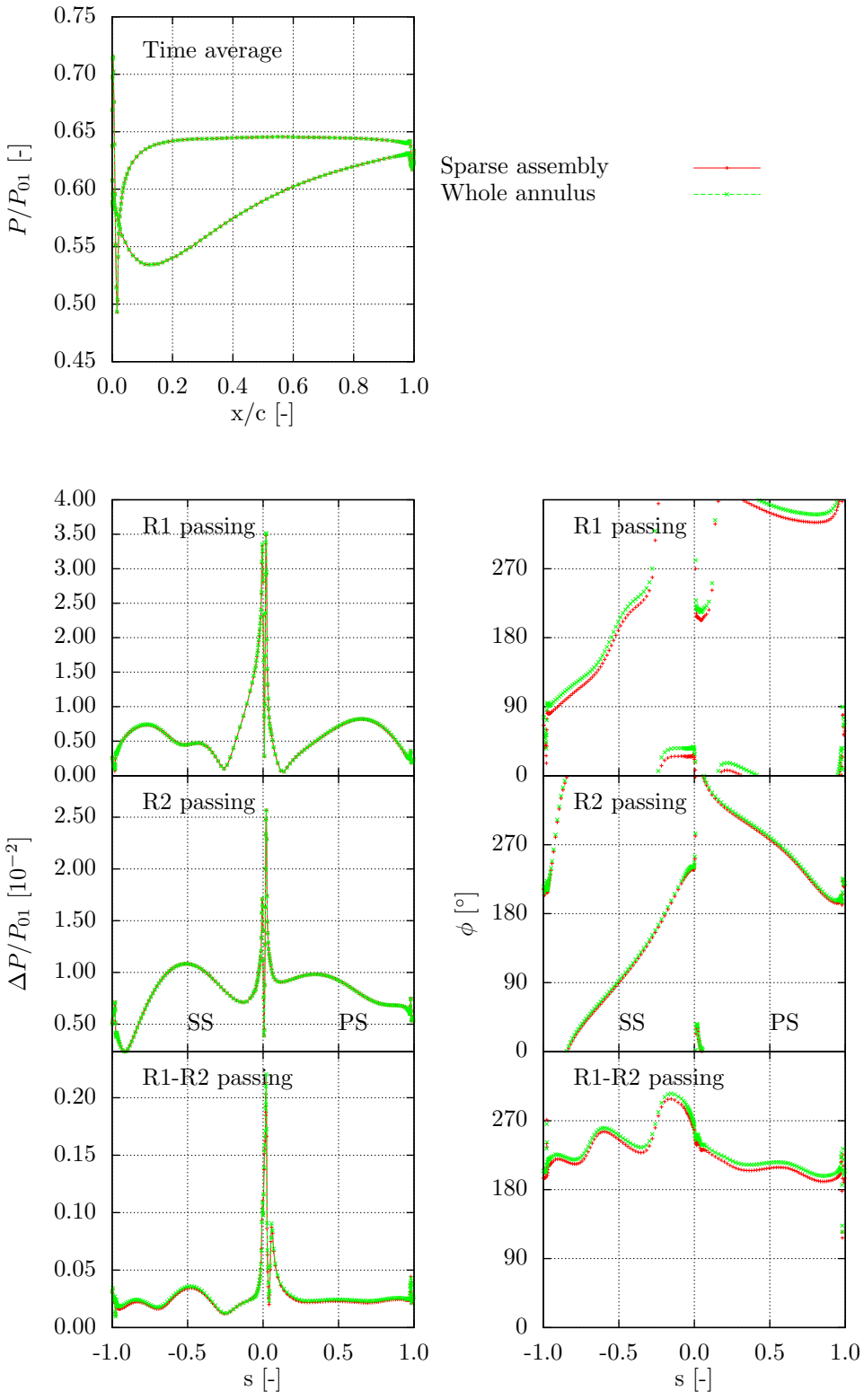


Figure 5.62.: Unsteady surface pressures on embedded stator

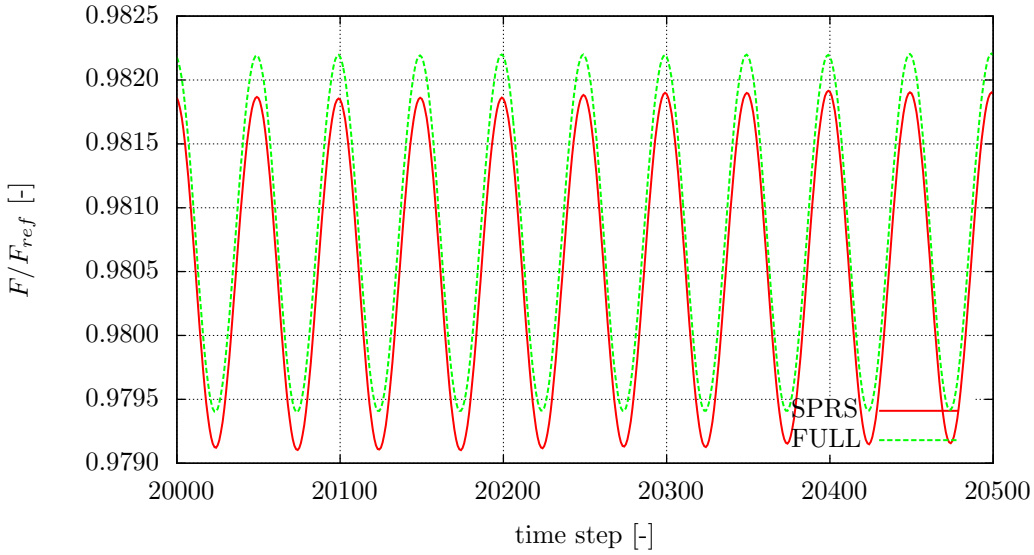


Figure 5.63.: Modal force history on first rotor

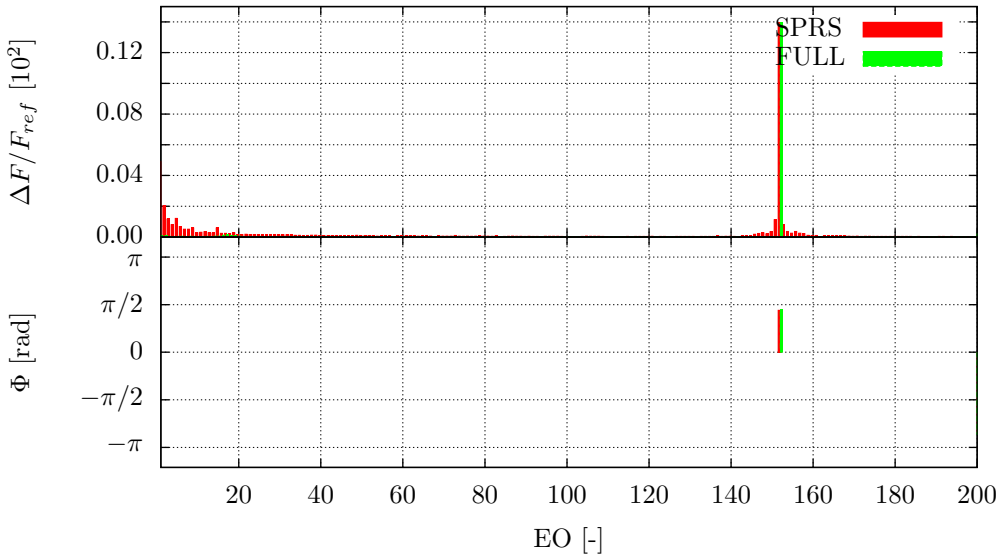


Figure 5.64.: Modal force amplitudes and phases on first rotor

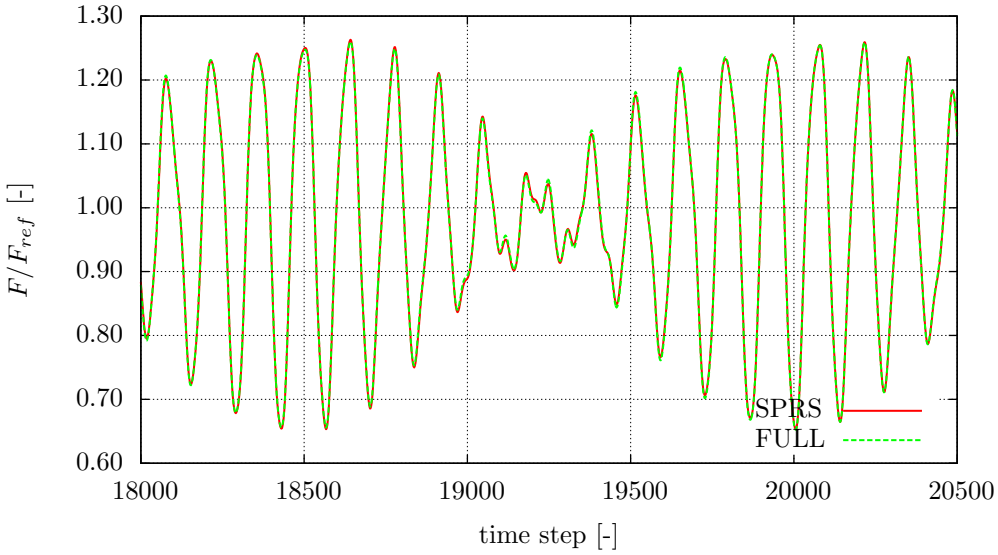


Figure 5.65.: Modal force history on embedded stator

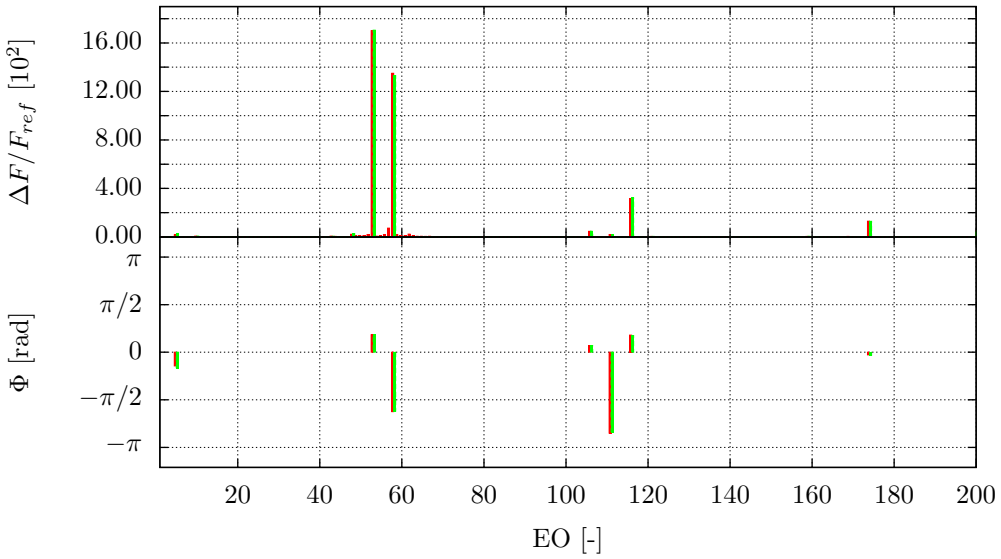


Figure 5.66.: Modal force amplitudes and phases on embedded stator

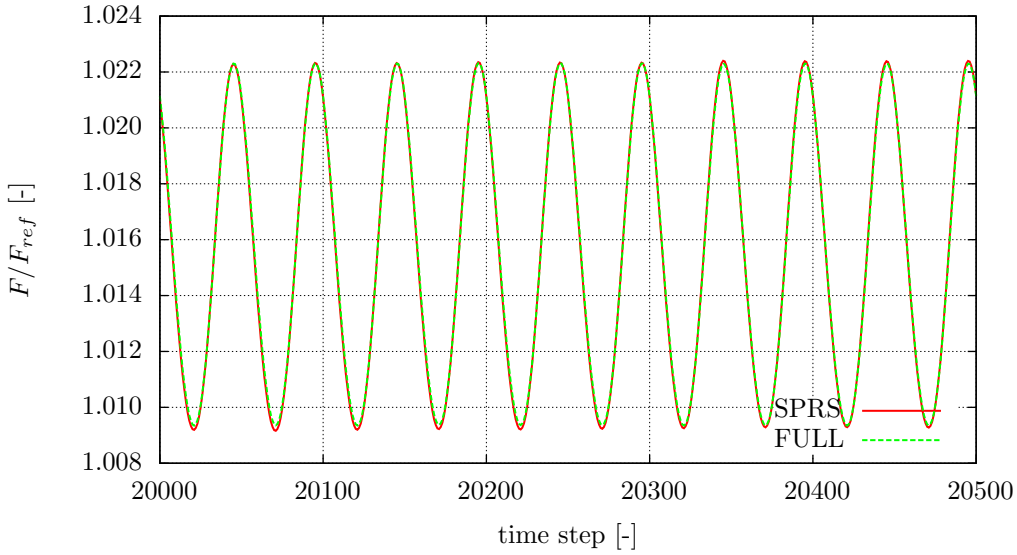


Figure 5.67.: Modal force history on second rotor

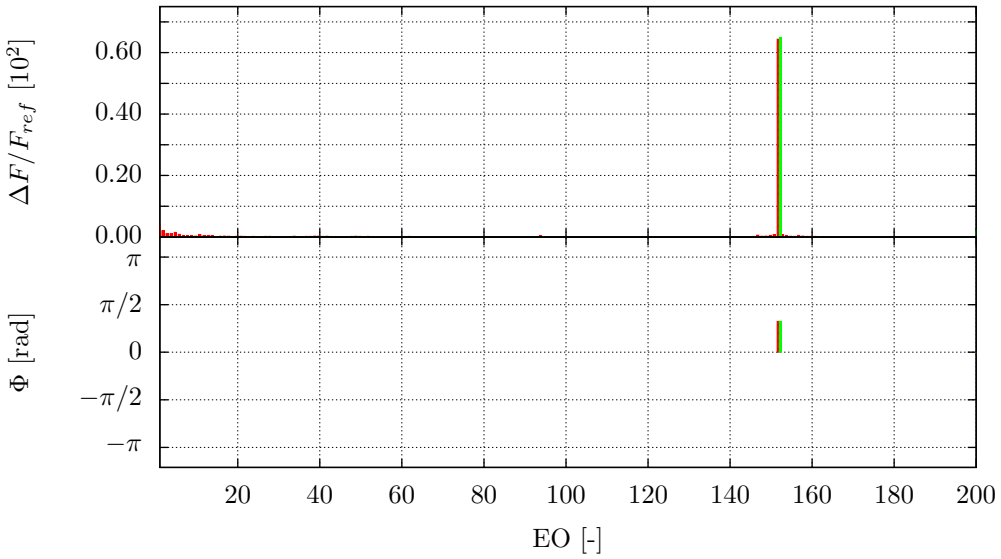


Figure 5.68.: Modal force amplitudes and phases on second rotor

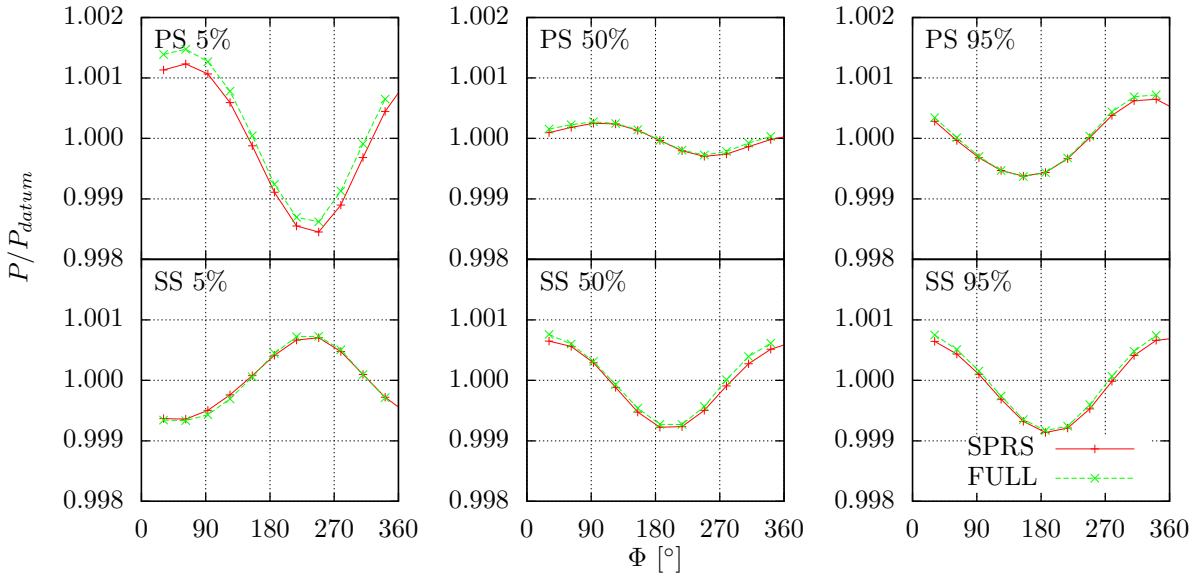


Figure 5.69.: Time-averaged pressure variation on first rotor

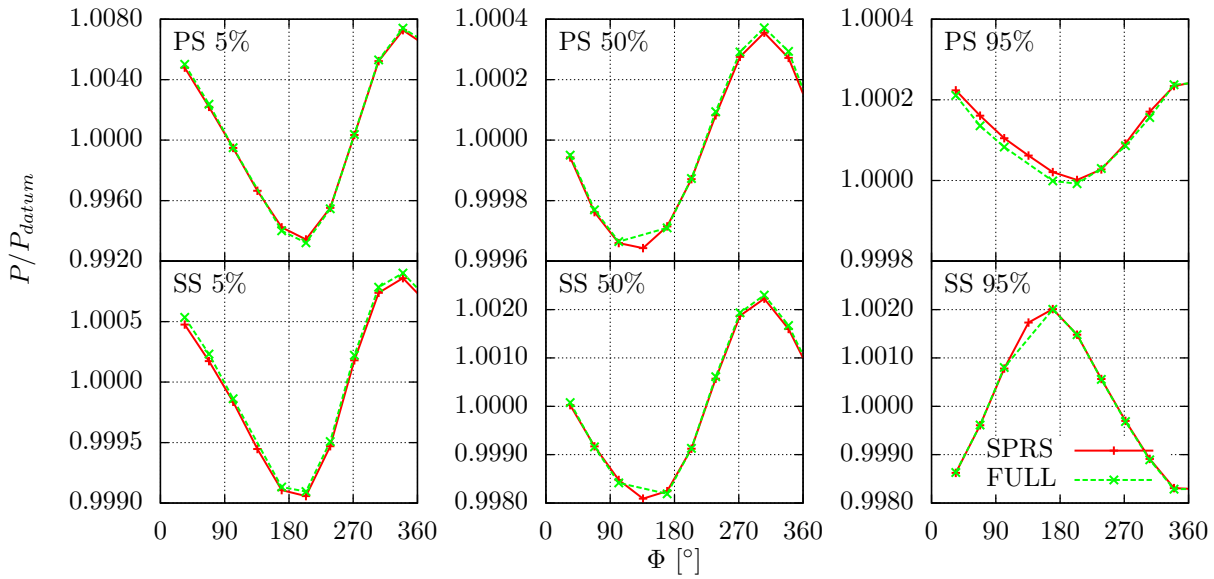


Figure 5.70.: Time-averaged pressure variation on second rotor

	SPRS	FULL
Grid points	300K	4M
CPUs	8	64
Total elapsed time [h]	370	1500

Table 5.16.: Comparison of computational resources required for 1.5 stage compressor

row over three revolutions. For clarity, only one time step per stator blade passing is shown in the rotor modal force histories and ten time steps per rotor-rotor-beat disturbance are shown in the stator history. The unsteady forcing on the embedded stator appears to converge faster than the forcing on the rotor blades which is affected by rotor-rotor interaction. This is to be expected, since disturbances have to propagate through the embedded stator blade before rotor-rotor interference can develop. The gradual correction of disturbances at blade row interfaces and boundaries slows down the propagation. The embedded stator, however, is exposed to the blade passing disturbances from the beginning, since the disturbance originates from the time-average in in the adjacent rotors. Convergence and the prediction of average pressure in R1 could possibly be improved by a non-reflecting treatment at the interface boundaries to prevent the occurrence of spurious reflections during start-up.

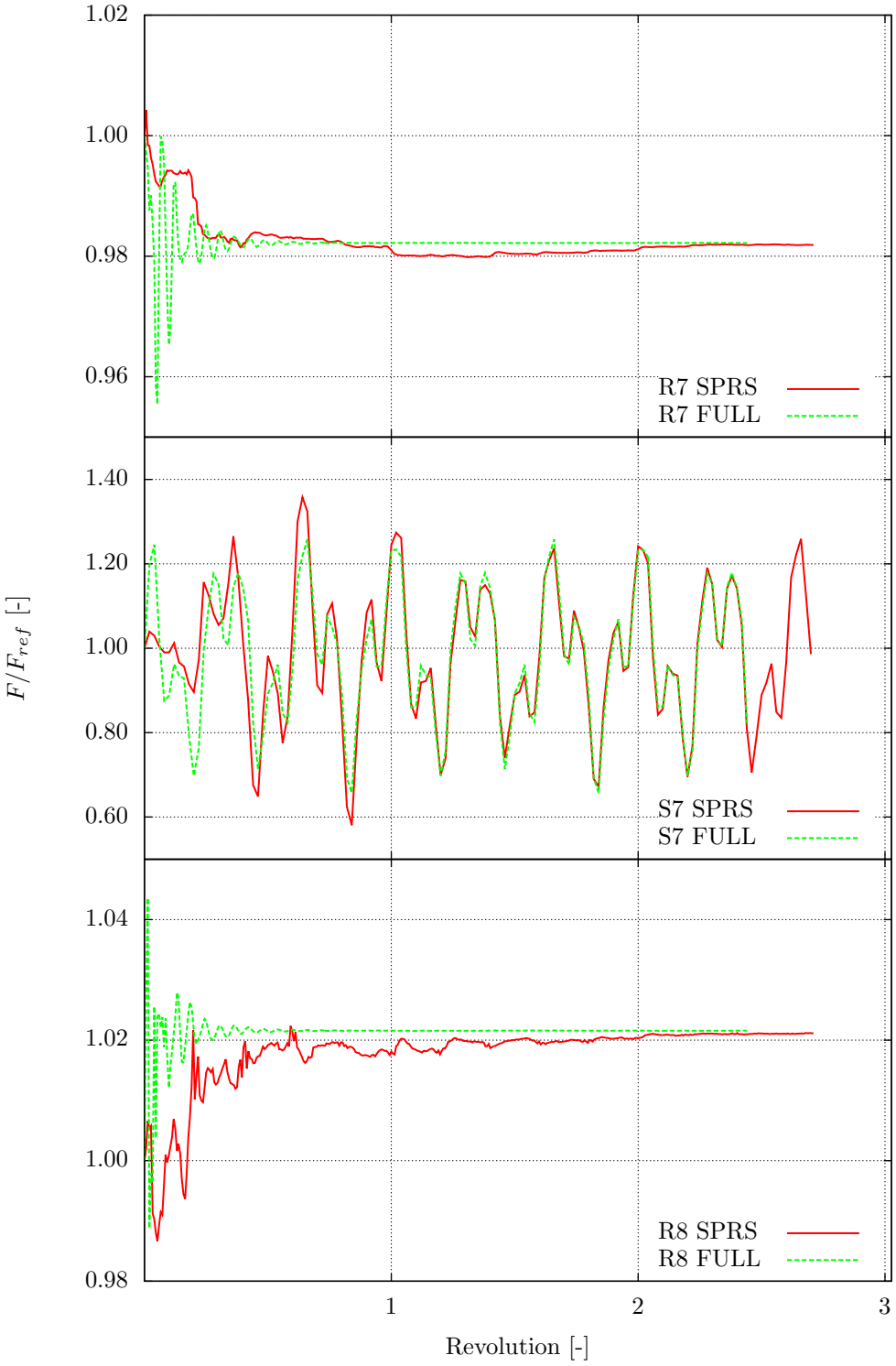


Figure 5.71.: Modal force comparison between whole annulus and sparse assembly solution

6. Applications

6.1. Full span study of rotor-stator interaction in a turbine with throat area variation in the stator

This section summarises the results of a full span study of the aerodynamically mistuned high pressure turbine of Section 5.3. The full span model may provide useful insights into the behaviour of the reduced passage model for three dimensional flows. Furthermore, it provides an opportunity for a detailed steady (NGV only) and unsteady analysis of rotor-stator interaction in a realistic configuration. As in the previous cases, the sparse assembly method is validated by comparison to the whole annulus solution. The steady results are also compared to experimental measurements taken at DLR [86].

6.1.1. Configuration

The turbine stage contains 44 NGVs and 64 rotor blades. The stator geometry parameters are summarised in Table 6.1. The stator row is designed with a sinusoidal throat area variation with maximum 4% deviation from the nominal blade. Rig measurements provided the corresponding change in pitch which is matched in the full circumference computational model. The sparse assembly model contains five passages distributed over 72° for a second order Fourier approximation of the 5ND throat area variation. The passage grids are topologically equivalent and each blade is shifted to follow the rig blade spacing pattern. Points in the vicinity of the periodic boundaries, which are used for the Fourier approximation of the boundary conditions and the corresponding points in the whole annulus domain, remain in their original position.

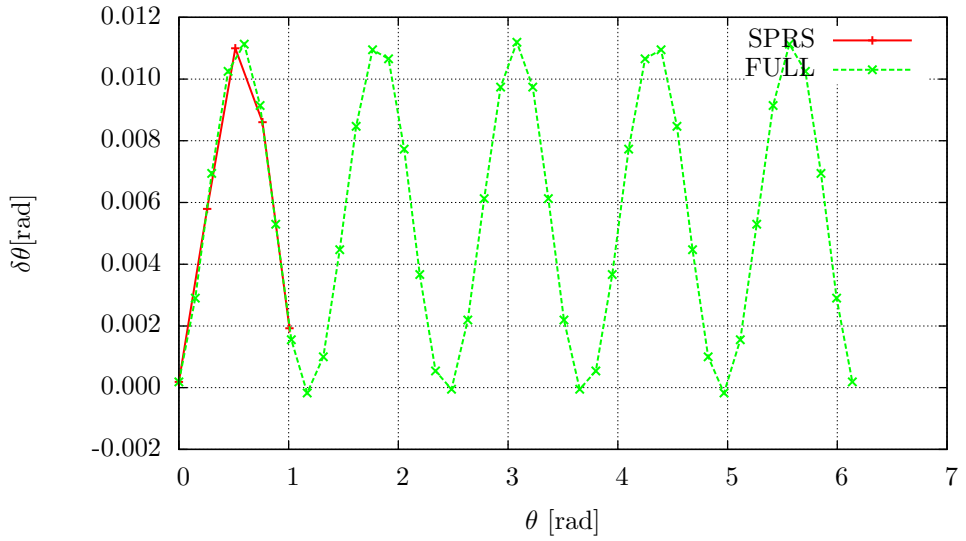


Figure 6.1.: Mesh movement

Chord	49.92 mm
Axial chord	29.86 mm
Tip radius	274.00 mm
Hub radius	238.84 mm
Stagger angle	51.90°

Table 6.1.: Stator geometry parameters

The maximum pitch according to design specifications is at Passage 29: $\Phi_{29} = 1.0276\Phi_{Datum}$. This corresponds to the following distribution:

$$\delta\Phi = 1.0283\sin(5\theta)$$

which can be achieved by moving the blades according to

$$\delta\theta = -5.66e^{-3}\cos(5\theta - 0.07306)$$

The shift in tangential position of the whole annulus and sparse assembly blades is indicated in Figure 6.1. Figure 6.2 shows the resulting pitch variation.

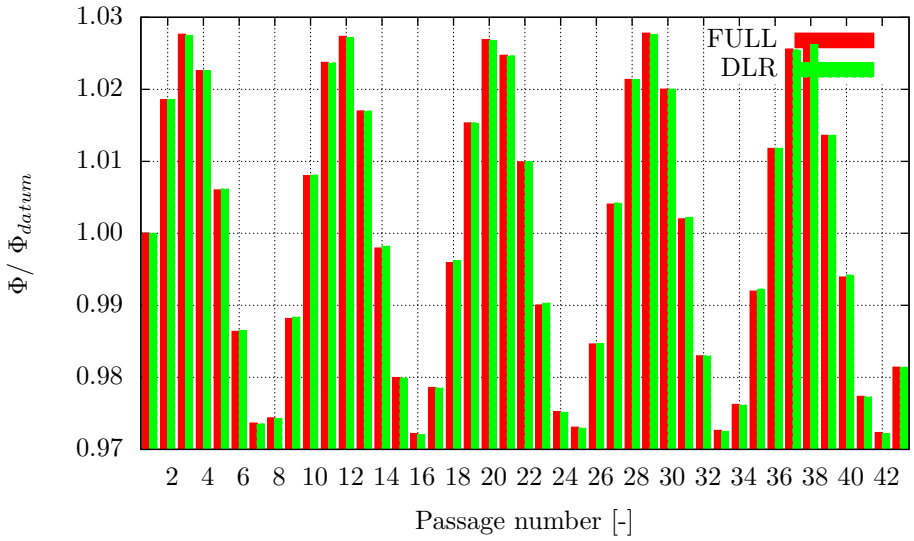


Figure 6.2.: Pitch variation

	Grid 1	Grid 2	Grid 3
Number of nodes	228K	385K	795K
Number of layers in the O-mesh	18K	22K	28K
Expansion ratio in the O-mesh	1.0	1.2	1.4
Number of points on blade surface	147	204	310

Table 6.2.: NGV grid dimensions

6.1.2. Grid convergence

Prior to the mistuning calculations, a grid convergence study was carried out with particular attention being paid to the NGV grid and its effects on static pressure distribution and boundary layer resolution. The steady state NGV solution on three different grids were compared. Table 6.2 lists important mesh parameters. The mesh contains 45 radial layers in the NGV and is refined towards the endwalls as seen in Figure 6.3a.

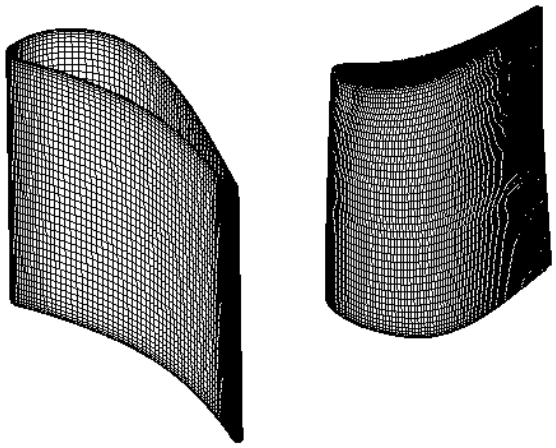
Figure 6.4 compares the boundary layer profiles at four chordwise positions on the NGV suction and pressure side. The two finer grids show no significant difference in boundary layer profiles. The isentropic Mach number profiles vary only slightly with grid resolution (see Figure 6.5). Differences between Grid 1 and Grid 2/Grid

3 are visible at peak suction and in the trailing edge region. However, there is no visible change in peak suction as the number of points on the surface is increased from 200 to 300 per radial level and the profile near the trailing edge changes only marginally between Grid 2 and Grid 3. Grid 2 was therefore selected for the steady NGV only and unsteady stator-rotor interaction study.

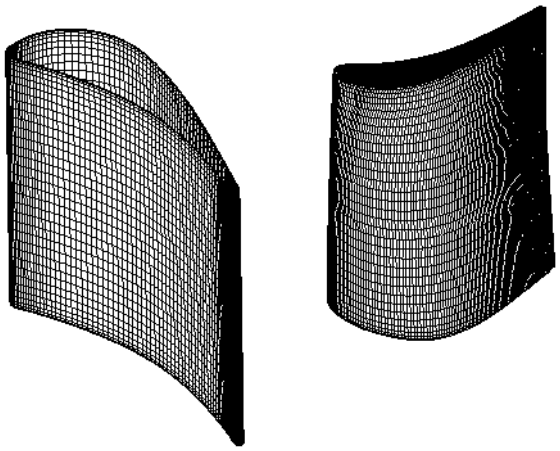
Similar mesh parameters defining the boundary layer and surface resolution were chosen to model the rotor blade. However, the passage mesh in the rotor is finer because the grid spacing has to match the spacing in the refined NGV wake region in order for the wake to propagate without spurious dissipation as seen in Figure 6.6a. For the steady NGV only calculations the stator grid was extended downstream into the rotor region (Figure 6.6b).

Originally, both blades were designed with 45 radial layers with an additional 10 layers in the rotor tip gap (approximately 1% span). However, the unsteady calculations exhibited convergence issues with a very fine resolution near the endwalls. The radial grid was hence coarsened to 35 layers with an additional 3 layers in the rotor tip gap for the unsteady calculations. The ratio between the finest layer of the original grid and the modified grid is approximately 3. The resolution of the tip gap mesh matches that of the endwall regions in the main mesh. Figure 6.3 shows the two radial distributions on the blade surface.

All unsteady calculations were started from the steady state starting solution shown in Figure 6.7.



(a) 45 radial layers



(b) 35 radial layer

Figure 6.3.: 3D Mesh (Grid 1)

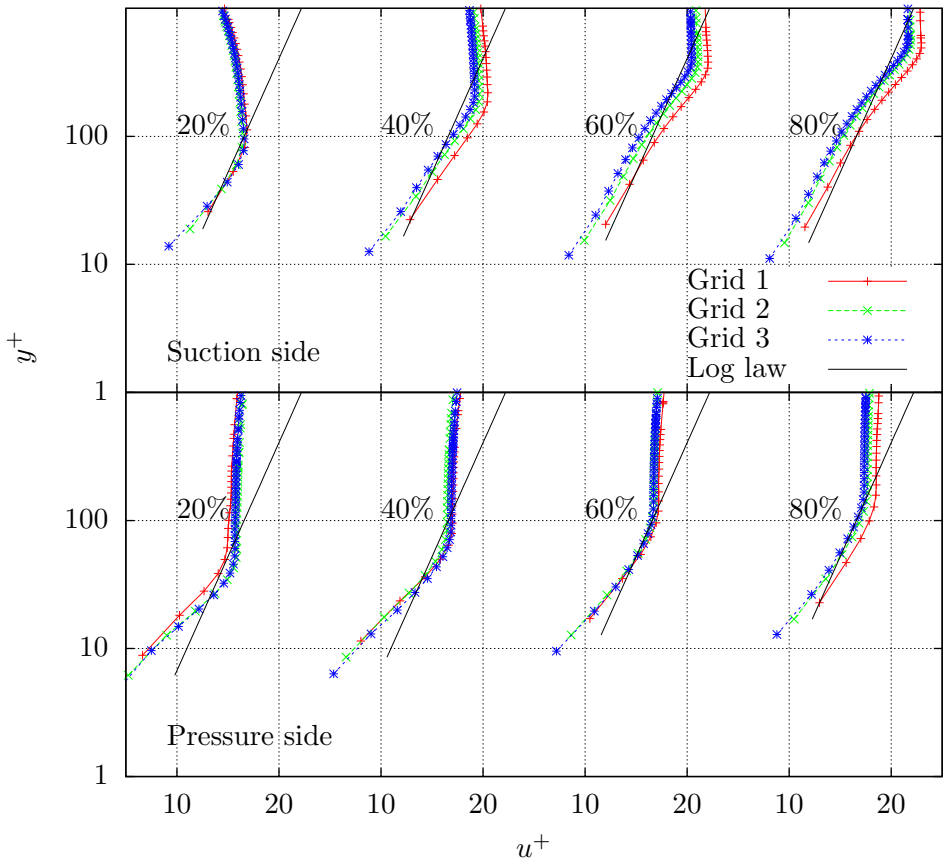


Figure 6.4.: NGV boundary layer profiles at four chordwise positions

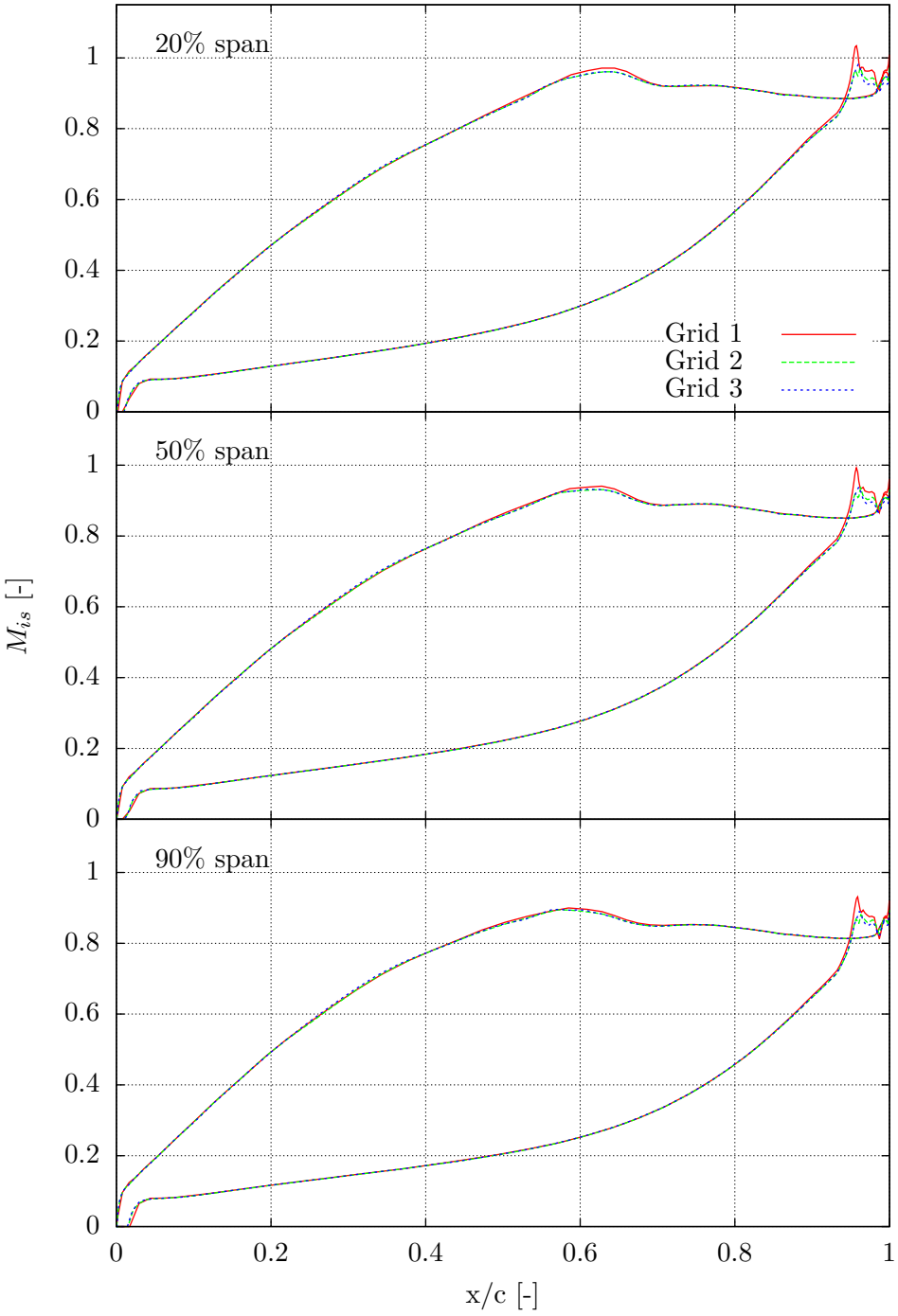
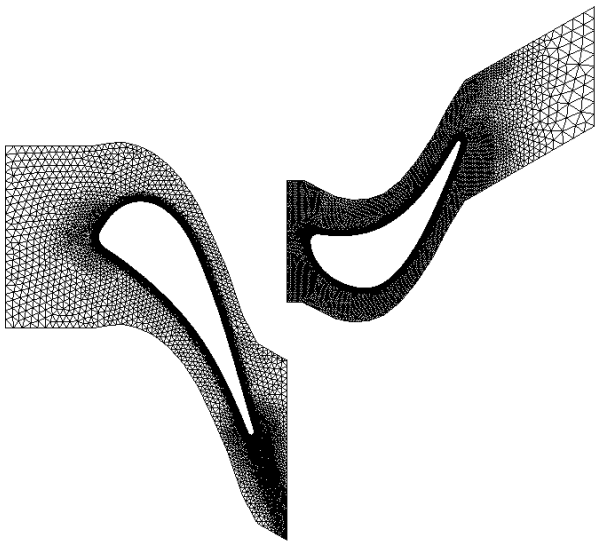
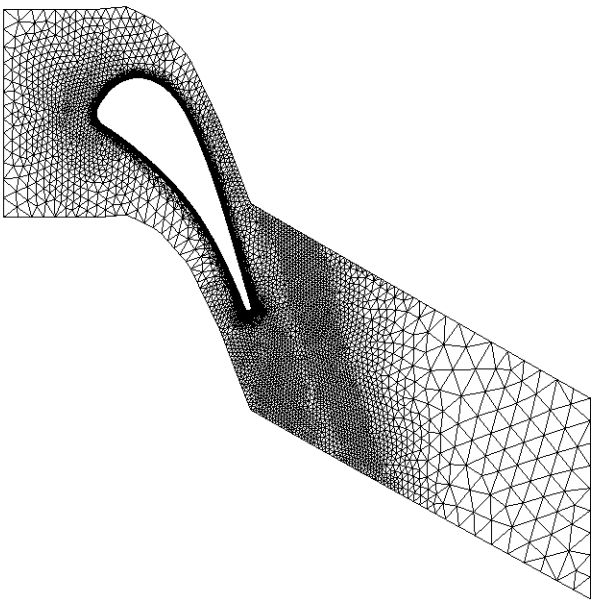


Figure 6.5.: NGV pressure profiles

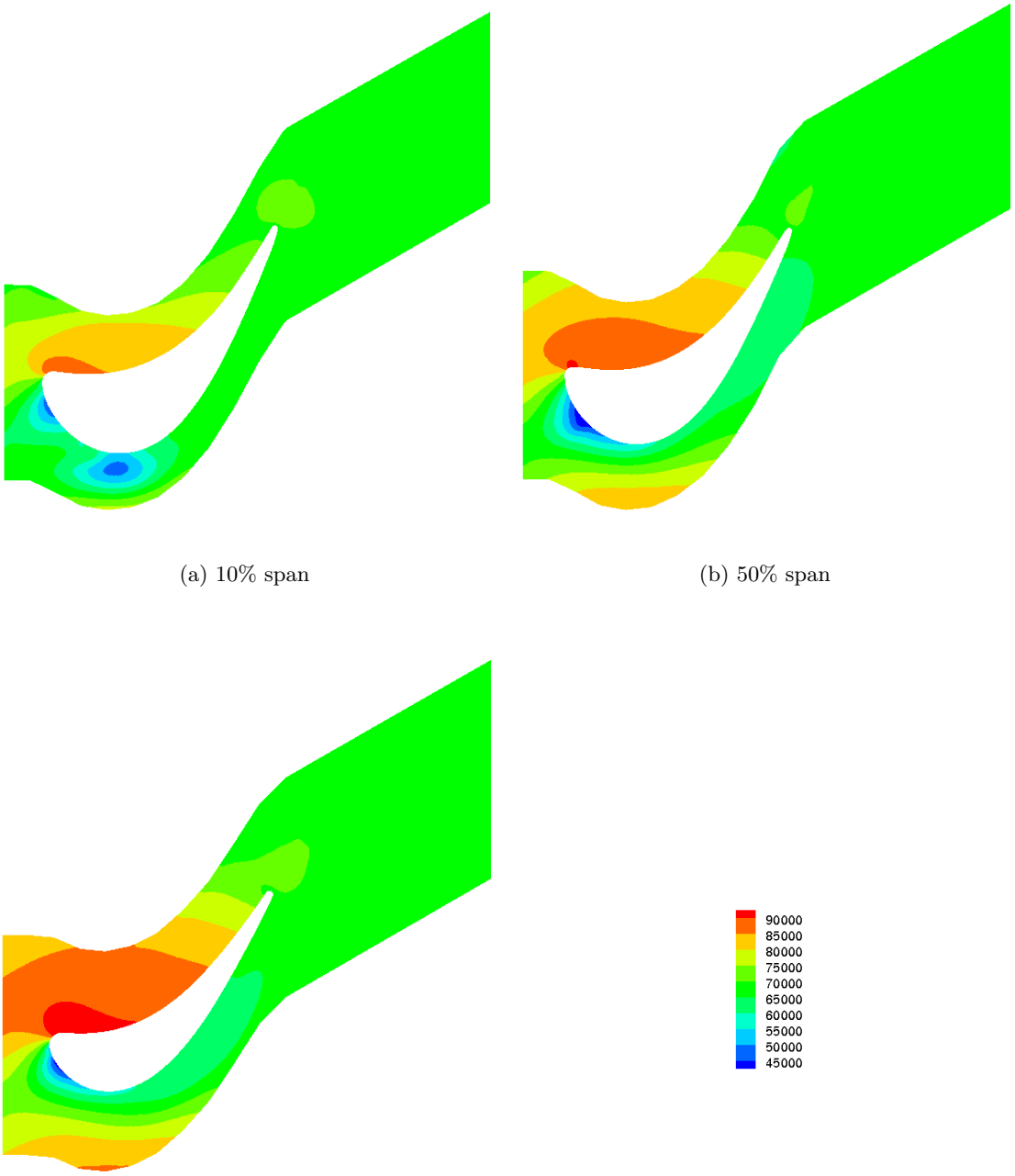


(a) SPMR mesh



(b) NGV only mesh

Figure 6.6.: 2D Mesh (Grid 1)



(a) 10% span

(b) 50% span

(c) 90% span

Figure 6.7.: Rotor static pressure from mixing plane starting solution

6.1.3. Steady flow through NGV with throat area variation

The solution of the sparse assembly is post-processed and reconstructed on the whole annulus for comparison with the full domain solution and experimental measurements. The two solutions were compared in terms of stator outlet flow at 128% chord and blade loading.

Figure 6.11 show total pressure contours at 128% chord. The corresponding wake profiles at three spanwise locations are shown in Figure 6.8. The numerical models underestimate the maximum total pressure loss in the wake region by approximately 5%. The small fluctuation in pressure in the mid-passage flow visible in Figure 6.8 is an artifact of the numerical solution. Petrov et al. [83] provide a detailed study of numerical predictions and experimental results using the same flow solver and found a better agreement with laminar flow in the leading edge region. A strong deviation exists between measured data and the numerical solution at 90% span, where the numerical model underestimates the total pressure deficit in the wake. This deviation is caused by the absence of a secondary flow region in the numerical prediction. In the rig, a secondary flow region which reaches across approximately 40% of the span develops as a result of a tip gap. The stator tip gap exists to enable L2F (Laser-two-focus) measurements and was not accounted for in the numerical model. There is no notable difference between sparse assembly and whole annulus solution in the wake profiles. A circumferential Fourier transform of the wake profile (Figure 6.9 and 6.10) confirms that the reduced passage model is capable of capturing the dominant spatial harmonics with the correct amplitude and phase. The effect of the throat area variation is small compared to the blade pressure field. The amplitude of the 5ND disturbance ranges from 0.91% (tip) to 0.16% (hub) of the inlet total pressure. The amplitude of the disturbances with wave numbers corresponding to the blade count and their sidebands (43±5 ND) also decreases from hub to casing. The sparse assembly method predicts the amplitude of all harmonics and their linear combinations to within 0.6% of the whole annulus solution. The amplitudes at 50% span are listed in Table 6.3.

A circumferential shift in the wake position exists between hub and tip, which can be observed in Figure 6.8 and Figure 6.11 for the numerical prediction. The shift is also present in the experimental values as seen in Figure 6.8 where the wake profiles at 20% and 90% span are reproduced. The comparison shows the migration of the wake in the positive circumferential direction from 20% to 90% span. This behaviour

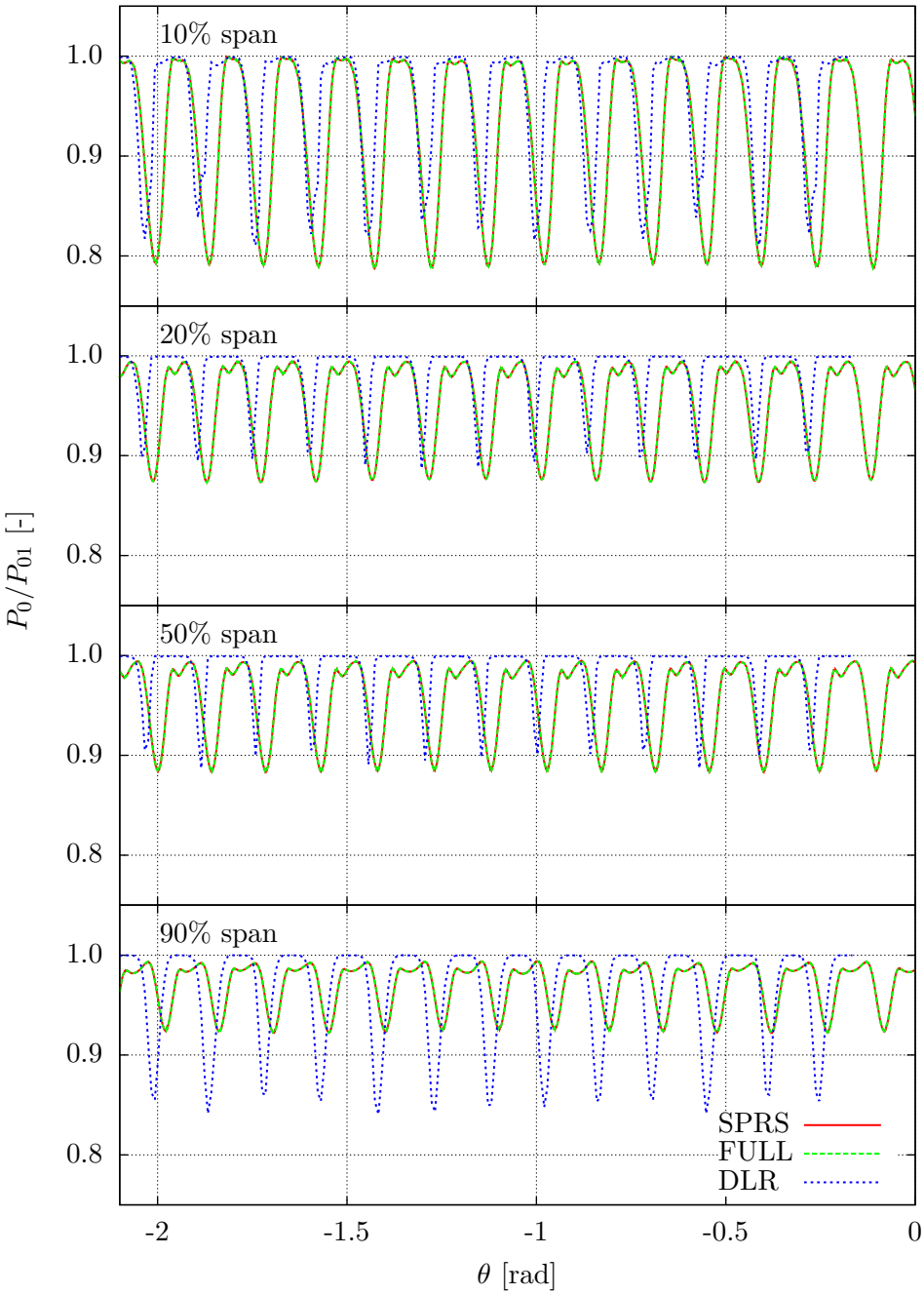


Figure 6.8.: NGV wake profiles at 128% chord

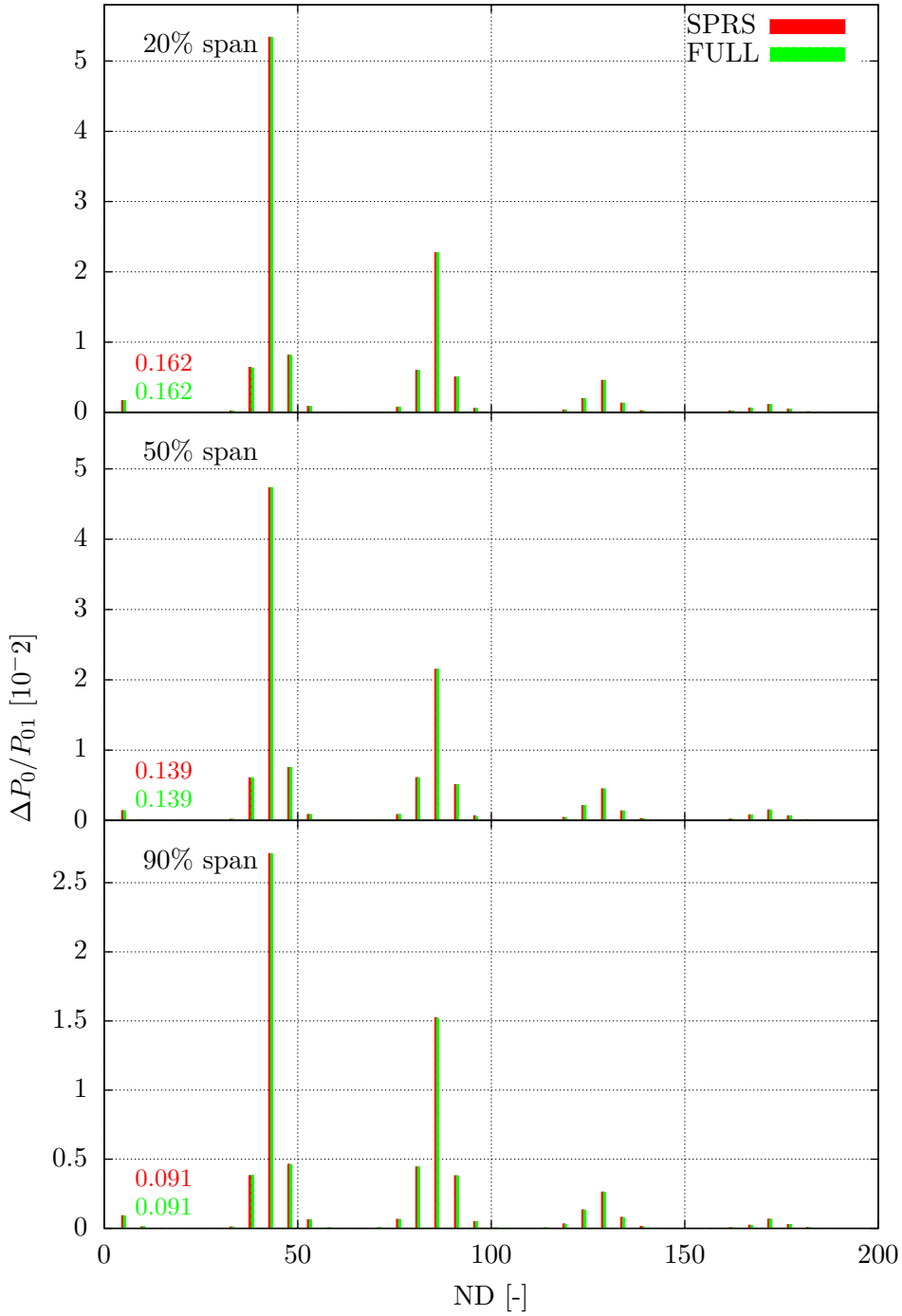


Figure 6.9.: NGV wake profiles at 128% chord: Amplitudes

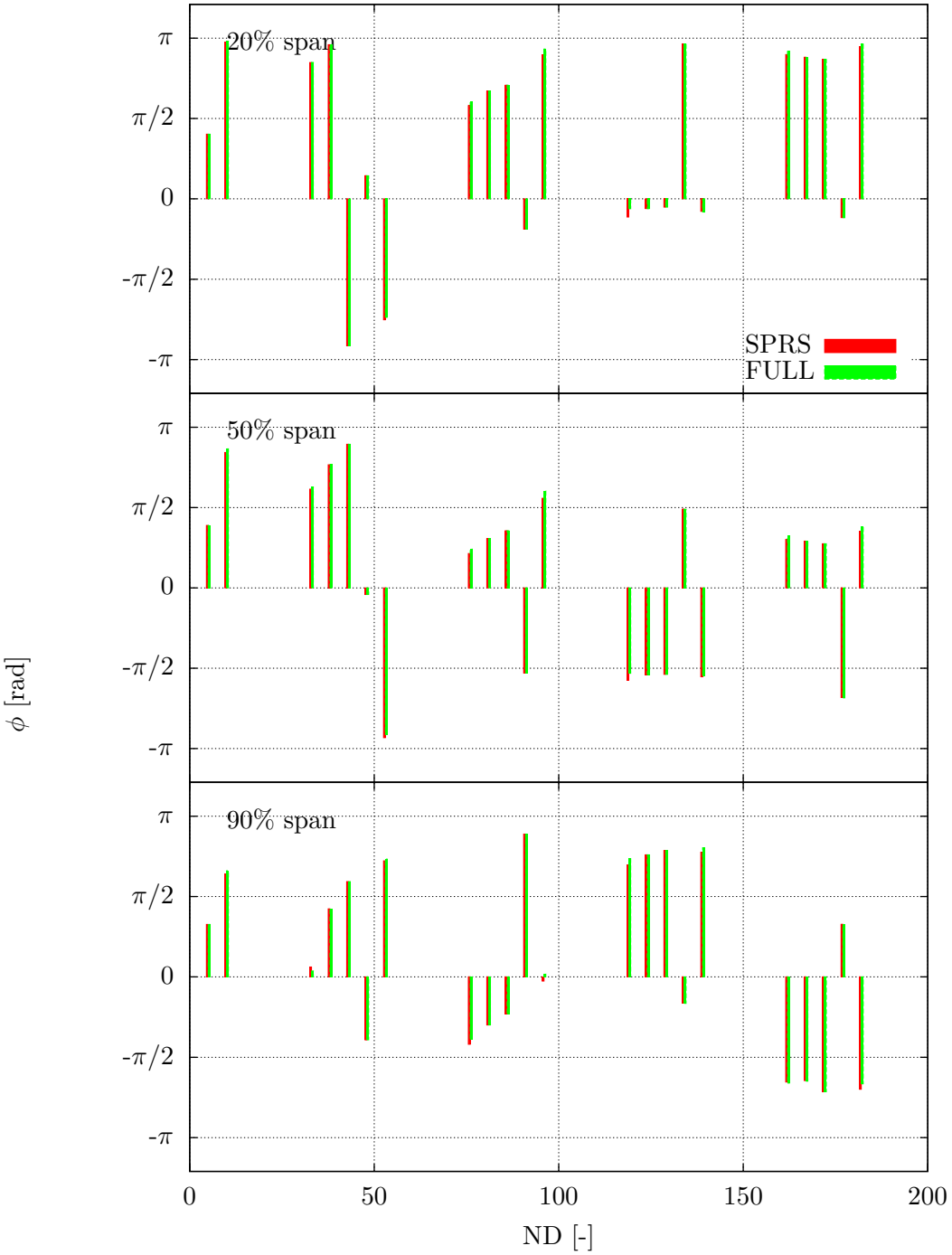
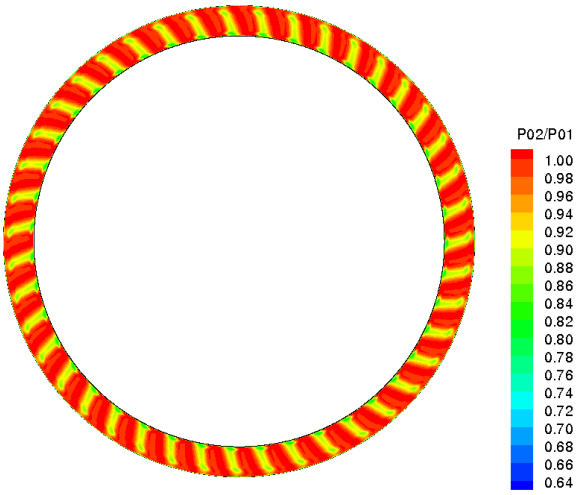
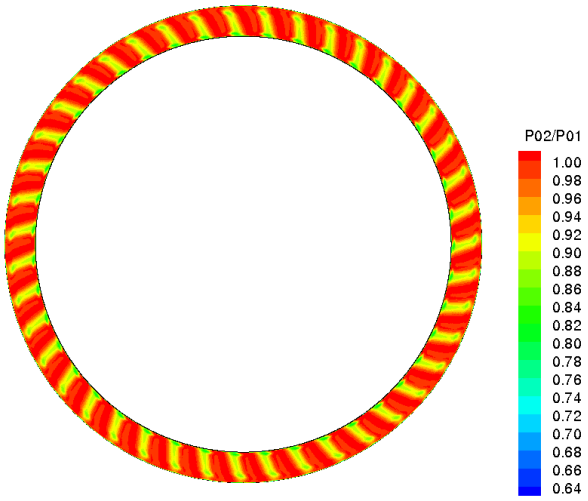


Figure 6.10.: NGV wake profiles at 128% chord: Phases



(a) Whole annulus



(b) Reconstruction

Figure 6.11.: Total pressure contours at stator outlet (view from inlet)

is the result of an unloading towards the tip due to the increased circumferential spacing. A smaller deflection at high radius results in smaller swirl component near the tip. This is confirmed by the radial variation of exit flow angles in Figure 6.13. This effect seems to be more prominent in the numerical prediction. The reason for this could not be further investigated since no flow angle measurements were available for this configuration.

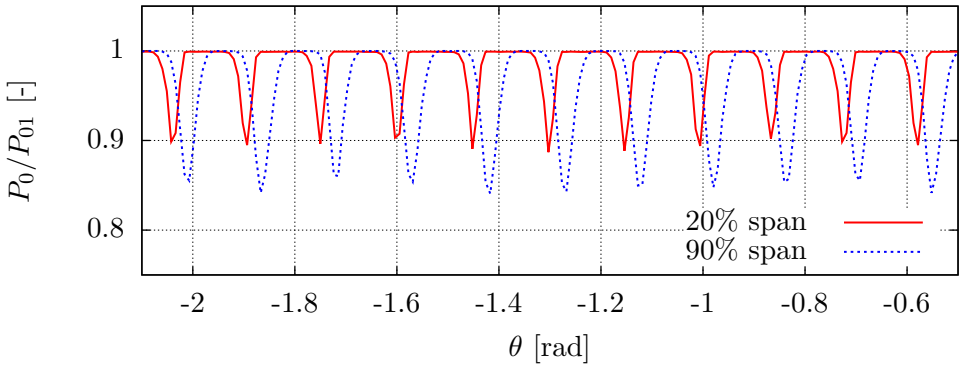


Figure 6.12.: Comparison of wake locations at 20% and 90% span

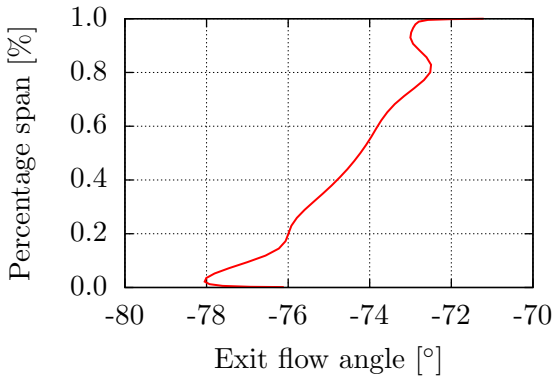


Figure 6.13.: Spanwise variation of exit flow angle

Figure 6.14, Figure 6.15 and Figure 6.16 compare blade surface Mach numbers at 10% and 50% span for the nominal, minimum and maximum throat area respectively. There are strong deviations between experimental and numerical results at 90% span due to the existence of the tip gap secondary flow region in the rig. At mid-span and hub, the numerical predictions agree with the experimental data and only small

ND	$\Delta P_0/P_{01}$ $[10^{-2}]$ Sparse assembly	$\Delta P_0/P_{01}$ $[10^{-2}]$ Whole annulus
5	0.139	0.139
38	0.606	0.606
43	0.473	0.473
48	0.752	0.751
81	0.609	0.609
86	0.215	0.215
91	0.508	0.508

Table 6.3.: Total pressure amplitudes normalised by inlet stagnation pressure at 50% span (128% chord)

deviations exist in the transonic region on the suction side.

The Mach number profiles indicate that the suction side static pressure decreases with increase in throat area, while the pressure side static pressure increases resulting in higher loading for larger blade spacing. The effect of the throat area variation is most pronounced in the mid-chord region, where the boundary layer is relatively thin. Towards the trailing edge the sudden change in curvature causes the flow to decelerate on the suction side. In this region, differences between the minimum and maximum throat area blades become less visible. The previously mentioned unloading towards the casings can also be observed.

The two numerical models predict the same loading with differences less than 1% of the total inlet pressure. Table 6.4 lists maximum value and L^2 norm of blade surface pressure difference between the two solutions. The highest difference exists at 90% span of the blade with minimum throat area. The differences are concentrated towards the trailing edge on the pressure side (see Figure 6.17). On the suction side, the deviation between the two models is spread across most of the chord. This distribution is possibly a consequence of reconstructing the solution on the whole annulus. The reconstruction process assumes a uniform spacing between corresponding grid points in the sparse assembly passages even in areas where the grid has been moved.

Blade	Position	Max ΔC_P $[10^{-2}]$	$\|\|\Delta C_P\|\|$ $[10^{-2}]$
Datum	20%	0.83	2.93
Datum	50%	0.87	3.28
Datum	90%	0.61	2.80
Min	20%	1.57	3.85
Min	50%	0.74	2.76
Min	90%	2.84	4.64
Max	20%	1.27	3.32
Max	50%	0.92	2.89
Max	90%	1.01	3.46

Table 6.4.: Difference in blade surface pressure between sparse assembly and whole annulus

6.1.4. Unsteady rotor-stator interaction

In order to assess the accuracy of the sparse assembly method for unsteady rotor-stator interaction, the unsteady rotor surface pressures are compared against the whole annulus prediction. Figure 6.18 to 6.23 show the amplitude and phase of the five dominant disturbances at three span-wise locations. The magnitude of the blade passing disturbances increases towards the casing. The phase and amplitude plots are comparatively smooth at 50% and 90% span whereas at 10% span the slope suddenly changes at several chordwise positions - particularly on the suction side. This behaviour can be attributed to a hub vortex on the suction side which is identifiable in the steady starting solution shown in Figure 6.7.

The stator blade passing is the most dominant disturbance with maximum amplitude of approximately 10% of the total inlet pressure near the hub. The higher harmonic (86ND) is significantly smaller and differences between the whole annulus and sparse assembly solutions are more noticeable. The maximum amplitude of the 5ND on the rotor surface is approximately 1% of the total inlet pressure and increases towards the tip. 38ND and 48ND are similar in magnitude to 5ND but, like the blade passing disturbance, show a small decrease in amplitude towards the casing.

Figure 6.18, 6.20 and 6.22 show a positive offset between the sparse assembly and whole annulus amplitudes at all spanwise positions. The smaller amplitude cannot be the sole reason for these errors as 38ND and 43ND show a better agreement despite being weaker disturbances. The reason for the discrepancy is likely to lie with the frequency of the disturbance. If the solution contains frequencies which are

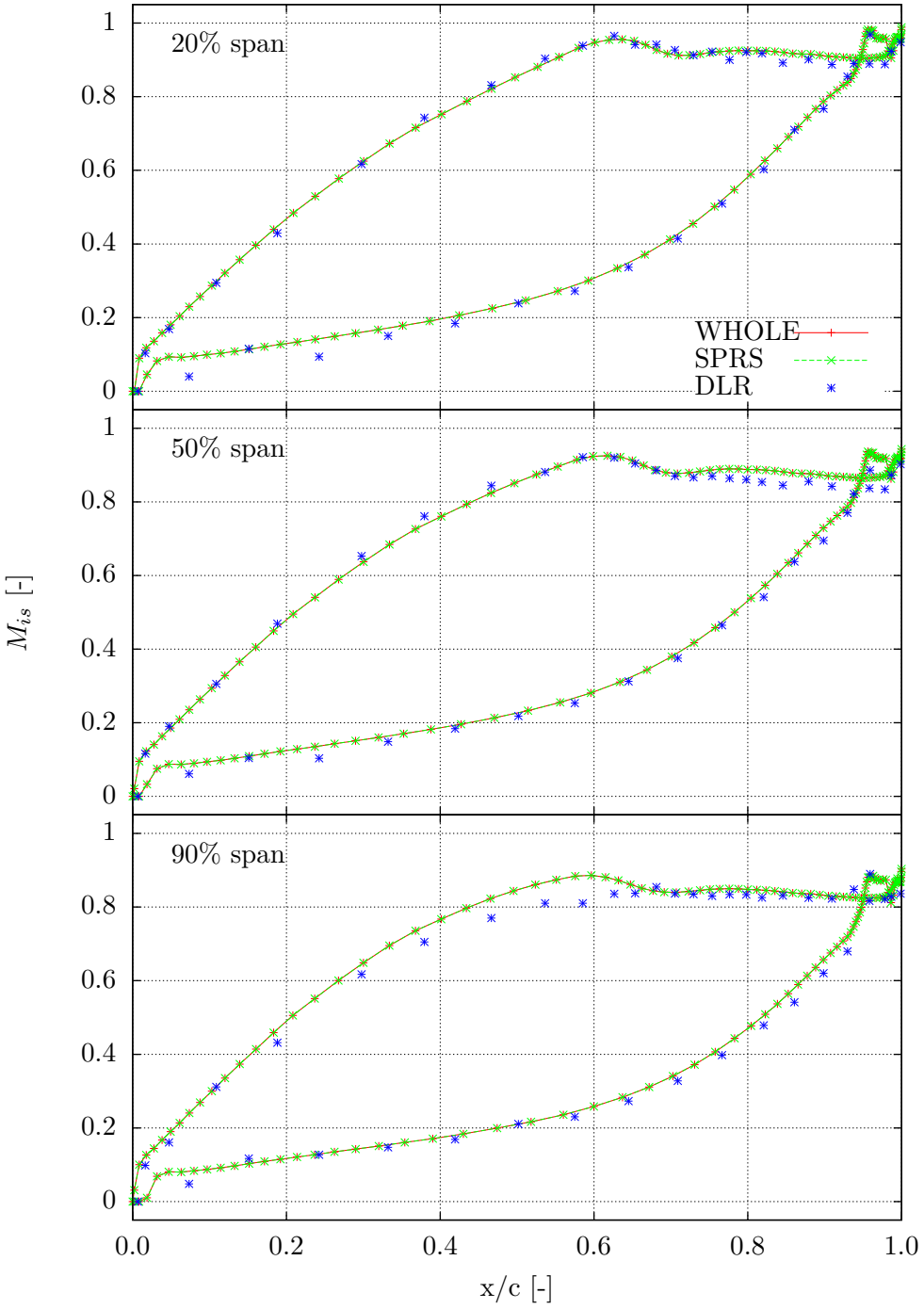


Figure 6.14.: Blade surface pressure at datum throat area

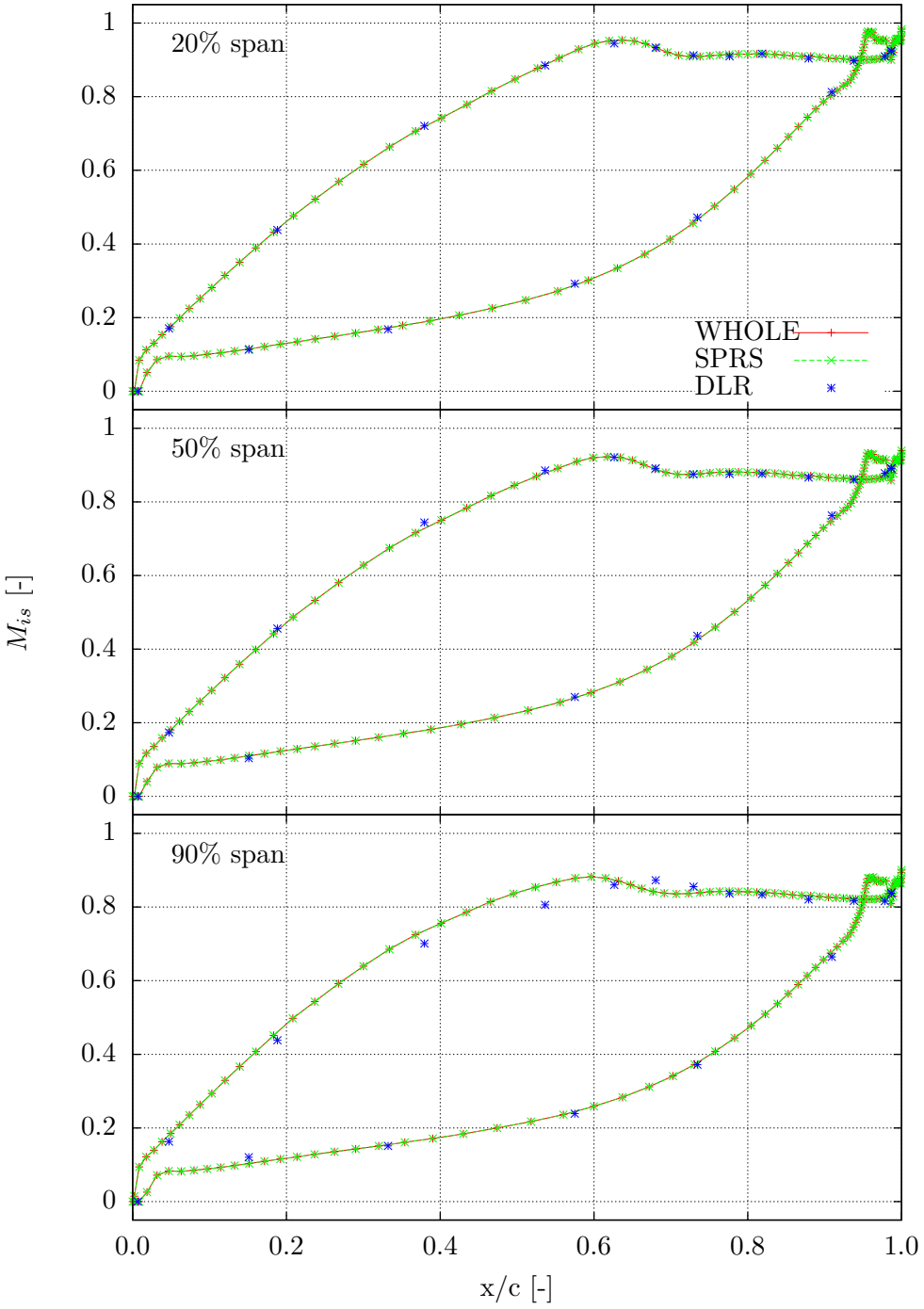


Figure 6.15.: Blade surface pressure at -4% throat area

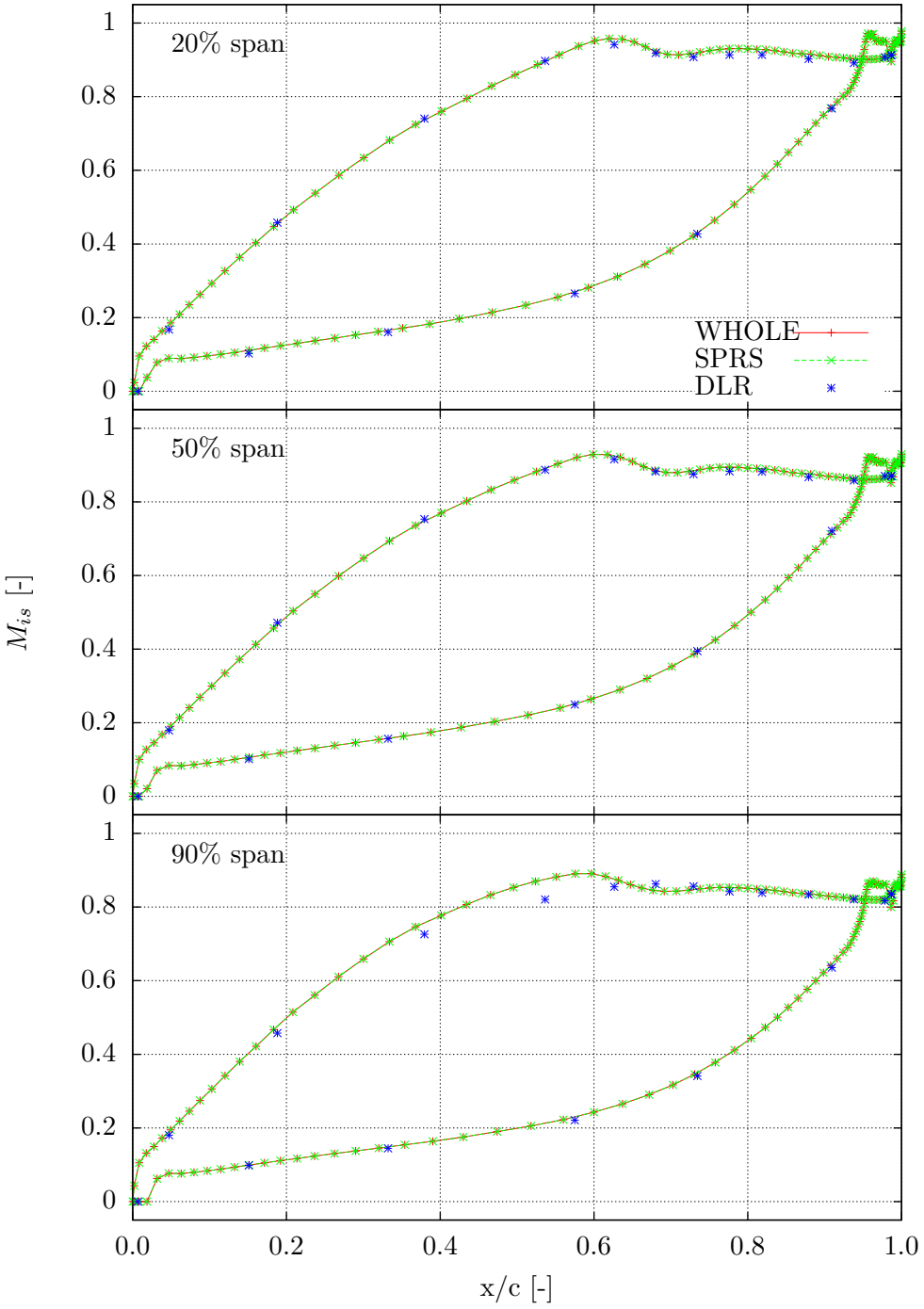


Figure 6.16.: Blade surface pressure at +4% throat area

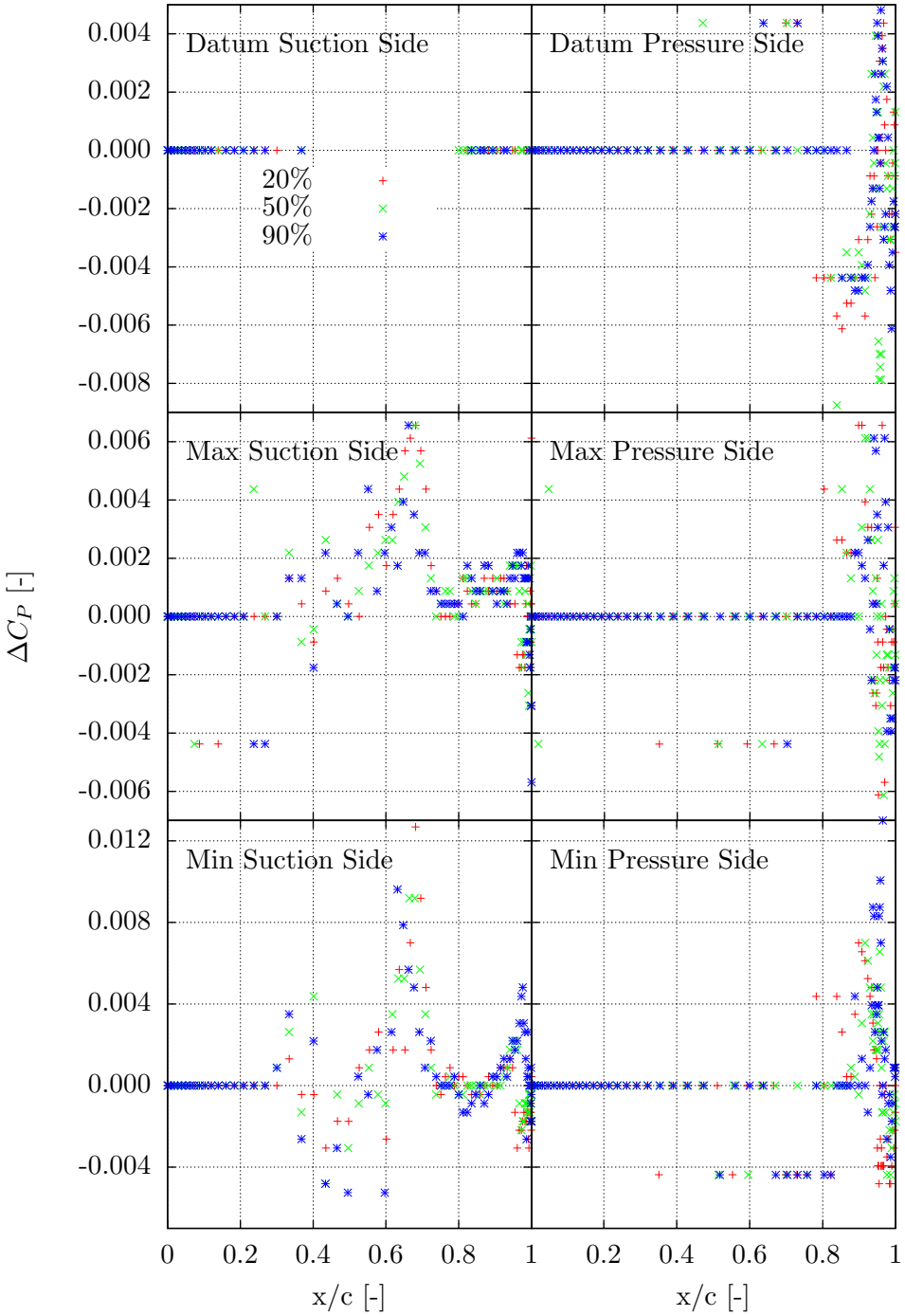


Figure 6.17.: Difference between sparse assembly and whole annulus blade surface pressures

close to 86EO but not contained in the Fourier approximation, they may be wrongly aliased to 86EO and increase its amplitude in the sparse assembly.

A similar difference between the two solutions can be observed for other disturbances at 10% span. For these disturbances, however, the sparse assembly approximation improves away from the hub. This is most obvious in the representation of the 5ND disturbance, where the sparse assembly method overestimates the maximum amplitude at the hub but provides an improved approximation at 50% and 90% span. This behaviour is likely to be caused by the existence of several frequencies in the separated region on the hub which are unaccounted for in the Fourier model and become wrongly aliased to engine orders.

Overall, the sparse assembly method provides a good approximation of local wave speeds as seen in the phase plots in Figures 6.19, 6.21 and 6.23. However, locally some disturbance show differences in slope which were not observed on previous quasi two-dimensional test cases. The 48ND disturbance, for example, appears to be travelling slightly slower on the suction side leading edge in the sparse assembly solution than in the full circumference solution. This effect is much more pronounced near the tip and at mid-span than at 10% span. Similarly, the 43ND disturbance shows differences in phase between the two solutions on the pressure side at 50% and 90% span which are not visible on the suction side. At 10% span differences are visible on both sides but, as in previous cases, the difference is approximately constant along the span and the slope of the two solutions agrees well. A possible explanation for this behaviour is the existence of spurious frequencies due to three-dimensional features such as the hub separation and the tip gap flow.

Whether these small differences render the method unsuitable for three-dimensional applications depend on the objectives of the calculations. If solutions are sought to provide insights into three-dimensional flows or the propagation of acoustic waves, the use of the sparse assembly method is not recommended. For aeroelastic purposes, however, such small differences in local wave speed and amplitude are unlikely to bear any significance.

6.1.5. Computational requirements and convergence

Simulations were run on the Imperial College High Performance Computing cluster with Nehalem CPUs running at 2.93GHz, 8 cores per node with 24GBytes of fast memory. As seen in Table 6.5, the sparse assembly method reduces the grid size by

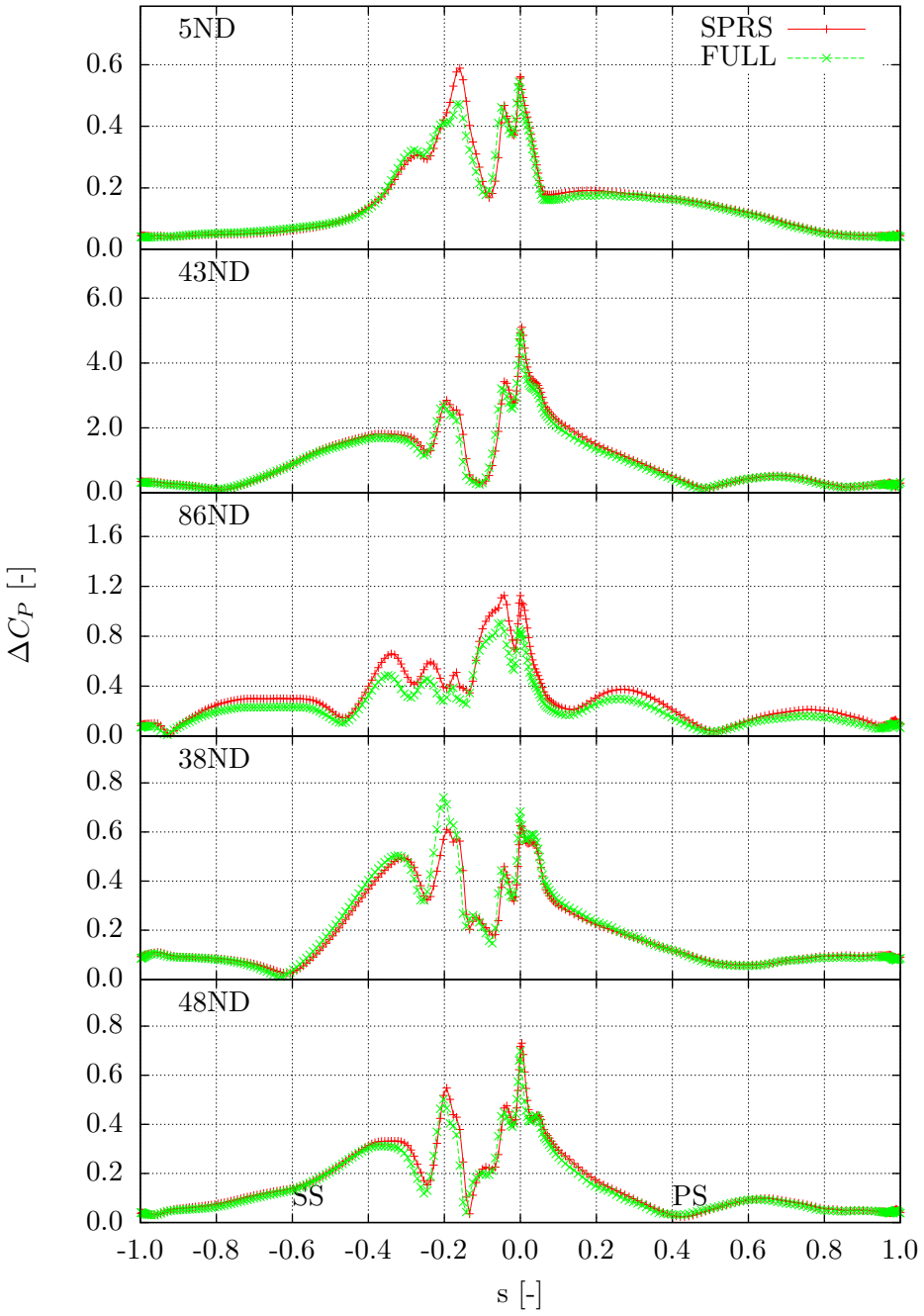


Figure 6.18.: Amplitudes of unsteady rotor surface pressure at 10% span

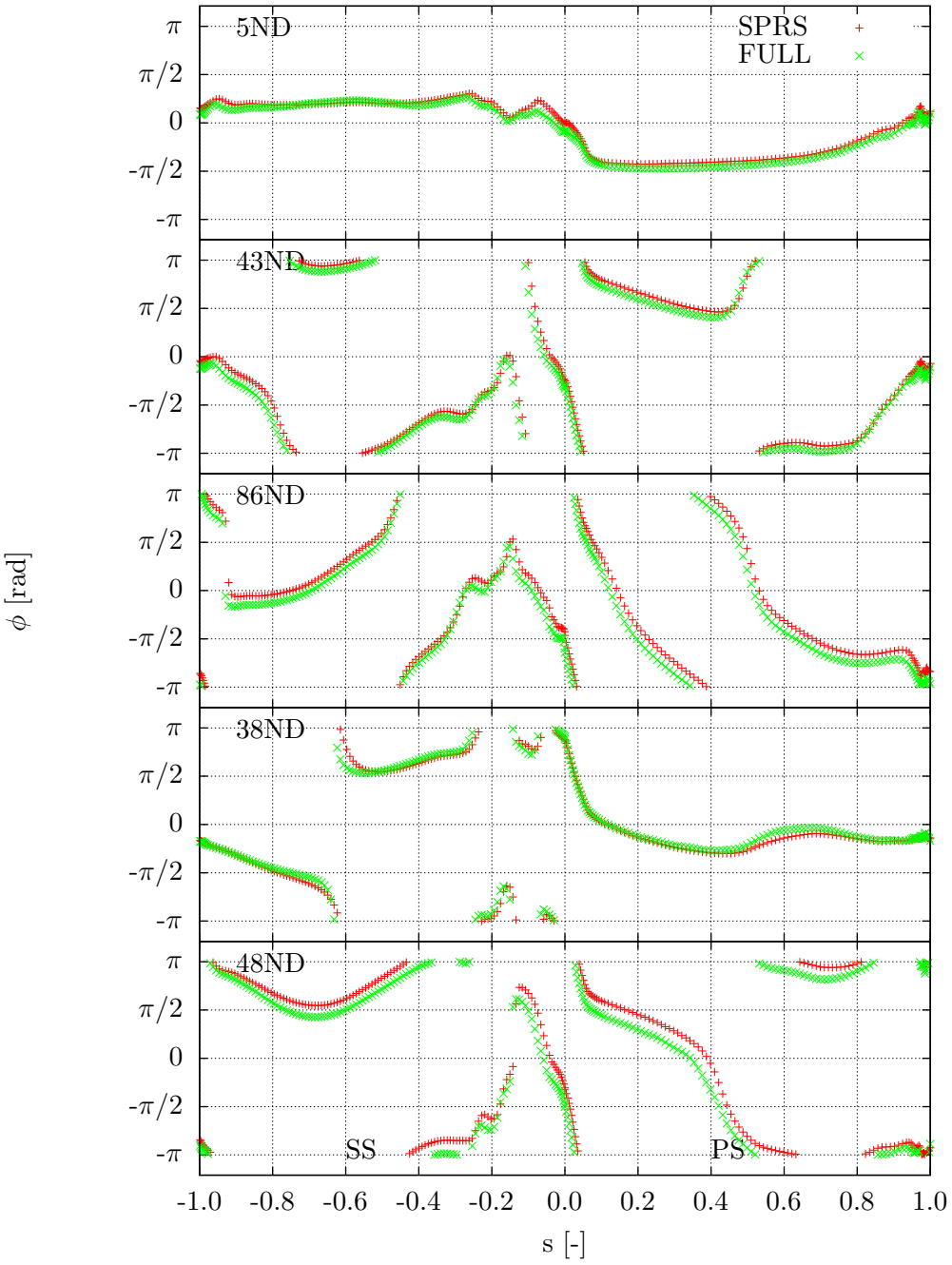


Figure 6.19.: Phases of unsteady rotor surface pressure at 10% span

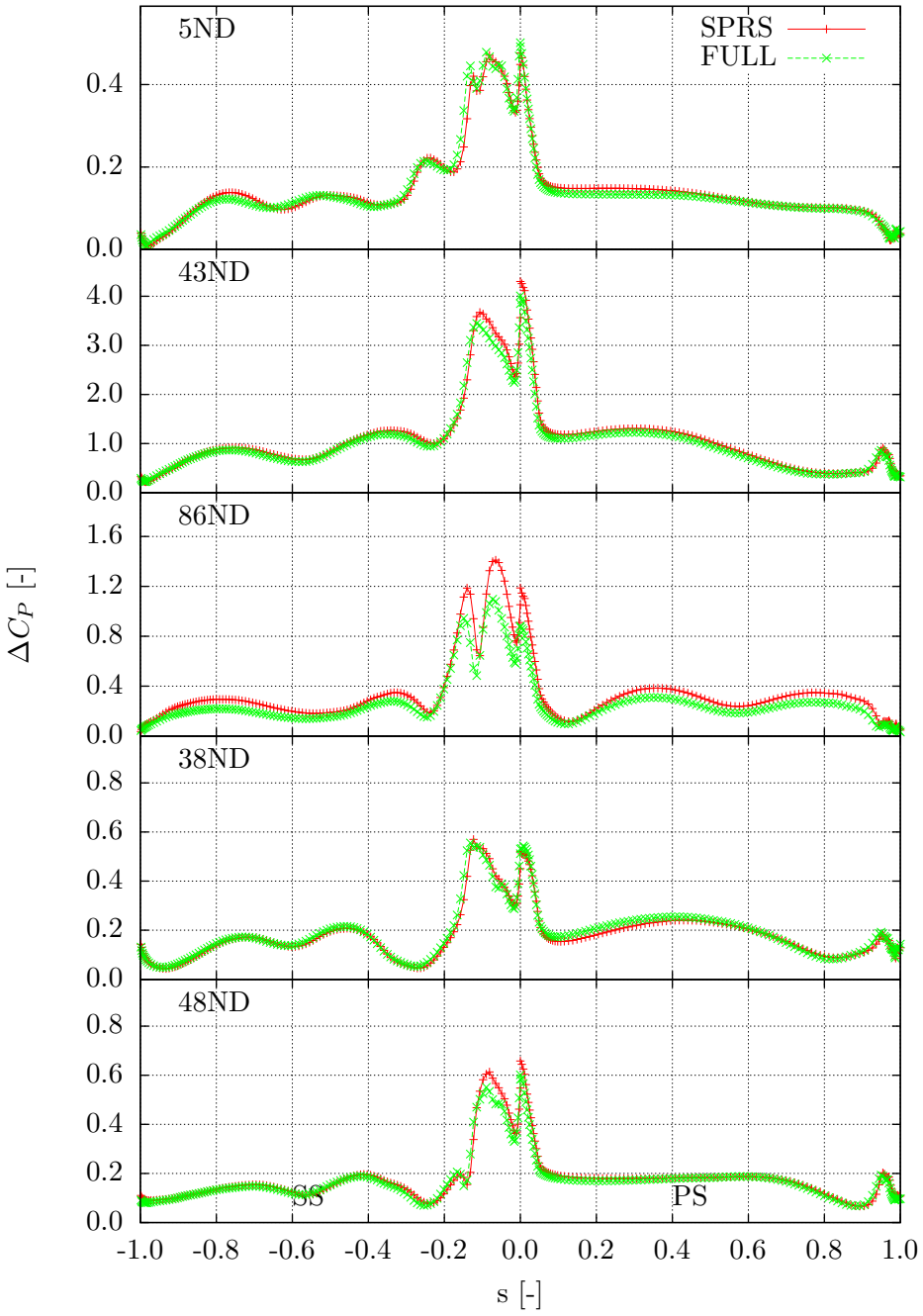


Figure 6.20.: Amplitudes of unsteady rotor surface pressure at 50% span

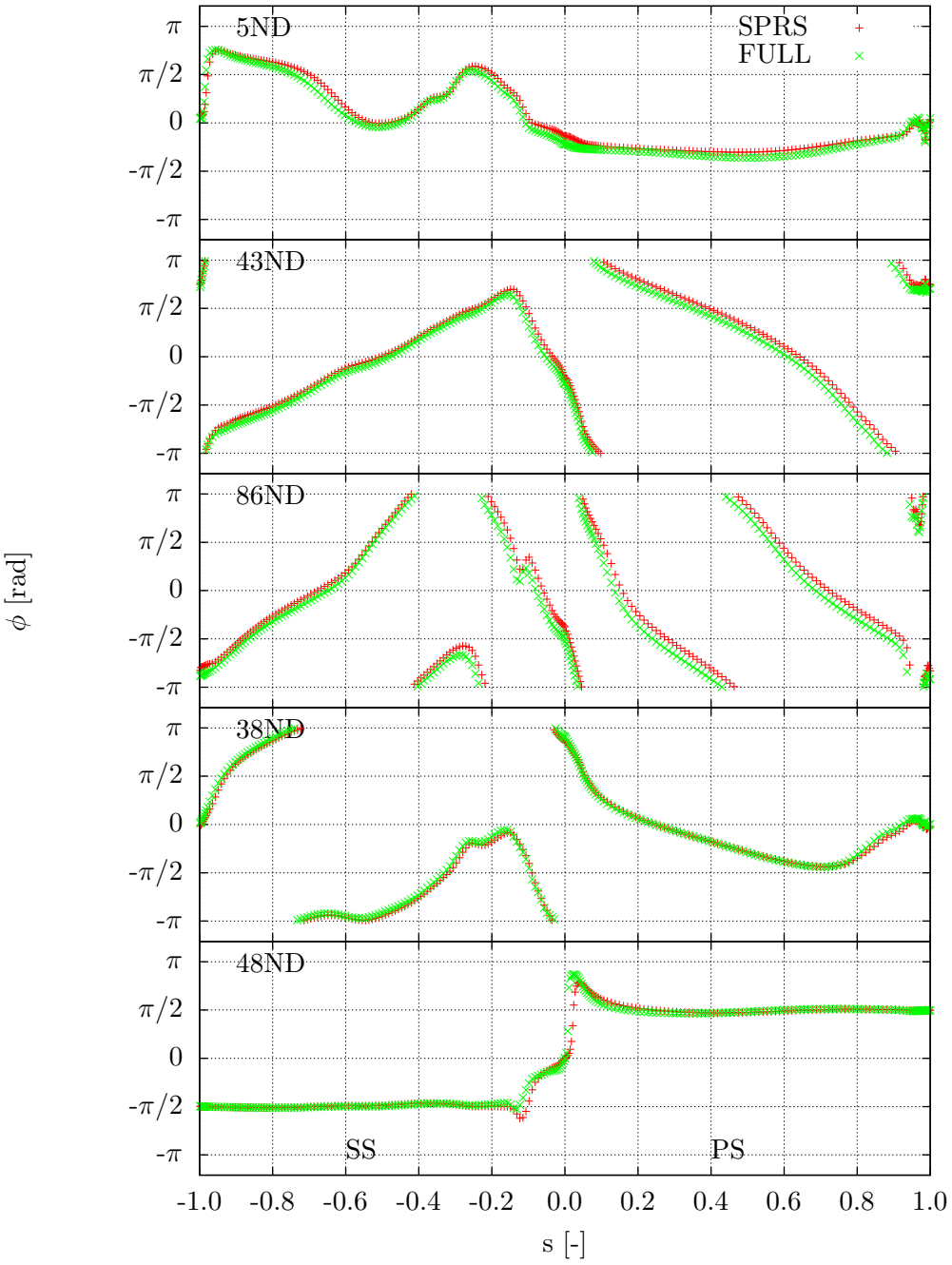


Figure 6.21.: Phases of unsteady rotor surface pressure at 50% span

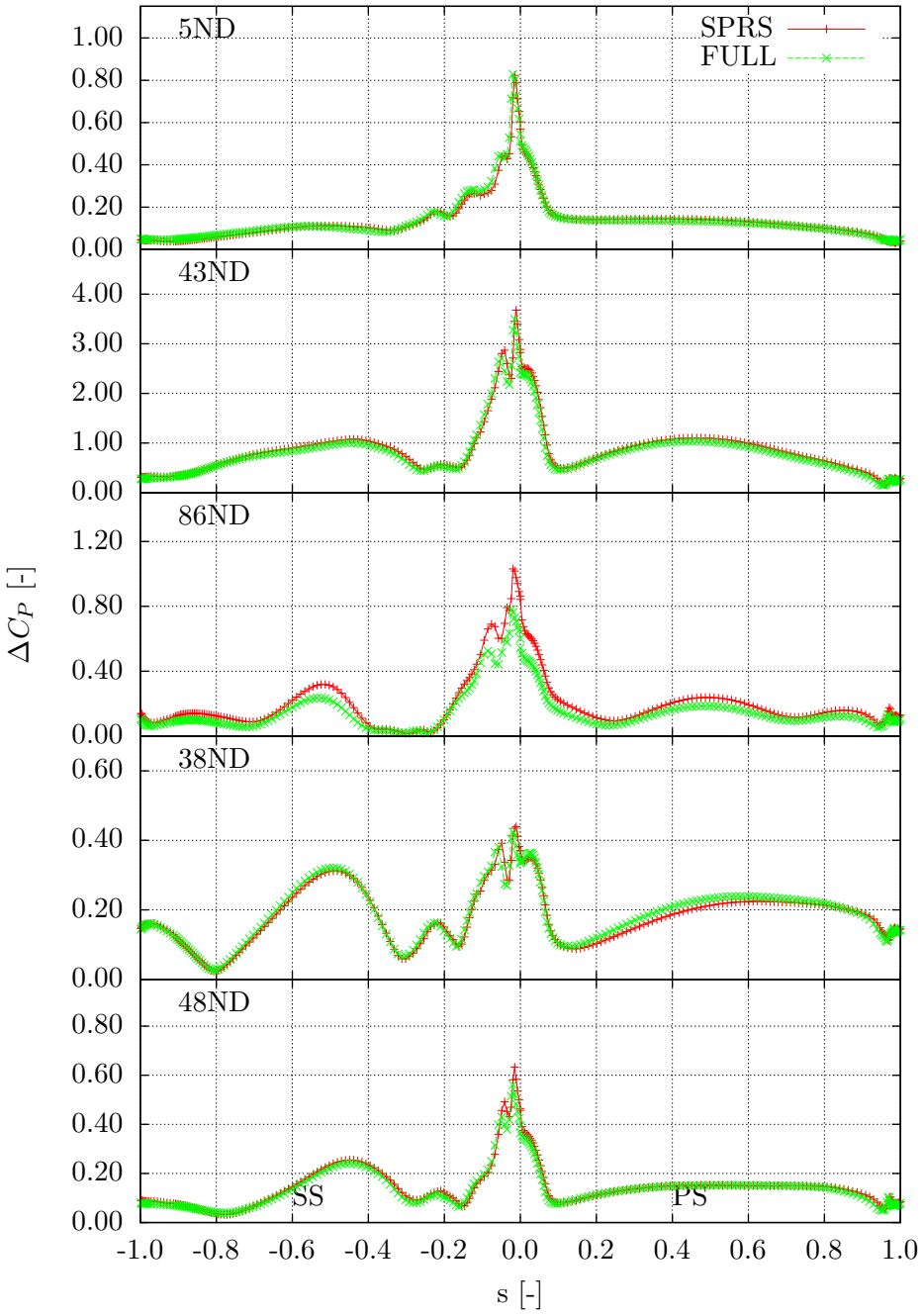


Figure 6.22.: Amplitudes of unsteady rotor surface pressure at 90% span

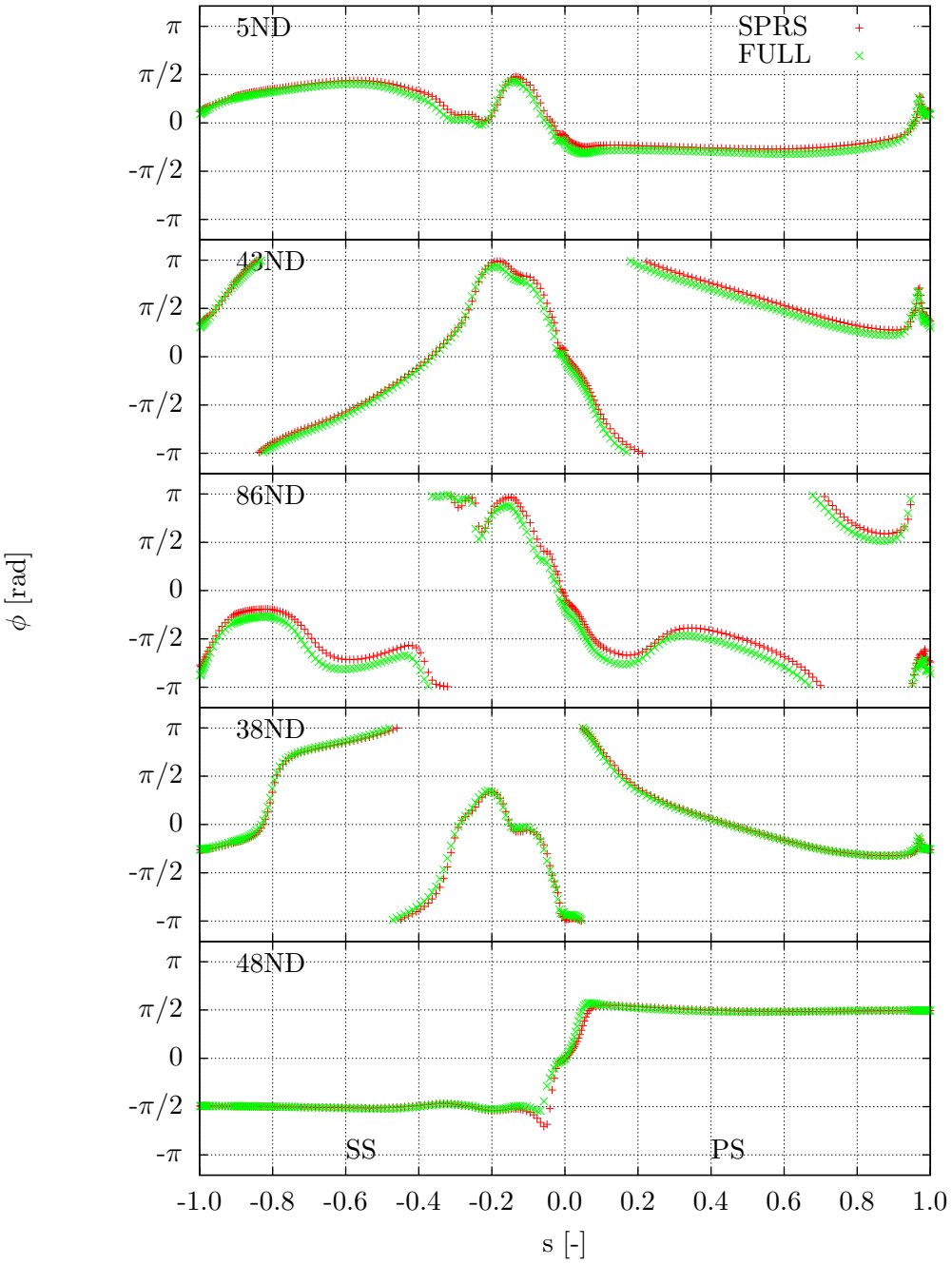


Figure 6.23.: Phases of unsteady rotor surface pressure at 90% span

	SPRS	FULL
Grid points	2.2M	40M
CPUs	16	128
Total elapsed time [h]	≈2200	≈9000

Table 6.5.: Comparison of computational resources required for full span turbine stage

a factor of 18. The computational effort does not scale directly with grid size since the Fourier coefficients must be computed at every time step. For this particular case with a total of 18 frequencies and two spatial harmonics, the reduced passage model requires only $1/8^{th}$ of the CPU-time per time step. However, due to the gradual correction of the periodic and inter-row boundaries, the reduced passage model takes longer to reach a periodic state. Taking all these factors into account, the sparse assembly method reduces the total elapsed time (defined as wall clock time multiplied by number of CPUs) for this turbine stage by a factor of approximately 4. An additional advantage of the reduced passage model is that it is small enough to be solved and post-processed on a workstation.

As previously mentioned, the reduced passage model exhibited poor convergence with very high resolution near the endwalls and the grid had to be coarsened for the present study. This and the difficulties observed near the hub in Figures 6.18 and 6.19 indicate that unsteady flow features such as tip clearance or hub vortices can impede the Fourier approximation.

6.1.6. Summary

The above full span study of a high pressure turbine stage with moderate throat area variation in the NGV demonstrates that the reduced passage model is capable of approximating large engine order distortions and the resulting excitation forces on a downstream row. The sparse assembly solution was compared to the whole annulus solution in terms of steady loads on the NGV, modal forces and unsteady pressures on the rotor surface. The two solutions were found to be in good agreement. The effects of hub vortex and tip clearance on the accuracy of the solution were minimal given a suitable grid resolution near the endwalls.

6.2. Part-span study of distortion transfer through a multi-stage turbine

In this section, the approximate multi-stage approach described in Section 4.5 is applied to model distortion transfer through two turbine stages. Aim of this study is to examine the feasibility of approximate distortion transfer modelling and gain insight into its limitations. The test case chosen is an application of interest to industry. To reduce computational times, however, only the quasi two-dimensional flow through a thin section at mid-span is modelled.

6.2.1. Background

Increasingly stringent environmental requirements have led to the development of a staged combustion process to reduce emissions of carbon monoxide (CO) and mono-nitrogen oxides (NO_x). This is particularly important for industrial gas turbines which are subject to stronger environmental regulations than aeroengines.

A main factor governing the emission of those two gases is the combustion temperature (or fuel-to-air ratio) and a compromise must be made between the formation of CO which is a product of incomplete combustion and NO_x which increasingly forms at higher temperatures. Combustion processes for gas turbines are thus designed to allow variations in operating conditions whilst keeping combustion within the narrow temperature range defined by emission requirements as schematically illustrated in Figure 6.24.

Operation at almost constant temperature is achieved by varying the number of active combustion chambers, or burners, around the combustor. Each burner consists of a primary and a secondary fuel nozzle. Fuel is supplied to the primary nozzles, secondary nozzles and individual combustion chambers in varying combinations to optimise fuel-to-air ratio at all operating conditions. Figure 6.25 shows a schematic of a multi-chamber combustor with primary and secondary fuel nozzles.[9]

Switching on the burners in stages gives rise to circumferential temperature distortions which are known to cause low-engine-order excitations in the downstream turbine.

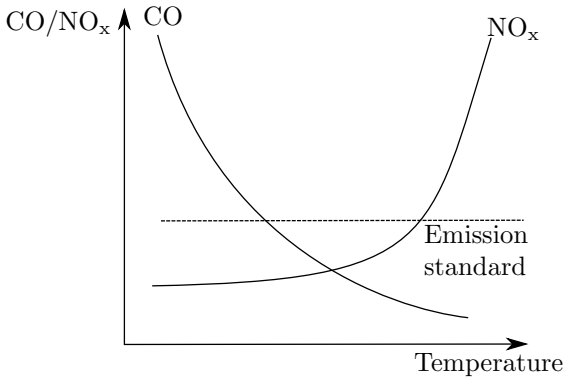


Figure 6.24.: Formation of CO and NO_x with temperature

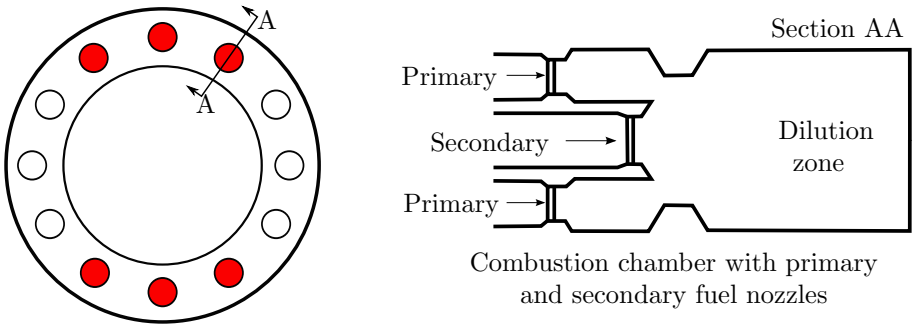


Figure 6.25.: Multiple combustion chamber system with 6 out of 12 burners active

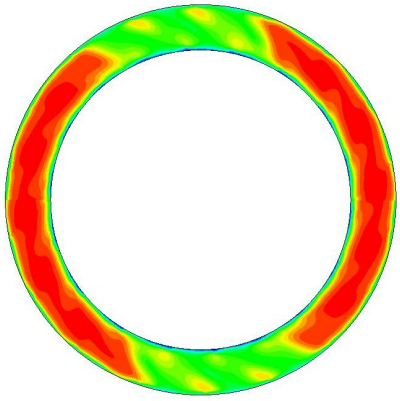


Figure 6.26.: Temperature contours at combustor outlet

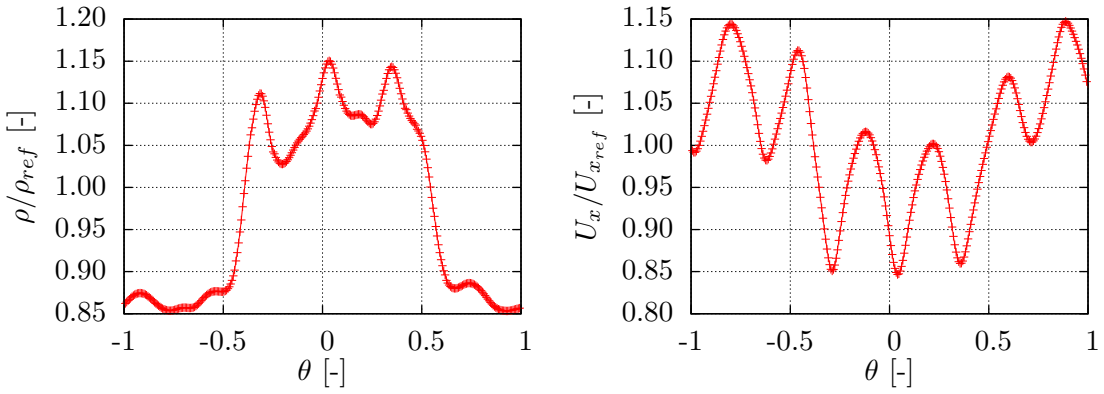


Figure 6.27.: Circumferential variation of density and axial velocity at combustor outlet

6.2.2. Test Case

The test case for the distortion transfer model is taken from the industrial derivative of an aeroengine. The current study is restricted to the one-stage high pressure (HP) and intermediate pressure (IP) turbines.

The combustor distortion, which is created by combination of primary and secondary burners, is transferred onto a sliding plane and acts as inlet boundary condition for the downstream stages. The distortion contains a 2ND circumferential variation and multiple higher harmonics. A contour plot of the temperature distortion is shown in Figure 6.26. The higher harmonics are clearly visible in the circumferential variations of density and pressure (Figure 6.27).

The two-spool configuration poses a challenge to reduced passage modelling as it creates a quasi-non-periodic unsteadiness. Cases with a single rotational speed always have a periodic time scale of at most one revolution. For two or three-spool assemblies with non-integer ratios of rotational speeds, such a periodicity does not exists. This may pose a challenge to Fourier based methods such as the reduced passage model if disturbances with a large frequency separation strongly interact.

The turbine considered contains N_{S1} and N_{R1} stator and rotor blades respectively in the HP turbine and N_{S2} and N_{R2} stator and rotor blades in the IP turbine. The two spool-speeds are labelled Ω_1 and Ω_2 as indicated in Figure 6.28. The blade counts are such that the highest common divisor is 2. The 2ND distortion can hence be modelled on 180° and the half-annulus solution serves as reference for the

validation of the sparse assembly model.

Flow through the two stages is transonic. Figure 6.29 shows the relative Mach number contours from the steady state starting solution. The flow coefficient at turbine inlet is approximately 0.2.

To ensure that the neglect of rotor-rotor interaction modes is a valid assumption, the cut-off frequencies of the rotor passing disturbances are calculated from the steady state solution using:

$$f_{cut-off} = \frac{ak}{2\pi}(\sqrt{1 - M_x^2} \pm M_\theta k) \tag{6.1}$$

where k is the circumferential wave number of the disturbance, a is the local speed of sound and M_θ and M_x are the local circumferential and axial wave number respectively [56]. The sign of the circumferential Mach number is positive if the wave fronts propagate with the swirl of the flow and negative if the wave fronts propagate against the swirl.

Table 6.6 compares the rotor cut-off frequencies at the three blade row interfaces with the fundamental blade passing disturbances. If local flow conditions are such that the blade passing disturbances decay, i.e. if the cut-off frequency is greater than the blade passing frequency, filtering the disturbance from the interface cannot produce strong reflections and the approximate distortion transfer model is applicable. The comparison only concerns rotor passing frequencies, since the stator passing disturbance has zero frequency in the absolute frame of reference and must decay in the axial direction.

Table 6.6 illustrates that waves from the HP rotor are cut-off upstream of the HP rotor and cut-on downstream at the HP rotor outlet. The downstream travelling waves then become cut-off at the inlet to the IP rotor where the the swirl increases. Removing the disturbance from the IP stator-rotor interface is therefore deemed acceptable. The IP rotor passing frequency is below the cut-off frequency at all blade row interfaces. Rotor-rotor interaction as well as reflections from the inter-row boundaries are hence expected to be negligible.

6.2.3. Computational domains and setup

The computational domain contains a thin section (10%) at mid-span. For the sparse assembly model, the number of distortion harmonics is truncated to 5 and the 2ND disturbance is modelled on 11 passages in the stator domains. The distortion

Position	k_θ	M_x	M_θ	$f_{cut-off}$ [Hz]	f [Hz]
HP Stator Outlet	N_{R1}	0.27	1.01	21866	15291
HP Stator Outlet	$2N_{R1}$	0.27	1.01	43732	30582
HP Stator Outlet	N_{R2}	0.27	1.01	29947	13805
HP Stator Outlet	$2N_{R2}$	0.27	1.01	59894	27610
HP Rotor Outlet	N_{R1}	0.37	0.33	13158	15291
HP Rotor Outlet	$2N_{R1}$	0.37	0.33	26317	30582
HP Rotor Outlet	N_{R2}	0.37	0.33	18022	13805
HP Rotor Outlet	$2N_{R2}$	0.37	0.33	36043	27611
IP Stator Outlet	N_{R1}	0.27	0.72	17270	15291
IP Stator Outlet	$2N_{R1}$	0.27	0.72	34540	30582
IP Stator Outlet	N_{R2}	0.27	0.72	23653	13805
IP Stator Outlet	$2N_{R2}$	0.27	0.72	47305	27611

Table 6.6.: Cut-off frequencies for rotor passing disturbances at the blade row interfaces

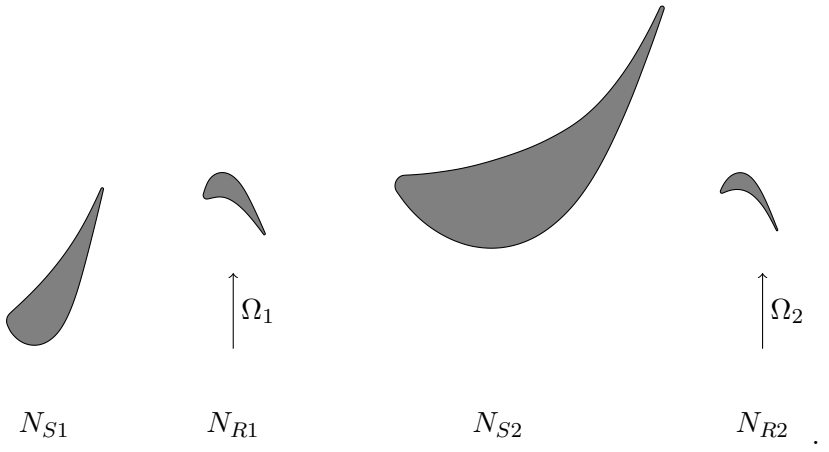


Figure 6.28.: HP and IP turbine

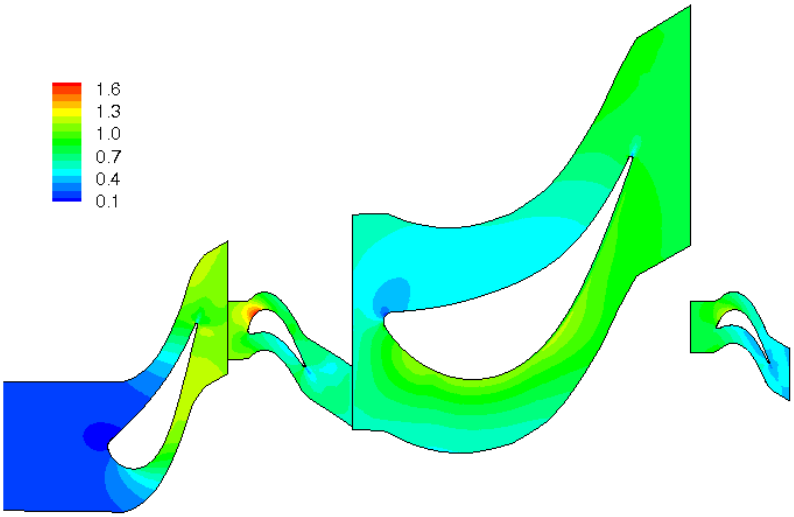
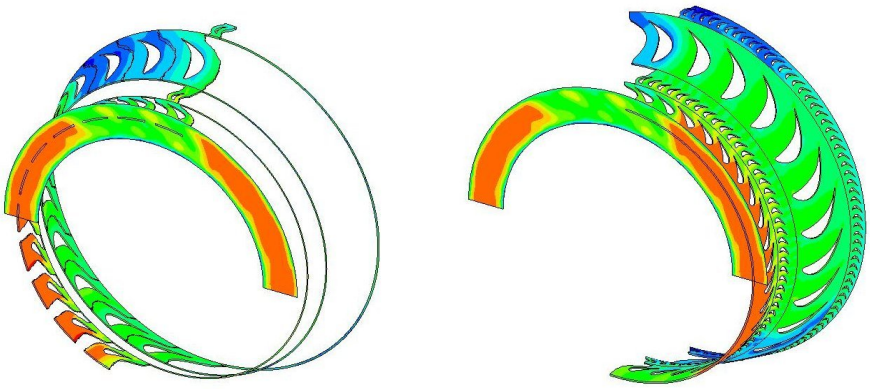


Figure 6.29.: Relative Mach number in steady state solution

transfer model neglects all rotor-rotor and stator-stator interaction and hence a single passage suffices in the rotor domains. Figure 6.30 compares the two domains and instantaneous temperature contours.

The time step for both computations corresponds to 11050 time steps per revolution of the HP spool. This results in approximately 120 time steps per period of the highest frequency perturbation. The temporal Fourier approximation includes three harmonics of blade passing frequencies between immediately adjacent rows. The rotor domains contain additional LEO excitations from the combustor (5 harmonics) and linear combinations of stator blade passing and combustor distortions. The frequency and wave number spectrum for an inlet distortion with circumferential wave number K is summarised in Table 6.7. The distortion transfer model neglects all rotor-rotor/stator-stator interactions.

Table 6.8 compares grid size and computational times of the two models. Because convergence of the sparse assembly method is very slow, the table compares wall-clock time per revolution multiplied by the number of CPUs rather than time to convergence. The sparse assembly method reduces the grid size by a factor of 5 and produces a 2x speed-up in terms of total time per revolution. However, the real speed-up is lower due to convergence issues as shown in the following section.



(a) Sparse assembly (b) Reference domain

Figure 6.30.: Computational domains for 2-stage distortion transfer calculation

Row	Stationary wave numbers	Travelling angular frequencies
S1	nK	$mN_{R1}\Omega_1$
R1	-	-$(nK \pm mN_{S1})\Omega_1$
S2	nK	-$mN_{R1}\Omega_1$,-$mN_{R2}\Omega_2$
R2	-	$(nK \pm mN_{S2})\Omega_2$

Table 6.7.: Wave number and frequency spectra in sparse assembly model for an inlet disturbance with fundamental wave number K ($n = 1, ..., 5$ and $m = 1, 2, 3$)

	Sparse assembly	Reference
Number of nodes	400K	1.9M
Time per revolution [h]	450	200

Table 6.8.: Comparison of computational resources required for distortion transfer case

6.2.4. Results

The focus of this study is low engine order excitation of turbine rotors caused by non-uniform combustor outlet conditions. We will hence assess the accuracy of the distortion transfer model by comparing the unsteady forcing on the sparse assembly blades against the reference solution. Since the reduced passage model does not take into account rotor-rotor interaction the time-averaged flow field in rotor passages is uniform in the circumferential direction and blade forces are collected on only one blade per row. All forces are normalised by their steady state value.

Figure 6.32 compares the forces on the HP stator after approximately 2 revolutions. The sparse assembly prediction for the amplitude of the unsteady fluctuations due to the downstream rotor lies within 4% of the whole annulus solution. However, an offset of approximately 3.5% of the steady state value exists between the two solutions. This offset could be caused by the truncation of harmonics as the distortion is transferred from the sliding plane onto the rotor. Furthermore, the sparse assembly force history exhibits a small fluctuation in time-averaged value. This could also be a consequence of the incomplete representation of the circumferential harmonics as the Fourier approximation never fully converges.

The HP rotor forces are shown in Figure 6.33. The low engine order excitation is clearly visible in the force history and Fourier spectrum. The reference spectrum contains 10 harmonics of the 2ND combustor distortion but the amplitudes of the first two harmonics, 2ND and 4ND, are more than twice as large as those of higher harmonics. The sparse assembly which is truncated to 5 harmonics therefore provides an adequate approximation of the low engine order forcing. The first, second and third HP stator blade passing frequencies are also present in the Fourier spectrum. The difference in amplitude of the fundamental blade passing frequency between the two solutions is approximately 3%. The effect of the downstream stator is not visible.

In the next stage, the IP stator experiences unsteady pressure fluctuations due to the upstream rotor and remains unaffected by the downstream rotor (Figure 6.34). It was seen earlier that the IP rotor disturbance is cut-off at the IP stator-rotor interface. The current observation hence confirms the assumption that disturbances which are cut-off at a blade row interface can legitimately be filtered from the solution. The unsteady forcing occurs at the frequency of the HP rotor passing and the frequency spectrum contains no further disturbances in either solution. Similarly

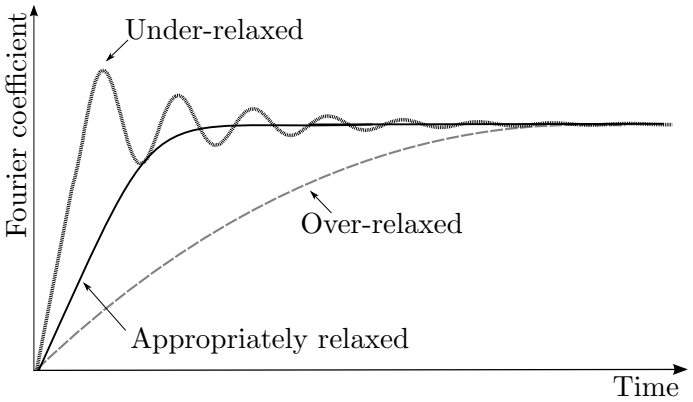


Figure 6.31.: Schematic of Fourier coefficient convergence for different relaxation factors

to the HP stator, the IP stator exhibits fluctuations in the time-averaged forces which point towards convergence problems. These could result from the harmonic truncation of the combustor distortion as suspected in the HP stator or from an inappropriate relaxation of unsteady perturbations in the IP stator. The different rotational speeds of the IP and HP spool combined with different blade counts in the IP and HP rotor give rise to multiple disturbances across a large frequency range. Although the IP rotor disturbance appears very weak, both IP and HP rotor passing frequencies are included in the Fourier approximation. The use of a common relaxation factor for the Fourier approximation leads to the over-relaxation of high frequency perturbations and under-relaxation of low frequency perturbations. An over-relaxation increases the time it takes for the Fourier coefficient to reach their final value while an under-relaxation can cause the Fourier coefficients to overshoot and oscillate around their converged value. This is graphically illustrate in Figure 6.31. As a result, the sparse assembly method underestimates the amplitude of the HP rotor disturbance by approximately 25%.

Figure 6.35 compares the IP rotor force history and its Fourier spectrum of the sparse assembly and reference solution. The low engine order disturbances from the combustor and IP stator blade passing are captured by both models. The reference solution contains a disturbance at the frequency of the HP stator passing which is not present in the approximate distortion transfer model because the disturbance cannot be represented in the IP stator. Note that the Fourier transform was evaluated over one revolution of the IP spool and hence fails to accurately present the rotor-rotor interaction. However, rotor-rotor coupling is absent from the reduced

passage model by construction. A separate Fourier analysis of the reference solution over one relative revolution of the HP and IP spools provided no further insights. The difference in amplitude of the 2ND disturbance between the two solutions is approximately 4.6%. This increases to approximately 8% for the second harmonic. The significant overestimation of the third harmonic is probably caused by aliasing of frequencies which are not included in the Fourier approximation. The amplitude of the IP stator passing disturbance is comparable in magnitude to the 2ND disturbance and appears approximately 6% larger in the reduced passage model.

Given the amount of simplification in the approximate distortion transfer model, the two results are in acceptable agreement. In particular the low engine order forcing in the rotor domains is well predicted and the relative significance of blade passing and LEO disturbances is captured.

The reduced passage model exhibits a slow convergence due to the truncation of harmonics as the distortion is transferred from the combustor to the stator domain. Even after 6 revolutions of the HP spool, or approximately two relative rotations of IP and HP spool, the solution does not reach a converged periodic state. This limits the practical use of the distortion transfer model for this particular application, since an approximate 2x speed-up can be achieved with the sparse assembly in terms of time per revolution (see Table 6.8). The model may still be of use for simpler applications with more sinusoidal distortions and smaller frequency separations.

6.2.5. Summary

The approximate distortion transfer model was applied to a two-stage turbine subject to a large wave length perturbation from the combustor. Given the number of simplifying assumptions made, the model offers a reasonable approximation to unsteady forcing in the rotor domains. In the stator domains, the incomplete representation of the combustor distortion causes a small offset in the time-averaged flow field. This and the wide frequency spectrum in the stator domain causes fluctuations and reduces the rate of convergence. Nevertheless, unsteady forces on the rotor blades are well captured. In terms of amplitude, the sparse assembly prediction lies within 5% of the reference solution for the fundamental distortion frequency. The relative magnitude of blade passing and combustor disturbances is well predicted by the approximate distortion transfer model. For this particular application, the computational savings offered by the sparse assembly model are minimal but bet-

ter results are expected for cases with more sinusoidal distortions and narrower frequency ranges.

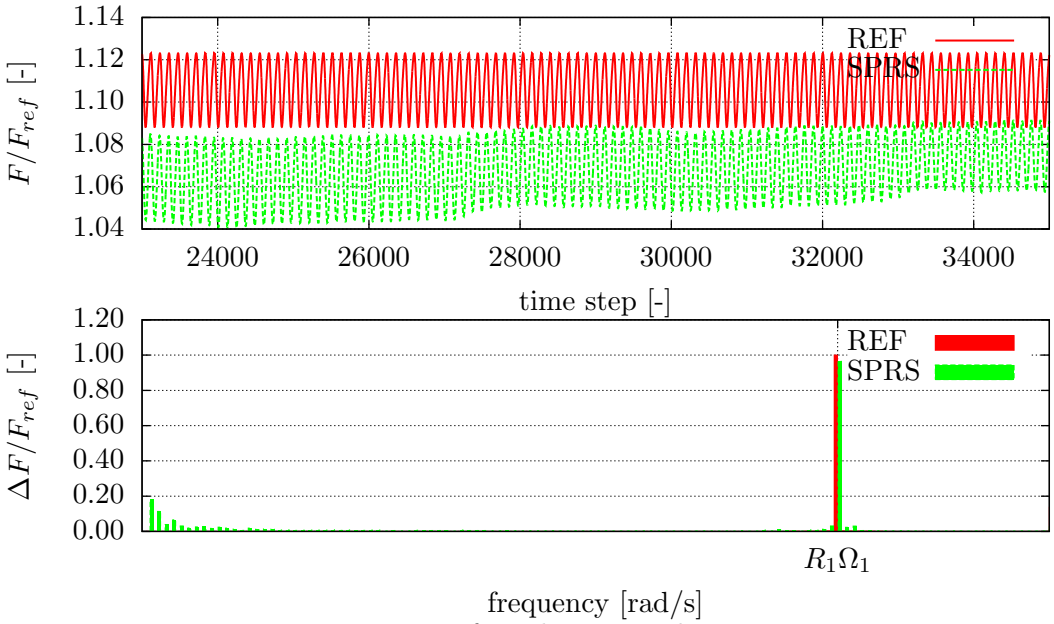


Figure 6.32.: HP stator force history and Fourier spectrum

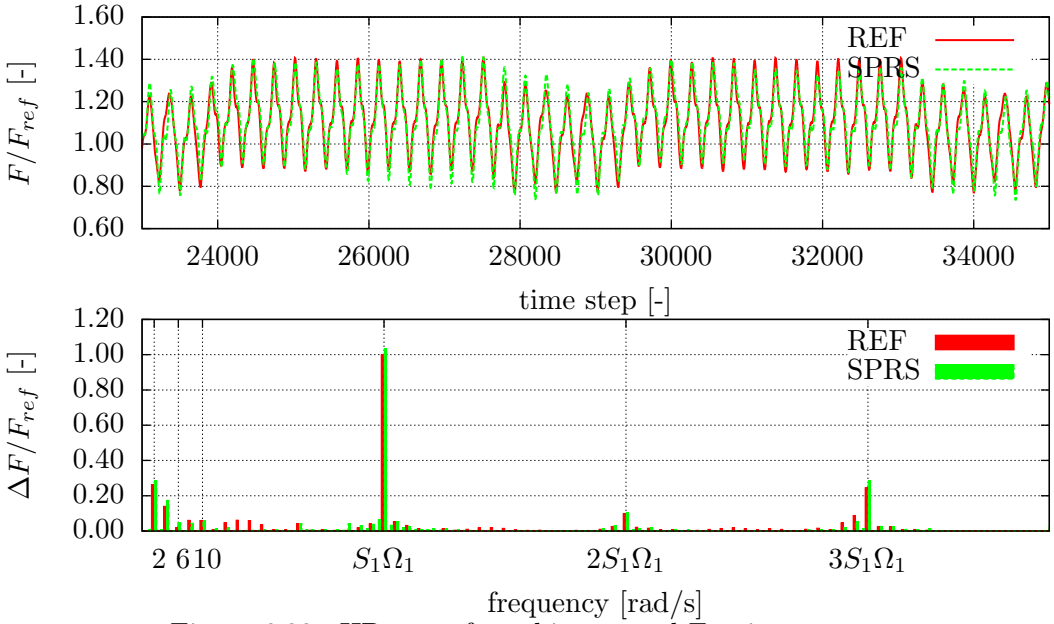


Figure 6.33.: HP rotor force history and Fourier spectrum

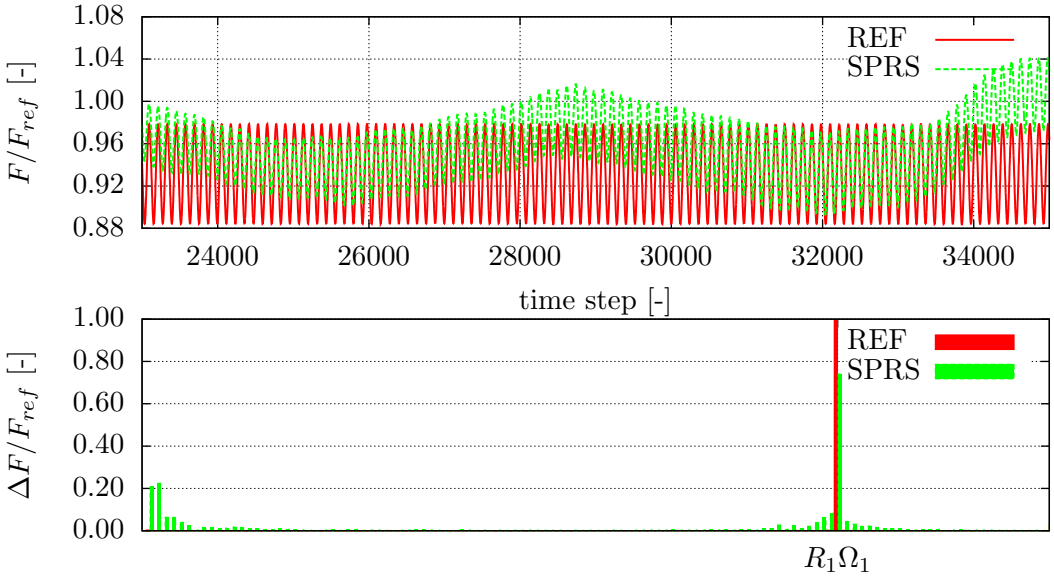


Figure 6.34.: IP stator force history and Fourier spectrum

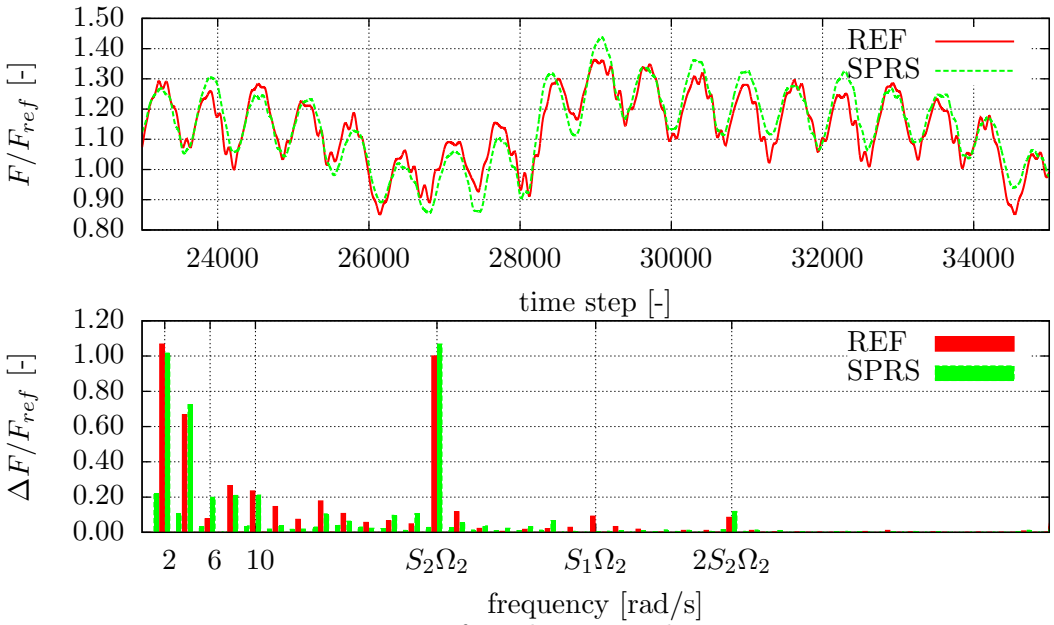


Figure 6.35.: IP rotor force history and Fourier spectrum

7. Conclusions and Recommendations

This chapter summarises the main achievements of this research and the findings presented in the previous chapters. It discusses the theoretical and practical limitations of the method and suggest potential improvements. Recommendations concerning future work are also made.

7.1. Accomplishment of objectives

The accomplishments of this work are summarised by addressing the main objectives which were set in Chapter 3 and are repeated here for clarity:

1. Formulation of a reduced-passage time-domain methods for steady and unsteady non-axisymmetric flows across multiple blade rows
2. Validation of this method for:
   (a) Steady flows with a stationary circumferential perturbation
   (b) Steady flows past non-axisymmetric configurations
   (c) Unsteady rotor-stator interaction with non-axisymmetry in the stator/rotor
   (d) Rotor-rotor (stator-stator) interaction
3. Assessment of the theoretical and practical limitations of the proposed method

All three objectives have been met by the work described in this thesis. A time-domain Fourier method for modelling steady and unsteady non-axisymmetric flows on a reduced number of passages was developed and validated on a range of turbomachinery applications. The method is theoretically limited by assumptions made during its formulation. During the course of this research further practical bounds were exposed and are summarised here. Each of the objectives is addressed in more detail in the following subsections.

7.1.1. Formulation of reduced-passage method

The method presented in Chapter 4 models steady and unsteady circumferential fluctuations on a reduced number of passages. It captures stationary circumferential variations by solving the flow inside several discrete passages. The passages are uniformly distributed over one wave length of the fundamental stationary disturbance and form a 'sparse assembly'. Boundary conditions at the azimuthal and inter-row surfaces are approximated from a time-space Fourier series and couple the individual passages. A phase-correction at the inter-row boundaries ensures the correct representation of disturbances in the sparse assembly domain.

7.1.2. Validation

The method was first validated for steady flows with stationary circumferential variations by applying it to an OGV with circumferential distortion at the outlet. The OGVs were then restaggered and the sinusoidal stagger pattern was modelled on the sparse assembly. A comparison of the full circumference and sparse assembly solution showed that the sparse assembly is capable of capturing outlet distortions with varying harmonic content as well as circumferential variations in the geometry.

A part-span study of a turbine stage with sinusoidal throat area variation validated the method for unsteady rotor-stator interaction with aerodynamic mistuning. It was demonstrated that the method provided a good approximation to unsteady rotor forcing in both subsonic and transonic flows.

The reduced passage model was then applied to a 1.5 stage compressor to validate it for multi-stage flows. A comparison with the full circumference solution proved that the approach is capable of predicting unsteadiness in an embedded blade row as well as circumferential variations caused by rotor-rotor/stator-stator interactions.

7.1.3. Assessment of theoretical and practical limitations

The method presented in this thesis relies on a time-space Fourier decomposition of the flow field. It is thus restricted to spatially and temporally periodic flows. Any stationary perturbations must be of a harmonic nature and the number of representable harmonics is limited by the number of passages in the sparse assembly as explained in Section 4.1.3 and demonstrated in Section 5.2.2. Difficulties thus arise when disturbances with large harmonic content are represented on a small

number of passages as attempted in the distortion transfer case (Section 6.2).

With regards to the unsteadiness, it is assumed that the time scales of interest are much larger than the time scales associated with turbulence (an implicit assumption if implemented in a RANS solver). To satisfy the time-space periodicity requirements, the unsteadiness must furthermore take the shape of a travelling wave with constant angular velocity and its circumferential wave number and frequency must be known *a priori*. This is the case for most types of forced response or flutter. If strong flow separations or vortex shedding dictate the unsteadiness, phase-lagged boundary conditions cannot be applied. The reduced passage model is therefore not able to model non-synchronous vibrations, rotating stall or surge.

From a practical point of view, a few further limitations became apparent during the validation procedure. Convergence of the Fourier approximation is increasingly slowed as more and more blade rows are added. This was observed in the 1.5 stage compressor (Section 5.4) and in the multi-stage turbine (Section 6.2) and minimises the computational advantage of the reduced passage model. The dependence of convergence speed on row numbers is not surprising, since the solution must converge in one row before it can correctly be transferred to adjacent rows.

Convergence problems also arise if a common relaxation factor is applied across a wide range of frequencies. This inevitably leads to an over-relaxation of high frequencies and under-relaxation of low frequencies which promotes fluctuations in the time-average as seen in the 1.5 stage compressor (Section 5.4) and in the multi-stage turbine (Section 6.2). Updating every frequency at a different rate is impossible since the signal cannot be split into its components before the Fourier coefficients have converged. The common relaxation factor is also responsible for a lower convergence rate of the higher harmonics compared to the lower harmonics.

7.2. Recommendations for future work

The method presented in this thesis provides an efficient means of approximating flows with stationary circumferential variations as caused by distortions, geometric variations or the interaction of rows in the same frame of reference. However, the studies performed are not exhaustive and a wider range of applications must be analysed to build a complete understanding of the advantages and disadvantages of the time-domain Fourier model.

The method's performance in transonic flows with oscillating shock waves, for

example, is yet to be assessed. Further insights into distortion transfer modelling may be gained by studying the propagation of a sinusoidal disturbance through multiple stages, preferably on a single spool. The sparse assembly's ability to capture multi-stage interaction can also be used for the prediction of embedded row flutter. This requires no further developments, as the vibrating frequency can be modelled with well established phase-lagged boundary conditions.

A major restriction of the time-domain Fourier method, and indeed any harmonic method, is the need to know the frequencies and wave numbers prior to the computation. Particularly for multi-stage calculations it is often impossible to know which interaction modes will be relevant and which can safely be neglected. Previous research has shown that a few blade passing harmonics and the interaction modes with the lowest circumferential wave numbers are often sufficient to capture multi-stage coupling. Nevertheless, the selection of spinning modes remains *"more art than science"* [45]. A conservative approach thus often leads to the inclusion of unnecessary many frequencies. If relevant spinning modes were identified beforehand, for example by means of low fidelity models or a circumferential Fourier decomposition of the steady flow field, computational costs of Fourier methods could be reduced.

Another issue of the time-domain Fourier approach is the slow convergence rate of flows with a wide frequency range caused by a common relaxation factor. A potential solution would be to adjust the relaxation factor over time such that it is suitable for the lowest frequencies at the beginning of the computation and raised to match the higher frequencies once the lower frequencies have converged. It may also be possible to adjust the time step and initially use a relatively coarse resolution for high frequencies thus allowing low frequencies to converge at a faster rate.

Convergence may also be accelerated by the use of non-reflecting treatments at the blade row boundaries. Since the boundary conditions require several disturbance cycles to reach a periodic state, a mismatch between the internal flow solution and the boundary conditions exists at the beginning of the calculation. This mismatch may cause waves to reflect from the azimuthal or inter-row boundaries and cause unphysical fluctuations which hinder convergence. A non-reflecting treatment based on characteristic theory or numerical damping near the boundaries will remove spurious reflections and may accelerate convergence.

Bibliography

[1] *Multilingual aeronautical dictionary*. Advisory Group for Aerospace Research and Development, 1980.

[2] *Lecture Series: Blade Row Interference Effects in Axial Turbomachinery Stages*. VKI, 1998-02.

[3] W. Schmidt A. Jameson and E. Turkel. Numerical solution of the Euler equations by finite volume methods using Runge-Kutta time-stepping schemes. *AIAA Paper 81-1259*, 1981.

[4] J.J. Adamczyk. Model equations for simulating flows in multistage turbomachinery. *ASME Paper 85-GT-226*, 1985.

[5] A. Arnone, M. Marconcini, R. Pacciani, C. Schipani, and R. Spano. Numerical investigation of airfoil clocking in a three-stage low pressure turbine. *ASME Paper 2001-GT-0303*, 2001.

[6] H. Atassi and T.J. Akai. Aerodynamic and aeroelastic characteristic of oscillating loaded cascades at low Mach number: Part 1: Pressure distribution, forces and moments. *ASME Paper 79-GT-181*, 1979.

[7] O.O. Bendiksen and P. Friedmann. Coupled bending torsion flutter in cascades. *British Aeronautical Research Council*, (ARC R&M 3386), 1980.

[8] A. Boelcs. Transonic flow in turbomachines. In *Lecture Series: Computerized Educational Platform Heat and Power Technology*, Stockholm/Lausanne, 2005.

[9] M. P. Boyce. *Gas Turbine Engineering Handbook*. Gulf Professional Publishing, Butterworth-Heinemann, 2002.

[10] W. Campbell. Protection of steam turbine disk wheels from axial vibration. *Transactions of the ASME*, pages 31–160, 1924.

[11] M.S. Campobasso and M.B. Giles. Effects of flow instabilities on the linear analysis of turbomachinery aeroelasticity. *Journal of Propulsion and Power*, 19:250–259, 2003.

[12] L. Castillon. Evaluation of a multiple frequency phase-lagged method for unsteady numerical simulations of multistage turbomachinery. In *28. International Congress of the Aeronautical Sciences*, Brisbane, Australia, September 2012.

[13] T. Chen, P. Vasanthakumar, and L. He. Analysis of unsteady blade row interaction using a nonlinear harmonic approach. *Journal of Propulsion and Power*, 17(3):651–658, 2001.

[14] J.P. Clark, G.M. Stetson, S.S. Magge, R.H. Ni, C.W. Haldemann, and M.G. Dunn. The effect of airfoil scaling on the predicted unsteady loading on the blade of a 1 and 1/2 stage transonic turbine and a comparison with experimental results. *ASME Paper 2000-GT-0446*, 2000.

[15] S.T. Clark, R.E. Kielb, and K.C. Hall. Developing a reduced-order model to understand non-synchronous vibration (NSV) in turbomachinery. In *Proceedings of ASME Turbo Expo 2012*, 2012.

[16] W.S. Clark and K.C. Hall. A time-linearized Navier-Stokes analysis of stall flutter. *Journal of Turbomachinery*, 122:467–476, 2000.

[17] A.R. Collar. The expanding domain of aeroelasticity. *Journal of the Royal Aeronautical Society*, 50:613–636, 1946.

[18] E.F. Crawley. Aeroelastic formulation for tuned and mistuned rotors. *AGARD-AG-298*, 2:19.1–19.24, 1987.

[19] E.F. Crawley and E.H. Ducharme. Parametric trends in the flutter of advanced turboprops. *Journal of Turbomachinery*, 112:741–750, 1990.

[20] N.A. Cumpsty and E.M. Greitzer. Ideas and method of turbomachinery aerodynamics: A historical review. *Journal of Propulsion and Power*, 20, 2006.

[21] N.A. Cumpsty and J.A. Horlock. Averaging uniform flow for a purpose. *Journal of Turbomachinery*, 128:120–129, 2006.

[22] J.D. Denton. Extension of finite volume time marching method to three dimensions. *VKI Lecture Series*, 7, 1979.

[23] J.D. Denton. Calculation of 3d viscous flow through multi-stage turbomachines. *Journal of Turbomachinery*, 114, 1992.

[24] J.D. Denton. The effects of lean and sweep on transonic fan performance: A computational study, 2002.

[25] S. Dewhurst and L. He. Unsteady flow calculations through turbomachinery stages using single passage domain with shape corrrection method. In *9th International Symposium on Unsteady Aerodynamics and Aeroelasticity in Turbomachines*, Lyon, France, September 2000.

[26] H. Doi. *Fluid/structure coupled aeroelastic computations for transonic flows in turbomachinery*. PhD thesis, Stanford University, 2002.

[27] D.J. Dorney, R.R. Croft, D.L. Sondak, U.E. Stand, and C.Z. Twardochleb. Computational study of clocking an embedded stage in a 4-stage industrial turbine. *ASME Paper 2001-GT-0609*, 2001.

[28] D.J. Dorney, O.P. Sharma, and K.L. Gundy-Burlet. Physics of airfoil clocking in a high speed axial compressor. *ASME Paper 98-GT-082*, 1998.

[29] K. Ekici and K.C. Hall. Linear frequency-domain analysis of unsteady flows in turbomachinery with multiple excitation frequencies. *AIAA Journal*, 46(8):1912–1920, 2008.

[30] K. Ekici, D.M. Voytovycht, and K.C. Hall. Time-linearized Navier-Stokes analysis of flutter in multistage turbomachines. In *43rd AIAA Aerospace Sciences Meeting and Exhibit*, pages 14259–14277. AIAA, 2005.

[31] J.I. Erdos, E. Alzner, and W. McNally. Numerical solution of periodic transonic flow through a fan stage. *AIAA Journal*, 15(11):1559–1568, 1977.

[32] T.H. Fransson. *Lecture Series: Aeroelasticity in Axial Flow Turbomachines*, chapter Dynamic Aeroelasticity. VKI, 1999-05.

[33] G. Fritsch and M.B. Giles. An asymptotic analysis of mixing loss. *Journal of Turbomachinery*, 117:367–374, 1995.

[34] G. A. Gerolymos, G. J. Michon, and J. Neubauer. Analysis and application of chorochronic periodicity in turbomachinery rotor/stator interaction computations. *Journal of Propulsion and Power*, 18(6):1139–1152, 2002.

[35] G. A. Gerolymos, G. J. Michon, and J. Neubauer. Filtered chorochronic interface as a capability for 3-d unsteady throughflow analysis of multistage turbomachinery. *International Journal of Computational Fluid Dynamics*, 27(2):110–117, 2013.

[36] M.B. Giles. Non-reflecting boundary conditions for the Euler equations, 1988.

[37] M.B. Giles. Stator-rotor interaction in a transonic turbine. *Journal of Propulsion and Power*, 6(5):621–627, 1990.

[38] M.B. Giles. SLIQ: A numerical method for the calculation of flow in multistage turbomachinery, 1991.

[39] A.K. Gopinath and A.Jameson. Time spectral method for periodic unsteady computations over two- and three-dimensional bodies. *AIAA Paper 2005-1220*, 2005.

[40] N. Gourdain. *Simulation numérique des phénomènes de décollement tournant dans les compresseurs axiaux*. PhD thesis, Ecole Centrale Lyon, 2005.

[41] J.S. Green. Forced response prediction within the design process. In *3rd European Conference on Turbomachinery*, 1999.

[42] L W Griffin, F W Huber, and Scharma O P. Performance improvement through indexing of turbine airfoils: Part 2: Numerical simulation. *Journal of Turbomachinery*, 118:636–642, 1996.

[43] K. C. Hall, J. P. Thomas, and W. S. Clark. Computation of unsteady nonlinear flows in cascades using a harmonic balance technique. *AIAA Journal*, 40(5):879–886, 2002.

[44] K.C. Hall and E F Crawley. Calculation of unsteady flow in turbomachinery using the linearised Euler equations. *AIAA Journal*, 27:777, 1989.

[45] K.C. Hall and K. Ekici. Multistage coupling for unsteady flows in turbomachinery. *AIAA Journal*, 43(3):624–632, 2005.

[46] K.C. Hall, C.B. Lorence, and W.S. Clark. Non-reflecting boundary conditions for linearized unsteady aerodynamic calculations. *AIAA Paper 93-0882*, 1993.

[47] D.E. Halstead, D.C. Wisler, T.H. Okiishi, G.J. Walker, H.P. Hodson, and H.W. Shin. Boundary layer development in axial compressors and turbines: Part 3 of 4 - LP turbines. *Journal of Turbomachinery*, 119(1):225–237, 1997.

[48] L. He. An Euler solution for unsteady flows around oscillating blades. *Journal of Turbomachinery*, 112(4):714–722, 1990.

[49] L. He. Method of simulating unsteady turbomachinery flows with multiple perturbations. *AIAA Journal*, 30(11):2730–2735, 1992.

[50] L. He. *Handbook of Turbomachinery*. 1995.

[51] L. He. Computational study of rotating-stall inception in axial compressors. *Journal of Propulsion and Power*, 13(1):31–38, 1996.

[52] L. He. Fourier modelling of non-axisymmetrical steady and unsteady flows. *Journal of Propulsion and Power*, 22(1):197–201, 2006.

[53] L. He. Fourier methods for turbomachinery applications. *Progress in Aerospace Sciences*, 46(8):329–341, 2010.

[54] L. He. Efficient computational model for non-axisymmetric flow and heat transfer in rotating cavity. *Journal of Turbomachinery*, 133(2):021018–9, 2011.

[55] L. He, T. Chen, R. G. Wells, Y. S. Li, and W. Ning. Analysis of rotor-rotor and stator-stator interferences in multi-stage turbomachines. *Journal of Turbomachinery*, 124(4):564–571, 2002.

[56] B. Hellmich and J.R. Seume. Causes of acoustic resonance in a high-speed axial compressor. *Journal of Turbomachinery*, 130:031003–1, 2008.

[57] C. Hirsch. *Numerical Computation of Internal and External Flows*. Butterworth-Heinemann, 2007.

[58] D.H. Hodges and G.A. Pierce. *Introduction to Structural Dynamics and Aeroelasticity*. Cambridge University Press, 2002.

[59] D.G. Holmes, B.E. Mitchell, and C.B. Lorence. Three dimensional linearized Navier-Stokes calculations for flutter and forced response. In *8th International Symposium on Unsteady Aeordynamics and Aeroelasticity in Turbomachinery*, 1997.

[60] F.W. Huber, P.D. Johnson, and O.P. Sharma. Performance improvement through indexing of turbine airfoils, Part 1 and Part 2. *ASME Paper GT-27, GT-28*, 1995.

[61] A. Kessar, M. Jöcker, and T.H. Fransson. Flow measurements for low engine order excitations in a high pressure turbine stage. In *6th European Conference on Turbomachinery*, 2005.

[62] Prof Joseph Hammond Kihong Shin. *Fundamentals of Signal Processing for Sound and Vibration Engineers*. John Wiley and Sons, 2008.

[63] F Lane. System mode shapes in the flutter of compressor blade rows. *Journal of Aeronautical Sciences*, 23:54–66, 1956.

[64] C.B. Laney. *Computational Gas Dynamics*. Cambridge University Press, 1998.

[65] R. J. LeVeque. *Numerical methods for conservation laws*. Birkhäuser, 1992.

[66] H. Li and L. He. Single-passage solution of three-dimensional unsteady flows in a transonic fan rotor. *Proceedings of the Institution of Mechanical Engineers, Part A: Journal of Power and Energy*, 215(6):653–662, 2001.

[67] H. Li and L. He. Blade count and clocking effects on three-bladerow interaction in a transonic turbine. *ASME Journal of Turbomachinery*, 125(1):632–640, 2003.

[68] H. D. Li and L. He. Single-passage analysis of unsteady flows around vibrating blades of a transonic fan under inlet distortion. *Journal of Turbomachinery*, 124(4):564–571, 2002.

[69] H. D. Li and L. He. Blade aerodynamic damping variation with rotor-stator gap: A computational study using single-passage approach. *Journal of Turbomachinery*, 127(3):573–579, 2005.

[70] H. D. Li and L. He. Toward intra-row gap optimization for one and half stage transonic compressor. *Journal of Turbomachinery*, 127(3):589–598, 2005.

[71] D R Lindquist and M B Giles. Validity of linearized unsteady Euler equations with shock capturing. *AIAA Journal*, 32:46, 1994.

[72] L.Sbardella, A.I. Sayma, and M. Imregun. Semi-unstructured mesh generator for flow calculations in axial turbomachinery blading. In *8th International Symposium on Unsteady Aerodynamics and Aeroelasticity of Turbomachines*. Kluwer Academic Publishers, 1997.

[73] J.G. Marshall and M. Imregun. A review of aeroelasticity methods with emphasis on turbomachinery applications. *Journal of Fluids and Structures*, 10:237–267, 1996.

[74] S. Mata, L. di Mare, M. Imregun, and J. Green. An efficient generalised single-passage method for turbomachinery forced response. In *Proceedings of the 12th International Symposium on Unsteady Aerodynamics, Aeroacoustics and Aeroelasticity of Turbomachines*, London, UK, September 2009.

[75] M.A. Mayorca, J.A. de Amdrade, D.M.Vogt, H.Martenson, and T.H. Fransson. Effect of scaling of blade row sectors on the prediction of aerodynamic forcing in a highly loaded transonic compressor stage. *Journal of Turbomachinery*, 133:021013, 2011.

[76] W.D. McNally. Review of experimental work on transonic flow in turbomachinery. In *Transonic Flow Problems in Turbomachinery*. Hemisphere Publishing Corporation, London, 1977.

[77] W.D. McNally and P.M. Sockol. Review - Computational methods for internal flows with emphasis on turbomachinery. *Journal of Fluids Engineering*, 107:6–22, 1985.

[78] P. Moinier and M.B. Giles. Eigenmode analysis for turbomachinery applications. *Journal of Propulsion and Power*, 23(5):981–986, 2005.

[79] R.H. Ni and F.Sisto. Numerical computation of nonstationary aerodynamics of flat plate cascades in compressible flow. *Journal of Engineering for Power*, 98:165–170, 1976.

[80] W. Ning and L. He. Computation of unsteady flows around oscillating blades using linear and linear harmonic Euler methods. *Journal of Turbomachinery*, 120(3):508–514, 1998.

[81] M. Olausson and L.-E. Eriksson. An absorbing inlet buffer layer for rotor wake/stator time domain computations. *ASME Paper GT2009-59346*, 2009.

[82] R. Parker. Relation between blade row spacing and potential flow interaction effects. *Proceedings of the Institution of Mechanical Engineers*, 184, 1969.

[83] E. Petrov, L. di Mare, H. Hennings, and R. Elliot. Forced response of mistuned bladed disks in gas flow: A comparative study of predictions and full-scale experimental results. *Journal of Engineering for Gas Turbines and Power*, 132, 2010.

[84] M.M. Rai. Navier-Stokes simulations of rotor-stator interaction using patched and overlaid grids. *AIAA Journal*, (1):282–298, 1985.

[85] M.M. Rai. Implicit conservative zonal boundary scheme for Euler equations calculations. *Computers and Fluids*, 14(3):295–319, 1986.

[86] H.J. Rehder, F. Kost, and A.Kessar. Low engine order only tests at DLR, 2002.

[87] S.K. Richards, X. Zhang, X.X. Chen, and P.A. Nelson. The evaluation of non-reflecting boundary conditions for duct acoustic computation. *Journal of Sound and Vibration*, 270:539–557, 2004.

[88] P.L. Roe. Approximate Riemann solvers, parameter vectors and difference schemes. *Journal of Computational Physics*, 43:357–372, 1981.

[89] G. Saiz. *Turbomachinery Aeroelasticity Using a Time-Linearized Multi Blade-Row Approach*. PhD thesis, University of London, Imperial College London of Science Technology and Medicine, 2008.

[90] A.P. Saxer and M.B. Giles. Quasi-three-dimensional reflecting boundary conditions for Euler equations calculations. *Journal of Propulsion and Power*, 9:263–271, 1993.

[91] A.I. Sayma, M. Vahdati, J.S. Green, and M. Imregun. Whole-assembly flutter analysis of a low pressure turbine blade. *Aeronautical Journal*, 102:459–463, 1998.

[92] A.I. Sayma, M. Vahdati, and M. Imregun. Multistage whole annulus forced response predictions using an integrated linear analysis technique, Part 1: Numerical model. *Journal of Fluids and Structures*, 14(1):87–101, 2000.

[93] L. Sbardella, A. Sayma, and M. Imregun. Semi-structured meshes for axial turbomachinery blades. *International Journal for Numerical Methods in Fluids*, 32(5):569–584, 2000.

[94] J. Schlienger, A.I. Kalfas, and R.S. Abhari. Vortex-wake-blade interaction in a shrouded axial turbine. *Journal of Turbomachinery*, 127:699–707, 2005.

[95] M. B. Schmitz, O. Schäfer, J. Szwedowicz, T. Secall-Wimmel, and T. P. Simmer. Axial turbine blade vibrations induced by the stator flow: Comparison of calculations and experiment. Torus Press Ltd, Moscow, 2006.

[96] C.E. Shannon. Communication in the presence of noise. *Proc. Institute of Radio Engineers - reprinted in Proc. IEEE 1998*, 37:10–21, 1949.

[97] P.D. Silkowski and K. C. Hall. A coupled mode analysis of unsteady multistage flows in turbomachinery. *Journal of Turbomachinery*, 120(1):410–421, 1998.

[98] F. Sisto. *A Modern Course in Aeroelasticity.* 1995.

[99] S.N. Smith. Discrete frequency generation in axial flow turbomachines, 1972.

[100] P.R. Spalart and S.R Allmaras. A one-equation turbulence model for aerodynamic flows. *AIAA Paper 92-0439*, 1992.

[101] A. V. Srinivasan. Flutter and resonant vibration characteristics of engine blades. *Journal of Engineering for Gas Turbines and Power*, 119:742–775, 1997.

[102] S. C. Stapelfeldt and L. di Mare. Modelling flow past non-axisymmetric configurations on reduced passage counts. In *13th International Symposium on Unsteady Aerodynamics, Aeroacoustics and Aeroelasticity in Turbomachinery*, Tokyo, Japan, 2012.

[103] S. C. Stapelfeldt and L. di Mare. Modelling rotor-rotor interaction on reduced passage counts. In *10th European Conference on Turbomachinery*, Lappeenranta, Finland, 2013.

[104] R.C. Swanson and E. Turkel. On central-difference and upwind schemes. *Journal of Computational Physics*, 101:292–306, 1992.

[105] T. Theodorsen. General theory of aerodynamic instability and the mechanism of flutter, 1934.

[106] J.M. Tyler and T.G. Sofrin. Axial flow compressor noise studies. *SAE Transactions*, 70:309–332, 1962.

[107] D.S. Whitehead. Force and moment coefficients for vibrating airfoils in cascade. *British Aeronautical Research Council*, (ARC R&M 3254), 1960.

[108] D.S. Whitehead. Bending flutter of unstalled cascade blades at finite deflection. *British Aeronautical Research Council*, (ARC R&M 3386), 1962.

[109] D.S. Whitehead. The effect of compressibility on unstalled torsion flutter, 1973.

[110] D.S. Whitehead. *AGARD Manual on aeroelasticity in axial flow turbomachines - Structural Dynamics and Aeroelasticity*, 2(AGARD-AG-298):1–30, 1988.

[111] D.C. Wisler. *Handbook of Fluid Dynamics: Axial Flow Compressor and Fan Aerodynamics*. CRC Press LLC and Springer-Verlag GmbH, 1998.

[112] D.C. Wisler and H.W. Shin. *Lecture Series: Blade Row Interference Effects in Axial Turbomachinery Stages*. VKI, 1998-02.

[113] D. Van Zante, J. Chen, M. Hathaway, and R. Chriss. The influence of compressor blade row interaction modeling on performance estimates from time-accurate, multi-stage, Navier-Stokes simulations. *Journal of Turbomachinery*, 130:11009–1, 2008.

A. Appendix

A.1. Flow solver

The methodology developed in the main part of this thesis was implemented in a finite volume compressible flow solver developed by Sayma et al. [92].

We start from the three-dimensional, unsteady, compressible Favre-averaged Navier Stokes equations for a control volume Ω with boundary Γ written in conservative form as:

$$\frac{d}{dt}\int_{\Omega}\mathbf{U}d\Omega+\int_{\Gamma}(\mathbf{F}-\frac{1}{Re}\mathbf{G})\cdot\mathbf{n}d\Gamma=\int_{\Omega}\mathbf{S}d\Omega \tag{A.1}$$

where $\vec{n}$ represents the outward unit vector of the boundary Γ and the solution vector $\mathbf{U}$, inviscid flux vector F and viscous flux vector G are given by:

$$\mathbf{U}=\begin{pmatrix}\rho\\ \rho\mathbf{u}\\ \rho e\end{pmatrix} \tag{A.2}$$

$$\mathbf{F}=\mathbf{U}\mathbf{v}+\begin{pmatrix}0\\ p\delta_{ij}\\ u_j p\end{pmatrix} \tag{A.3}$$

where $\mathbf{u}=(u_i,u_j,u_k)^T$ is the vector of absolute velocities and $v=(v_i,v_j,v_k)$ is the vector of relative velocities in Cartesian coordinates $\mathbf{x}=(x_i,x_j,x_k)$ and δ_{ij} represents the Kronecker delta function.

For a perfect gas (i.e. a gas satisfying the ideal gas law $P=\rho RT$ and equation of state $e=C_vT$ or $h=C_pT$) the pressure p and total enthalpy h can be expressed in terms of the density ρ, absolute velocity u and internal energy e:

$$p = (\gamma - 1)\rho\left(e - \frac{1}{2}|\mathbf{u}|^2\right) \quad h = e + \frac{p}{\rho} \tag{A.4}$$

where $\gamma = \frac{C_p}{C_v}$ is the ratio of specific heats. For a rotating blade row, Equation A.1 can be solved in a relative Non-Newtonian reference frame rotating with the blades at angular velocity ω.

The viscous flux vector G contains the following terms:

$$\mathbf{G} = \begin{pmatrix} 0 \\ \sigma_{ij} \\ u_k\sigma_{ik} + \frac{\gamma}{\gamma-1}\left(\frac{\mu_l}{Pr_l} + \frac{\mu_t}{Pr_t}\right)\frac{\partial T}{\partial x_i} \end{pmatrix} \tag{A.5}$$

where the stress tensor σ_{ij} is given by:

$$\sigma_{ij} = \mu\left(\frac{\partial u_i}{\partial x_j} + \frac{\partial u_i}{\partial x_j}\right) + \lambda\delta_{ij}(\nabla \cdot \mathbf{u}) \tag{A.6}$$

$$\tag{A.7}$$

In the above evaluation of the stress tensor μ is the total viscosity of the fluid:

$$\mu = \mu_l + \mu_t \tag{A.8}$$

The terms involving the *molecular viscosity coefficient* μ_l describes the transport of momentum and energy through random molecular motion which prevails in laminar flow. The molecular viscosity is determined from Sutherland's law. The transport of energy and momentum by random motion of large turbulent eddies is expressed by the concept of eddy viscosity which assumes that the turbulent viscous stresses are proportional to the mean velocity gradients (analogous to viscous stresses in laminar flow). The coefficient of proportionality or *turbulent eddy viscosity* μ_t must be calculated by an appropriate turbulence model. All cases in the main body of this thesis use the one-equation turbulence model by Spalart and Allmaras [100]. The last term in Equation A.6 represents the *bulk viscosity* or the viscous-induced normal forces acting on a control volume in addition to the pressure. The *bulk viscosity coefficient* λ takes the value $-\frac{2}{3}\mu$ proposed by Stokes. The laminar and turbulent Prandtl numbers are taken as $Pr_l = 0.7$ and $Pr_t = 0.9$ respectively. In

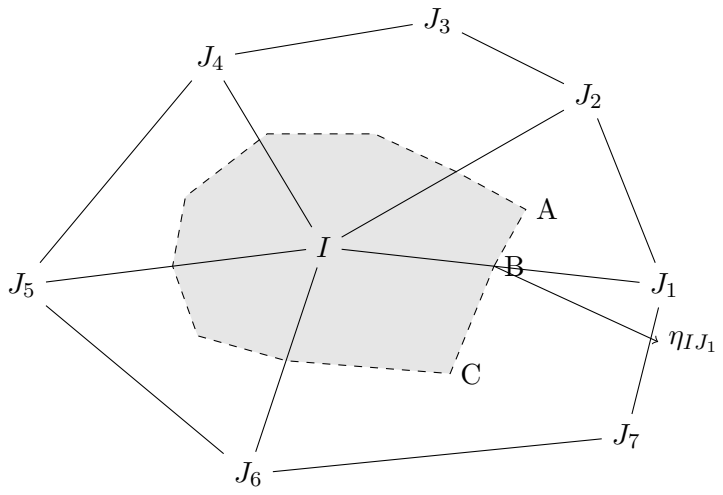


Figure A.1.: 2D vertex-centred grid cell (solid lines=grid lines, dashed lines=control volume boundaries (originally from Sayma et al. [92])

Equation A.1 the viscous flux vector is non-dimensionalised by the Reynolds number.

The source term in Equation A.1 is given by:

$$S = \begin{pmatrix} 0 & 0 & \rho\omega u_2 & \rho\omega u_3 & 0 \end{pmatrix}^T \tag{A.9}$$

A.1.1. Numerical discretisation

The spatial domain is discretised using semi-structured grids created by an in-house mesh generator [72]. A pre-processor step translates a structured or unstructed mesh into pairs of nodes linked by edges and calculates the edge weights at inter-cell boundaries. The solver stores flow variables at the cell vertices and evaluates numerical fluxes along the cell edges.

The numerical scheme will be explained in more detail for a two dimensional cell as shown in Figure A.1. Let node I denote the grid point at the centre of the cell. The point is connected to node J_S by the edge $S_{IJ_S} = |(\mathbf{x}_{J_S} - \mathbf{x}_I)|$. The total number of nodes connected to I will be denoted by n_S. The control volume around internal node I is formed by connecting the centroids of cells surrounding node I and the midpoint of the edges S_{IJ_S}. The resulting volume is known as as the median dual

around node I. Equation A.1 can then be written in semi-discrete form as:

$$\frac{d}{dt}(\Omega_I \mathbf{U}_I) + \sum_{s=1}^{n_S} \frac{1}{2} |\vec{\eta}_{IJ_s}| (\mathbf{F}_{IJ_s} - \mathbf{G}_{IJ_s}) + B_I = \Omega_I \mathbf{S}_I \tag{A.10}$$

where U_I is the solution vector at node I and B_I is the boundary integral and F_{IJ_s} and G_{IJ_s} are the inviscid and viscous numerical fluxes along side IJ_s. The weight of a side $\vec{\eta}_{IJ_s}$ is found by summing the two dual medians connecting the edge centre with the centroid of the adjacent cells and taking the normal vector. The weight of side IJ_1, for example, is calculated as follows:

$$\vec{\eta}_{IJ_1} = -\vec{\eta}_{J_1 I} = \vec{AB} + \vec{BC} \tag{A.11}$$

A central scheme with artificial viscosity developed by by Swanson and Turkel [104] is used to evaluate the inviscid fluxes. The numerical flux along side IJ_S is written as:

$$F_{IJ_s} = \frac{\vec{\eta}_{IJ_s}}{|\vec{\eta}_{IJ_s}|} \cdot (\mathbf{F}_I + \mathbf{F}_{J_s}) - \mathbf{D}_{IJ_s} \tag{A.12}$$

where the integral of the artificial dissipation $\mathbf{D}_{IJ_s}$ is given by:

$$\mathbf{D}_{IJ_s} = |\mathbf{A}_{IJ_s}| \left[\Phi(\mathbf{U}_{J_s} - \mathbf{U}_I) - \epsilon_4(1-\Phi)(\mathscr{L}(U_{J_s}) - \mathscr{L}(U_I))\right] \tag{A.13}$$

where $\mathbf{A}_{IJ_s}$ is the Roe matrix [88] and

$$\mathscr{L}(\mathbf{U}_I) = \left(\sum_{s=1}^{n_S} \frac{\mathbf{U}_{J_s} - \mathbf{U}_I}{S_{IJ_s}}\right) \left(\sum_{s=1}^{n_S} \frac{1}{S_{IJ_s}}\right)^{-1} \tag{A.14}$$

is the pseudo-Laplacian operator.

The second order flux limiter Φ ensures monotonicity of the scheme:

$$\Phi = \max(\Phi_I, \Phi_{J_s}) \tag{A.15}$$

$$\Phi_I = \frac{2|p_{J_s} - p_I - \mathbf{S}_{IJ_s}(\nabla p)_{J_s}|}{\left(\begin{smallmatrix}(1-\omega)[|p_{J_s}-p_I|+|p_I-p_{J_s}+2(\nabla p)_{J_s}S_{IJ_s}|] \\ +2\omega[p_{J_s}-P_I+S_{IJ_s}(\nabla p)]\end{smallmatrix}\right)} \tag{A.16}$$

This pressure switch is based on the switch by Swanson and Turkel [104]:

$$\Phi_i = \frac{|p_{i+1} - 2p_i + p_{i-1}|}{(1-\omega)[|p_{i+1} - p_i| + |p_i - p_{i-1}|] + \omega[p_{i+1} + 2p_i + p_{i-1}]} \tag{A.17}$$

where node I and node J_s are substituted for pressures at nodes i and $i+1$ respectively. The pressure at node $i-1$ is approximated from the local pressure gradient and vector $S_{IJ_s} = |\mathbf{x}_{J_s} - \mathbf{x}_I|$. The parameter ω in the denominator is ≈ 0.5. If $\omega << 1$ a limiter of the form

$$\Phi_i = \frac{|p_{i+1} - 2p_i + p_{i-1}|}{[|p_{i+1} - p_i| + |p_i - p_{i-1}|] + \epsilon} \tag{A.18}$$

is recovered, where $\epsilon << 1$ prevents a zero denominator in regions of uniform pressure.

The pressure sensor reverts the scheme to Roe's first order upwind method in the vicinity of discontinuities where $\Phi_{i+1/2} \approx 1$. The second-order dissipation term then damps numerical oscillations. In smooth regions of the flow, the shock switch is approximately zero and the scheme becomes biased towards the second-order flux where the fourth order dissipation ensures stability. Since the fourth order artificial viscosity may be destabilising near shocks, the parameter $\epsilon^{(4)}$ is introduced which sets the fourth order viscosity to zero if $|\Phi| > \epsilon^{(4)}$. The value for the artificial dissipation coefficient ϵ_4 is taken as $\approx 1/8$. The hybrid method was originally developed by Jameson, Schmidt and Turkel [3] and variants of the shock switch were later developed by Swanson and Turkel [104].

A.1.2. Temporal discretisation

Equation A.10 can be rewritten as:

$$\frac{d}{dt}(\Omega_I \mathbf{U}_I) = \mathbf{R}(\mathbf{U}) \tag{A.19}$$

Using second-order implicit backward time-integration, this equation can be expressed as:

$$\frac{3(\Omega\mathbf{U})_I^{n+1} - 4(\Omega\mathbf{U})_I^n + \Omega\mathbf{U})_I^{n-1}}{2\Delta t} = \mathbf{R}(\mathbf{U}^{n+1}) \tag{A.20}$$

where Δt is the physical time step and n denotes the time level. The system of equations A.20 is solved iteratively at every time step by adding a pseudo time-derivative to the left hand side:

$$\frac{d\mathbf{U}}{d\tau} + \frac{3(\Omega\mathbf{U})_I^{n+1} - 4(\Omega\mathbf{U})_I^n + (\Omega\mathbf{U})_I^{n-1}}{2\Delta t} = \mathbf{R}(\mathbf{U}^{n+1}) \tag{A.21}$$

Rewriting Equation A.21 for the m^{th} approximation to $\mathbf{U}_I^{n+1}$ in terms of $\Delta\mathbf{U}_I = \mathbf{U}_I^{m+1} - \mathbf{U}_I^m$ (by adding and subtracting $\frac{3}{2\Delta t}U^m$) gives:

$$\Omega_I^{n+1}\left(\frac{1}{\Delta\tau} + \frac{3}{2\Delta t}\right)\Delta\mathbf{U}_I + \frac{3\Omega_I^{n+1}\mathbf{U}_I^m - 4(\Omega\mathbf{U})_I^n + (\Omega\mathbf{U})_I^{n-1}}{2\Delta t} = \mathbf{R}(\mathbf{U}^{m+1}) \tag{A.22}$$

where $\Delta\tau$ is the pseudo time step and $\Delta\mathbf{U}_I = \mathbf{U}_I^{m+1} - \mathbf{U}_I^m$. This system of equations can now be linearised around $\mathbf{U}_I^m$ using the Jacobian $\mathbf{J}^m = (\partial\mathbf{R}/\partial\mathbf{U})^m$. The pseudo-time intergation which advances the solution from t_n to t^{n+1} then becomes:

$$\left(\frac{\Omega_I^{n+1}}{\Delta\tau} + \frac{3\Omega_I^{n+1}}{2\Delta t} - \mathbf{J}^m\right)\Delta\mathbf{U}_I = \mathbf{R}(\mathbf{U}^m) - \frac{3\Omega_I^{n+1}}{2\Delta t}U_I^m - \frac{4(\Omega\mathbf{U})_I^n - (\Omega\mathbf{U})_I^{n-1}}{2\Delta t} \tag{A.23}$$

and solved iteratively using Newton's method for a specified number of iterations or until $\Delta\mathbf{U}_I$ reaches a specified tolerance. At each Newton iteration or outer iteration level, a Jacobi sub-iteration is needed to solve the matrix problem of Equation A.23.

The advancement in pseudo time can be performed using acceleration techniques such as local time stepping and residual smoothing. For unsteady calculations, the time-accuracy is ensured by the outer iteration level and dual time stepping ensures stability at high Courant numbers. A detailed description of the scheme is given in Sayma et al. [92].

A.2. Sliding plane search and interpolation procedure

At blade row interfaces the inlet and outlet boundary conditions are obtained by interpolation from the upstream and downstream row respectively. This section describes the inter-row information exchange in more detail.

The boundary conditions for rectangular face i on an inlet or outlet surface of a row with rotational speed Ω are found by interpolation from the whole annulus sliding

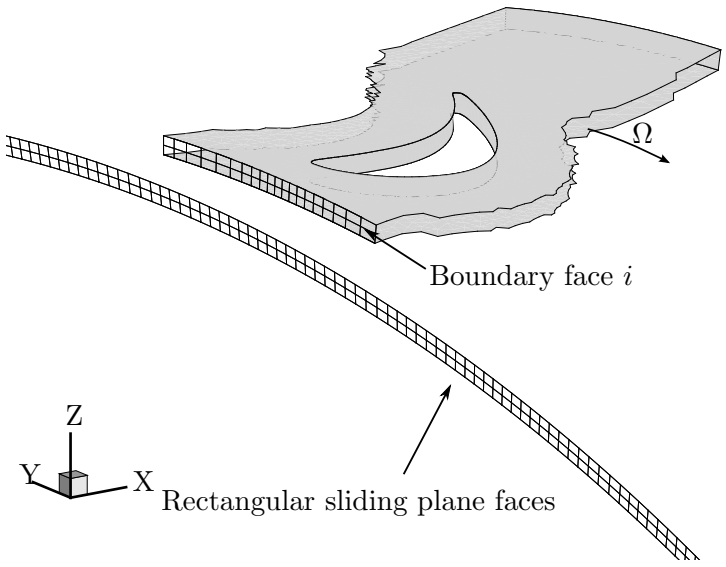


Figure A.2.: Boundary faces at blade row interface

plane (Figure A.2). First, the circumferential position θ_i of the face is calculated by averaging the coordinates of the boundary nodes and rotating the face to its current rotational position at time t.

$$y_i = \frac{1}{4}(y_1 + y_2 + y_3 + y_4)$$
$$z_i = \frac{1}{4}(z_1 + z_2 + z_3 + z_4)$$
$$\theta_i = arg(y_i + iz_i) + \Omega t$$

In the next step, the sliding plane's rectangular faces are divided into triangles which are searched to find the triangular element on the sliding plane which contains point $P(y_i, z_i)$. An initial guess based on the circumferential location θ_i provides the starting element with vertices A, B and C. The routine then tests if point P with coordinates (y_i, z_i) lies within a triangle ABC by comparing the signed area Δ_{ABC} to the three areas formed by point P and two of the triangle's vertices.

The signed area of the triangle ABC is given by:

$$\Delta ABC = \frac{1}{2}\begin{vmatrix} x_A & y_A & 1 \\ x_B & y_B & 1 \\ x_C & y_C & 1 \end{vmatrix}$$

The other three signed areas are given by:

$$\Delta PBC = \frac{1}{2}\begin{vmatrix} x & y & 1 \\ x_B & y_B & 1 \\ x_C & y_C & 1 \end{vmatrix} \qquad \Delta APC = \frac{1}{2}\begin{vmatrix} x_A & y_A & 1 \\ x & y & 1 \\ x_C & y_C & 1 \end{vmatrix}$$

$$\Delta ABP = \frac{1}{2}\begin{vmatrix} x_A & y_A & 1 \\ x_B & y_B & 1 \\ x & y & 1 \end{vmatrix}$$

If an area formed by the edge AB of the triangle and point P has the same sign as the area of the triangle ABC, the point P lies on the same side of edge AB as the vertex C. In other words, the normal between edge AB and P is in the same direction as the normal between edge AB and C. If not, the point must lie on the other side of AB. To illustrate, consider the example shown in Figure A.3. Starting from Triangle 1 and moving along the edges:

$\overline{\mathbf{BC}}$: The signed area ratio is positive as PBC lies on the same side of $\overline{BC}$ as A.

$\overline{\mathbf{CA}}$: The signed area ratio is positive as CPA lies on the same side of $\overline{CA}$ as A.

$\overline{\mathbf{AB}}$: The signed area ratio is negative as ABP lies on the opposite side of $\overline{AB}$ as A.

The search then moves into the direction given by the normal vector from $\overline{AB}$ to point P and Triangle 2 is analysed.

$\overline{\mathbf{CA}}$: The signed area ratio is positive as PCA lies on the same side of $\overline{CA}$ as D.

$\overline{\mathbf{AD}}$: The signed area ratio is positive as APD lies on the same side of $\overline{AD}$ as C.

$\overline{\mathbf{DC}}$: The signed area ratio is negative as DCP lies on the opposite side of $\overline{DC}$ as D.

As before the search then moves into the direction given by the normal vector from $\overline{DC}$ to point P. If the analysis is repeated for Triangle 3, all area ratios are positive

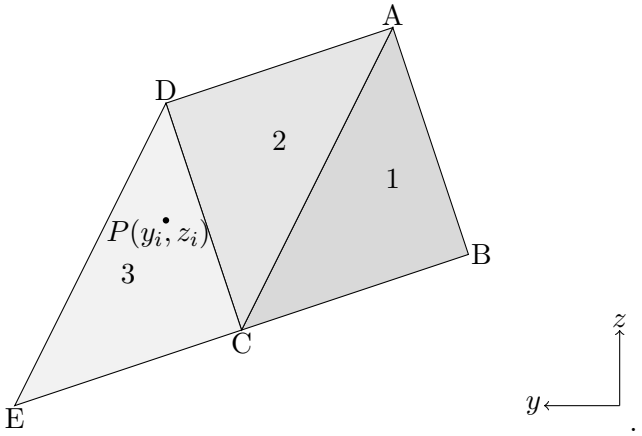


Figure A.3.: Sliding plane search procedure

and the correct triangle is found. The area ratios are then used to find the weights of the three vertices C,D and E used for the evaluation of flow variables at point P:

$$w_C = \frac{\Delta PCE}{\Delta CDE} \quad w_D = \frac{\Delta CPE}{\Delta CDE} \quad w_E = \frac{\Delta CDP}{\Delta CDE} \tag{A.24}$$

$$U_P = w_C U_C + w_D U_D + w_E U_E \tag{A.25}$$

The variables at sliding plane nodes C, D and E are reconstructed from the Fourier coefficients of the corresponding nodes on the master surface.

For the evaluation of boundary fluxes, the flow variables at point P serve as the boundary value while the flow variables on the interior domain are approximated by an average of the nodal values of the boundary face. The inviscid boundary fluxes are evaluated using using Roe averages and artificial dissipation based on an upwind scheme by Swanson and Turkel [104] (see Appendix A.1).

A.3. A summary of relevant results from signal processing

The methodology developed in the main body of this thesis approximates continuous unsteady perturbations and circumferential variations by taking samples of the flow variables at discrete points in time and space. For an accurate approximation, it must be ensured that the discrete samples uniquely define the continuous signal.

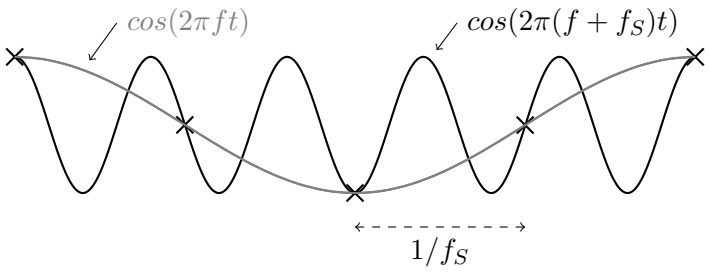


Figure A.4.: Aliasing of signal with frequency f when sampled at frequency f_S

The processes of sampling and reconstructing has been studied in detail in the field of signal processing and some relevant results are summarised here. A detailed explanation can be found in any text book on signal processing (e.g. Shin and Hammond [62]).

A.3.1. Sampling theorem

Sampling refers to a process which converts a continuous signal $g(x)$ into a discrete signal $g(n\Delta x)$ by measuring its value at discrete intervals Δx, where x represents the time or space variable. The reciprocal of the interval is known as the sampling rate $f_S = \frac{1}{\Delta x}$. According to the *Nyquist-Shannon* sampling theorem [96], a continuous band-limited signal which contains no frequency higher than f_H can be perfectly reconstructed if sampled at a rate exceeding $2f_H$:

$$f_S > 2f_H \tag{A.26}$$

The highest frequency which can be perfectly reconstructed at a given sampling rate, is known as the *Nyquist-frequency* and no additional information is gained from sampling beyond the Nyquist frequency.

A.3.2. Aliasing

If the sampling rate of a signal is not high enough to distinguish high frequency components from lower frequency components, a phenomenon known as *aliasing* occurs. To illustrate consider two continuous harmonic functions in time or space

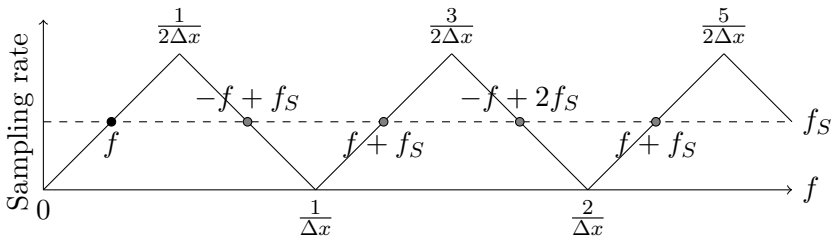


Figure A.5.: Possible aliases of frequency f sampled at rate f_S

as seen in Figure A.4. The low frequency signal is described by the function:

$$g(x) = cos(2\pi f x) \tag{A.27}$$

where f is the frequency of the signal and x represents the time or space variable. If this signal is sampled at a sampling rate f_S the sampled function is given by:

$$g(n\Delta x) = cos(2\pi f n\Delta x) \text{ for integer values of } n \tag{A.28}$$

If the sampling rate is high enough $f_S > 2f$, the continuous signal is recovered. However, if the frequency signal with frequency $f + f_S$ is sampled at the same rate, the sampled sequence is identical to the lower frequency signal:

$$\begin{aligned} g(n\Delta x) &= cos(2\pi(f + f_S)n\Delta x) \text{ for integer values of } n \\ &= cos(2\pi f n\Delta x + 2n\pi) \end{aligned} \tag{A.29}$$

and the two signals become indistinguishable. This phenomenon is known as *aliasing*. Signals with frequency $\pm f + kf_S$ $(k = 1, 2, 3...)$ are possible aliases of a signal with frequency f. The aliases of a given frequency are commonly depicted on a diagram with pleated frequency axis as seen in Figure A.5. In order to avoid aliasing, the signal must be *band-limited* with maximum frequency f_H and the sampling rate must be high enough to resolve the highest frequency ($f_S > 2f_H$).

A.3.3. Application to reduced-passage modelling

For the representation of stationary circumferential variations on a reduced number of passages the sampling is performed in space. The sampling rate represents the number of passages in the sparse assembly and f_H is the highest circumferential

wave number of the perturbation. However, the number of passages can be reduced by taking advantage of circumferential periodicity and reducing the domain from 360° to $360°/k$ where k is the circumferential wave number of the fundamental stationary disturbance. This reduces the number of samples without reducing the sampling interval/sampling rate and the Nyquist criterion remains satisfied.

Aliasing occurs in turbomachines when a disturbance with circumferential wave number k exists in a row with N_B blades and k is greater than the Nyquist mode $N_B/2$.

In the Fourier representation of unsteady flow the presence of additional frequencies can lead to aliasing errors. Higher frequencies may exists due to unsteady phenomena such as vortex shedding in the wake or separation of a boundary layer. Although periodic, this unsteadiness does not necessarily follow a travelling wave pattern which is consistent with the aliased disturbance and introduces errors in the Fourier approximation.

A.4. Non-reflecting boundary conditions: A review

Spurious reflections at boundaries are a result of a mismatch between flow variables inside the domain and boundary conditions. They are frequently observed when an infinite domain is artificially truncated and the prescription of steady conditions leads to reflections of waves at the boundary. Various ways to prevent the occurrence of such reflections exists in literature. If it is possible to extend the domain, 'buffer' or 'sponge' layers which artificially damp out any unsteadiness are often used. This can be done by gradually coarsening the grid towards boundaries or by adding artificial numerical dissipation.

In turbomachinery applications, however, incoming disturbances from upstream blade rows must be allowed to propagate. It is therefore often not possible to use buffer layers and exact or approximate non-reflecting boundary conditions (NRBC) must be used. NRBC decompose the flow field into a sum of modes of different frequencies and wave numbers superposed onto a steady flow. For small amplitude perturbations, this linearisation is exact. Each mode can then be treated independently and expressed in terms of pressure, vorticity and entropy waves according to characteristic theory. NRBC then forms the boundary condition by using the contribution from the incoming waves from outside the domain and from the outgoing waves from inside the domain.

Various NRBC with different levels of approximations have been used in the past. Giles' report [36] condenses previous work on non-reflecting boundary conditions and applies these to the 2D Euler equations and turbomachinery flows. Hall et al. [46] later generalised Giles' work for three-dimensional inviscid flows using a mixed analytical and numerical approach to approximate radial eigenmodes. The most general non-reflecting treatment was developed for the 3D Navier-Stokes equations by Moinier and Giles [78] and also includes viscous radial eigenmodes. Most of these two- and three-dimensional NRBC were implemented on harmonic linearised solvers.

In the time-domain, the decomposition of the flow into a sum of modes of different frequencies and radial and circumferential wave numbers presents an additional hurdle. While it is possible to decompose the flow at the boundaries into eigenmodes and use the treatment developed by Monier and Giles, it is practically difficult since it involves a Fourier transform in the circumferential direction and Fourier-Bessel decomposition in the radial direction. On unstructured grids this requires an additional extrapolation to a uniform grid such as Gerolymos' 'chorochronic harmonic surface' [34]. Due to the complexity involved, this approach is not favoured in time-accurate calculations. Instead, the one-dimensional non-reflecting boundary conditions are used in two or three dimensions by doing a local analysis normal to the boundary and ignoring all tangential variations. This approach is also commonly referred to as quasi-one-dimensional, local one-dimensional boundary condition or characteristic extrapolation and remains in use for unsteady time-domain calculations [70].

An alternative approach in the time-domain would be to use buffer layers with additional numerical dissipation at the boundary. Any unwanted unsteady disturbance could be filtered out by adding a numerical damping term to the flow variables in the vicinity of the boundaries - similar to the term added by Olausson et al. [81] for improved convergence (see Section 2.5.2.3). By adding a correction to the flow variables based on the Fourier approximation, frequencies which are not part of the specified spectrum can be filtered out. In a domain with N unsteady disturbances, the m^{th} disturbance could be removed using Equation A.30 on all nodes in the vicinity of the boundary

$$\frac{\partial U}{\partial t} = ... - \epsilon[U(t) - \sum_{n \neq m}^{N} \hat{U}_n e^{i(\omega_n t)}] \tag{A.30}$$

where ϵ is the damping factor which would have to be gradually changed as the distance from the boundary increases in order to avoid internal reflections.

A very similar approach was followed by Olausson [81] at a rotor-stator interface where upstream interaction is neglected and the buffer layer rotates with the rotor. This makes it possible to remove reflections by damping out unsteadiness:

$$U^{n+1} = \bar{U}^{n+1} - \epsilon(\bar{U}^{n+1} - U_0) \tag{A.31}$$

Olausson's work is based on Richards [87] who specifies the following variation of the damping factor in an axial buffer layer with length L :

$$\epsilon(x) = \epsilon_{max}(1 - \frac{x - L}{L})^{\beta} \tag{A.32}$$

where ϵ_{max} and β are set coefficients. The smooth variation of damping factor prevents the occurrence of internal reflections in the buffer layer. The buffer layer would require additional temporal Fourier transforms and adjustments to the flow solver. A further disadvantage of this approach is that the solution inside the domain is modified. The approach removes all waves of a given frequency regardless of their direction of propagation and can therefore not be used to remove spurious reflections which occur at the beginning of a computation. Furthermore, the choice of appropriate damping factor and buffer layer length would require additional investigations.